A BIOMECHANICAL ANALYSIS OF LIMB COMPRESSION INDUCED BY PNEUMATIC SURGICAL TOURNIQUETS

By

Stephen Francis Paul Callaghan

B. A. Sc., The University of Sherbrooke, 1987

A THESIS SUBMITTED IN PARTIAL FULFILLMENT OF

THE REQUIREMENTS FOR THE DEGREE OF

MASTERS OF APPLIED SCIENCE

in

THE FACULTY OF GRADUATE STUDIES

(DEPARTMENT OF MECHANICAL ENGINEERING)

We accept this thesis as conforming

to the required standard

THE UNIVERSITY OF BRITISH COLUMBIA

August 1989

© Stephen Francis Paul Callaghan, 1989

In presenting this thesis in partial fulfilment of the requirements for an advanced degree at the University of British Columbia, I agree that the Library shall make it freely available for reference and study. I further agree that permission for extensive copying of this thesis for scholarly purposes may be granted by the head of my department or by his or her representatives. It is understood that copying or publication of this thesis for financial gain shall not be allowed without my written permission.

(Department of Mechanical Engineering)
The University of British Columbia
6224 Agricultural Road
Vancouver, Canada
V6T 1W5

Date:

August 29, 1989

Abstract

The introduction of the pneumatic tourniquet has greatly facilitated orthopedic limb surgery. However, the use of this occlusive device is still associated with recurring cutaneous, vascular and neuromuscular injuries. The present research investigates the transmission of pressure from the pneumatic tourniquet to the underlying limb in order to isolate and perhaps minimize the destructive forces causing post-surgical injuries.

A finite element analysis of the tourniquet/limb combination is performed for several patient and cuff parameters. In particular, the influence of cuff design features (such as cuff width and applied surface pressure profile) and patient features (such as arm radius and fat content) on the levels of destructive forces is assessed. Additionally, the use of an Esmarch bandage together with a pneumatic tourniquet is investigated and compared to the conventional tourniquet configuration.

Results from this numerical investigation suggest that high levels of shear and negative axial strain at the cuff edges may account for experimentally observed nerve damage. Furthermore, using wider cuffs which exhibit smooth surface pressure profiles may reduce the risk of post-operative tourniquet-induced nerve injuries. Larger limb radii and greater fat contents generate higher destructive strain levels. And finally, wrapping an Esmarch bandage around the limb at the cuff edges significantly reduces the levels of shear and negative axial strains experienced under occlusion conditions.

Table of Contents

Abstract ii

List of Tables viii

List of Figures ix

Nomenclature xvii

Terminology xx

Acknowledgement xxiv

1 INTRODUCTION 1

1.1 Historical Evolution of the Tourniquet 2

1.2 Injuries Caused by the Use of Pneumatic Tourniquets 4

1.3 Problem Definition 6

1.3.1 Research Objectives 7

2 REVIEW OF LITERATURE 10

2.1 Studies Investigating Pressure Profiles in Soft Tissue 11

2.1.1 Studies Using Artificial Limb Models 11

2.1.2 Studies Using Animals 13

2.1.3 Studies Using Cadavers 14

2.1.4 Studies Using Humans 16

2.1.5 Auerbach's Finite Element Model 17

2.1.6 Hodgson's Analytical Model 19
2.2 Studies Investigating the Mechanisms of Nerve Damage 21
2.2.1 Evidence Supporting the Theory of Ischemia 21
2.2.2 Evidence Supporting the Theory of Mechanical Damage 23
2.2.2.1 Ochoa's Proposed Mechanism of Mechanical Damage . . 25

3 DEFINITION OF MODEL PARAMETERS 26
3.1 Mechanical Properties of Biological Tissue 27
3.1.1 Mechanical Behaviour of Muscle Tissue 28
3.1.2 Mechanical Properties of Blood Vessels 32
3.1.3 Mechanical Properties of Bone 35
3.2 Interactions at the Boundaries 36
3.2.1 Bone/Muscle Interface 36
3.2.2 Skin/Tourniquet Interface 37
3.2.3 Axial Constraint of the Limb Model Ends 38
3.3 Surface Pressure Distribution under the Tourniquet 38
3.3.1 Previous Experimental Results 39
3.3.2 Mathematical Characterization of the Surface Pressure Distribution 40
3.4 Blood Flow Occlusion 42
3.4.1 Experimental Investigations of Blood Flow Occlusion 43
3.4.2 Analytical and Numerical Modelling of Blood Flow Occlusion . . 45

4 FINITE ELEMENT MODELS 48
4.1 Finite Element Method 49
4.1.1 Basic Theory Behind the Finite Element Method 50
4.1.2 Applications of the Finite Element Method to Biological Structures 51
4.2 Model Assumptions 52

4.2.1 Assumptions Pertaining to the Limb 52
4.2.1.1 Assumptions Pertaining to the Limb Structure 53
4.2.1.2 Assumptions Pertaining to the Limb Geometry 54
4.2.2 Assumptions Pertaining to the Main Artery of the Limb 55
4.2.3 Assumptions Pertaining to Loading Conditions 56
4.3 Soft Tissue Compression Models 57
4.3.1 Single-Layer Limb Model 58
4.3.2 Multi-Layer Limb Model 59
4.4 Blood Vessel Occlusion Model 60

5 RESULTS AND DISCUSSION 62

5.1 Comparison of the Finite Element Models with Previous Models 64
5.1.1 Thick-Walled Cylinder Theory 64
5.1.2 Auerbach's Finite Element Model 66
5.1.3 Hodgson's Analytical Model 68
5.1.4 Thomson's and Doupe's Experimental Results 69
5.2 Identification of the Destructive Stress(es) or Strain(s) 70
5.3 Influence of Cuff and Patient Parameters 72
5.3.1 Influence of Boundary Condition Settings 74
5.3.1.1 Bone/Muscle Interface 75
5.3.1.2 Skin/Cuff Interface 75
5.3.1.3 Axial Ends of the Model 76
5.3.2 Influence of Cuff Width 76
5.3.3 Influence of Surface Pressure Profile 78
5.3.3.1 Variable Parameters of the Sinusoidal Pressure Profile . 81
5.3.4 Influence of Limb Radius 81

5.3.5 Influence of Fat Content 83
5.4 Improved Cuff Design 85
5.4.1 Combined Use of the Esmarch Bandage and the Tourniquet Cuff . 85
5.4.1.1 Esmarch/tourniquet Overlap 86
5.4.1.2 Esmarch Relative Pressure 87
5.4.1.3 Esmarch Width 87
5.4.1.4 Discussion 88
5.5 Results from the Blood Vessel Occlusion Model 89

6 CONCLUSIONS AND RECOMMENDATIONS 92

6.1 Conclusions 92
6.1.1 General Conclusions Resulting from the Present Research 93
6.1.2 Specific Conclusions Resulting from the Present Research 94
6.2 Recommendations 97
6.2.1 Recommendations for Clinical Use 97
6.2.2 Recommendations for Future Cuff Designs 98
6.3 Recommendations for Further Investigations 98
6.3.1 Clinical and Experimental Investigations 99
6.3.2 Numerical and Analytical Investigations 100

Bibliography cii

Appendices 222

A NERVE ANATOMY 222

B FINITE ELEMENT THEORY 224

C ANSYS PROGRAM LISTINGS 229

D THICK-WALLED CYLINDER THEORY 252

E LIMB COMPRESSION MODEL SIMULATIONS 256

List of Tables

3.1 Mechanical properties of muscles 108

3.2 Mechanical properties of blood vessels 109

3.3 Mechanical properties of bone 110

5.1 Model properties used for the thick-walled cylinder analysis 111

5.2 Model properties used for replicating Hodgson's model 112

5.3 Model properties of the artery compression model 113

E.1 Code name nomenclature 256

E.2 Cuff width vs limb radius (HON & NON) 258

E.3 Cuff width vs pressure profile (HON & NON) 259

E.4 Limb radius vs pressure profile (HON & NON) 260

E.5 Offset vs peaks (HON & NON) 261

E.6 Cuff width vs fat content (NON) 262

E.7 Fat content vs limb radius (NON) 263

E.8 Fat content vs pressure profile (NON) 264

E.9 Boundary conditions (HON & NON) 265

E.10 Esmarch overlap vs Esmarch width (HOE & NOE) 266

E.11 Esmarch overlap vs Esmarch pressure (HOE & NOE) 267

E.12 Esmarch width vs Esmarch pressure (HOE & NOE) 268

List of Figures

2.1 Limb cross-sections 114

2.2 Griffiths' and Heywood's models 115

2.3 Griffiths' and Heywood's models subjected to a twisting force 115

2.4 McLaren's and Rorabeck's experiments 116

2.5 Pressure profiles recorded by McLaren and Rorabeck 117

2.6 Surface pressure profiles for the pneumatic tourniquet and the Esmarch bandage 117

2.7 Pressure probe used by Shaw and Murray 118

2.8 Shaw's and Murray's experimental setup 119

2.9 Nomogram relating leg circumference, tissue pressure and tourniquet pressure 120

2.10 Relationship between leg circumference and average tissue pressure . . . 120

2.11 Pressure probe used by Breault 121

2.12 Breault's experimental setup 122

2.13 Thomson's and Doupe's experimental results 123

2.14 Effect of cuff width on recorded arterial pressure 123

2.15 Auerbach's finite element mesh of the analyzed limb section 124

2.16 Hydrostatic pressure distribution numerically evaluated by Auerbach compared to Thomson's and Doupe's experimental results 125

2.17 Octahedral shear stress profiles as computed by Auerbach 126

2.18 Hydrostatic pressure distribution analytically calculated by Hodgson compared to Thomson's and Doupe's experimental results 127
2.19 Invagination phenomenon observed by Ochoa et al. 128
2.20 Direction of displacement of the nodes of Ranvier with respect to cuff position 129
2.21 Histogram illustrating the distribution of nerve lesions relative to cuff site 129
3.1 Hill's three element muscle model 130
3.2 Stress-strain curves for three muscle samples 130
3.3 Stress-strain curves for different human squeletal muscles 131
3.4 Stress-strain curves for elastin and collagen 131
3.5 Setup to load arteries in axial tension and internal compression 132
3.6 Material properties of a human brachial artery 132
3.7 Stress-strain curves for arteries 133
3.8 Collapsing process 134
3.9 Cross-sections 135
3.10 Area-perimeter relationship for latex tubes and arteries 135
3.11 Limb model showing the three main boundaries 136
3.12 Experimental parabolic surface pressure profile measured by Breault . . . 137
3.13 Three-dimensional view of the surface pressure profile under a pneumatic tourniquet 137
3.14 Hodgson's surface pressure profiles 138
3.15 Comparison between smooth and discretized surface pressure profiles . . 139
3.16 Three main pressure profiles applied to the limb model 140
3.17 Varying offset and multiple peak characteristics of the sinusoidal pressure profile 141
3.18 Setup to simulate blood flow through the arteries 142

3.19 Experimental results of occlusion pressure vs the ratio of cuff width to arm circumference 143
3.20 Results from beam model simulation of artery collapse 143
4.1 Steps performed to obtain the limb compression model 144
4.2 Muscle structure 145
4.3 Finite element models of an axisymmetric limb 146
4.4 Loading conditions imposed 147
4.5 Boundary conditions as applicable to the limb compression model 148
4.6 Boundary conditions as applicable to the artery model 149
4.7 Single-layer limb compression model 150
4.8 Multi-layer limb compression model 151
4.9 Full section of the finite element artery model 152
4.10 Quarter section of the finite element artery model 153
5.1 Single-layer finite element limb compression model subjected to thick-walled cylinder conditions 154
5.2 Influence of radial mesh on the model's accuracy (absolute average percentage difference) 155
5.3 Influence of radial mesh on the model's accuracy (maximum percentage difference 155
5.4 Influence of axial mesh on the model's accuracy (absolute average percentage difference) 156
5.5 Influence of axial mesh on the model's accuracy (maximum percentage difference) 156
5.6 Comparison of stress profiles for varying E_z 157
5.7 Comparison of stress profiles for varying ν_{rz} and $\nu_{\theta z}$ 158
5.8 Radial stress profiles for varying $\nu_{r\theta}$ 159

5.9 Circumferential stress profiles for varying $\nu_{r\theta}$ 160
5.10 Hydrostatic pressure distributions (14 elements) 161
5.11 Hydrostatic pressure distributions (24 elements) 162
5.12 Axial strain distributions for a sinusoidal surface pressure profile 163
5.13 Axial strain distributions for a rectangular surface pressure profile 163
5.14 Axial strain distributions when the smallest arm radius considered in Hodgson's study is assumed 164
5.15 Axial strain distributions when the largest arm radius considered in Hodgson's study is assumed 164
5.16 Comparison of the maximum relative pressure at the bone level 165
5.17 Comparison of the width of the 100% pressure zone at the bone 165
5.18 Component stress profiles 166
5.19 Principal stress profiles 167
5.20 Combination stress profiles 168
5.21 Component strain profiles 169
5.22 Predicted axial strain profiles for varying boundary condition setting at each nerve location (single-layer model) 170
5.23 Predicted shear strain profiles for varying boundary condition setting at each nerve location (single-layer model) 171
5.24 Predicted axial strain profiles for varying cuff width (single-layer model) . 172
5.25 Predicted shear strain profiles for varying cuff width (single-layer model) 173
5.26 Predicted axial strain profiles for varying cuff width at each nerve location (single-layer model) 174
5.27 Predicted shear strain profiles for varying cuff width at each nerve location (single-layer model) 175
5.28 Maximum axial strain intensities for varying cuff width 176

5.29 Maximum shear strain intensities for varying cuff width 177
5.30 Average maximum axial strain intensities for varying cuff width and limb radius 178
5.31 Average maximum shear strain intensities for varying cuff width and limb radius 179
5.32 Predicted axial strain profiles for varying surface pressure profile (single-layer model) 180
5.33 Predicted shear strain profiles for varying surface pressure profile (single-layer model) 181
5.34 Predicted axial strain profiles for varying surface pressure profile at each nerve location (single-layer model) 182
5.35 Predicted shear strain profiles for varying surface pressure profiles at each nerve location (single-layer model) 183
5.36 Maximum axial strain intensities for varying surface pressure distribution 184
5.37 Maximum shear strain intensities for varying surface pressure distribution 185
5.38 Average maximum axial strain intensities for varying surface pressure distribution and cuff width 186
5.39 Average maximum shear strain intensities for varying surface pressure distribution and cuff width 187
5.40 Average maximum axial strain intensities for varying surface pressure distribution and limb radius 188
5.41 Average maximum shear strain intensities for varying surface pressure distribution and limb radius 189
5.42 Average maximum strain intensities for varying surface pressure distribution and fat content (multi-layer model) 190

5.43 Average maximum axial strain intensities for varying pressure offset (sinusoidal pressure distribution) 191
5.44 Average maximum shear strain intensities for varying pressure offset (sinusoidal pressure distribution) 192
5.45 Predicted axial strain profiles for varying limb radius (single-layer model) 193
5.46 Predicted shear strain profiles for varying limb radius (single-layer model) 194
5.47 Predicted axial strain profiles for varying limb radius at each nerve location (single-layer model) 195
5.48 Predicted shear strain profiles for varying limb radius at each nerve location (single-layer model) 196
5.49 Maximum axial strain intensities for varying limb radius 197
5.50 Maximum shear strain intensities for varying limb radius 198
5.51 Average maximum axial strain intensities for varying limb radius and cuff width 199
5.52 Average maximum shear strain intensities for varying limb radius and cuff width 200
5.53 Predicted axial strain profiles for varying fat content at each nerve location (multi-layer model) 201
5.54 Predicted shear strain profiles for varying fat content at each nerve location (multi-layer model) 202
5.55 Maximum axial strain intensities for varying fat content (multi-layer model)203
5.56 Maximum shear strain intensities for varying fat content (multi-layer model)203
5.57 Proposed Esmarch/tourniquet combination and its resulting pressure profile204
5.58 Average maximum axial strain intensities for varying Esmarch overlap and width 205

5.59 Average maximum shear strain intensities for varying Esmarch overlap and width 206
5.60 Average maximum axial strain intensities for varying Esmarch overlap and cuff pressure 207
5.61 Average maximum shear strain intensities for varying Esmarch overlap and cuff pressure 208
5.62 Average maximum axial strain intensities for varying Esmarch width and cuff pressure 209
5.63 Average maximum shear strain intensities for varying Esmarch width and cuff pressure 210
5.64 Comparison of predicted axial strain profiles (single-layer model) 211
5.65 Comparison of predicted shear strain profiles (single-layer model) 212
5.66 Schematic representation of the pneumatic tourniquet as it is inflated . . 213
5.67 Load reduction induced by upward-curving of the cuff edges 214
5.68 Cross-section of the collapsed artery 215
5.69 Predicted occlusion pressures for varying cuff width and artery length . . 216
5.70 Predicted occlusion pressures for varying cuff width and E_r 216
5.71 Predicted occlusion pressures for varying cuff width and E_θ 217
5.72 Predicted occlusion pressures for varying cuff width and E_z 217
6.1 Proposed multi-bladder tourniquet 218
6.2 Proposed Esmarch/tourniquet configuration 219
6.3 Examples of pressure sensors 220
6.4 Example of experimental setup to investigate blood flow occlusion 221

A.1 Structural features of a peripheral nerve 222
A.2 General plan of a myelinated nerve fiber 223

B.1 Single finite element 224
B.2 Simple two element structure 228

D.1 Thick-walled cylinder under limb compression constraints 252
D.2 Free body diagram of a selected annulus 253

Nomenclature

$\mathbf{a}$	Inner radius of the cylinder (m)
$\{\mathbf{a}\}$	Displacement vector (m)
$\mathbf{a_i}$	Displacements associated with node i (m)
$\mathbf{A}$	Cross-section area of the artery (m^2)
$\mathbf{A_0}$	Initial cross-section area of the artery (m^2)
$\mathbf{b}$	Outer radius of the cylinder (m)
CIRC	Limb circumference (m)
DOP	Doppler occlusion pressure (Pa)
$\overline{\mathbf{error}}$	Average error (%)
$\mathbf{E}$	Young's modulus (Pa)
$\mathbf{E_r}$	Radial Young's modulus (Pa)
$\mathbf{E_z}$	Axial Young's modulus (Pa)
$\mathbf{E_\theta}$	Circumferential Young's modulus (Pa)
$\{\mathbf{f}\}_\mathbf{i}$	Force vector of element i (N)
$\{\mathbf{F}\}$	Body force vector of an element (N/m^3)
$\mathbf{h}$	Wall thickness of the vessel (m)
$\mathbf{I}$	Moment of inertia (m^4)
$[\mathbf{k}]_\mathbf{i}$	Stiffness matrix of element i (N/m)
$\mathbf{K}$	Bulk modulus (Pa)
$[\mathbf{K}]$	Global stiffness matrix of the structure (N/m)
$\mathbf{l}$	Half-length of the artery section (m)
MESH	Number of elements in the axial or radial direction

$\mathbf{n}$	Number of lobes in the collapsed configuration
$\mathbf{N}$	Number of peaks in the sinusoidal pressure distribution
$\mathbf{N_i}$	Linear shape functions associated with node i
$\mathbf{O_E}$	Esmarch overlap (%)
$\mathbf{OFF}$	Pressure offset at the edges of the cuff (%)
$\mathbf{P}$	Transmural pressure on the artery (Pa)
$\mathbf{P_0}$	Outer pressure on the cylinder (Pa)
$\mathbf{P_{dia}}$	Diastolic pressure (Pa)
$\mathbf{P_E}$	Esmarch pressure (Pa)
$\mathbf{P_{max}}$	Maximum pressure at the center of the cuff (Pa)
$\mathbf{P_{occ}}$	Occlusion pressure (Pa)
$\mathbf{P_e(z)}$	Exponential pressure distribution (Pa)
$\mathbf{P_r(z)}$	Rectangular pressure distribution (Pa)
$\mathbf{P_s(z)}$	Sinusoidal pressure distribution (Pa)
$\mathbf{PD}$	Pressure distribution
$\mathbf{PE}$	Potential energy (J)
$\mathbf{r}$	Radial position (m)
$\mathbf{r_0}$	Outer radius of the artery (m)
$\mathbf{r_b}$	Bone radius (m)
$\mathbf{r_l}$	Limb radius (m)
$\mathbf{t}$	Thickness of the element (m)
$\{\mathbf{T}\}$	Traction force vector of an element (N/m)
$\mathbf{u}$	Displacement in the x direction (m)
$\mathbf{U}$	Strain energy of an element (J)
$\mathbf{v}$	Displacement in the y direction (m)
$\mathbf{W}$	Total energy of an element (J)

$\mathbf{W_E}$	Esmarch width (m)
WIDTH	Cuff width (m)
$\mathbf{\Gamma}$	Boundary of an element (m)
$\{\varepsilon\}$	Strain vector (m/m)
$\varepsilon_{\mathbf{z}}$	Axial strain (m/m)
ε_θ	Circumferential strain (m/m)
$\mu(\mathbf{z})$	Step function
ν	Poisson ratio
$\nu_{\mathbf{rz}}$	Poisson ratio from radial to axial direction
$\nu_{\mathbf{r}\theta}$	Poisson ratio from radial to circumferential direction
$\nu_{\theta\mathbf{z}}$	Poisson ratio from circumferential to axial direction
$\{\sigma\}$	Stress vector (Pa)
$\overline{\sigma}$	Octahedral shear stress (Pa)
$\sigma_{\mathbf{h}}$	Hydrostatic pressure (Pa)
$\sigma_{\mathbf{n}}$	Principal stresses for n=1,2,3 (Pa)
$\sigma_{\mathbf{x}}$	Stress in the x direction (Pa)
$\sigma_{\mathbf{y}}$	Stress in the y direction (Pa)
$\sigma_{\mathbf{i,F.E.}}$	Stress at position i as determined by the finite element method (Pa)
$\sigma_{\mathbf{i,theo}}$	Stress at position i as determined by the thick-walled cylinder theory (Pa)
$\sigma_{\mathbf{r}}(\mathbf{r})$	Radial stress distribution (Pa)
$\sigma_\theta(\mathbf{r})$	Circumferential stress distribution (Pa)
$\tau_{\mathbf{xy}}$	Shear stress in the xy plane (Pa)
$\{\psi\}$	Displacement vector (m)

Terminology

Acidosis: an abnormal state of reduced alkalinity (measured acidity) of the blood and of the body tissues.

ANSYS (analysis system): finite element software package developed by Swanson Analysis Systems.

Arteriole: any of the small terminal twigs of an artery that ends in capillaries.

Asphyxia: a lack of oxygen or excess of carbon dioxide in the body that is usually caused by interruption of breathing and that causes unconsciousness.

Axon: a usually long and single nerve-cell process that usually conducts impulses away from the cell body.

Axoplasm: the protoplasm (organized colloidal complex of organic and inorganic substances that constitutes the living nucleus of the cell) of an axon.

Brachial artery: artery located in the upper part of the arm or forelimb from shoulder to elbow.

Circulatory stasis: slowing of the current of circulating blood.

Collagen: an insoluble fibrous protein that occurs in vertebrates as the chief constituent of connective tissue fibrils and in bones and yields gelatin and glue on prolonged heating with water.

Cranial: of or relating to the skull or cranium.

Degeneration: deterioration of a tissue or an organ in which its function is diminished or its structure is impaired.

Demyelinated: caused or characterized by the loss or destruction of myelin.

Diastolic pressure: pressure associated with the period of dilatation of the heart, especially of the ventricles.

Doppler flowmeter: apparatus which measures fluid flow using ultrasound vibrations.

Elastin: a protein that is similar to collagen and is the chief constituent of elastic fibers.

Exsanguination: action of draining blood out of a limb.

Extracellular fluid: fluid located outside a cell or the cells of the body.

Femoral artery: the chief artery of the thigh lying in its anterior inner part.

Femur: the proximal bone of the hind or lower limb.

Fasciculus: a slender bundle of anatomical fibers.

Fibrinolytic activity: enzymatic breakdown of fibrin (fibrous protein necessary for the clotting of blood).

Fibula: the outer and usually the smaller of the two bones of the hind limb of tetrapod vertebrates between the knee and ankle.

Hemostasis: cessation of blood flow.

Humerus: the long bone of the upper arm or forelimb extending from the shoulder to the elbow.

Hypertension: abnormally high blood pressure, especially arterial blood pressure; the systemic condition accompanying high blood pressure.

Invagination: an act or process of invaginating (folding in so that an outer becomes an inner surface).

Ischemia: local deficiency in red blood cells, in hemoglobin, or in total blood volume.

Manometer: an instrument (as a pressure gauge) for measuring the pressure of gases and vapors.

Myelin: a soft white somewhat fatty material that forms a thick myelin sheath about the protoplasmic core of a myelinated nerve fiber.

Myelinated: having a myelin sheath (layer of myelin surrounding some nerve fibers).

Node of Ranvier: a constriction in the myelin sheath of a myelinated nerve fiber.

Occlusion pressure: tourniquet pressure necessary to cause the cessation of blood flow.

Schwann cell: a cell of the neurilemma (delicate nucleated outer sheath) of a nerve fiber.

Slit catheter: diagnostic device for compartmental syndrome to determine whether or not surgery is necessary.

Systolic pressure: pressure associated with the period of contraction of the heart, especially that of the ventricles during which blood is forced into the aorta and the pulmonary trunk.

Thrombosis: the formation or presence of a blood clot within a blood vessel during life.

Tibia: the inner and usually larger of the two bones of the vertebrated hind limb between the knee and ankle.

Unmyelinated: lacking a myelin sheath (layer of myelin surrounding some nerves).

Vascular surgery: surgery relating to a channel for the conveyance of a body fluid or to a system of such channels.

Vena cava: any of the large veins by which in air-breathing vertebrates the blood is returned to the right atrium of the heart.

Acknowledgements

I wish to thank the Natural Science and Engineering Research Council of Canada and the Centre for Integrated Computer Research Systems for their financial assistance which provided me with the opportunity to undertake and complete this project.

The assistance and support of Dr. D. P. Romilly throughout this endeavor are greatly appreciated. Without his help, this project could not have been realized. Additional thanks are due to Gerry Rohling for answering all my questions concerning computer matters. In addition, I wish to thank Swansons Analysis Systems for their suppport pertaining to ANSYS.

I also wish to acknowledge the substantial contribution of Martine Breault who, through her work, provided a clinical definition of the problem upon which the present numerical investigation is based.

Finally, my special thanks to Louise Charlebois for her moral and secretarial support.

Chapter 1

INTRODUCTION

The tourniquet is a surgical device generally used to control bleeding during surgery on upper and lower limbs. It was originally designed to provide a bloodless field at the surgical site in order to facilitate and accelerate required operations [1,2]. The tourniquet achieves hemostasis by applying external pressure to the limb. This constricts the underlying blood vessels, thereby preventing the flow of blood to the extremities.

The most widely accepted form of tourniquet used in surgery today consists of a pneumatic cuff inflated by a pressure controller. The pressure level is determined by the surgeon. However, since limited accurate information on the safe use of tourniquets is currently available, the pressure level employed is typically subjective, being selected predominantly on experience and skill. Overpressurization is therefore often encountered when this type of selection method is used. Consequently, damage to the underlying soft tissues, such as muscles, arteries, and nerves, is sometimes a resulting side effect of vascular surgery [3].

The mechanisms responsible for the impairment of underlying soft tissues subjected to external pressure by a pneumatic cuff are not well understood due to insufficient anatomical and mathematical evidence. Nevertheless, two distinct hypotheses have emerged which may account for soft tissue damage incurred during vascular surgery. The first relates to asphyxia and ischemia, i.e., the lack of blood and/or oxygen supply to the tissues [4,5,6], while the second pertains to excess stress and strain on the tissues [3,7]. While the former appears more likely, there is sufficient evidence to conclude that damage

to soft tissues, especially nerves, is the direct result of mechanical compression by the tourniquet and not of lack of blood and/or oxygen supply [3].

Present day surgical tourniquets possess certain structural features, such as pressure distribution and width, which may not be optimum for their defined task; i.e., to occlude the blood vessels without injury to the soft tissues at the constriction site. Consequently, with the goal of defining the optimum characteristics of tourniquets, there is a need to understand the mechanisms governing the transfer of pressure from the tourniquet to the soft tissues and to isolate the causes of soft tissue damage. As a result, the purpose of the current investigation is first, to determine the stress and strain distributions in a limb subjected to external pressure from a pneumatic tourniquet and then, to suggest possible solutions for optimizing the cuff design and the occlusion procedure.

The historical evolution of the tourniquet has been extensively reviewed in the literature [13,40] and is presented here for completness due to the multi-disciplinary nature of this work.

1.1 Historical Evolution of the Tourniquet

The evolution of occlusive devices spans several centuries. Roman surgeons used constrictive devices to avoid hemorrhages when performing amputations [8]. Around 100 A.D., Archigenes and Heliodorus tied narrow bands above and below the surgical site to control venous bleeding [9,10]. In 1653, William Fabry of Hilden improved this procedure by inserting sticks to control the tightness of the occlusive bandage [9-11]. In 1674, Morell further modified this technique by using a paddled spanish windlass, originally employed for strangulation, to achieve hemostasis [9-11]. And eventually, Ambroise Pare employed a wider bandage above the amputation site to effect occlusion [2,9,10].

However, it was not until 1718 that the first significant improvement to occlusive

devices was effected, when the French surgeon Jean-Louis Petit introduced the screw mechanism, which served to tighten the cloth bandage wrapped around the limb. The now common reference "tourniquet" originates from this device and has its root in the French word "tourner" which means to turn. The Petit tourniquet remained in use until the end of the eighteenth century [9,10,12].

In 1864, Joseph Lister discovered that by elevating the limb prior to applying the tourniquet, exsanguination resulted. Shortly afterwards, this blood draining process was instead induced by strapping the limb with a rubber bandage. Several improvements to the exsanguination technique followed, notably by Niçoise and Grandesso-Sylvestri [10,13], and by 1873, this method replaced the tourniquet altogether. In particular, Johann Friederich August van Esmarch made use of a two inch wide elastic rubber tube to achieve a bloodless field distal to the constricted site [9,10]. Most surgeons adopted the Esmarch bandage since it maintained a constant pressure on the limb for the whole duration of the surgical procedure. This differed from the Petit tourniquet which often slackened during the operation resulting in flooding of the surgical field. However, in 1881, Volkman recognized that there was a greater risk of injury and trauma with the Esmarch bandage, after observing and recording the sensation loss in the limbs of patients on whom the bandage was used [12].

In 1904, Cushing developed the first version of the pneumatic tourniquet [8,9,14,56]. Despite its crude design, this cylindrical rubber bladder, inflated with a bicycle pump, fulfilled the needs of the surgeon and considerably reduced the risk of injury or trauma. A manometer connected to the rubber bladder was used to monitor the applied pressure. In later years, modifications to this instrument were introduced. Specifically, August Brier initiated the use of two adjacent tourniquets in 1908, and Holmes designed the dual tourniquet (two adjacent bladders) in 1963.

Although the basic concept of the pneumatic tourniquet still remains today, the control system that regulates the amount of pressure applied is much more sophisticated than the initially employed surgical manometer. In 1982, J.A. McEwen and R.W. McGraw devised a tourniquet system which utilizes a microprocessor to control the pressure level. This innovative system provides a much more detailed regulation of cuff pressure thereby greatly reducing the risk of post-operative injuries associated with overpressurization or underpressurization [15].

1.2 Injuries Caused by the Use of Pneumatic Tourniquets

There is historical evidence that blood flow occlusion in a limb may damage both soft and hard tissues due to ischemia and/or mechanical compression [15,16]. The main factors associated with such impairments are the level of pressure applied [17-20], the duration of the surgical procedure [5,18,21,22] and the temperature of the limb during the operation [18]. These factors are responsible for several kinds of injuries including cutaneous [8], vascular [23], muscular [22,23], and neurological [22,24]. In addition, compression of the limb was found to induce abnormal levels of swelling subsequent to tourniquet release. Furthermore, cuff overinflation may cause vascular problems such as deep vein thrombosis [25,26], fibrinolytic activity increase [3], acidosis [28], systemic circulation deregulation [29], hypertension [30], and circulatory stasis [28]. In extreme cases, external compression may even induce structural changes in bone marrow [31]. However, the most significant and discomforting side effect of pneumatic constriction is damage to the peripheral neurological system, i.e., the peripheral nerves [32]. This was confirmed in 1943 by Bentley and Schlapp who reported that direct nerve damage was considered more important than blood vessel damage [33].

Despite the multiple improvements made to the design of occlusive devices since their

introduction, recent surveys indicate that there still remains some risk of injury as a result of blood flow arrest. For example, over an eighteen month period, Dr. McEwen of Vancouver General Hospital's Biomedical Engineering Department surveyed approximately 10 000 surgical procedures which required the use of a pneumatic tourniquet. During this time, he identified fifteen incidences of suspected tourniquet-induced complications [34]. Six of these involved varying degrees of nerve paralysis. Consequently, the risk of injury was estimated at 0.06%; however, certain factors such as transient and reversible nerve damage were unaccounted for in this figure. Furthermore, some incidents may not have been reported by the surgeons for fear of potential liability claims. For these reasons, McEwen estimated that 0.1%, rather than 0.06%, of all procedures involving the use of pneumatic tourniquets resulted in some degree of nerve paralysis or trauma. Assuming this result is valid and considering that annually over one million surgical procedures involve the use of pneumatic tourniquets, then approximately 1 000 patients per year suffer from post-surgical nerve paralysis or trauma induced by pneumatic tourniquets.

Besides the above survey, additional evidence also establishes pneumatic tourniquets as one of the direct causes of nerve damage. In 1969, Brunner observed several incidents of nerve palsy, subsequent to operations on the arm utilizing pneumatic tourniquets [18]. And, in 1980, Kellerman suggested that tourniquet pressure, rather than prolonged ischemia, was the main factor responsible for nerve palsies [22]. Since then, several scientists have researched the impact of tourniquet pressure, surgery duration, and limb temperature on underlying nerves. This has led to the formulation of several relationships between these parameters and the subsequent tourniquet-induced nerve damage.

McEwen has reported that the widespread use of tourniquets in surgery has been accompanied by continuing reports of limb paralysis, nerve damage and other such injuries [34]. He suggested that these complications are often caused by: overpressurization

resulting in nerve compression at the cuff site; underpressurization resulting in passive congestion of the nerve; lengthy application period of the tourniquet; and specialized application of tourniquet pressure without consideration of local anatomy. Although the pressure level and duration of application of pneumatic tourniquets are under the direct control of the physician, these factors are increasingly being recognized as directly responsible for varying degrees of nerve damage. In 1944, Denny-Brown and Brenner addressed the issue of nerve damage intensity by ranking nerve injury according to increasing severity [5]. Their ranking was as follows: no nerve damage, paralysis with quick and complete recovery upon release of pressure, paralysis with delayed recovery devoid of degeneration, and complete anatomic lesion with degenerative phenomena. Most clinical and experimental studies focus on the third categorization, i.e., paralysis with delayed recovery devoid of degeneration. This may be described in general terms as a pressure lesion lasting from one to nineteen days (possibly longer), with no signs of excitability loss distal to the lesion and with preservation of gross sensation throughout the limb.

Finally, the suggested mechanisms responsible for nerve damage are as diversified as the number of researchers themselves. In earlier studies, ischemia and asphyxia were usually designated as the main causes of nerve palsies incurred subsequent to tourniquet use. Today, direct mechanical compression is the preferred explanation; however, the underlying cause of nerve lesions is under constant investigation. The study at hand addresses this issue as well as others which are described in the next section.

1.3 Problem Definition

Pneumatic tourniquets presently in use in hospitals across North America succeed in stopping blood flow to the distal regions of the limb during surgery, but not in the most optimal manner. Although the guidelines for pressure level and duration of application

of the cuff have been extensively reviewed by hospitals, cuff manufacturers and medical researchers, design improvements have been minimal since the appearance of Cushing's bicycle pump inflated model. Based on the shortcomings of pneumatic tourniquets presented in Section 1.2, it is obvious that such improvements are necessary. However, before the present tourniquet design can effectively be improved, a fundamental understanding of the pressure transmission between the pneumatic cuff and the limb must be acquired. This implies that an accurate stress, strain and pressure mapping of the limb must first be completed.

The current research initiative is directed towards fulfilling this task and is structured into four phases. In the first phase, a numerical limb model is constructed which attempts to replicate the actual limb anatomy. The second phase consists of locating the regions of maximum stresses and strains in the limb subjected to cuff pressure and then correlating these regions with experimentally observed locations of nerve damage to determine possible contributions to injuries. The third phase evaluates the effect of varying cuff and patient parameters on the regions of maximum stresses and strains. And the fourth phase utilizes these findings to suggest possible improvements to tourniquet designs. The objectives of this research are outlined below.

1.3.1 Research Objectives

The ultimate goal of this research is to eventually minimize the risk of injuries induced by the application of a pneumatic tourniquet. Thus, the mechanical states experienced by a limb subjected to external pressure must be determined. In order to accomplish this, the following six objectives are defined.

- **I. Identify and critically review the existing research literature related to stress and strain distributions in a limb subjected to pressure from a**

pneumatic tourniquet. Previous experimental, theoretical and numerical studies relevant to stress and strain mapping are examined to serve as a basis for this research. Particular attention is given to research utilizing the finite element method as a tool to simulate anatomical systems and to describe their behaviour when subjected to specified external conditions. This literature review is presented in Section 2.1.

- **II. Clearly describe the frequently cited mechanisms considered responsible for nerve damage resulting from the use of pneumatic cuffs.** The proposed mechanisms endorsed by various researchers, along with the results of biological (animal and human) dissections on which these proposals are based, are presented. Furthermore, locations of the nerve lesions relative to positions on the cuff are discussed. This literature review is presented in Section 2.2.

- **III. Define the parameters necessary for modelling a biological system using finite element theory.** In order to accurately simulate anatomical systems, key features such as material properties, boundary conditions and surface pressure profiles, are reviewed. The elasticity and viscoelasticity of muscles, arteries and bones are quantified by stiffness and compressibility factors, i.e., by the Young's modulus and the Poisson ratio respectively. Interactions between bone and muscle, as well as between cuff and skin are also defined. The pressure profile applied to the limb surface by the pneumatic cuff, which was previously determined through experimental investigations, is redefined in mathematical terms. This work is discussed in Chapter 3.

- **IV. Accurately simulate a limb subjected to surface pressure from a pneumatic cuff using the finite element method.** With the assistance of a sophisticated finite element package (ANSYS), two feasible models of a human

limb are constructed and analyzed: in one, the limb consists of a single homogeneous orthotropic elastic material, and in the other, it is composed of three soft tissue layers. Comparisons between these models and the currently existing models discussed in Section 2.1 are made in order to assess the accuracy of the former in predicting the sites of reported nerve damage. This work is presented in Chapters 4 and 5.

- **V. Numerically determine the effects of variations in tourniquet and limb parameters on the stress and strain profiles of specific nerves within the limb.** The stress and strain profiles at three positions (corresponding to the locations of the four major nerves of the arm) are determined for different cuff characteristics (i.e., surface pressure distribution and cuff width). The effects of variations in anatomical structure (i.e., limb radius and fat content) are also investigated. Moreover, the influence of boundary condition settings is quantified. This analysis is presented in Chapter 5.

- **VI. Translate the results obtained from the numerical analysis to recommendations for improving current tourniquet designs.** General conclusions drawn from the numerical and theoretical research work are followed by more specific conclusions on the effects of axial and shear strain and their possible association with the proposed mechanisms of nerve damage. Optimum surface pressure distributions as well as optimum cuff widths for specific patient parameters are also suggested. Finally, recommendations for further numerical and experimental work are presented. These conclusions and recommendations are presented in Chapter 6.

The following chapter provides the background information necessary to provide a comprehensive understanding of the current problems associated with pneumatic cuffs. This is introduced by reviewing existing research on the subject.

Chapter 2

REVIEW OF LITERATURE

Since its appearance in 1904, the surgical pneumatic tourniquet has been the subject of several investigations, many of them providing information necessary to produce a more efficient design. Nevertheless, the automated version which is routinely used in orthopedic surgery today still results in a number of compression-related nerve injuries. Many researchers have investigated the probable causes of these injuries. In doing so, the limb portion located beneath the pneumatic cuff has been extensively analyzed (experimentally, numerically and analytically).

Research in this area can be generally discussed as a two step process. The first step towards obtaining a better understanding of compression-related nerve injuries is to determine the load distribution on and within a limb subjected to tourniquet pressure. To provide this information, pressure, stress and strain patterns produced by an inflated tourniquet placed around a limb have been obtained both numerically and experimentally. Areas of predicted peak stress or strain were then compared to experimentally observed regions of nerve damage. Subsequent experiments have also been performed on artificial limbs, animals, cadavers, and human subjects to determine the pressure distribution of soft tissue when it is subjected to surface pressure from a pneumatic tourniquet.

The next step is to identify the mechanisms responsible for creating the nerve lesions observed beneath the tourniquet. Previous work has concentrated predominantly on possible mechanisms responsible for observed lesions in the peripheral nerves located near the constricted area. The following two sections elaborate on these steps.

2.1 Studies Investigating Pressure Profiles in Soft Tissue

Several researchers have acknowledged the dangers associated with the use of pneumatic tourniquets. Lewis et al. [4] observed that the interruption of blood flow to the nerves of the arm was followed by the paralysis of these nerves. In 1972, Fowler et al. [21] recorded ascending action potentials from the sciatic nerves of live baboons and noted a net decrease in impulse velocity when the limb was compressed. By dissecting baboon thighs that had been subjected to pressure from a tourniquet, Ochoa et al. [3] found that the large nerve fibers had incurred significant morphological changes. Today, overpressurization is generally accepted as the primary cause of nerve injuries induced by tourniquet pressure, while ischemia is considered a secondary cause [3,7]. Thus, there is a significant need to understand and quantify the distribution of pressure applied by a tourniquet cuff. Research on stress and strain mapping is discussed below.

2.1.1 Studies Using Artificial Limb Models

Before attempting to identify pressure distributions in anatomical systems, a few researchers have experimentally mapped pressure profiles using biomechanical models. In 1973, Griffiths and Heywood [19] proposed a simple theoretical model to investigate the effects of surface pressure on underlying soft tissue. This model was based on two assumptions: first, mechanical nerve damage may result from contortion of nerve tissues; and second, nerve tissue is very tolerant to simple ischemia, even if prolonged for several hours. From these assumptions, they inferred that high pressure over a short period of time would be more likely to produce nerve damage than low pressure over a long period of time. Sinclair [36] has suggested that "a pressure cuff does not necessarily deliver a perfect uniform developing pressure to the limb, and transmission of this pressure to any individual point in the limb is a function of numerous factors, such as depth and

consistency of the intervening structure." Eckhoff [37] confirmed this concept in practice by acknowledging both the relative immunity of the lower limbs to the effects of pressure and the observed selective vulnerability of the radial nerve.

Griffiths and Heywood offered two variations of their limb model. The first consisted of a rigid bony core surrounded by tissue exhibiting the properties of a fluid, i.e., with no resistance to shear. The second considered the surrounding tissue as having the properties of an elastic solid. If Griffiths' and Heywood's first model is accepted, then any pressure applied to the surface of the limb will be equally transmitted throughout the tissue. This suggests that all nerves are equally vulnerable, since pressure effects will produce similar reactions and will be independent of their position on the arm or the leg. This observation is contrary to previous reports [37]. On the other hand, the second model substitutes this uniform pressure distribution with a system consisting of two mutually perpendicular stresses whose magnitudes vary with radial position. This suggests that if direct stress is the cause of tissue damage, then deeply embedded nerves will be more susceptible to injury, since the magnitudes of radial and shear stress increase with tissue depth. It also suggests that arterial pressure must be greater than cuff pressure, despite the fact that this is contrary to accepted evidence [38]. Figures 2.1a and 2.1b illustrate the cross-sections of the upper and lower limbs, including the positions of the major nerves. Figures 2.2a and 2.2b present Griffiths' and Heywood's two models, with their corresponding radial and circumferential stress profiles. In addition to these two normal stresses, a shear stress may develop when pressure is applied to a non-fluid material. Figure 2.3 shows this shear stress profile when the models are subjected to a twisting force. It should be noted that the radial nerve is more susceptible to damage when a pneumatic cuff is employed [37], and that its location coincides with the area of maximum shear and radial stresses (according to Griffiths' and Heywood's elastic solid model).

To explain the discrepancies encountered between the experimental and theoretical

observations regarding pressure transmission to soft tissues, Griffiths and Heywood proposed a two-phase deformation theory to describe limb compression. During the first phase, the tissues surrounding the bone are simply squeezed away from the compression zone, since the tissues in this location are assumed to exhibit fluid properties. The second phase begins as the blood flow ceases, at which point the tissues display the properties of an elastic solid material. The first phase of the limb compression theory provides for correlation with blood pressure measurements, while the second offers a possible explanation for tourniquet-induced nerve injuries (and the particular vulnerability of the radial nerve). However, the theory fails to replicate the pressure distribution patterns developed experimentally by other researchers.

2.1.2 Studies Using Animals

McLaren and Rorabeck [39] performed a series of experiments in order to measure the pressure distribution in the hind limbs of anesthetized large mongrel dogs. The two researchers used a standard 8.5 cm wide surgical pneumatic cuff inflated to 200 mmHg and a 10 cm wide Esmarch bandage wrapped three to seven times around the limb. Figure 2.4a illustrates their setup and includes the canine's thigh as well as the catheter and pressure transducer employed to measure soft tissue pressure. Figure 2.4b shows the five paths followed by the slit catheter: each of the four stars represents an entry point, while each black circle, i.e., each grid point intersection, indicates the location of a pressure measurement recording. Additionally, Figure 2.4c displays the three longitudinal planes in which these pressure measurements were obtained.

Figures 2.5a and 2.5b illustrate two of the six pressure profiles recorded by McLaren and Rorabeck under the pneumatic tourniquet and the Esmarch bandage. Both figures indicate a noticeable decrease in surface pressure axially from the center to the edge of the cuff/bandage. However, they reveal no significant change in pressure from the skin

surface to the bone. Since the two researchers obtained similar pressure profiles in all three longitudinal planes (refer to Figure 2.4c), they concluded that the position of the bone had no effect on surrounding soft tissue pressure profiles.

During these experiments, McLaren and Rorabeck also reported a concentration of pressure at the center of the limb, but only when the Esmarch bandage was used. The surface pressure profiles applied by a pneumatic tourniquet and an Esmarch bandage are traced and superimposed in Figure 2.6. As can be seen, the pneumatic cuff exerts a bell-shaped pressure distribution, while the Esmarch bandage displays a flatter profile. From this information, and in view of the fact that the pressure distributions show no abrupt changes or steps in pressure level, McLaren and Rorabeck deduced that the exsanguinated tissue in the compressed region possessed the characteristics of a homogeneous solid. This conclusion corroborates the findings of previous authors [19].

It should be noted that in conducting their research, McLaren and Rorabeck assumed that soft tissue pressure was analogous to hydrostatic fluid pressure. But given their conclusion that exsanguinated soft tissue behaves as a homogeneous solid, any pressure measurements taken must thereafter be expressed as geometrical combinations of radial, circumferential and axial stresses rather than as a hydrostatic pressure value. Furthermore, the ratios of these three major stresses will vary according to the insertion angle of the catheter. These factors could lead to misinterpretations with respect to actual hydrostatic pressure profiles.

2.1.3 Studies Using Cadavers

Although studying animals provides a general understanding of tourniquet-induced nerve damage, it is essential to investigate human limbs to achieve a genuine comprehension of this phenomenon. However, no non-intrusive technique exists for measuring the

pressure distributions within the limbs of living patients. Therefore, to obtain information using human anatomy, several researchers have performed experiments on cadavers in order to provide more relevant results than those of previous studies involving artificial limb models and animal subjects.

Shaw and Murray [17] performed pressure mapping experiments on the lower limbs of cadavers, expecting to corroborate the results previously obtained on animals (see Section 2.1.2). Figure 2.7 portrays the rigid stainless steel rod which was used as a pressure probe. As illustrated in Figure 2.8, this probe was inserted in the thigh at five different locations. This enabled the researchers to record the pressure levels experienced at five distinct areas of the limb (which were then averaged) while the tourniquet cuff was inflated from 100 to 900 mmHg.

From these measurements, Shaw and Murray observed that the mean tissue pressure induced by the tourniquet was consistently lower than the tourniquet pressure applied. They also found that the percentage of mean tissue pressure with respect to applied tourniquet pressure decreased as the circumference of the thigh increased. For example, mean soft tissue pressure decreases of 5% and 32%, relative to applied tourniquet pressure, were recorded for thigh circumferences of 34 cm and 59 cm, respectively. Figures 2.9 and 2.10 illustrate this inverse relationship. Also from these measurements, Shaw and Murray noted that the tissue pressure readings tended to decrease as the pressure probe was imbedded more deeply in the thigh, i.e., was moved from subcutaneous locations toward the bone. This differs from McLaren's and Rorabeck's results which revealed no significant change in radial pressure from the skin surface to the bone [39].

Although these experiments provide invaluable assistance towards the understanding of soft tissue damage, they still incorporate a few significant sources of error. Firstly, the pressure profiles obtained above were found to be affected by the large diameter of the sensory probe. Secondly, since the experiments were performed on disarticulated limbs,

no account was taken of axial tension or compression of the limb. In such experiments, the use of a rigid probe usually precompresses the soft tissue to compensate for the tissue disturbance. Consequently, the pressure patterns obtained by Shaw and Murray are not completely accurate in representing actual pressure profiles.

To overcome these shortcomings, Breault [40] measured soft tissue pressures in articulated cadaver limbs using a radial pressure sensor. Figure 2.11 shows a diagram of the pressure transducer which served to record radial stress while Figure 2.12 illustrates the overall setup. With this apparatus, Breault obtained internal pressure measurements at two nerve locations in each limb, for cuff pressures of 100, 200 and 300 mmHg. Since no statistical difference was registered between the pressure readings taken at the two distinct nerve locations of the limb, these two readings were averaged. Like Shaw and Murray, Breault observed that the soft tissue pressure induced by the cuff was lower than the cuff inflation pressure applied, and that the resulting decrease was inversely proportional to the limb circumference. However, the magnitude of this decrease was much less significant in Breault's experiment: in the upper limb, a pressure decrease of only 0.75%, compared to 5% for Shaw and Murray, was recorded, while in the lower limb, a decrease of 4.6%, compared to 32%, was recorded.

2.1.4 Studies Using Humans

Due to anatomical and structural mutations occurring postmortem, the mechanical properties of human soft tissue change, normally within a few hours of death [35]. Thus, despite the fact that cadaver studies provide us with more relevant information than animal studies, it is necessary to develop pressure profiles for living human limbs in order to ascertain the effects of cuff pressure in an *in vivo* situation (notwithstanding the many difficulties which this involves).

This was attempted by Thomson and Doupe [41], who generated pressure patterns

from multiple measurements taken on one individual. Specifically, they recorded the tissue pressure level induced by a 12, 8 and 4 cm wide cuff at, respectively, 29, 9 and 26 distinct locations of the limb beneath the cuff using a modification of an apparatus described by Wells et al. [27]. Figure 2.13 presents the pressure profiles thus obtained, with each measurement expressed as a percentage of the applied cuff pressure. Although no isobaric lines were traced, a definite pattern emerged. Indeed, the highest relative pressures occurred towards the center of the cuff while the lower relative pressures were obtained near the cuff edges, with the area occupied by these pressure values definitely increasing with tissue depth. Furthermore, the intermediate pressure zone seemed to broaden with greater tissue depth, thus infringing on the high pressure zone.

Based on this work, Thomson and Doupe concluded that systolic and diastolic pressure readings should be a function of cuff width. Figure 2.14 reveals the systolic and diastolic pressure readings obtained with varying cuff widths, and incorporates the highest relative pressure measurement and the width of the 100% pressure zone at the bone level. The steep parts of the systolic curves seem to correspond to the transition from a cuff which does not induce a high relative pressure zone at the bone to one which does. On the other hand, the level part of the systolic curve seems to correspond to increases in width of the high pressure zone induced by wider cuffs. In other words, the blood pressure measurements obtained with narrower cuffs should be consistently higher than those obtained with broader cuffs. These results were later verified by Breault [40].

2.1.5 Auerbach's Finite Element Model

Although experiments on animals, cadavers and patients help in understanding the effects of cuff pressure on limbs, the applicability of the results obtained is limited to the specific combinations of tourniquet and patient parameters studied. In order to extend the relevance of these results to all possible parameter combinations, extrapolations must

be effectuated. Indeed, the compression phenomenon must be simulated under a variety of circumstances to eventually optimize cuff design. To this end, analytical and numerical models have been developed.

In an attempt to verify the work of Thomson and Doupe, Auerbach simulated the effects of tourniquet pressure using an axisymmetric finite element model [42]. The simulated cuff pressure was set at 100 mmHg and was applied uniformly. This corresponded to a force of 22 N/node in the region covered by the cuff and 11 N/node at the cuff edges. Within this model, the behaviour of the soft tissue elements was assumed to be linear, elastic, homogeneous, and isotropic. Young's modulus was set at 15 000 Pa and Poisson's ratio at 0.49 based on the results of an earlier experiment by Chow and Odell [43]. Figure 2.15 shows Auerbach's finite element mesh of the analyzed limb section. The limb was considered to be axially symmetric, with the bone (femur or humerus) assumed infinitely stiff with respect to the soft muscle tissue. It should be noted that the model implicitly assumed that strains would remain small even if deformations were large.

Auerbach first calculated the hydrostatic pressure and octahedral shear stress in the soft tissue elements beneath the cuff and then compared his results to the experimental profiles obtained by Thomson and Doupe. This comparison is provided in Figure 2.16. In this analysis, Auerbach defined the hydrostatic pressure as the mean value of the three principal stresses on one given element. Equations 2.1 and 2.2 below relate Auerbach's expressions of hydrostatic pressure and octahedral shear stress.

$$\sigma_h = \frac{1}{3}(\sigma_1 + \sigma_2 + \sigma_3) \tag{2.1}$$

$$\overline{\sigma} = \sqrt{\frac{1}{2}(\sigma_1 - \sigma_2)^2 + \frac{1}{2}(\sigma_2 - \sigma_3)^2 + \frac{1}{2}(\sigma_3 - \sigma_1)^2} \tag{2.2}$$

As in Thomson's and Doupe's pressure map, Auerbach also observed three pressure zones. However, the high pressure zone of the numerical model showed a 10 to 20%

pressure increase from the skin to the bone. Furthermore, Auerbach's model shows the transition distance, i.e., the longitudinal length of the intermediate pressure zone at the skin, where pressure drops from 100 to 0% of cuff pressure, as being much shorter than in the experimental case. Nonetheless, Auerbach felt that his model could be employed to simulate the application of a tourniquet to a limb and produce quantitatively valid results.

Auerbach's model served to examine the effects of edge radii of the cuff. He found that the level of octahedral shear stress at each extremity of the cuff was inversely proportional to the radius of curvature of the cuff edges. Figure 2.17 shows the octahedral shear stress profiles for different values of cuff edge radii. Auerbach noted that the shear stress remained constant under the midsection portion of the cuff and that its level was independent of the edge curvature. For instance, the shear stress at the edge of the cuff was 10 to 15% higher than the level midway across the cuff. The changes in octahedral shear stress levels at the surface seem to be influenced solely by the rounding of the cuff edges. In view of this, there appears to be some form of stress concentration due to the rapid change of loading; furthermore, its effects should die out in the deeper regions of the tissue. Consequently, the correlation between octahedral shear stress and soft tissue damage does not account for the apparent susceptibility of the deeply embedded radial nerve [37].

2.1.6 Hodgson's Analytical Model

Hodgson investigated the effects of pressure on a limb by using basic linear elasticity theory to model the soft tissues [44]. As in Auerbach's work, Hodgson made several assumptions and simplifications to reduce the complexity of the simulations. He visualized the limb as a rigid bone surrounded by homogeneous linear elastic material. His simulations also assumed the limb was axisymmetric. However, Hodgson improved Auerbach's

model by considering the orthotropic nature of soft tissue.

The purpose of his work was to determine the effects of limb and cuff parameters on stress and strain distributions in the limb. He performed four series of nine simulations assuming isotropic material properties, and an additional series of six simulations assuming anisotropic features. He traced pressure patterns for all possible permutations of various values of cuff width, arm radii, surface pressure distribution, and bone/muscle interface conditions. Figure 2.18 compares the hydrostatic pressure distribution from Hodgson's model with Thomson's and Doupe's experimental results. As in Auerbach's pressure profiles, there were three distinctive zones: a high pressure zone beneath the cuff, a transient zone at the edge of the cuff, and a low pressure zone in the uncompressed region of the limb.

Hodgson concentrated on the level of negative axial strain developed in the limb and its effect on underlying nerve fibers. He computed compressive axial strains of 0.15 to 0.20 at the edges of the cuff, which is where most occurrences of nerve lesions have been observed [3]. Furthermore, Hodgson observed that ignoring the shear stress at the skin/cuff interface did not lead to overestimations of negative axial strain. He then went on to suggest possible cuff design improvements, based on the assumption that compressive axial strain is responsible for tourniquet-induced nerve damage.

Five conclusions were drawn from the forty-two simulations performed. First, a smoother loading distribution reduces the magnitude of maximum negative axial strain, more noticeably so in limbs having a small circumference. Second, an increase in cuff width reduces the magnitude of the peak compressive axial strain, especially for wider limbs. Third, a decrease in friction between the limb and the tourniquet reduces the level of maximum negative axial strain. Fourth, under identical loading conditions, larger limbs experience a lower magnitude of negative axial strain than smaller limbs. And fifth, if all of Hodgson's tourniquet design recommendations are adopted, the peak compressive

axial strain may be reduced by 50 to 70%.

Although Hodgson's work proved to be important in predicting the areas of peak stresses and strains, it did not accurately reflect their levels under clinical conditions. Since occlusion pressure depends on limb radius and cuff width, the peak values of internal stresses and strains will vary according to patient and cuff parameters. By conducting his simulations at a constant external pressure, Hodgson did not account for the variances in stresses and strains due to changing occlusion pressure. Additionally, he stipulated that nerve damage was caused by negative axial strain even though earlier studies suggest that some form of shear may be responsible and this hypothesis does not explain the selective vulnerability of the radial nerve.

2.2 Studies Investigating the Mechanisms of Nerve Damage

Since its first appearance, the pneumatic tourniquet has constantly been associated with reports of nerve damage incurred during surgery. The degree and form of such injuries depends on the applied pressure intensity. In severe compression cases, nerve fibers have sometimes been crushed, resulting in the demyelination of the nerves distal to the constriction site. According to Denny-Brown, in these cases, recovery may take several months [5]. By comparison, mild compression may simply result in a slowing or a cessation of conduction, which is completely restored upon release of tourniquet pressure [4]. This type of vascular surgery side effect is attributed to asphyxia, rather than to a crushing of the nerves.

2.2.1 Evidence Supporting the Theory of Ischemia

There have essentially been two hypotheses presented since the 1930s regarding the cause of tourniquet-induced nerve damage: ischemia (reduced or eliminated blood supply)

and direct mechanical damage. For years, the theory of oxygen starvation prevailed as the predominant explanation for nerve injuries being supported by three important pieces of evidence. In 1931, Lewis et al. demonstrated that asphyxia was responsible for conduction blocks, in cases of mild compression [4]. To arrive at these conclusions, they applied a 12 cm cuff, inflated between 150 and 180 mmHg, and then recorded the sensation loss and the conduction speed decrement experienced by the major nerves of the arm. They noted that once circulation ceased, the limb no longer functioned due to paralysis of the nerves. From this, they concluded that ischemia was responsible for conduction blocks in clinical situations. Furthermore, their observations led them to believe that large myelinated fibers were more readily affected by ischemia than small unmyelinated fibers. However, no evidence suggests an association between ischemia and conduction speed decrement or nerve degeneration.

The second supporting argument for ischemia came in 1936 when Gundfest experimentally proved that excessive compressive pressure applied directly to the nerve does not induce structural changes or degeneration [6]. To prove this, he subjected excised frog nerves to pressures of one thousand atmospheres (approximately two thousand times clinical levels) before recording evidence of conduction decrement. However, Gundfest failed to consider the effects of surrounding tissues on the stresses and strains experienced by nerves in *in vivo* situations.

Finally, Denny-Brown and Brenner [5] provided evidence showing that pressures in the clinical range may induce nerve damage through ischemia. They gathered experimental data by applying pressure on excised cat nerves. They noted that the major changes observed were demyelination of the nerves without evidence of crushing or interruption of axoplasm continuity. The researchers assumed that these lesions were similar to those discovered by Lewis et al., and consequently attributed them to the lack of oxygen supply due to restricted blood flow. However, since the distal portions of the nerves experience

the same levels of ischemia as the portions located directly beneath the cuff, the selective occurrence of nerve damage in the constriction site is not likely to be caused by reduced blood supply. Nonetheless, in light of Gundfest's results [6], these researchers felt that ischemia, rather than mechanical damage, more adequately explained the lesions they observed.

2.2.2 Evidence Supporting the Theory of Mechanical Damage

In the early 1970s, Ochoa and other researchers performed a series of tests to isolate the cause of nerve damage due to excess pressure from a tourniquet [3,7]. Pneumatic cuffs were applied to the hind limbs of female baboons, inflated to pressures varying from 500 to 1 000 mmHg and left in place for one to three hours. The baboons were then killed for anatomical study at times ranging from a few minutes to six months after the tourniquets were released. Nerve samples were then gathered from the constriction site of each specimen.

Ochoa et al. [3] discovered characteristic lesions in the nerves which preceded the demyelination phenomenon observed by previous researchers. (For a greater understanding of nerve anatomy, refer to Appendix A.) This lesion occurred almost exclusively in large myelinated fibers (diameter greater than 5 μm) and was characterized by partial invagination of one side of the node of Ranvier into the other. The degree of invagination ranged from mild to severe, with the most severe cases exhibiting a displacement of the node of up to fifteen axon diameters into the adjacent internode. Figures 2.19a through 2.19c show the invagination phenomenon observed in some large myelinated fibers. Even in cases of mild invagination, the nodal gap was obliterated and the membrane separating the myelin from the extracellular fluid was ruptured.

The direction of displacement of the nodes proved to be an important clue in associating nerve lesions with mechanical damage. Ochoa et al. noted that at any given axial

location relative to the cuff, the direction of displacement of the nodes of Ranvier was identical for all affected fibers. The nodes were always displaced away from the center of the cuff towards the uncompressed region. Figure 2.20 shows the direction of nodal movement relative to the cuff position. This strongly suggested that mechanical damage, and not ischemia, was responsible for the observed nerve lesions.

In addition, the sparing of small fibers was investigated and compared to previous experimental work [4]. Ochoa et al. noted that small myelinated and unmyelinated fibers could resist pressures reaching 1 000 mmHg, while larger myelinated fibers suffered from degeneration when pressures in the clinical range were applied. Since motor neurons tend to be the largest nerve fibers, and sensory neurons tend to be the smallest, the correspondence between function impairment (motor ability) and the presence of lesions suggests that these may be the cause of nerve paralysis. This observation correlates with data gathered by previous researchers, who noted that pain sensation was preserved even when motor ability was eliminated [4].

The distribution of nerve lesions beneath the cuff also supports the hypothesis of mechanically induced nerve damage. Ochoa et al. analyzed several transverse sections at various longitudinal positions relative to the constriction site. They counted the number of damaged nerve fibers exhibiting characteristic nerve lesions. The histogram of Figure 2.21 shows the percentage of damaged fibers with respect to their relative axial position beneath the cuff. The damage is almost entirely limited to a pair of one centimeter wide regions centered under each edge of the cuff, with a significantly greater proportion of nerve fibers being damaged at the proximal end.

If it can be convincingly argued that these characteristic lesions are mechanically induced, then, given the fact that all nerves under the cuff suffer the same level of ischemia, it can be concluded that mechanical damage is the most likely mechanism capable of inducing nerve damage.

2.2.2.1 Ochoa's Proposed Mechanism of Mechanical Damage

Ochoa et al. suggested a mechanism which they believe explains the characteristic lesions observed in large myelinated fibers located at the edges of the compression site [3]. They postulated that when compression was applied to the nerves, the axoplasm was forced away from the site of compression, in the same manner that water in a hose would be if it were crushed. When the axoplasm encounters the narrowing of the channel at the node of Ranvier, the node could act as a plug and be forced into the adjoining segment if the viscosity of the fluid was high enough, thus causing invagination. This explanation accounts for the sparing of small fibers since they do not exhibit a narrowing at the nodes of Ranvier. The specific locations of the lesions relative to the cuff may be due to the high pressure gradient at the edges of the tourniquet. Citing Gundfest's experiments on excised frog nerves, Ochoa et al. claim that in the absence of pressure gradients, no axoplasmic motion would occur. Therefore, they conclude that the high ratio of damaged nerve fibers at the edges of the cuff is due to the pressure gradient, which is at its peak in these regions.

Although Ochoa et al.'s proposed mechanism explains the sparing of small fibers and the location of the characteristic nerve lesions relative to the cuff, it does not account for the apparent susceptibility of the deeply embedded nerves [37]. Referring to Thomson's and Doupe's hydrostatic pressure distribution in Figure 2.13, the maximum pressure gradient is located at the skin surface and gradually decreased towards the bone. For this reason, it may be suggested that other mechanical stresses or strains are responsible for the characteristic nerve lesions discovered by Ochoa et al.

Chapter 3

DEFINITION OF MODEL PARAMETERS

When attempting to model any structural system using the finite element method, there are three essential parameters which must be accurately defined: structural geometry, material behaviour and boundary conditions including the applied loading conditions. To define these parameters for the anatomical system under study, this chapter begins with an in-depth analysis of the physical characteristics of biological tissues which are present in the limb. This includes a definition of the mechanical properties of muscles, blood vessels and bones, as well as a description of the physical interactions between them. The second parameter discussed in this chapter pertains to the boundary conditions associated with the specific anatomical system of a limb. Basically, three such boundary conditions must be considered: at the bone/muscle interface, at the skin/cuff interface, and at the uncompressed axial ends of the limb model. Finally, the load applied to the limb resulting from pneumatic tourniquet pressure is characterized using experimental results obtained by previous researchers.

In addition to parametric definitions, an understanding of the mechanics of blood vessel constriction is necessary to truly master the intricacies inherent in the present model formulation. To provide this understanding, a review of existing theoretical and experimental analyses of blood flow occlusion is presented in the last section of this chapter. The mechanism which causes the artery to collapse is investigated and then compared to the mechanisms which govern the behaviour of non-biological tubing. A discussion of how tourniquet and patient parameters influence the amount of pressure

required to successfully occlude blood flow concludes the section.

3.1 Mechanical Properties of Biological Tissue

In recent years, there has been a growing interest in using finite element analysis for modelling the behaviour of biological systems. Any such system is predominantly composed of soft tissues, which may be classified as soft connective tissues (i.e., lung tissues, skin, blood vessels, ligaments, tendons, and mesenteries and other membranes), muscles, organs or brain tissue. These soft tissues are made up of biomechanically different constituents. The mechanics of a specific soft tissue depend largely on the particular responses, proportion and location of each such constituent in the structure.

Elastic fibers are the most fundamental and the major force-bearing components of soft tissues [46]. These fibers may be considered as passive elements, with the most prominent ones being the elastins and the collagens. In view of their diversified mechanical characteristics, elastic fibers are found in several structures. For example, they form bundles in tendons, plane matrices in membranes, and spatial frameworks in proteins and other biological solids of the lungs.

However, when considered as a continuum, soft tissues typically possess four basic characteristics.

1. The force deformation relationships of soft tissues are non-linear, with extension ratios ranging from 10% to over 100%, depending on the loading conditions.

2. Soft tissues contain a large fluid component.

3. The deformational response of soft tissues is both path and rate dependent (hysteresis).

4. Most soft tissue responses are controlled and coordinated through internal voluntary and/or involuntary reactions.

There are two distinct approaches for gathering experimental data to study the material properties of soft tissues: one attempts to measure *in vivo* properties, while the other favours experiments using excised specimens. The latter is considerably more easily performed but does not necessarily produce valid results from which the behaviour of intact systems can be predicted.

3.1.1 Mechanical Behaviour of Muscle Tissue

To establish the elastic behaviour of any material, the applied loads and the deformations they produce must be measured and a theory adopted to relate these two sets of values through the desired elastic parameters [51]. In general, two methods have been established to observe the mechanical properties of soft tissues. The first ignores the naturally deformed state of *in vivo* soft tissues and simply applies a longitudinal load on a relaxed tissue specimen until it fails. The data gathered throughout this process is normally analyzed using large strain elastomeric theory or non-linear viscoelastic theory. The second method attempts to simulate the inherent longitudinal and lateral elongation of soft tissues in living organisms by loading the relaxed tissue sample until it approximates the deformed state of *in vivo* tissues. Once this point is reached, the amount of load applied is varied about the deformation state selected with the resulting perturbations recorded and analyzed using small strain linearized theory [47].

Muscle tissues combine the elasticity inherent in soft tissues with the added ability to actively contract and produce force. Hill [48] proposed a model of the muscle which consists of two passive elements and one contractile element. Figure 3.1 is a schematic

representation of this model. Furthermore, in order to more clearly define the mechanical properties of skeletal muscles, stress-strain experiments were performed by various researchers. For instance, Advani et al. [47] examined relaxed muscles in three different animal species. They noted that the muscles became increasingly stiff with elongation, and that the relaxed muscle stiffness varied between species and between squeletal, cardiac and smooth muscles. Figure 3.2 shows three of the stress-strain curves obtained by Advani et al. The slope of these curves represents the Young's modulus of the tissue samples and varies from 5 000 to 21 000 Pa. These results qualify and quantify the muscle stiffness when tensile stress conditions are applied parallel to the muscle fibers. It should be noted that no data regarding the behaviour of muscle tissues when a load is applied perpendicular to the fibers was gathered during Advani et al.'s studies.

In subsequent work, Yamada [35] analyzed the data obtained from stress-strain tests which were performed on a variety of human squeletal muscles and studied the influence of age, sex, size, and postmortem time on the ultimate strength of muscle tissues. Specifically, he discovered that the ultimate tensile strength decreased with increasing age and size; for example, a thin man would exhibit an ultimate muscle strength corresponding to 1.8 times that of a normal man. However, no definite relationship was established between the ultimate strength of muscle tissues and the thickness of muscle fibers. With respect to postmortem time, Yamada observed that "in general, the postmortem decrease in the ultimate strength of muscle tissue occurs quite rapidly during the first 24 hrs, slows down somewhat between 24 and 36 hrs, and becomes substantially constant at 48 hrs." This seems to imply that experiments performed on cadavers cannot accurately report the mechanical properties of *in vivo* muscle tissues. Figure 3.3 shows the stress-strain curves obtained by Yamada for several human squeletal muscles. Once again, the variance in the Young's modulus is evidenced by the range of slope intensities. Note that all the curves exhibit one common feature: they begin with a mild slope, i.e., with a

low stiffness, and then increase sharply upon reaching the 50% elongation mark. This behaviour suggests that the elastin fibers support the load during the first stage, while the collagen fibers increase the resistance to elongation during the second stage. Figure 3.4 displays the stress-strain curves of elastin and collagen fibers. It is noted that the slope of the elastin curve roughly parallels that of the initial stage of the muscle curve, while the collagen curve seems to correspond to the second stage of elongation. From this observation, it can be said that muscle tissues exhibit an almost constant elasticity modulus up to the 50% elongation point. Thus, for this study, the slope of the first portion of the stress/strain curves serves to define the Young's modulus of muscle tissues parallel to the fibers.

Chow and Odell [43] performed a finite element analysis to investigate the deformations and stresses in the buttocks of a sitting person. The two researchers noted that although soft tissues are typically easily deformed uniaxially within a structure, individual components are nearly incompressible. In other words, while the Young's modulus (E) is very low, the bulk modulus (K) is very high. Chow and Odell suggested that localized pressure may cause deformation, mechanical damage and blockage of blood vessels but demonstrated that hydrostatic pressure (with equal stress intensities applied in all directions) caused little or no deformation in the muscle tissues. Other researchers have also found that body tissues can tolerate up to 1 655 000 Pa of hydrostatic pressure with no difficulty, but that uniaxial pressure approaching 6 700 Pa induces pathological changes in body tissues [49]. Consequently, since the maximum levels of hydrostatic pressure felt by the soft tissues of a limb under pneumatic tourniquet loading conditions generally do not exceed 75 000 Pa, it is unlikely that hydrostatic pressure is the cause of tourniquet-induced tissue damage. However, uniaxial loads exceeding 6 700 Pa may be present under occlusion conditions and therefore may be responsible for this type of injury.

The state of stress observed in the buttocks may be viewed as a combination of shear and hydrostatic stresses. If the hypothesis of hydrostatic pressure being relatively harmless to biological tissues is accepted, then the harmful stress observed must be related to the presence of a shear stress. According to elasticity theory [50], a shear stress results within a material subjected to uniaxial pressure, localized pressure, any non-uniform distribution of pressure and in general, any form of applied pressure causing distortion. In the case of a three-dimensional stress state, the factor used for quantifying overall shear will be representative of either the distortion energy or the octahedral shear stress (the von Mises stress). This research focuses on determining if these shear stresses (or associated shear strains) may be responsible for the observed soft tissue damages caused by the overinflation of tourniquet cuffs.

Various other researchers have generated, reviewed or utilized quantitative estimates of soft tissue behaviour. Table 3.1 provides an overview of the mechanical properties attributed to muscle tissues by these researchers. The variance in these results may be partially explained by the wide range of methods used to collect and analyze data.

The Young's modulus and the Poisson ratio which Chow and Odell used for their analysis were 15 000 Pa and 0.49, respectively. Since these two values were based on stresses and strains actually recorded in a living subject, they should properly reflect the soft incompressible nature of *in vivo* tissues. Whereas Yamada's and Advani et al.'s quantities were representative of a positive tensile state, Chow's and Odell's values were associated with a negative or compressive stress state. Consequently, Chow's and Odell's results were considered to be well suited to accurately model the elastic behaviour of muscle tissues in the directions perpendicular to the fibers and have been adopted for the orthotropic analysis of the current study. However, neither study addressed the issue of anisotropic properties which predominate in the multi-dimensional stress state typically found in biological tissues. This issue is discussed further in Section 4.2.1.

3.1.2 Mechanical Properties of Blood Vessels

As one of the objectives of this research is to investigate the occlusion mechanisms of blood vessels, their mechanical properties must be clearly defined. Generally, test methods for establishing these properties begin by applying a load (such as internal pressure or axial tension) to the artery specimen and then recording the induced arterial deformations, i.e., the changes in mean radius, wall thickness, and/or axial length. However, as with muscle tissues, the mechanical properties obtained by previous researchers for blood vessel constituents vary according to the specific testing methods employed (see Table 3.2).

Tickner and Sacks [51] claimed that the arterial walls behave as a non-linear, homogeneous, anisotropic, compressible material which can be characterized by six elastic constants for each strain level (three Young's moduli and three Poisson ratios). They arrived at these conclusions by performing stress-strain tests using four types of human arteries and two types of canine arteries. Figure 3.5 illustrates the setup which was used to apply axial tension and internal pressure to the arteries. The results indicated that at low pressures and with no axial loading, the three elastic constants associated with the three main axes of blood vessels exhibited Young's moduli within the same order of magnitude (from 140 000 Pa to 700 000 Pa) for all of the specimens tested. This led them to conclude that at low loads, arteries behave isotropically, with an elasticity modulus equivalent to that of elastin (about 500 000 Pa). The two researchers further noted that radial stiffness was the smallest of the three moduli and was basically independent of internal pressure and axial tension. Hence, the common assumption which envisions the arterial wall as having a constant thickness seems to be verified. Despite the fact that human arteries exhibit some viscosity and plasticity, Tickner and Sacks considered these effects minimal for low rates of loading.

Figure 3.6 shows the three Young's moduli and the three Poisson ratios as a function of both external and internal loading conditions. If the *in vivo* internal pressure range is considered to be the zone between diastolic and systolic levels of internal pressure (i.e., between 70 mmHg and 150 mmHg), then the material properties of a functioning artery can be accurately defined using these charts. However, a great deal of uncertainty still remains with respect to the levels of axial tension actually present in *in vivo* arteries. Tickner and Sacks noted that the Young's modulus is consistently lower in the axial direction than in the circumferential direction. Since the fibers are parallel to the artery, these observations lead to the conclusion that soft tissues are stiffer in the transverse direction than in the longitudinal direction.

Next, Yamada [35] investigated the anisotropic properties of human blood vessels by performing stress-strain experiments on excised blood vessel samples, both in the longitudinal and the circumferential directions. These stress-strain curves are shown in Figure 3.7. From this diagram it is apparent that the curves resulting from transient tension consistently exhibit stiffer properties than the corresponding longitudinal curves, thus corroborating the results obtained by Tickner and Sacks.

Another group of researchers, Peterson et al. [52], performed experiments on *in vivo* arteries to determine the effects of blood pressure on the mechanical properties of arterial walls as well as on the diameter of blood vessels. They observed that variations in artery circumference due to physiological changes in arterial pressure were minimal and could therefore be ignored. They further noted that subsequent to a pressure pulse, the artery's length changed by less than 1% per unit length and that during the cardiac cycle, under normal circumstances, its volume changed by less than 5% per unit length.

Finally, Moreno et al. [53] compared the behaviour of canine veins and other thin-walled structures, in an attempt to characterize the pressure-volume relationship. They performed experiments and computer simulations on excised dog veins and on latex tubes

to try to determine the relationship between transmural pressure and cross-sectional area. Equation 3.1 expresses the coordinates (x,y) of each point of an annulus for given values of transmural pressure (P), Young's modulus (E), artery wall geometry (I) and initial conditions (k). Using numerical methods, Moreno et al. solved this equation. Figure 3.8a presents the experimental and analytical results obtained for a latex tube, while Figure 3.8b shows the corresponding results for one of the venae cavae of a dog. Equations 3.2 and 3.3 below correspond to these two sets of results.

$$-\frac{\frac{d^2y}{dx^2}}{(1+(\frac{dy}{dx})^2)^{\frac{3}{2}}} = \frac{P(x^2+y^2)}{2EI} + \frac{k}{EI} \tag{3.1}$$

$$\frac{(A-A_0)}{A_0} = 0.0091 \arctan(P+4.1) - 0.70 \tag{3.2}$$

$$\frac{(A-A_0)}{A_0} = 0.019 \arctan[3(P+0.35)] - 0.81 \tag{3.3}$$

Through their experiments, Moreno et al. hoped to point out the limitations inherent in using latex tubes for blood vessel simulation experiments. They noted that both veins and latex tubes experienced a loss of circular cross-section as the transmural pressure value approached zero, i.e., that the vessel walls of both were structurally not self-supporting. However, while the perimeters of the latex tubes remained constant throughout the transformation from oval to circular cross-sections, those of the veins did not. Thus, for latex tubes, such transformations were due exclusively to bending deflections; but for veins, such transformations were due to a combination of bending and circumferential stretchings of the wall. Figures 3.9a and 3.9b show the computer solutions for the cross-sectional area of a latex tube and a vein, respectively. The latter has an EI factor more than 500 times smaller than the former. Figure 3.10 illustrates the change in area versus the change in perimeter for the two aforementionned samples.

As evidenced by the literature review presented above, most of the experiments conducted on blood vessels do not accurately reflect the conditions present when blood flow

occlusion is induced by a pneumatic tourniquet. Basically, there are three sources of error associated with the previously discussed procedures: first, they do not contemplate a non-uniform pressure distribution on the artery; second, they disregard a non-axially symmetric pressure profile; and third, they neglect the effects of pulsating flow. Although the last two assumptions are often valid, the longitudinal pressure applied to the artery does not possess a uniform distribution, which indicates that transmural pressure is a function of axial position. The effect of a non-uniform distribution on blood vessel occlusion is considered and evaluated more specifically in Section 3.4.

Several features from the studies presented in this section have been incorporated into the present investigation of blood vessel occlusion. The material properties (i.e., the elasticity modulus and the Poisson ratio) chosen for the finite element models are based on the results of Tickner and Sacks [51] and Yamada [35].

3.1.3 Mechanical Properties of Bone

A bone is a composite, viscoelastic, anisotropic material primarily composed of organic fibers (mainly collagen), inorganic crystals (hydroxyapatite), a cement substance and water [54]. Although the presence of bones plays an important part in tourniquet-induced tissue damage, if they can be considered infinitely stiff with respect to muscle tissues, then accurate assessment of their properties is not required for the valid modelling of the system. Since bone consists mainly of collagen and crystalline structures, it follows that its Young's modulus should be much higher than that of soft tissues. This is confirmed by Table 3.3, which lists the Young's moduli and the Poisson ratios recorded for bones by various researchers. The data shows that the stiffness of bone tissues is about 10 000 000 kPa, which is approximately 700 000 times stiffer than muscle tissues (approximately 15 kPa). Consequently, it may be assumed that bone deformations are negligible when compared to soft tissue deformations under identical loads.

3.2 Interactions at the Boundaries

Numerical modelling of a structural system eventually requires the identification of a physical domain, based on which the problem is defined and formulated. For a biological system consisting partially of soft tissues, defining the physical model (and the associated boundary conditions) is not an easy task. Often, the boundary conditions are part of the desired solution to the problem. In many biomechanical soft tissue studies, the constitutive relationships are formulated using data from excised specimens where a stress-free state was assumed to exist. Typically, the latter assumption provides the reference state for analyzing the stresses or deformations of a physical model. Unfortunately, the excised specimen tissue behaviour characterized cannot be readily correlated with *in vivo* conditions, where the reference states (within the structure and along its boundaries) are not clearly known. Consequently, in order to eliminate the possibility of the boundary conditions being part of the solution, they must be uniquely defined by imposing constraints at their locations (e.g., free to move, restrained in a certain direction, imposed displacement, etc.).

The finite element method utilized in this research also requires the input of boundary condition states prior to solving the problem. There are essentially three boundary states encountered when considering the problem at hand: the interaction between the bone and the surrounding muscle tissue, the interaction between the cuff and the skin, and the load and/or displacement restrictions at the axial ends of the limb model. Figure 3.11 shows the limb model and identifies these three boundaries.

3.2.1 Bone/Muscle Interface

The shear stress and strain levels developing at the bone surface are highly dependent on the nature of the material which links the muscle tissue and the bone (location A on

Figure 3.11). Muscle fibers, nerves and bones are surrounded by a layer of connective tissue, which serves as a bridge between skin and fat, fat and muscle, or muscle and bone. Anatomical investigations show that this tissue offers a substantial resistance to shear stress [46,55]. Thus, muscle tissues are restricted from moving in either the longitudinal or the circumferential direction. Previous researchers [42,44] have also defined this boundary as fixed. The potential high shear stresses and strains at the bone level are shown later to be the cause of the susceptibility of the deeply embedded nerves (with respect to characteristic nerve lesions [3]), as observed by Eckhoff [37]. Simulations were performed assuming both fixed and free boundary conditions at the bone/muscle interface. These results are presented and analyzed in Section 5.3.1.

3.2.2 Skin/Tourniquet Interface

The level and distribution of tourniquet pressure applied on the limb determines the shear stress borne by the skin and governs the cuff sliding at the skin junction (location B on Figure 3.11). Since the maximum pressure level supplied to the cuff during surgery is usually around 200 mmHg (thus resulting in a maximum applied pressure to the limb of close to 190 mmHg), and since the combined friction coefficient of skin and cuff is relatively high, the possibility of skin movement in the axial and/or circumferential direction is minimal. However, during lengthy surgical procedures, a thin layer of perspiration may form between the cuff and the skin thereby reducing the friction coefficient and increasing the possibility of axial skin movement. For this reason, simulations were performed assuming both restrictive and non-restrictive skin/cuff interface conditions. The results of these simulations are presented and discussed in Section 5.3.1.

3.2.3 Axial Constraint of the Limb Model Ends

Since axial motion is restricted both at the bone level and at the skin level (for the entire width of the tourniquet), it may be assumed that the axial displacement at the ends of the limb model will be minimal when pressure is applied (locations C and D on Figure 3.11). For this reason, the axial ends are granted freedom of movement in the axial and radial directions. Previous researchers [42,44] have made similar assumptions concerning the free ends of their models. To ascertain the effects of such an assumption, simulations were performed assuming free and fixed axial extremities. These results are presented in Section 5.3.1.

Finally, since each of the three model boundaries discussed above may be considered fixed or free with respect to axial movement, there are eight possible combinations of boundary condition states. These eight possibilities are also investigated and analyzed in Section 5.3.1.

3.3 Surface Pressure Distribution under the Tourniquet

An essential step in the development of a finite element model is to define the surface pressure distribution beneath the tourniquet cuff. Previous researchers have experimentally measured this distribution using a variety of pressure sensors positioned between the tourniquet and the skin. However, to apply this pressure distribution to analytical and numerical models, mathematical expressions which characterize this pressure profile must be established. To this end, previous researchers such as Auerback [42] and Hodgson [44] have employed various mathematical techniques in order to replicate the pressure profiles applied to a limb.

The pressure profile associated with a pneumatic tourniquet varies greatly depending on cuff design. For example, a typical pressure profile beneath a pneumatic tourniquet

is bell-shaped [39]. However, several tourniquets presently used possess a double bladder and exhibit a completely different pressure profile. Hence, various pressure distributions are contemplated in this investigation in order to ascertain their effects.

3.3.1 Previous Experimental Results

As revealed in Section 2.1.2, McLaren and Rorabeck [39] were the first researchers to determine that the pressure profile under a pneumatic tourniquet resembles a bell-shaped curve. Later, Breault [40] experimentally verified these results using a newly designed pressure sensor. Having verified the pressure profiles, she then employed curve-fitting routines to mathematically define them.

McLaren and Rorabeck [39] gathered their data from experiments performed on the hind limbs of large mongrel dogs. They applied an 8.5 cm pneumatic cuff to one of the limbs, while the other limb supported an Esmarch bandage. As previously described, a slit catheter was used to measure the amount of pressure at different longitudinal positions under the tourniquet. Figure 2.7 shows the surface pressure distribution obtained by McLaren and Rorabeck with a pneumatic tourniquet inflated to 200 mmHg. The pressure at the leading edge of the cylindrical cuff on the conical thigh was slightly higher than that at the distal edge. Indeed, the pressure at the proximal edge was 12% of the cuff inflation pressure, compared to only 9% at the distal edge. Furthermore, the peak pressure value, which was 97% of the cuff inflation pressure, occurred approximately halfway along the tourniquet width. Finally, the pressure readings decreased for the tissues closer to the tourniquet edges, with a drop in pressure of about 90% from the middle to the periphery of the cuff.

Breault [40] experimentally measured the surface pressure distributions induced by different pneumatic tourniquet designs. She used a pressure-regulated sensor to gather data from artificial limb models, cadavers and patients. In this way, she ascertained the

effects of cuff snugness, overlap and number of wraps on the surface pressure profile. Figure 3.12 shows the parabolic pressure distribution measured by Breault. Figure 3.13 gives a three-dimensional view of the pressure profile under the cuff and shows the effect of cuff overlap. With respect to the latter, the pressure readings were lower in the overlap region, thereby creating a notch in the pressure surface distribution. The number of times the cuff was wrapped around the limb was found to not significantly affect the pressure profiles. However, the snugness of the cuff was shown to be an important parameter in determining the pressure delivered to the limb surface.

3.3.2 Mathematical Characterization of the Surface Pressure Distribution

As stated earlier, in order to apply a pressure distribution to a numerical or analytical model, it must be mathematically defined. Previous theoretical investigations concerning the effects of tourniquet pressure have made use of a wide range of techniques to simulate the pressure distribution under the cuff. The resulting mathematical characterization of the surface pressure profile varies from Auerback's constant force per node model to Hodgson's Fourier series model.

Auerback [42] employed a finite element model to determine the stress distributions sustained by a limb submitted to tourniquet pressure. To perform his simulations, he assumed a mid-range cuff pressure of 100 mmHg with a uniform pressure distribution. Figure 2.16 shows the model with the applied external forces. Considering his 205 node, 320 element finite element model, this 100 mmHg pressure corresponds to a 34.6 N/m pressure. This in turn translates to a force of 22 N/node under the cuff-covered region and to a force of 11 N/node at the cuff edges. It should be noted here that this simplification technique may lead to errors in underlying soft tissue pressure readings, due to the concentration of pressure at selected nodes and the relatively large distance between the points of pressure application.

Another approach was taken by Hodgson [44] who used an analytical model based on the theory of linear elasticity to simulate the effects of tourniquet pressure. In this study, he employed the Fourier series technique to adapt two pressure profiles to the model. Being unaware of the true pressure profile beneath the cuff, Hodgson considered two possible pressure distributions: sinusoidal (see Figure 3.14a) and rectangular (see Figure 3.14b). For the rectangular, he utilized a thirteen-term Fourier series while for the sinusoidal, he used from seven to thirteen terms, depending on cuff width. He solved the elasto-static problem by first decomposing these distributions into their Fourier components, solving individually for each component and then summing the results. It should be noted that in view of the approximation technique used in applying the pressure profiles to the surface of the model, the rectangular distribution shows a wavy configuration due to its definition by Fourier series decomposition. Although this technique appears to be more suitable than the pressure concentration technique employed by Auerbach in replicating applied pressure, the computational time may have been a drawback.

Since there is a unique pressure profile for each individual cuff, this profile may be considered a design criterion. While this study simulates the tourniquet-limb system using the finite element method, the utilized software allows a pressure to be applied to the elements' surface, i.e., there is no restriction to a single force per node as in Auerback's case. However, each element can only support a constant surface pressure along its outer boundary, i.e., each element can not support a non-uniform pressure profile. For this reason, the applied pressure profile contains discrete steps rather than having a smooth distribution. Figure 3.15 shows the difference between Hodgson's smooth pressure profile and this study's discretized approximation.

As an improvement to previous investigators' models, various pressure profiles are

applied to the limb model: specifically, a bell-shaped sinusoidal profile, a flattened exponential profile, and a simple uniform profile. Figure 3.16 illustrates the three pressure profiles selected for the simulations. The model is non-dimensionalized with respect to cuff width and cuff pressure. This leads to Equations 3.4, 3.5 and 3.6 which mathematically characterize the sinusoidal, exponential and rectangular pressure profiles, respectively, along a longitudinal axis (z).

$$P_s(z) = \frac{P_{max}}{2}\left[1 + OFF - (1 - OFF)\cos\left(\frac{2\pi z}{WIDTH * N}\right)\right] \tag{3.4}$$

$$P_e(z) = P_{max}\left[1 - e^{1 - \frac{1}{4\left(z - \frac{WIDTH}{2}\right)^2}}\right] \tag{3.5}$$

$$P_r(z) = P_{max}\,\mu(z) \tag{3.6}$$

In addition, two variable features of the sinusoidal pressure distributions are investigated: the number of peaks and the offset at the edges of the cuff. Figure 3.17 illustrates the pressure profiles obtained with these two features.

Finally, in order to isolate the effects of pressure distribution on the underlying soft tissue stresses, simulations are performed using the pressure profiles discussed above; the results are presented in Section 5.3.3.

3.4 Blood Flow Occlusion

The pressure needed to occlude blood flow varies with cuff and patient parameters. Since the study at hand investigates the effects of both these characteristics on underlying soft tissue stresses and strains, the relationships between them and the necessary pressure for adequate blood flow occlusion must be established before an analysis may be undertaken. The main cuff-related parameters which may influence occlusion pressure are the surface pressure profile and the cuff width. Furthermore, patient parameters such as arm radius may also have a significant effect on occlusion pressure readings. To

define the relationships between these parameters and the occlusion pressure, previous experimental, analytical and numerical investigations are compiled in the following two sections.

3.4.1 Experimental Investigations of Blood Flow Occlusion

Many studies have been performed to investigate the nature of blood flow through arteries and veins [57,58]. In general, these have resulted in expressions relating blood flow and transmural pressure. Experimental test setups, similar to that shown in Figure 3.18, were used to simulate blood flow when a cuff is applied to the limb. Other researchers, such as Moreno et al. [53], performed experiments on dog veins to investigate the effects of transmural pressure on the shape of the cross-section. However in all cases, blood flow was considered to be steady state rather than pulsating, thereby creating a certain potential for error. Furthermore, these studies did not consider pressure profile effects since the pressure in the chamber was held constant thereby implying a rectangular pressure distribution. Finally, in most investigations, cuff width was also neglected.

However, Moore et al. [20] did investigate the effect of variations in cuff width on the pressure required to arrest blood flow in upper limb extremities. Specifically, blood flow was occluded using three different tourniquet sizes on each of ten human subjects while monitoring with an ultrasonic Doppler flowmeter. Hemostasis was achieved by inflating a wide cuff at pressures lower than the preoperative systolic pressure of the patient. A wider cuff (15.5 cm) occluded blood flow below systolic pressure while a narrower cuff (4.5 cm) occluded blood flow above systolic pressure. Moore et al. related cuff width, arm circumference and Doppler occlusion pressure through Equation 3.7 below.

$$DOP = 86.14 - 3.94\,(WIDTH) + 2.60\,(CIRC) \tag{3.7}$$

Based on this work, they concluded that artery deformation parallelled the surface pressure profile. Hence, blood flow could approach zero without total collapse of the vessel because of the accumulation of frictional resistance to flow along the compressed length of the artery. To minimize the risk of nerve injuries, the researchers proposed the use of wider tourniquets to occlude at lower pressures and reduce the pressure gradient at the cuff edges.

Breault [40] also investigated the effects of cuff width and limb circumference on the pressure needed to arrest blood flow in upper and lower extremities. She performed experiments on several subjects in order to relate cuff width and limb circumference to occlusion pressure. Her results verified those of Moore et al. [20] in that wider cuffs occluded at subsystolic pressure values while narrower cuffs occluded at suprasystolic pressure values. Figure 3.19 shows the trend in occlusion pressure versus the ratio of cuff width to arm circumference. She concluded that occlusion pressures are related to cuff design, limb geometry, and blood pressure. By curve-fitting the data of Figure 3.19, she obtained a relationship which predicted occlusion pressure when the cuff width, the limb circumference and the diastolic pressure are known. Equation 3.8 shows this relationship.

$$P_{occ} = P_{dia} + \frac{16\,(CIRC)}{(WIDTH)} \tag{3.8}$$

This equation is subsequently employed in this study to apply the necessary pressure to the limb compression models given the specific cuff and patient parameters (WIDTH and CIRC). In so doing, simulations are performed at a predicted occlusion pressure rather than at a nominal pressure value as in Hodgson's study [44].

3.4.2 Analytical and Numerical Modelling of Blood Flow Occlusion

Several researchers have proposed models to predict the behaviour of blood flow through collapsible tubes. This phenomenon has been extensively analyzed in the literature [57-70]. Emphasis on the cross-sectional shape of collapsible tubes at varying transmural pressure values has also been the subject of many studies [53,65]. Although these studies have reduced the area of uncertainty with respect to blood flow through arteries and veins, the mechanism of artery collapse under tourniquet pressure still remains undefined.

Subsequent to the discovery of tourniquet-induced soft tissue damage, the influence of cuff parameters on the occlusion pressure became the subject of many investigations. In 1969, Conrad [69] developed a pressure-flow relationship for collapsible tubes and derived an expression for the transmural pressure needed to collapse a soft thin-walled tube. Contrary to Holt's [57] Equation 3.9, Conrad considered the cuff width, and therefore the underlying pressure profile, in his solution. Equation 3.10 shows the expression which relates tube properties, mode of collapse and pressure chamber geometry to the occlusion pressure value.

$$P_{occ} = \frac{Eh^3}{(1-\nu^2)4{r_0}^3} \tag{3.9}$$

$$P_{occ} = \frac{Eh^3(n^2-1)}{12\,{r_0}^3(1-\nu^2)} + \frac{1}{1+(\frac{n\,WIDTH}{\pi r_0})^2}\left[\frac{Eh^3}{12\,{r_0}^3}\left(\frac{2\,n^2-1-\nu}{1-\nu^2}\right)+\frac{Eh}{r_0\,(\nu^2-1)}\right] \tag{3.10}$$

By plotting this equation for both the mechanical properties of blood vessels and the first mode of collapse (two lobes) and then overlaying the curve on experimental data gathered by previous researchers, it may be observed that there is consistency between wider cuff configurations but discrepancies between narrower cuffs. This occurs because Conrad uses a uniform pressure distribution in his expression while the actual transmural pressure profile is bell-shaped.

Wild et al. [66] used the lubrication theory to predict the behaviour of collapsible

tubes subjected to non-uniform pressure distributions from a pneumatic cuff. Their analytical solution was very complex and presented several assumptions that may have produced significant errors. Although this recent development predicts the behaviour of veins under external pressure, it does not predict the behaviour of arteries under similar conditions. According to Wild et al., this is predominently due to the lack of information on mechanical properties of arteries and the inability to predict the area-transmural pressure relationship. Furthermore, this model assumes that the pressure is applied directly to the tube and is not transmitted through several layers of skin, fat and muscle.

A simpler model using beam deflection theory was considered by Breault [40]. She analytically predicted the deflection of a beam under a variety of different loading conditions ranging from a uniform profile to a Fourier series. This simple characterization of an artery closely replicated the experimental results presented earlier. Figure 3.20 shows the results from this analytical model together with experimentally gathered data. She concluded that the hypothesis of hemostasis occurring as a result of elastic constriction of the blood vessels over a finite length of the limb supported this model and occurred more readily with increased cuff length when pressure approached the diastolic threshold.

In order to verify the results presented by the aforementionned research, a finite element model of the artery is constructed and analyzed under different external pressure conditions and material properties. Using the ANSYS finite element package, the brachial artery is modelled and an axisymmetric external pressure is applied. The material properties of the artery are defined as those of Section 3.1.2 and a constant internal pressure of 100 mmHg is used to simulate a mean blood pressure value. External pressure is applied using a sinusoidal profile. Variations in Young's moduli are studied and related to occlusion pressure. In addition, cuff width is varied to reproduce the experimental results obtained by Breault [40]. Modelling parameters and assumptions are presented

in Chapter 4 and results from this investigation are discussed in Section 5.5.

Chapter 4

FINITE ELEMENT MODELS

The parameters needed to numerically model and analyze a specific biological system were presented in the previous chapter. This chapter describes the formulated finite element models employed to represent the described system. The models' main objectives are to investigate the mechanisms of blood vessel collapse and to identify possible causes of injuries associated with the use of occlusive devices. The soft tissue finite element models developed are modified to address variations in both patient and cuff parameters, and are dealt with in two phases.

During the first phase, the pressure transferred from a pneumatic cuff to the limb tissues is investigated. Compression of the soft tissues is modelled using two approaches: a simple approach where the limb structure is considered as a rigid core surrounded by homogeneous material; and a more complex structural approach which incorporates skin, fat, and orthotropic muscle tissues. In both models, limb radius and fat content are variable limb parameters, while cuff width and pressure distribution are variable tourniquet parameters. The purpose of this initial phase is to provide insight into the possible causes of tourniquet-induced nerve injuries by generating stress and strain maps for various combinations of geometric and static loading conditions.

In the second phase, the characteristics of collapsing blood vessels are studied. The constriction phenomenon is modelled based on large deflection theory and numerically solved using the finite element method. Correlations between the previously described experimental results and this study's finite element results are elicited.

To provide the necessary background for understanding the method and assumptions required for numerical modelling of a biological system, a brief discussion outlining the theory and previous applications of the finite element method is presented at this point. The underlying assumptions used throughout the modelling process are then presented in Section 4.2 with respect to the specific biological structure (i.e., limb, artery, etc.) considered in the models. Finally, Sections 4.3 and 4.4 then outline the development of the specific models for both phase one (soft tissue compression models) and phase two (blood flow occlusion model) based on these assumptions.

4.1 Finite Element Method

Reddy [71] has written that: "Virtually every phenomenon in nature, whether biological, geological or mechanical, can be described with the aid of the laws of physics, in terms of algebraic, differential, or integral equations relating various quantities of interest." Although the derivation of many noteworthy practical problems is not excessively difficult, solving for their closed-form solution through exact methods of analysis may well be an overwhelming task. In such cases, approximate methods of analysis provide a viable alternative. Among these, the most popular are the finite difference method and the variational methods (e.g., the Ritz and Galerkin methods). However, approximate methods incorporate inaccuracies, difficulties in defining boundary conditions along curved borders, and difficulties in accurately modelling geometrically complex domains. Furthermore, they do not support non-rectangular or non-uniform meshes.

The finite element method is an improvement over simpler approximation methods since it provides a systematic procedure for deriving approximation functions. Basically, it embodies two superior features. First, problems exhibiting a geometrically complex domain are broken down into a collection of simple subdomains which are called finite

elements. Second, for each element, approximation functions are derived based on the assumption that any continuous function can be represented by a linear combination of algebraic polynomials. Reddy provides a clear and concise description of the finite element method: "Thus, the finite element method can be interpreted as a piecewise application of the variational methods, in which the approximation functions are algebraic polynomials and the undetermined parameters represent the values of the solution at a finite number of preselected points, called nodes, on the boundary and on the interior of the structure."

4.1.1 Basic Theory Behind the Finite Element Method

The finite element method for solving complex problems consists of four basic steps. Variations to the method may extend its application to nonlinear and time-dependent problem solving. However, in this section, only the basic method, which is used for linear elasticity problems, is presented.

Step 1. Finite element discretization. The continuous domain under study is separated into a finite number of sub-regions of a given shape (e.g., triangular, rectangular, prismatic). Each sub-region is called an element. All the elements together form the finite element mesh. The mesh can be either uniform, i.e., all elements have the same shape and size, or non-uniform.

Step 2. Element equations. A typical element is isolated, and its properties (geometrical and mechanical) are defined. The governing equations (i.e., the approximation functions) are established and incorporated into the problem using specified shape functions. (For additional details on the development of approximation functions, refer to Appendix B.)

Step 3. Combination of element equations and solution. The problem is solved by combining all the individual element equations into one matrix and then solving for the unknowns. Compatibility of the finite element structure is also verified with respect to the actual system. Furthermore, the boundary and loading conditions are incorporated into the problem at this stage.

Step 4. Convergence and error estimate. To ensure that the finite element model solution closely approximates the actual solution, the domain mesh must be sufficiently refined. In other words, the number of elements within the domain must be increased until further refinement no longer significantly affects the solution.

Notwithstanding these basic steps, the finite element method incorporates certain fundamental characteristics. For instance, many shapes and sizes of elements may be used in a single model. Furthermore, a single model may incorporate a variety of elements, each exhibiting specific material behavioural characteristics. It is noted that three main sources of error can be identified : geometric approximations, solution approximations, and numerical computations (e.g., truncated decimals). In order to assess the impact of these errors, data from the finite element models is compared to existing theoretical data; thereafter, the finite element mesh of the models is refined to eventually minimize the effect of approximation and truncation errors.

4.1.2 Applications of the Finite Element Method to Biological Structures

Since its appearance more than twenty years ago, the finite element method has progressed from solving simple structural mechanical problems to modelling complex biological systems. It has been used for problems dealing with bone structure, with dentition, with soft biological tissues such as veins, arteries and muscles, and with biological fluid flow such as blood flow through vessels and air flow to the lungs [45]. Considering

the study at hand, the soft tissue applications of the finite element method are the most relevant.

The finite element analysis of soft tissue mechanics differs from the conventional rigid body structural mechanics in two ways: the normal response of soft tissues cannot be uniquely defined; and the experimental data regarding the mechanical properties of soft tissues is scarce. The property data which is available often raises more questions than it provides answers, due to the conditions and limitations under which it was gathered. Hence, the assumptions concerning the mechanical properties and interactions of soft tissues are among the most difficult to postulate.

4.2 Model Assumptions

Limb compression and blood vessel occlusion are anatomical phenomena which must first be simplified before they can be mathematically modelled. To achieve this simplification, assumptions must be made concerning the properties of the limb, the pneumatic tourniquet and the main artery. These assumptions then serve as a foundation for developing the soft tissue compression models and the blood vessel occlusion model.

4.2.1 Assumptions Pertaining to the Limb

The biological domain under consideration in this study is extremely complex. The human limb is composed of several distinct tissue types such as bones, muscles, fat, skin, connective tissues, nerves, blood vessels, etc. The presence of blood and interstitial fluids further increase the complexity of the limb model. And some tissues, predominantly muscles, are subject to nervous control, which means their properties are variable.

Biological tissues are generally viewed as nonlinear anisotropic bodies exhibiting viscoelastic/plastic behaviour. Furthermore, they are grouped together in non-symmetrical

configurations. Since limbs are conical rather than prismatic, and possess distinct masses of tissue, such as biceps and triceps, they are not axisymmetric.

Given this underlying complexity, the proposed limb compression models involve the following simplifications with respect to the limb structure and the limb geometry.

4.2.1.1 Assumptions Pertaining to the Limb Structure

The following assumptions concerning the limb structure apply to the single-layer and multi-layer soft tissue compression models. To help understand this simplification procedure, Figures 4.1a through 4.1d illustrate the steps undertaken to obtain the final limb compression models.

1. The limb is a circular cylinder.
2. The bone is located at the center of the limb.
3. The limb is axisymmetric around its longitudinal axis.
4. A plane of symmetry, perpendicular to the limb, passes midway through the cuff. Hence, only one half of the limb model is considered.
5. The limb is composed of three superimposed layers of tissue: cutaneous tissues (skin and fat), soft tissues (muscles, ligaments and tendons), and hard tissues (bone).
6. The muscle layer is made of orthotropic elastic materials (no viscoelastic/plastic effects).
7. The skin layer is made of orthotropic elastic materials (no viscoelastic/plastic effects).
8. The bone is infinitely stiff with respect to the surrounding tissues.

9. The elastic tissues are non-porous solids.

10. The fatty tissue layer exhibits the properties of a fluid (has no resistance to shear).

11. The mechanical properties of fatty tissues are characterized by a bulk modulus (K).

12. The nervous control of tissues is ignored.

Furthermore, the orthotropic nature of elastic soft tissues is analogous to the mechanical properties of composite materials. Soft tissues, particularly muscles, are formed by a multitude of fibers, which are usually parallel to the limb. Figure 4.2a provides a schematic representation of the muscle structure. Given this structure, the mechanical properties of such tissues exhibit a degree of symmetry. For orientations parallel to the muscle fibers, the Young's moduli are equivalent. The same holds true for orientations perpendicular to the muscle fibers. However, the magnitudes of the Young's moduli differ between the two directions (i.e., orthotropic characteristics). Similar observations can be made with respect to the Poisson ratios of the material.

Figure 4.2b illustrates the finite element model of a muscle structure which exhibits the mechanical properties selected for this study. Based on the discussion of Section 3.1.1 regarding the material properties of muscles, the orthotropic factor (x) is set at 0.5. Note that in the case of isotropic materials, it would be set at 1.0.

4.2.1.2 Assumptions Pertaining to the Limb Geometry

The reason for simplifying the geometric properties of the limb compression model is to facilitate the processing of multiple computer simulations by minimizing the number of interventions needed for each computer run and the amount of computer processing. As an illustration, Figures 4.3a and 4.3b show the finite element models of an axisymmetric limb including its relative bone diameter and the nerve positions as well as cuff width

and location. The following is a list of the limb geometry assumptions made prior to constructing the limb compression models.

1. The diameter of the bone is a fixed proportion of the diameter of the limb (30%).
2. The skin thickness is constant regardless of the limb diameter and the fat content.
3. The fatty tissues are located between the skin and the muscles.
4. The percentage of fat is based on the limb's volume rather than on its weight.
5. The four main nerves are positioned as follows: the radial nerve lies directly on the bone, the musculocutaneous nerve is midway through the muscle layer and the ulnar and median nerves lie one element from the limb surface.
6. The length of the limb is fixed and its extremities are unconstrained.

4.2.2 Assumptions Pertaining to the Main Artery of the Limb

The following assumptions apply only to the finite element blood vessel occlusion model in which the occlusion of blood vessels is investigated. It should be noted that for this investigation occlusion occurs by collapse of the vessel and not by any other competing mechanisms. Furthermore, collapse is defined as the point where the inside artery wall comes in contact with either of the symmetry axis.

1. The main artery is parallel to the limb.
2. The axial ends of the artery are restricted in all three directions (axial, radial and circumferential).
3. The artery wall is made of a homogeneous, orthotropic, elastic material.

4. The internal blood pressure can be simulated by applying a constant surface pressure to the inside wall of the artery (there is no pulsating effect).

The orthotropic properties of the artery are assumed to be similar to those of muscle tissues based on the directional fibrous nature of the former. Hence, the radial and circumferential directions exhibit stiffer properties since they are perpendicular to the tissue fibers. To reduce the computational problem, the circular cross-section of the artery is divided into quarters and appropriate boundary conditions are applied to simulate a closed annulus.

4.2.3 Assumptions Pertaining to Loading Conditions

For both the limb compression models and the blood vessel occlusion model, the following assumptions regarding the loading scheme apply. Figures 4.4a through 4.4c provide a graphic representation of these loading conditions.

1. The level of pressure applied is calculated using Breault's relationship shown in Equation 3.8 [40].

2. The surface pressure compresses in the radial direction, even when large deformations occur, i.e., when the blood vessels collapse.

3. The pressure distribution is symmetrical about the center of the cuff.

4. Pressure is applied in an axisymmetric manner around the limb or artery.

5. The pressure profile can be represented as a stepwise pressure configuration.

For the purposes of this study, the loading conditions are defined as a combination of boundary conditions and of exterior forces and pressures. Figure 4.5 shows the boundary

conditions encountered in the limb models while Figure 4.6 is the corresponding illustration for the artery model. In the case of the limb compression models, boundaries are described as being free (F) or restrained (R); the three letters of the code correspond to the bone/muscle, skin/cuff and axial end boundaries respectively.

4.3 Soft Tissue Compression Models

The underlying assumptions upon which the numerical model is based have now been defined. Prior to outlining the specifics of the three models developed in this study, a review of several of the more relevant experimental results obtained by previous researchers as presented in Chapters 2 and 3 may be helpful.

1. The hydrostatic pressure induced by a pneumatic cuff is highest at the limb's surface and decreases until the peripheral nerves along the bone surface are reached [42].

2. There is a concentration of axial strain at the cuff edges, midway through the muscle tissues [44].

3. Although the specific nerves damaged by cuff pressure have not yet been identified [3], several researchers believe the deeply embedded nerves are more prone to injuries [37].

Given these results, knowledge of the stress and strain distributions within a limb is essential so that a particular stress or strain may be associated with a specific nerve injury. Therefore, a finite element analysis of soft tissue compression is performed in the first phase of this study in order to map the stress and strain distributions of the compressed and uncompressed regions of the limb.

In this analysis, the limb is assumed to be a thick-walled cylinder composed of both elastic and fluid materials. The bone is located at the center of this cylinder and its

outer radius is equal to the inner radius of the soft tissue. This means that no radial displacement occurs at the bone/muscle interface. An external pressure profile is then applied over a finite length which represents the width of the cuff. Next, using the finite element method, stress and strain patterns are produced for typical and nontypical patient and cuff parameter combinations. The model is investigated assuming two different soft tissue compositions: in one, the limb consists of a single homogeneous orthotropic elastic material, and in the other, it is composed of three soft tissue layers (two have orthotropic material properties and one is similar to a gel-like substance).

4.3.1 Single-Layer Limb Model

The finite element soft tissue compression model consists of axisymmetric elements possessing isotropic and orthotropic capabilities. This axisymmetric nature restricts movement in the circumferential direction. The problem is therefore downgraded from a three-dimensional state to a two-dimensional one. The material properties are selected so as to reflect the soft, incompressible and orthotropic characteristics of muscle tissues.

An illustration of the single-layer finite element model of the limb is given in Figure 4.7. The loading and boundary conditions are based on the previously discussed experimental data. Sinusoidal, rectangular and exponential pressure profiles are applied on the outer surface of the limb model (refer back to Figure 3.16). Due to the axis of symmetry through the center of the cuff, the longitudinal distance over which pressure is applied corresponds to one half of the cuff width. In addition, displacement restrictions are imposed at the plane of symmetry, at the skin/cuff and bone/muscle interfaces and at the axial ends of the model. No longitudinal movement is permitted at the plane of symmetry located midway through the cuff. (Note that this assumption is only valid with a cylindrical model and would need to be abolished with a conical model.) Also, nodes lying at the bone/muscle interface are held fixed, i.e., have no radial or longitudinal

displacement. The nodes at the skin/cuff interface are only restricted with respect to axial movement while the nodes aligned radially along the axial ends of the model are granted freedom of movement in both the radial and axial directions.

The limb geometry is based on genuine anatomical data. The bone radius is equal to 30% of the limb radius, which varies from 30 mm to 70 mm. The length of the limb is 300 mm and can accomodate cuff widths of up to 250 mm. (Note that only half of the limb model is investigated.) The more highly refined mesh of the model in the longitudinal direction (one element = 2.5 mm) minimizes measurement errors in applied pressure, especially for smaller cuff widths.

Stress and strain distributions are generated for several combinations of limb parameters (i.e., arm radius and interface conditions) and cuff parameters (i.e., surface pressure profile and cuff width). In particular, the stress and strain profiles at the nerve locations are of significant interest and are presented in Sections 5.2 and 5.3.

4.3.2 Multi-Layer Limb Model

Figure 4.8 is the equivalent of Figure 4.7 for the multi-layer finite element model of the limb. The fatty tissue layer of the limb is simulated by a gel-like substance for modelling purposes. Fluid elements between the skin and muscle layers simulate this subcutaneous layer of fat. The mechanical properties of these elements are specified by a bulk modulus (K) of 250 000 Pa. This value is a combination of both stiffness and compressibility factors. As noted previously, the percentage of fatty tissue is based on volume rather than on weight.

Most of the geometric features of the multi-layer compression model are similar to those of the single-layer model. However, the skin thickness is held constant at one millimeter with the underlying fat content now a variable feature of the model, thus allowing for a wider range of anatomical configurations. Finally, the loading scheme and

boundary conditions are identical to those of the single-layer model.

As with the single-layer model, an investigation of the stress and strain profiles at the nerve locations is performed to assess the influence of cuff and patient parameters and is presented in Section 5.3.

4.4 Blood Vessel Occlusion Model

Sufficient compression of the limb through a pneumatic cuff results in the occlusion of arterial blood flow. Although many arteries supply blood to the limb, the main artery is the primary concern in the second phase of this study. Two parameters affect the pressure level required to occlude the main artery: the surface pressure profile of the cuff and the width of the cuff. Using the finite element method helps to predict the reactions of a blood vessel subjected to specific external loading conditions.

Using the finite element method, a thin-walled tube having the geometric proportions of the brachial artery is modelled. Figure 4.9 shows a full section of the finite element model used to replicate the artery. The material properties of the vessel walls are assumed to be orthotropic in nature and symmetric in their definition (as were the properties of muscle tissues). Given this symmetry condition, only one quarter of the artery is required for computational analysis. Figure 4.10 shows a three-dimensional view of a portion of the quarter section under investigation. Boundary conditions are established to account for the planes of symmetry and the fixed nature of the uncompressed axial ends of the model (as shown in Figure 4.6). The blood pressure loading is approximated by applying a constant internal pressure to the inner wall of the artery. To represent transmitted cuff pressure, an external pressure loading is applied radially over a fixed length exhibiting a sinusoidal pressure profile.

In this phase, the effects of loading parameters and material properties on occlusion

pressure are investigated. Because of the uncertainty concerning the material properties of biological tissues, the influence of the Young's modulus on occlusion pressure is also investigated. Additionally, the cuff width is varied and the corresponding occlusion pressure results are compared to previous experimental results. The results of this numerical modelling of the artery are presented in Section 5.5.

Chapter 5

RESULTS AND DISCUSSION

When dealing with engineering designs, experimental and analytical procedures are essential to the development of new products. In the case of new medical instrumentation, clinical investigations also need to be performed. With respect to tourniquet cuffs, extensive experimental and clinical investigations have already been conducted by previous researchers [40,41]. Therefore, the current study concentrates on the analytical and numerical evaluation of the use of surgical tourniquets. In doing so, the data obtained from the models described in Chapter 4 is analyzed in five phases.

The first phase assesses the accuracy of the limb compression finite element models by comparing the results obtained from these models to those of Hodgson, Auerbach and Thomson and Doupe (refer to Section 2.1). Furthermore, by comparing the finite element results with those generated by the thick-walled cylinder theory, an appropriate mesh is chosen to minimize the level of error under specific external conditions.

The second phase attempts to identify the destructive stresses or strains associated with observed nerve lesions at the cuff edges [3]. To isolate the components that may be responsible for inducing nerve damage (as recorded by other researchers), stress and especially strain profiles at the nerve locations are examined. Since the regions of nerve lesions underneath and at the edges of the cuff are already known, the stresses and strains exhibiting peak values in these regions are assumed to be responsible for inducing the observed structural changes in peripheral nerves. The reported vulnerability of the radial nerve [37] is also considered when attempting to identify the destructive stresses

or strains.

The third phase focuses on determining the influence of patient and cuff parameters on the intensity of destructive strains developed in soft tissues beneath and at the edges of the cuff. Of the patient and cuff parameters, the pressure distribution and cuff width are considered the most significant since they represent the only variable features which may be modified to optimize tourniquet design. However, patient features such as limb radius, fat content and interface conditions are also studied to identify the optimum conditions for tourniquet application on any given individual.

The fourth phase investigates the combined use of the Esmarch bandage and the tourniquet cuff as a possible way of reducing the levels of destructive stresses and/or strains. In doing so, several hypothetical occlusion situations are simulated under multiple cuff/Esmarch bandage configurations.

The last phase reports the results obtained from the blood vessel occlusion model. Arterial properties and cuff widths are varied and the resulting occlusion pressures are compared to previous experimental results in order to assess the accuracy of the model. The five sections contained in this chapter describe each of the above phases in more detail.

It should be noted that the models developed in Chapter 4 have been implemented using the ANSYS ('analysis system') finite element software package developed by Swanson Analysis Systems. Furthermore, listings of the computer programs are provided in Appendix C. Finally, for clarity purposes, the models are referred to as 'ANSYS models' from hereon in this document.

5.1 Comparison of the Finite Element Models with Previous Models

The comparisons effected in this section serve to delimit as accurately as possible the advantages and disadvantages of the finite element limb compression models of this study and to assess the limitations of these two models. In particular, four comparisons are done: one with the thick-walled cylinder theory, one with Auerbach's finite element analysis of tourniquet use, one with Hodgson's analytical investigation of the limb compression phenomenon, and finally, one with Thomson's and Doupe's experimental results obtained from a human patient.

5.1.1 Thick-Walled Cylinder Theory

Since the region under study can generally be characterized as a thick-walled cylinder subject to specific loading conditions, the accuracy of the finite element models replicating this region can be assessed by first subjecting the models to thick-walled cylinder loading conditions and then comparing the results obtained with the hypothetical ones resulting from the thick-walled cylinder theory. It should be noted that this comparison is based on the radial and circumferential stress profiles along the radial axis.

Figure 5.1 illustrates the single-layer finite element limb compression model subjected to thick-walled cylinder conditions. Since the bone is assumed to be infinitely stiff with respect to the surrounding muscle tissues, there is no radial displacement at the bone/muscle interface, i.e., no circumferential strain ($\varepsilon_\theta = 0$ at $r = r_b$). Furthermore, as axial movement is granted to all nodes and elements, this corresponds to an FFF boundary condition configuration (see Figure 4.5). Note that the material properties of the limb are assumed to be orthotropic (refer to Section 4.2.1) and that, in this case, a uniform pressure distribution is applied to the entire length of the section. Equations 5.1 and 5.2 below represent the radial and circumferential stress distributions along the radial axis.

(Appendix D shows how these equations are derived.)

$$\sigma_r(r) = \frac{-P_0 {r_l}^2}{{r_l}^2(1+\nu_{r\theta}) + {r_b}^2(1-\nu_{r\theta})} \left[(1+\nu_{r\theta}) + \frac{{r_b}^2}{r^2}(1-\nu_{r\theta})\right] \tag{5.1}$$

$$\sigma_\theta(r) = \frac{-P_0 {r_l}^2}{{r_l}^2(1+\nu_{r\theta}) + {r_b}^2(1-\nu_{r\theta})} \left[(1+\nu_{r\theta}) - \frac{{r_b}^2}{r^2}(1-\nu_{r\theta})\right] \tag{5.2}$$

As can be seen, for a given geometry (r_b, r_l) and a given external pressure (P_0), the stress profiles depend solely on the Poisson ratio between the circumferential and the radial directions $(\nu_{r\theta})$.

Radial and circumferential stresses are calculated at the node locations and then compared to the theoretical values. The difference between these two sets of values is averaged over the radial depth using Equation 5.3 below, and plotted for varying radial and axial meshes.

$$\overline{error} = \frac{1}{MESH+1} \sum_{n=1}^{MESH+1} \left| \frac{\sigma_{n,theo} - \sigma_{n,F.E.}}{\sigma_{n,theo}} * 100 \right| \tag{5.3}$$

Figures 5.2 through 5.5 show the influence these meshes have on the accuracy of the finite element models. In particular, Figure 5.2 shows the absolute average error percentage versus the number of elements forming the mesh in the radial direction. Although the error percentage stabilizes when approximately six elements are used, a radial mesh formed of seven elements is used hereafter in order to reduce the risk of error under clinical conditions and to more closely predict the nerve locations in the radial direction. With this mesh, the average error is below 2%. However, the maximum error at a particular radial location must also be considered, Figure 5.3 shows the corresponding maximum error percentages. These also level out at approximately six elements. Furthermore, with the seven element mesh adopted, the maximum error is less than 5%.

A similar procedure is followed to determine the optimum number of elements for the axial mesh. Keeping the radial mesh constant at seven elements, the longitudinal

mesh is varied from ten to one hundred elements. Figures 5.4 and 5.5 are the analogues of Figures 5.2 and 5.3 for the axial mesh. Based on these, a sixty element axial mesh is selected. This signifies an average error of less than 2% and a maximum error of less than 5%. It also signifies that each element's length is equal to 2.5 mm, which accomodates practical cuff widths (i.e., 2.5 cm, 5.0 cm, etc.).

Next, to assess the influence of material properties on the accuracy of the finite element model, simulations under thick-walled cylinder conditions are performed for various material properties, as listed in Table 5.1. Figures 5.6a and 5.6b represent the radial and circumferential stress profiles for different values of E_z, while Figures 5.7a and 5.7b illustrate comparable profiles for different values of ν_{rz} and $\nu_{\theta z}$. As these figures show, there is a close fit between the finite element model numerical results and the thick-walled cylinder theoretical results. Note that since E_z, ν_{rz}, and $\nu_{\theta z}$ are not present in Equations 5.1 and 5.2, then the radial and circumferential stress profiles are independent of these values. However, the profiles are dependent of $\nu_{r\theta}$ and so this particular variable is given more attention. In this respect, Figures 5.8a and 5.8b represent the theoretical and finite element radial stress profiles for different values of $\nu_{r\theta}$. As may be observed, the largest discrepancy occurs as $\nu_{r\theta}$ approaches 0.10. However, the error level observed is minimal (less than 5%) and is centralized near the bone/muscle interface. Finally, comparable observations apply to the theoretical and finite element circumferential stress profiles illustrated in Figures 5.9a and 5.9b.

5.1.2 Auerbach's Finite Element Model

Although the previous comparison with the thick-walled cylinder theory shows a close fit between the numerical and theoretical results, the ANSYS finite element models must be tested under actual clinical conditions in order to truly ascertain their accuracy. Since Auerbach's [42] clinical investigation of tourniquet usage employed the finite element

method, it is appropriate to verify if the ANSYS models closely approximate Auerbach's results under identical geometric and static conditions. Therefore, the single-layer limb compression model presented in Section 4.3.1 is subjected to loading conditions identical to those chosen by Auerbach in his study. A uniform pressure distribution of 100 mmHg is applied. The Young's modulus and the Poisson ratio are set at 15 000 Pa and at 0.49, respectively; and an arm radius of 4.32 cm is used. Since the only uncertain factor in Auerbach's model is the arm section's length, two different arm lengths are considered: a half-arm length of 8.96 cm which is given as an example in Auerbach's paper, and a 15.36 cm half-arm length which allows a greater portion of the uncompressed region to be analyzed.

Figures 5.10a through 5.10c compare the hydrostatic pressure distribution (as a percentage of cuff pressure) obtained by Auerbach to that obtained with ANSYS when a half-arm length of 8.96 cm is assumed. Overall, the ANSYS model quite closely replicates Auerbach's model in that the three pressure zones (high, intermediate, low) occur in the same regions in both cases. However, ANSYS consistently overestimates the hydrostatic pressure at the bone/muscle interface and underestimates it at the skin/cuff interface when compared to Auerbach's values. If the lower right hand side corner node is disregarded, the greatest discrepancies (i.e., 16 to 17%) occur just inside the region directly beneath the cuff. Despite the magnitude of these differences, the average variance is only 7.13% (7.61% if the corner node is included). Figures 5.11a through 5.11c are similar to Figures 5.10a through 5.10c, except that the ANSYS model assumes a half-arm length of 15.36 cm. This assumption serves to eliminate the errors due to boundary effects at the corner nodes. In this case, the greatest discrepancies also occur just inside the region directly beneath the cuff and exhibit approximately the same magnitudes (i.e., 17 to 18%). However, the average variance has dropped to 5.27%.

As demonstrated in the previous subsection, a coarse mesh may produce significant

error levels and thereby reduce the model's accuracy. By using a radial mesh of four elements and a longitudinal mesh of twenty-four elements, the error percentages in radial and/or circumferential stress prediction may reach 10 to 18%. This could account for the discrepancies encountered between Auerbach's model and the ANSYS model. Another explanation could be that Auerbach neglected to verify his model's accuracy and therefore produced inconclusive results.

5.1.3 Hodgson's Analytical Model

To further verify the accuracy of the ANSYS finite element limb compression models, numerical simulations under the analytical model configurations developed by Hodgson [44] are performed. Because Hodgson was predominantly interested in the effects of axial strain, he plotted several axial strain maps assuming various cuff and patient parameters. If ANSYS can replicate the axial strain distributions thus obtained for identical geometric and static conditions, then it can be deemed accurate with respect to Hodgson's results. With this in mind, the single-layer limb compression model is tested with four distinct loading and geometric situations, i.e., the effects of two surface pressure distributions and two limb radii are investigated. Table 5.2 lists the conditions assumed for each simulation. The maximum level of axial strain as well as its location are then compared to Hodgson's model in each of the four cases.

The two pressure profiles investigated are sinusoidal and rectangular. Figures 5.12a and 5.12b illustrate the axial strain distribution obtained by Hodgson and ANSYS, respectively, for a sinusoidal surface pressure profile. Both exhibit a maximum negative axial strain of about -0.15 located midway through the muscle tissue at the cuff's edge. Figures 5.13a and 5.13b show similar distributions, but for a rectangular surface pressure profile. In this case, the maximum negative axial strain is closer to -0.25 but is located in the same region as for the sinusoidal profile.

Next, the effects of two limb radii on axial strain distributions are established. Figures 5.14a and 5.14b show the resulting distributions obtained by Hodgson and ANSYS respectively, when the smallest arm radius considered in Hodgson's study is assumed. It can be observed that the level of maximum axial strain as well as its location are the same for both models. Similar observations can also be made when the largest arm radius considered in Hodgson's study is assumed. The distributions obtained by Hodgson and ANSYS assuming this arm radius are depicted in Figures 5.15a andf 5.15b. Since the ANSYS single-layer limb compression model closely replicates the axial strain distributions obtained by Hodgson under a variety of pressure profile and limb radius configurations, it can be deemed as accurate as his complex analytical model.

5.1.4 Thomson's and Doupe's Experimental Results

It has been shown that the ANSYS limb compression model can accurately replicate the hydrostatic pressures and axial strain profiles obtained numerically by other researchers. However, since a comparison with experimental results is also an essential step in the validation of research, Thomson's and Doupe's [41] experimentally determined pressure profiles are compared to profiles obtained by ANSYS under similar conditions.

Thomson and Doupe recorded the pressure levels induced by an inflated tourniquet at multiple locations under the cuff for different cuff widths. Figure 5.16 compares the highest relative pressure with respect to cuff pressure at the bone location for different cuff widths as measured by Thomson and Doupe to that predicted by the single-layer ANSYS limb compression model under RRF boundary conditions. Although the highest relative pressure falls below 100% with a 12 cm cuff in the experimental case and with a 10 cm cuff in the numerical case, both models exhibit similar trends of reductions in relative pressure level at the bone location with decreasing cuff width. Given the shape of the intermediate pressure zone (see Figure 2.16), at a specific cuff width (approximately

8 cm) the high pressure zone disappears completely at the bone surface. This may account for the sharp drop in maximum relative pressure observed with smaller cuff widths.

Thomson and Doupe also investigated the width of the 100% relative pressure zone at the bone location. Figure 5.17 compares the width obtained by Thomson and Doupe to that of ANSYS. It can be seen that the zero width mark is reached at the same cuff width in both the numerical and experimental cases. However, the trends differ beyond the 12 cm point. This may indicate reduced reliability of the model at larger cuff widths. Notwithstanding the differences observed between ANSYS' numerical predictions and Thomson's and Doupe's experimental measurements, the finite element limb compression model seems capable of accurately predicting the actual pressure profiles under various geometric cuff configurations.

In conclusion, this section has shown that the limb compression finite element models developed in Section 4.3 can accurately replicate hydrostatic pressures and axial strain profiles measured and computed in earlier studies. This indicates that these models are sufficient and reliable for the purposes of this study. In the next section, an attempt is made to isolate the destructive strains and stresses responsible for nerve damage.

5.2 Identification of the Destructive Stress(es) or Strain(s)

In order to eventually improve the design of surgical tourniquets, the stresses or strains responsible for inducing characteristic nerve lesions [3] at the cuff edges must be isolated. To this end, a simulation assuming typical cuff and patient parameters is performed and the resulting stress and strain patterns studied (nine stress and four strain mappings). To associate a particular stress or strain with the observed nerve lesions, the areas of maximum stress or strain are correlated with the areas of reported lesion occurrences. Furthermore, as discovered by Ochoa et al. [3], the magnitudes or levels of maximum

stress or strain must be sufficient to induce displacement at the nodes of Ranvier (see Section 2.2.2). Consequently, both the position and the magnitude of the peak stresses or strains are considered while investigating their related maps. Each of the stress/strain maps of interest in this section are generated within one of three defined steps.

In the first step, the component stresses are mapped and their relative stress levels are observed. Figures 5.18a through 5.18d show the radial, circumferential, axial and shear stress patterns obtained. For the first three stress profiles, the relative maximum levels are between 0.8 and 1.0 and are located directly beneath the tourniquet cuff. These findings cannot be correlated with the observations of previous researchers who found that nerve damage occurred mostly at the cuff edges. However, the shear stress peak is located at the edge of the cuff along the bone surface. Therefore, of the four component stresses, shear stress seems to be the most likely justification for the nerve lesions observed at the edge of the cuff and for the apparent susceptibility of the radial nerve.

In the second step, three principal stress patterns and two combination stress profiles are mapped. Figures 5.19a through 5.19c show the principal stress distributions in order of decreasing intensity ($\sigma_1 > \sigma_2 > \sigma_3$). All three distributions exhibit peak values directly under the tourniquet at the bone level. Therefore, no apparent relationship between these three stresses and the observed nerve injuries can be established. Figures 5.20a and 5.20b show the hydrostatic and octahedral stress distributions. While the former figure shows a hydrostatic pressure peak located directly beneath the center of the cuff, the latter shows a peak octahedral shear stress at the edge of the cuff midway through the muscle tissues. But since an even higher peak is found in the midcuff region, this restricts the possibility of associating octahedral shear stress with tourniquet-induced nerve damage.

In the last step, four strain profiles are mapped and studied. These are considered more important than the stress profiles because they provide information on the associated displacement patterns. Figures 5.21a through 5.21d show the radial, circumferential,

axial and shear strain patterns obtained. Each of these strain profiles incorporates a peak close to the edge of the tourniquet. However, the directional nature (i.e., the slope) and the magnitude of these peaks varies. With respect to the radial strain profile, the peak values (-0.40 and 0.15) are located just inside and outside the compression zone. Given the nature and the orientation of the observed lesions (see Figure 2.20), it is unlikely that radial strains are responsible for this type of structural change. And although the circumferential strain peak values occur in the lesion area, their levels are most likely insufficient to induce serious damage ($0.000 < \varepsilon_\theta < 0.075$). On the other hand, the axial and shear strain distributions exhibit a marked correlation with the invagination phenomenon and account for the location of measured changes. Moreover, the levels of these strains (i.e., their order of magnitude) seem sufficient to induce invagination in large myelinated nerve fibers. In addition, the high shear strain levels found at the bone/muscle interface may also account for the apparent susceptibility of the radial nerve.

Although no definite answer as to the destructive stress(es) or strain(s) exists presently, the current study bases itself on the most likely patterns responsible for the observed structural changes in nerve fibers. Of the stress and strain patterns investigated in this section, the axial and shear strain profiles seem to be the most capable of causing invagination in large myelinated nerve fibers. Thus, the next section concentrates on the axial and shear strain profiles at the four main nerve locations. Furthermore, the optimization of cuff design undertaken in Section 5.4 is based on the minimization of the peak axial and shear strains.

5.3 Influence of Cuff and Patient Parameters

The purpose of this study is to develop a numerical model capable of simulating the limb compression phenomenon when a pneumatic tourniquet is employed during

surgery. Now that this model has been developed and its capabilities assessed, this section investigates the influence of both patient and tourniquet parameters on the profiles of destructive strains found along selected nerves within the limb. In doing so, the axial and shear strain levels at three radial positions, corresponding to the main nerve locations, are investigated in four phases.

The first phase provides a global view of the strain distribution for the entire limb section. Axial and shear strain maps are produced for a range of values of each parameter under investigation. This allows the areas of peak strain to be readily visualized and the nerves subjected to the highest levels of strains to be easily identified.

The second phase takes a closer look at these nerves. Axial and shear strain levels for each nerve location are plotted as a function of their longitudinal position. Although these figures serve to better illustrate the level of nerve strains, the influence of one particular parameter cannot be ascertained from a single map or profile.

Hence, the third phase considers the maximum strain values obtained for multiple cuff/patient parameters. Specifically, it establishes the direct influence of a particular parameter on the maximum level of axial and shear strain existing at each nerve location. This phase considers both the single-layer and the multi-layer models. (The two previous phases considered only the single-layer model to determine the sensitivity of a parameter.)

The fourth phase attempts to establish a possible relationship between two parameters (e.g. between cuff and arm radius). To better understand the effects of combining parameters, the peak strains at each nerve location are summed and averaged. This final phase also introduces cuff design optimization. Although no definite steps are taken to improve the basic cuff design, suggestions are provided regarding cuff selection based on specific patient configurations.

The above procedure is generally followed for each of the five parameters investigated

in the following subsections. These parameters can be associated either with the tourniquet (cuff width and transmitted pressure profiles) or with the patient (arm radius, fat content and interface conditions). Although the skin/cuff interface should be associated with the tourniquet, it is investigated along with patient-associated parameters since two of the three boundaries pertain to the patient. Note that Appendix E provides an overview of the simulations performed for each of the five parameters discussed below.

To provide a realistic compilation of strain levels, the pressure applied to the outer surface of the limb is established using Breault's experimentally determined equation relating occlusion pressure, diastolic pressure, limb circumference and cuff width [40]. Equation 5.4 below expresses this relationship in terms of Pa rather than mmHg.

$$P_{occ} = P_{dia} + 133 * \left[\frac{16(CIRC)}{(WIDTH)}\right] \tag{5.4}$$

Using this equation implies that all simulations are performed at predicted occlusion pressures. Therefore, the resulting levels of stresses and strains are realistic and are not expressed as a relative proportion of cuff pressure as in previous studies. It should be noted that whereas cuff width and limb circumference vary, the mean diastolic pressure is held constant at 10 000 Pa, i.e., 80 mmHg.

5.3.1 Influence of Boundary Condition Settings

As discussed in Section 3.2, there are three distinct boundary conditions associated with the limb compression models under study: the bone/muscle interface, the skin/cuff interface, and the uncompressed axial ends of the limb. This section investigates the effect that freeing or restraining these boundary conditions has on the axial and shear strain profiles at each nerve location. Referring back to Figure 4.5, there are eight such combinations of boundary conditions.

5.3.1.1 Bone/Muscle Interface

Of the three boundary conditions encountered, the bone/muscle interface is the most important and the most documented in the literature. The latter specifically restricts the bone/muscle interface in all directions. If it were granted freedom of movement in the axial direction (as in FFF), the resulting axial and shear strain profiles would be different than those obtained with the actual RFF setting. This is confirmed by Figures 5.22a through 5.22c, which show the predicted axial strain profiles at each nerve location for five possible boundary settings (FFF, FFR, FRF, RFF and RRF) and by Figures 5.23a to 5.23c, which show the predicted shear strain profiles for similar settings. By comparing the FFF curves to the RFF curves, it can be observed that restricting the bone/muscle interface produces: no axial strain increase at the radial nerve; significant axial strain increases at the other nerve locations (approximately 0.25); a definite increase in peak shear strain at the radial nerve (approximately 1.75); a significant shear strain increase at the musculocutaneous nerve (approximately 0.50); and no change in shear strain at the median/ulnar nerve location. Hence, restricting axial movement at the bone/muscle interface results in higher peak shear strains (which grow in magnitude as nerve depth increases) and in higher peak axial strains (with the musculocutaneous nerve incurring the largest increase).

5.3.1.2 Skin/Cuff Interface

The skin/cuff interface setting represents the friction coefficient between the tourniquet and the limb surface. Since the pressure levels applied by a tourniquet are relatively high, it is doubtful that any axial movement will occur at this junction. However, in order to verify this statement, the influence of this boundary setting must still be investigated. Hence, referring once more to Figures 5.22a through 5.22c and 5.23a through 5.23c, the

FFF and FRF curves are compared to assess the influence of restricting the skin/cuff interface. The first set of figures show that an increase in peak negative axial strain of approximately 0.45 occurs at the radial and musculocutaneous nerve locations, whereas a sharp positive peak appears at the median/ulnar nerve location. The second set of figures shows no significant change in peak shear strains at the radial nerve but a positive increase in these strains at the musculocutaneous and median/ulnar nerve locations.

5.3.1.3 Axial Ends of the Model

This last boundary condition is considered the least important of the three since it exhibits minimal influence on axial and shear strain trends. Figures 5.22a to 5.22c show that by restricting axial movement at the uncompressed ends of the model (refer to the FFF and FFR curves), axial strains increase negatively by a constant value all along the limb at each nerve location. Furthermore, shear strain predictions exhibit no significant variations when this boundary setting is restricted.

It has been shown in this section that generally, the FFF setting generates the least severe levels of axial and shear strains at the cuff edges while the RFF setting induces the most severe strain levels at this location. However, because the RRF boundary condition configuration most closely replicates actual anatomical and clinical conditions (see Section 3.2), all simulations performed in subsequent sections assume this boundary setting.

5.3.2 Influence of Cuff Width

Since the pneumatic tourniquets employed in surgery today vary in width depending on the procedure being performed, the influence of this parameter is investigated. The tourniquet cuffs studied have width ranging from 2.5 cm to 20.0 cm, which realistically represents the range of actual cuff dimensions.

Figures 5.24a through 5.24d show the axial strain maps resulting from the application of 5.0, 10.0, 15.0 and 20.0 cm cuffs respectively, while Figures 5.25a through 5.25d represent the corresponding shear strain maps. As each figure illustrates, the strain levels at the cuff edges decrease when the cuff width increases. However, whereas the high levels of shear strain are concentrated at the bone/muscle interface along the radial nerve, the peak negative axial strains mostly attack the musculocutaneous nerve located midway through the muscle tissues.

To allow for a more detailed analysis, the strain profiles are traced for each nerve location. Figures 5.26a to 5.26c illustrate the axial strain profiles at the radial, musculocutaneous and median/ulnar nerves. Figures 5.27a through 5.27c show the corresponding shear strain profiles. The peak negative strains are always located near the cuff edges except for the shear strain profile at the median/ulnar nerves which exhibits a peak positive strain in this location. This exception can be explained by the restrictive boundary condition settings at the skin/cuff interface which may result in the overestimation of the actual shear strains developed at the median/ulnar nerve location. Although the peak negative values of axial and shear strain occur in the same region, their magnitudes vary from nerve to nerve.

By studying the peak negative strains at each nerve location when different cuff widths are assumed, the direct influence of tourniquet size on the intensity of these destructive strains can be addressed. Figures 5.28a and 5.28b show the maximum axial strain intensities for varying cuff widths, as predicted by the single-layer and the multi-layer models respectively. Figures 5.29a and 5.29b are similar but show the maximum shear strain intensities. In general, the multi-layer model predicts lower axial strains and higher shear strains than the single-layer model. However, an overall trend can still be identified. Indeed, for all nerve locations, the predicted peak axial and shear strains tend to reduce as the cuff width increases. As an example, the radial nerves experience a

decrease in peak shear strains ranging from 20 to 55% and a decrease in peak axial strains ranging from 50 to 65%. (Note that the magnitudes of the latter are well below those of the former.) Furthermore, all nerves exhibit similar patterns as the tourniquet width increases, which may be related to two factors. The first is the actual level of pressure applied to the surface of the limb. From Breault's relationship (see Equation 5.4), for a given limb circumference and diastolic pressure, as the cuff width increases, the predicted occlusion pressure drops, which signifies a reduction in predicted axial and shear strains. The second factor is the slope of the applied surface pressure profile at the cuff edges. Since a sinusoidal pressure profile is assumed for all simulations, its slope at the cuff edges decreases as cuff width increases (refer to Equation 3.4).

Finally, the influence of cuff width combined with limb radius is studied. Figures 5.30a and 5.30b show the resulting average peak axial strains predicted by the single-layer and the multi-layer models, while Figures 5.31a and 5.31b show the resulting average peak shear strains. As cuff width increases, the smaller limbs benefit from larger reductions in average peak strains more than the larger limbs. For instance, a limb with a radius of 30 mm experiences an average peak axial strain drop of 59 to 82% when the cuff width increases from 2.5 to 20.0 cm, while a 70 mm limb experiences a drop of 30 to 50% for a similar cuff width expansion (these percentages are for the multi-layer and single-layer models respectively).

5.3.3 Influence of Surface Pressure Profile

Although the exact pressure profile applied to the surface of the limb is difficult to define, it may be described as being sinusoidal, exponential or rectangular. Hence, the influence of these three profiles is investigated in this section. Possible variations of the sinusoidal pressure profile are given special attention since this distribution seems the most viable [39]. Note that in order to isolate the effects of pressure profile, all other

parameters of the limb compression models are held constant throughout this subsection, unless stated otherwise. That is, cuff width is fixed at 10 cm, limb radius at 50 mm, fat content at 10%, diastolic pressure at 10 000 Pa and occlusion pressure as determined by Equation 5.4.

As an overview, Figures 5.32a to 5.32c present the predicted axial strain maps resulting from sinusoidal, exponential and rectangular pressure profiles respectively (see Section 3.3.2), while Figures 5.33a to 5.33c represent the predicted shear strain profiles. From these figures, it may be observed that the areas of peak strains at the edge of the cuff tend to increase as the pressure profile approaches the rectangular configuration.

To provide a more detailed view, Figures 5.34a to 5.34c present the axial strain profiles at the radial, musculocutaneous and median/ulnar nerve locations and Figures 5.35a to 5.35c show the corresponding shear strain profiles. As the pressure profile approaches a uniform distribution, the magnitude of the peak strains increases while their position moves outward towards the uncompressed regions of the limb. It should be noted that the exponential pressure profile's peak strains are located directly beneath the edge of the cuff, which is where most nerve lesions have been observed. This suggests that the surface pressure profile applied to the limb may be represented more closely by an exponential rather than a sinusoidal distribution. Also note that as observed while investigating cuff width, the model predicts high positive strain peaks at the median/ulnar nerve location (which can be explained by the restrictive boundary settings at the skin/cuff interface).

Figures 5.36a and 5.36b illustrate the peak axial strains predicted by the single-layer and multi-layer limb compression models while Figures 5.37a and 5.37b represent the shear strain equivalents. Within each figure, the x-axis corresponds to the applied pressure profile (i.e., 1 = sinusoidal, 2 = exponential and 3 = rectangular). As above, the predicted peak axial and shear strains tend to increase as the surface pressure profile approaches a uniform distribution. Furthermore, the musculocutaneous nerve suffers the

highest increase in axial strain (from 40 to 50%), while the radial nerve incurs the highest increase in shear strain (from 40 to 60%). Notwithstanding these two observations, each of the other profiles exhibits similar tendencies. This may be partly explained by the slope of the pressure profiles at the cuff edges and/or by the increasing value of the total load applied to the limb, i.e., the total load from the sinusoidal distribution ($CIRC \int_0^{WIDTH} P_s(z)dz$) is half that from the uniform distribution ($P_{max} * WIDTH * CIRC$). However, reducing the amount of pressure applied by half in the latter case in order to equalize the total load applied would not result in blood flow occlusion for regions distal to the cuff site. Consequently, the trend observed in the axial and shear strain figures is best explained by the slope of the pressure profiles at the cuff edges. Therefore, a smoother pressure profile may lead to a reduced risk of nerve injury.

Finally, the effects of surface pressure profile when cuff width, arm radius and fat percentage vary are investigated. Figures 5.38a and 5.38b show for the single-layer and the multi-layer models, the predicted average maximum axial strain intensities for each pressure profile when the cuff width is varied. If the portions of the curves representing cuff widths of less than 5.0 cm are disregarded, then the rectangular and the sinusoidal curves are seen to grow further apart as the cuff width increases (single-layer model). Consequently, the slope of the pressure profiles at the cuff edges is once again deemed important. Similar observations and comments apply to the predicted average maximum shear strain intensities shown in Figures 5.39a and 5.39b. Figure 5.40a, 5.40b, 5.41a and 5.41b are the analogues of the four preceding figures, except that limb radius, rather than cuff width, is varied. In this case, the rectangular and the sinusoidal curves grow closer as the limb radius increases but the general trend is towards increased strains. Thus, the slope is still emphasized. Finally, varying the fat content in the multi-layer model produces similar trends as those observed for cuff width and arm radius. Figures 5.42a and 5.42b illustrate the resulting curves. Note that the specific effects of fat

content are investigated in Section 5.3.5.

5.3.3.1 Variable Parameters of the Sinusoidal Pressure Profile

Since the surface pressure profile which a tourniquet applies to the limb is essentially sinusoidal in shape, a closer investigation of this distribution may provide more specific information on how to optimize tourniquet designs. As introduced in Section 3.3, two variable features of sinusoidal pressure distributions are investigated: the number of peaks and the pressure offset at the cuff edges. Refer back to Figure 3.17 for an illustration of the surface pressure profiles associated with these varying parameters.

To conduct this investigation, the predicted peak axial and shear strains are first averaged over the three nerve locations. The peaks and pressure offsets are then mapped against the average maximum axial and shear strain intensities for both the single-layer and the multi-layer models. These mappings are presented in Figures 5.43a, 5.43b, 5.44a and 5.44b. As these figures show, the intensity of the average maximum strains tends to increase with pressure offset. This is because an offset value of 1.0 corresponds to a rectangular pressure distribution, which results in an increased pressure slope at the cuff edges. It can also be observed that the number of peaks has little or no effect on the average strain levels. Consequently, it would seem that an offset of 0.0 for a single peak profile induces minimal levels of axial and shear strains, and therefore minimizes the risks of nerve injury.

5.3.4 Influence of Limb Radius

Although only the parameters directly linked to the tourniquet can be modified, the influence of patient-associated parameters is also important since understanding this influence can assist the medical profession in selecting the appropriate cuff for a given individual, thereby further reducing the risk of nerve injuries. The first such investigation

relates to the effects of limb radius on the levels of peak axial and shear strains. The range of limb radii studied varies from 30 mm to 70 mm and is considered realistic.

As an introduction, Figures 5.45a through 5.45c illustrate the predicted axial strain maps associated with limb radii of 30, 50 and 70 mm respectively. Additionally, Figures 5.46a through 5.46c reflect the shear strain maps for identical configurations. Generally, it can be observed that as larger limbs are considered, the areas of maximum axial and shear strains increase and move outward towards the uncompressed regions of the limb.

When profiles of the axial and shear strain distributions are traced for each nerve location, the peak values always occur at the cuff edges. This is confirmed by Figures 5.47a to 5.47c, which provide the axial strain profiles at each nerve location for varying limb radii and by Figures 5.48a to 5.48c, which provide the corresponding shear strain profiles. As above, the highest negative axial strains correspond to the largest limb, for each nerve location. And as for cuff width and pressure distribution, a sudden positive peak occurs at the median/ulnar nerve location, which may be explained by the restrictive skin/cuff boundary settings.

Next, Figures 5.49a and 5.49b show the peak axial strains for various limb radii as predicted by the single-layer and the multi-layer models, respectively. The only major difference encountered between the two figures is the position of the median/ulnar nerve curve. This may be caused by the hypothesis made in the multi-layer model whereby these nerves are assumed to lie directly beneath the fatty tissue layer. However, both figures show that the musculocutaneous nerve suffers the greatest increase in peak axial strains (between 60 and 120%), which is partly due to the increased level of applied pressure required to achieve blood flow occlusion in larger limbs. Note that this rise in predicted peak shear strain may also be partly due to a form of stress/strain concentration effect. Figures 5.50a and 5.50b are the analogues of Figures 5.49a and 5.49b, except

that they illustrate the peak shear strains rather than axial strains. In this case, the highest peak shear strain values lie along the radial nerve. Indeed, this nerve suffers the largest increases in shear strain as the limb radius is increased, whereas the other nerves experience little or no variations in shear strain. Succintly stated, increasing the limb radius results in increases of both peak axial and peak shear strain levels.

Finally, the effect of limb radius combined with cuff width is investigated. Figures 5.51a and 5.51b map the average maximum axial strain intensities for four different cuff widths against increasing limb radii as predicted by the single-layer and the multi-layer models respectively, while Figures 5.52a and 5.52b map the average maximum shear strain intensities for identical configurations. When the cuff widths is expanded from 5.0 cm to 20.0 cm, the average peak axial strains drop by 55 to 80% for a 30 mm limb radius, and by 25 to 50% for a 70 mm limb radius. On the other hand, for similar cuff width expansion, the average peak shear strains experience a constant absolute drop for all limb radii. From these observations, it may be stipulated that increasing cuff width benefits smaller limbs more than larger limbs with respect to axial strain intensities but benefits all limb sizes equally with respect to shear strain intensities.

5.3.5 Influence of Fat Content

Since fatty tissues are found exclusively in non-homogeneous configurations, only the multi-layer limb compression model is considered in the following investigation of the influence of fat content. Since the densities of both muscle and fatty tissues are equivalent (i.e., close to that of water), the percentage of fatty tissue can be interpreted as a measure of weight or volume. However, as specified in the model assumptions (see Section 4.2), the percentage of fat is based on the limb's volume rather than on its weight. Furthermore, the fat content investigated ranges from 5 to 20%, which embodies the majority of the population.

The predicted axial and shear strain profiles at each nerve location are first plotted for varying fat content. These profiles are presented in Figures 5.53a through 5.53c and 5.54a through 5.54c. It can be observed that as the fat content increases, so do the predicted peak strains. It should also be noted that the curves for the 10, 15 and 20% fat contents are almost identical, except in the case of the predicted shear strain profiles at the median/ulnar nerve location where the peak shear strain level for the 20% fat content model is five times higher than that of the 5% fat content model. This large increase may again be explained by the restrictive nature of the skin/cuff interface.

Similarly, the peak axial and shear strain intensities exhibit no significant variations when the fat percentage varies, as illustrated in Figures 5.55 and 5.56. Although there is a significant increase in predicted peak axial strains at the median/ulnar nerve location, the other curves are characterized by a slope approaching zero. The former exception may be partly explained by the fact that the median/ulnar nerves are located between the muscle and fatty tissue layers, where the interface conditions can not be controlled. This may suggest a reduction in credibility of the multi-layer model with respect to strain predictions at the median/ulnar nerve location. Based on these findings, the changes in peak strain intensities when fat content varies are not considered meaningful in the pursuit of an optimum tourniquet design. However, given that the material properties and the boundary conditions surrounding the fatty tissue layer are hypothesized, rather than factual, this last statement should not be viewed as conclusive. Indeed, to obtain an accurate model of the fatty tissue layer, additional data regarding the interactions between layers and the actual material properties of human fatty tissues would need to be gathered.

5.4 Improved Cuff Design

It has been shown that high levels of shear and axial strains are found at the cuff edges under conventional tourniquet/limb configurations. These areas of high intensity strains strongly correlate with experimentally observed nerve lesions [3], especially those at the radial nerve location [37]. Since the ultimate goal of this study is to suggest possible recommendations for future cuff designs, then investigating alternative tourniquet designs which may produce lower levels of peak axial and shear strains at the cuff edges without creating high intensity areas elsewhere is definitely of interest in this study.

5.4.1 Combined Use of the Esmarch Bandage and the Tourniquet Cuff

In an attempt to reduce the risk of injury caused by pneumatic tourniquets, the existing cuff is modified so as to decrease the levels of axial and shear strains felt at the nerve locations. If the slope of the applied pressure profile at the cuff edges is accepted as the major cause of high axial and shear strains (which is supported by the findings of Section 5.3), then wrapping an Esmarch bandage around the limb at the cuff edges may reduce the slope of the surface pressure profiles, thereby minimizing the strain intensities. Figure 5.57 provides an illustration of the proposed Esmarch/tourniquet solution along with the resulting surface pressure profile. From this illustration, it is clear that in order to implement this solution, three variables must be defined: the Esmarch/tourniquet overlap (O_E), the relative Esmarch pressure (P_E), and the Esmarch bandage's width (W_E). To determine the optimum values of these variables, i.e., to find the values which will produce the greatest reductions in peak strains, each of them is investigated. The results of this investigation serve as a basis for proposing a clinical apparatus which combines features of both the Esmarch bandage and the pneumatic tourniquet, and its accompanying procedure.

All the simulations conducted in this section are performed for both the single-layer and the multi-layer models and assume that the Esmarch bandage transmits a sinusoidal surface pressure profile to the limb [39]. The Esmarch/tourniquet overlap parameter characterizes the extent to which the two occlusive devices are combined. This parameter can take on any value between 0 and 1, where 0 signifies that the Esmarch bandage does not overlap at all with the cuff and 1 signifies that it is completely covered by the cuff. The three possibilities which result from pairing the three parameters to be defined in the Esmarch/tourniquet configuration are investigated below.

5.4.1.1 Esmarch/tourniquet Overlap

First, the Esmarch/tourniquet overlap and the Esmarch bandages's width are varied (from 0 to 1 and from 20 to 50 mm, respectively), while the Esmarch pressure is held constant at 10% of the tourniquet cuff pressure applied. Figures 5.58a and 5.58b provide the resulting average maximum axial strain intensities as predicted by the single-layer and multi-layer models respectively, while Figures 5.59a and 5.59b provide the corresponding average maximum shear strain intensities. As the figures show, a 50% Esmarch/tourniquet overlap and a 50 mm Esmarch bandage width produce the largest reductions in predicted peak strains (i.e., are the optimum values). However, the magnitude of these reductions differs from figure to figure. A comparison of Figures 5.51 and 5.52 to Figures 5.58 and 5.59 with respect to these two parameter values shows that the single-layer model predicts an average peak axial strain reduction of 30% (from 0.165 to 0.117) and an average peak shear strain reduction of 27% (from 0.205 to 0.150), while the multi-layer model predicts reductions of 13% (from 0.600 to 0.520) and 3% (from 0.870 to 0.845) respectively. Furthermore, with this optimum configuration, the initial tourniquet cuff width is increased by 50 mm (50% times 50 mm at both edges of the cuff). Referring back to Equation 5.4, this increased width should produce even larger

peak strain reductions than those observed in Figures 5.58a, 5.58b, 5.59a and 5.59b, since wider cuff widths necessitate lower occlusion pressure levels, which in turn reduce the load applied to the limb. Consequently, an Esmarch overlap of 50% offers the greatest reduction in destructive strains located at the edges of the tourniquet.

5.4.1.2 Esmarch Relative Pressure

Next, the Esmarch/tourniquet overlap and the relative Esmarch pressure are varied (from 0 to 1 and from 10 to 50% of the tourniquet cuff pressure applied, respectively), while the Esmarch bandage's width is held constant at 40 mm. Figures 5.60a and 5.60b provide the resulting average maximum axial strain intensities as predicted by the single-layer and multi-layer models respectively, while Figures 5.61a and 5.61b show the corresponding average maximum shear strain intensities. Once again, a 50% Esmarch/tourniquet overlap produces the largest reductions in predicted peak strains. However, the optimum relative Esmarch pressure value differs for axial and shear strains. In the former case, an Esmarch pressure corresponding to 20 or 30% of the tourniquet cuff pressure applied is best, while in the latter case, a relative pressure of 50% or more is indicated. Based on an Esmarch pressure value equal to 50% of the tourniquet cuff applied pressure, the average peak axial strain reductions range from 12 to 42% and the average peak shear strain reductions range from 6 to 25%. Consequently, an Esmarch pressure value equal to 30 to 50% of tourniquet pressure is most effective in reducing the peak levels of axial and shear strains.

5.4.1.3 Esmarch Width

Finally, the Esmarch bandage's width and the relative Esmarch pressure are varied (from 20 to 50 mm and from 10 to 50% of the tourniquet cuff pressure applied, respectively), while the Esmarch/tourniquet overlap is fixed at its previously found optimum

value of 50%. Figures 5.62a and 5.62b illustrate the resulting average maximum axial strain intensities as predicted by the single-layer and multi-layer models respectively, while Figures 5.63a and 5.63b present the corresponding average maximum shear strain intensities. Generally, the average peak strain intensities decrease as the width of the Esmarch bandage increases. Thus, theoretically, it would seem that a width value equal to infinity would produce optimal results. However, in practice, the Esmarch bandage's width is restricted to that of the tourniquet cuff width, given a 50% Esmarch/tourniquet overlap value. Furthermore, it has been reported that the excessive use of Esmarch bandages may produce detrimental pressure concentrations inside the arm [12].

5.4.1.4 Discussion

From these investigations, it appears that applying an Esmarch bandage at each edge of the cuff would improve the efficiency of the tourniquet, i.e., reduce the risks of nerve injuries. Figures 5.64 and 5.65 compare the axial and shear strain profiles obtained for a conventional pneumatic tourniquet and the optimal Esmarch/tourniquet configuration, as predicted by the single-layer model. Both assume a 10 cm cuff width, a 50 mm arm radius and a sinusoidal surface pressure profile, while the Esmarch/tourniquet configuration further assumes a cuff/bandage overlap of 50%, an Esmarch bandage width of 50 mm and a relative Esmarch pressure of 50%. This comparison demonstrates that the areas of peak axial and shear strain shrink considerably when an Esmarch bandage is superimposed. It should be noted that the radial nerve shows the largest decrease in peak shear strain, while the musculocutaneous nerve benefits from the largest reduction in peak negative axial strain.

Further justification for implementing the Esmarch/tourniquet solution is provided by the fact that the edges of the pneumatic tourniquet tend to curve upwards when it is inflated, thereby reducing the effective tourniquet cuff width. This is illustrated

in Figure 5.66, which is a schematic representation of the pneumatic tourniquet as it is inflated. Reductions of 0.5 to 1.5 cm at each end of the tourniquet cuff have been measured, the exact length depending on the cuff's width and configuration. Although the amount of pressure transmitted to the cuff edges is limited, for a 10.0 cm cuff, a 3.0 cm width decrease corresponds to a total load reduction of 30%, as shown in Figure 5.67. This implies that a higher pressure level (about 20 to 25 mmHg higher) would be required to compensate for this loss. By using the Esmarch/tourniquet combination, the peak axial and shear strain levels would be reduced since: the effective length of the tourniquet is physically increased, the occlusion pressure level is indirectly reduced, and the slope of the pressure profile at the cuff edges is alleviated.

5.5 Results from the Blood Vessel Occlusion Model

A complementary purpose of this study is to construct a working artery model to be used in subsequent studies relating blood flow occlusion with constrictive devices (such as the pneumatic tourniquet). To this end, the finite element model of the brachial artery developed in Section 4.4 is subjected to various clinical conditions. For this study, the accuracy of the artery model is verified by first computing the occlusion pressure for varying cuff width, artery length and material properties of the artery, and then comparing the results obtained to those of previous experimental studies [20,40,41]. The assumptions made for each simulation performed in this section are listed in Table 5.3. Furthermore, blood pressure is simulated by applying a constant 100 mmHg pressure level to the inner surface of the artery (which corresponds to the mean value between diastolic and systolic pressure). The externally applied pressure exhibits a sinusoidal profile as described in Section 4.2.3. Boundary conditions are set to account for the planes of symmetry and the restrictive nature of the ends of the model (see Section 4.2.2). As an

overview, Figure 5.68 illustrates a cross-section of the collapsed artery.

The first investigation studies the effect of varying cuff width and artery length (from 5.0 to 45.0 cm and from 30.0 to 45.0 cm, respectively) on the pressure level needed to occlude, while the material properties of the artery are held constant. Figure 5.69 shows the resulting occlusion pressure levels. These stabilize at a pressure of 155 mmHg and a cuff width of 10 cm. Although the model exhibits the same asymptotic tendencies as observed clinically [20,40,41], the pressure level at which it converges is 40 mmHg higher than that measured experimentally. Of the factors which could cause this discrepancy, the material property settings provide the most likely explanation.

The second investigation studies the effect of varying cuff width (from 5.0 to 45.0 cm) and material properties of the artery, while the artery length is held constant at 30 cm. Given the wide variance of material properties measured by previous researchers (refer to Section 3.4), three Young's moduli (i.e., the most likely values plus or minus 50% that amount) in each of the radial, circumferential and axial directions are studied. Figures 5.70, 5.71 and 5.72 provide the resulting occlusion pressure levels. Generally, these increase as the artery wall becomes stiffer. This indicates that the choice of material properties is an important factor in determining the validity of the artery occlusion model. Furthermore, by comparing the experimental curves to the numerical curves, these figures show that for smaller cuff widths, the artery exhibits stiffer properties. This may be explained by the higher strain levels experienced with smaller cuff widths, which imply that the 50% elongation mark of the tissues may have been reached. This in turn may lead to the assumption that the collagen fibers have now entered into the problem (as explained in Section 3.1.1). Consequently, the stress stiffening properties of the artery wall undoubtedly play an important role in its behaviour under external loading conditions.

Although this model does not accurately replicate clinical results, it shows similar

trends. The next chapter suggests possible improvements to this model so that eventually it may be used in conjunction with the limb compression model and provide valuable information which will assist in the task of optimizing tourniquet designs.

Chapter 6

CONCLUSIONS AND RECOMMENDATIONS

The final phase of this research project is to recommend possible improvements to the present tourniquet design in order to minimize the frequency of nerve injuries caused by this occlusive device. Now that a fundamental understanding of the pressure transmission between the pneumatic cuff and the limb has been acquired, the conclusions reached in this process can be translated into such recommendations. Hence, in this chapter, general conclusions drawn from the numerical and theoretical research work are presented, followed by more specific conclusions on the effects of axial and shear strains and their association with the proposed mechanisms of nerve damage. Suggestions regarding the best method of utilizing the existing tourniquets as well as recommendations on how to optimize their design are proposed. Finally, since scientific research is a never-ending task, future clinical/experimental and numerical/analytical work which may provide greater insight into this field are also suggested.

6.1 Conclusions

From the literature search and numerical analysis of the single-layer and multi-layer limb compression models and of the blood vessel occlusion model, five general conclusions and seven specific conclusions concerning the effect of patient and cuff parameters on limb compression are elicited.

6.1.1 General Conclusions Resulting from the Present Research

THE STRESS AND STRAIN DISTRIBUTIONS IN A LIMB SUBJECTED TO EXTERNAL PRESSURE FROM A PNEUMATIC TOURNIQUET CAN BE ADEQUATELY PREDICTED USING THE FINITE ELEMENT METHOD. The two finite element limb compression models developed produced acceptable results when compared to previous studies. In particular, the single-layer model closely approximated Hodgson's analytically produced strain patterns [44], Auerbach's numerically obtained hydrostatic pressure profiles [42], and Thomson's and Doupe's experimentally measured hydrostatic pressure profiles [41]. The additional features of the multi-layer model produced an even more accurate replica of the actual limb anatomy. Furthermore, the finite element mesh adopted for both models resulted in average errors in radial and circumferential stress profiles of less than 2% and maximum errors of less than 5%.

THE PRESENCE OF PEAK SHEAR STRAINS INDICATES THAT THIS IS THE MOST PROBABLE EXPLANATION FOR THE DISTRIBUTION OF OBSERVED NERVE LESIONS. The position and magnitude of the predicted shear and axial strains correlate with the tourniquet-induced nerve lesions recorded by Ochoa et al. [3]. Although both axial and shear strain exhibit peak regions at the edges of the cuff, only shear strain shows a correlation with the directional nature of the invagination phenomenon observed by Ochoa et al. [3]. In addition, due to their radial location, peak shear strains (not axial strains) correspond with the apparent susceptibility of the deeply embedded nerves [37].

THE MAGNITUDE AND LOCATION OF THE PEAK SHEAR AND AXIAL STRAINS ARE HIGHLY DEPENDENT ON TOURNIQUET AND PATIENT PARAMETERS. Variations in tourniquet parameters (cuff width and surface pressure profile) and patient parameters (limb radius, fat content and interface conditions) produced significantly

different levels of maximum shear (and axial strains), and displaced the areas of peak strains. That is, wider cuffs and smoother pressure profiles exhibited lower peak values of shear strains, while larger limbs and greater fat contents exhibited higher peak values.

NUMERICAL RESULTS INDICATE THAT MODIFICATIONS TO THE CONVENTIONAL PNEUMATIC TOURNIQUET PRESSURE DISTRIBUTION SHOULD PROVIDE A REDUCED RISK OF POST-SURGICAL TOURNIQUET-RELATED NERVE INJURIES. The shear strain levels found at the edges of the cuff under simulated optimum occlusion cuff pressures decreased when an additional pressure profile (not unlike that provided by an Esmarch bandage) is imposed at both ends of the tourniquet cuff. Shear strain levels further decreased with the optimal 'Esmarch/tourniquet' configuration obtained in Section 5.4. These results suggest that a reduction in tourniquet-related injuries should accompany the introduction of this modified pressure distribution.

THE FINITE ELEMENT METHOD MAY BE USEFUL IN UNDERSTANDING AND PREDICTING BLOOD VESSEL COLLAPSE UNDER SURGICAL CONDITIONS. The finite element blood vessel occlusion model constructed predicted similar trends as those previously obtained through experimental and analytical investigations. However, the pressure levels at which the model predicted blood flow occlusion would occur differed from the experimental and analytical ones by up to 80 mmHg or 100%.

6.1.2 Specific Conclusions Resulting from the Present Research

HIGH SHEAR STRAIN LEVELS AT THE BONE/MUSCLE INTERFACE ARE DUE TO THE RESTRICTIVE NATURE OF THIS BOUNDARY AND MAY ACCOUNT FOR THE APPARENT SUSCEPTIBILITY OF THE DEEPLY EMBEDDED NERVES. Simulations with restrained and unrestrained conditions at the bone/muscle interface show that shear

strain concentrations at the cuff edges occur only when the nodes at the interface are restricted in the axial direction. However, this interface must be restricted to accurately reflect the actual limb structure (this is supported by the stress and strain profiles obtained by other researchers). Additionally, for each combination of patient and tourniquet parameters studied, a concentrated region of peak shear strain (up to 1.5) is observed at the bone/muscle interface at the cuff edges. This region coincides with the position of the radial nerve where most lesions have been recorded [37].

THE INTERFACE CONDITION SETTINGS AT THE SKIN/CUFF JUNCTION DO NOT SIGNIFICANTLY AFFECT THE LEVELS OF PEAK DESTRUCTIVE STRAINS. Although restraining movement in the axial direction at this interface causes a large positive shear strain peak at the median/ulnar nerve location, it does not significantly alter peak shear and negative axial strain predictions at the other nerve locations.

LARGER CUFF WIDTHS REDUCE THE MAGNITUDE OF THE PEAK SHEAR STRAINS CONCENTRATED AT THE CUFF EDGES. Lower levels of potentially destructive strains are predicted with increased cuff widths for two reasons. Since the pressure required to achieve blood flow occlusion diminishes as cuff width increases (refer to Equation 5.4), the shear strain peaks are reduced. And since the slope of the assumed sinusoidal pressure profile decreases as cuff width increases, the predicted peak shear strains decrease further.

LARGER LIMB RADII EXPERIENCE HIGHER DESTRUCTIVE STRAIN LEVELS AT PREDICTED OCCLUSION PRESSURE. Contrary to previous numerical results [44], larger limbs exhibit higher levels of shear and negative axial strains. This may have been caused by the fact that for larger limbs, a higher pressure is needed to effect blood flow occlusion (refer to Equation 5.4), which could result in higher peak axial and

shear strains. It may also be explained by the fact that if shear and axial strains increase with depth, then a larger limb provides more depth than a smaller one. It follows that patients having large diameter, fatty tissued limbs (obese patients) should be most susceptible to post-surgical nerve injuries.

APPLYING A SMOOTHER PRESSURE PROFILE (REDUCED PRESSURE GRADIENT) AT THE CUFF EDGES DECREASES THE DESTRUCTIVE STRAIN INTENSITIES AT THE NERVE LOCATIONS. Simulations assuming three different surface pressure profiles show that as the profile changes from a smooth sinusoidal configuration to a sharper rectangular one, the peak shear strains increase dramatically (by 50%). Similarly, simulations assuming various offsets at the cuff edges and different number of peaks for the sinusoidal pressure profile show that as the offset increases from 0 to 1 (i.e., the profile changes from sinusoidal to rectangular), the peak shear strains suffer considerable increases. These simulations also show that for a given cuff width, as the number of peaks increase, so do the pressure gradients at the cuff edges and the predicted peak strains.

USING THE OPTIMAL 'ESMARCH/TOURNIQUET' COMBINATION PROPOSED MAY REDUCE DESTRUCTIVE STRAIN LEVELS BY UP TO 42%. Simulations using several Esmarch/cuff configurations resulted in an optimum combination of Esmarch bandage specifications which reduces the levels of peak shear and negative axial strains. Specifically, a 0.5 Esmarch/tourniquet overlap and a 50 mm Esmarch bandage width produce the largest reductions in both axial and shear strains, while relative Esmarch pressures equal to 25 and 50% of the tourniquet cuff pressure applied produce the largest reductions in axial and shear strains, respectively.

THE BEHAVIOUR OF THE BLOOD VESSEL OCCLUSION MODEL IS SENSITIVE TO MATERIAL PROPERTY DEFINITIONS. Simulations of the blood vessel occlusion model

show that the length of the artery section has no bearing on the occlusion pressure but that the material property values (i.e., the Young's moduli) do. They also show that for smaller cuff widths, the strain levels in the artery have to be higher in order for blood flow occlusion to occur. Thus, it may be that the artery tissues enter the second phase of deformation in these cases and exhibit much stiffer material properties. Notwithstanding the shortcomings of this model, it exhibits similar trends to those observed by previous researchers [20,40,41].

6.2 Recommendations

Based on the conclusions presented in the previous section, two suggestions regarding utilization of existing surgical tourniquets and two recommendations for optimizing future cuff designs are proposed.

6.2.1 Recommendations for Clinical Use

THE WIDEST AVAILABLE CUFFS SHOULD BE USED DURING LENGTHY SURGICAL PROCEDURES, ESPECIALLY ON LARGER LIMBS. This would decrease the load applied to the limb which would lower the destructive shear strain levels and thus minimize the risk of nerve injuries. Note that if the surgical field is large, the medical advantages of a wider cuff should be weighed against the disadvantage of obstructing the surgeon's movements.

A LUBRICANT SHOULD BE APPLIED AT THE SKIN/CUFF INTERFACE PRIOR TO TOURNIQUET APPLICATION. This would allow axial movement of the skin under pressurized conditions. This procedure should reduce the shear stress and strain levels near the limb surface, and also eliminate the stretching of the skin and thus reduce post-surgical sensitivity at the occlusion site.

6.2.2 Recommendations for Future Cuff Designs

A MODIFIED PRESSURE PROFILE AT THE CUFF EDGES SHOULD BE INCLUDED IN THE DESIGN REQUIREMENTS OF FUTURE PNEUMATIC TOURNIQUETS. Because the currently used surgical tourniquets normally exhibit pressure profiles somewhere between sinusoidal and exponential, the pressure gradient at the cuff edges may not be optimal. A possible solution may be to design a tourniquet with separate bladder compartments and multiple bladders, each having its own pressure controller (i.e., microprocessor). In this way, the pressure profile could be determined by computer and become one more controllable feature of occlusive devices. As an example, Figure 6.1 illustrates a possible design for this proposed multi-bladder tourniquet. A proposed pressure distribution is that of the 'Esmarch/tourniquet' combination presented in Section 5.4.1 (which has been shown to reduce the levels of peak axial and shear strains).

IMPLEMENTING THE 'ESMARCH BANDAGE/TOURNIQUET' CUFF CONFIGURATION PROPOSED IN SECTION 5.4 SHOULD BE GIVEN SERIOUS CONSIDERATION. This would reduce the levels of destructive strains inside the limb in three ways: first, by physically increasing the effective cuff width; second, by indirectly reducing the maximum load needed to achieve blood flow occlusion; and third, by directly alleviating the slope of the pressure profile at the cuff edges. Figure 6.2 provides an illustration of the proposed 'Esmarch/tourniquet' configuration.

6.3 Recommendations for Further Investigations

The prediction of occlusion pressure is only possible if the compression patterns beneath the cuff are known and the blood flow mechanics in limb vessels are understood. In this respect, recommendations for future work pertaining to pressure profile and blood

flow occlusion experiments are presented below.

6.3.1 Clinical and Experimental Investigations

INVESTIGATE THE HYPOTHESIS THAT SHEAR STRAINS ARE RESPONSIBLE FOR OBSERVED NERVE LESIONS. Using disarticulated cadaver limbs, the muscle layer could be separated from the bone tissues. This would allow the muscle tissues to move axially at the bone/muscle interface, and thus eliminate the high regions of shear strain beneath the cuff edges at this interface. It would also enable the effects of axial and shear strains to be investigated separately. Thereafter, the peripheral nerves could be dissected (as in Ochoa et al.'s study [3]) to locate the areas of nerve lesion occurrences and to assess an order of vulnerability for both free and restricted boundary condition settings at the bone/muscle interface.

GATHER BLOOD FLOW OCCLUSION MEASUREMENTS USING THE ESMARCH/CUFF CONFIGURATION. As in earlier clinical investigations pertaining to blood flow occlusion [40], the influence of Esmarch bandage pressure, width and overlap could be investigated in order to produce similar curves showing the relationships between these parameters.

ACCURATELY MEASURE THE SURFACE PRESSURE PROFILES TRANSMITTED TO THE LIMB FROM A VARIETY OF CUFF DESIGNS. By using a more complex pressure probe, the pressure distribution applied to the limb could be mapped in both the axial and circumferential directions. Figures 6.3a and 6.3b show two examples of pressure sensors which could be employed to this end. The first operates using a piezoelectric sensor with a measurement ability of up to one pressure reading per square millimeter. The second operates as a potentiometer where the electrical resistance of the circuits changes as pressure is applied. Although the first option

necessitates extensive electrical wiring, it offers a greater resolution. This is important to assess the effect of a multiple bladder design. Eventually, this pressure mapping sensor could also be employed during surgery to help regulate the actual pressure transmitted to the limb.

EXPERIMENTALLY INVESTIGATE THE BLOOD FLOW OCCLUSION PHENOMENON BASED ON A VARIETY OF THICK-WALLED VESSEL MODELS. Using an experimental setup such as that shown in Figure 6.4, the collapse phenomenon of any given thick-walled vessel could be studied. The multi-level pressure chamber could be used to simulate different pressure profiles applied to the artery. In this way, the optimum pressure profile needed to occlude blood flow would be established. Furthermore, the number of pressure chambers could be modified to simulate increasing or decreasing cuff width. The complexity of the study could vary from steady state fluid flow to time-dependent pulsating flow. In addition, vessels ranging from latex tubes to actual human blood vessels could be studied.

6.3.2 Numerical and Analytical Investigations

IMPROVE THE PRESENT FINITE ELEMENT LIMB COMPRESSION MODELS TO ACCOUNT FOR THE NON-LINEAR AND TIME-DEPENDENT FEATURES OF *in vivo* MUSCLE TISSUES. Using the non-linear and viscoelastic capabilities of a more complex element, the time-dependent nature of nerve lesion occurrences could be investigated. Furthermore, the non-linear features of human tissue stress/strain curves could be incorporated into the model with this type of analysis. Although the axisymmetric elements employed in this study did not possess non-linear or viscoelastic capabilities, other elements do possess these properties (in addition to being three-dimensional). This more complex element could allow a more rigourous study of

the unsymmetrical properties of human limbs.

INCORPORATE THE TOURNIQUET IN THE FINITE ELEMENT LIMB COMPRESSION MODELS. In this way, the material and geometrical properties of the tourniquet could be studied. Furthermore, the multi-bladder configuration proposed earlier could also be investigated with this additional feature.

IMPROVE THE FINITE ELEMENT BLOOD VESSEL OCCLUSION MODEL IN ORDER TO ACCURATELY REPRODUCE THE RESULTS OBTAINED EXPERIMENTALLY. Using a more complex element, the blood vessel occlusion model could reflect the non-linear characteristics of the artery wall. Furthermore, the model could incorporate the non-homogeneous configuration of *in vivo* arteries (i.e., smooth muscle, collagen and elastin). Additionally, a dynamic investigation of the effects of pulsating flow in comparison to steady state conditions could be performed.

USE THE LIMB COMPRESSION MODELS AND THE ARTERY OCCLUSION MODEL CONJOINTLY TO FURTHER OPTIMIZE CUFF DESIGN. While the limb compression model would predict stress and strain patterns in the limb, the blood vessel occlusion model would gather the stress profiles along the artery site from the previous model and apply this distribution to its outer surface in order to ensure that collapse results. Consequently, minimization of peak destructive strains could be done while the blood vessel collapse would be verified.

Bibliography

[1] Aspen Labs, Inc. *Use of Surgical Tourniquets, A Self-Instructional Program.* 1988.

[2] Mullick, S. The tourniquet in operations upon the extremities. *Journal of Surgery, Gynecology, and Obstetrics*, **146**: 821-826, 1978.

[3] Ochoa, J., Fowler, T. J., and Gilliatt, R. W. Anatomical changes in peripheral nerves compressed by a pneumatic tourniquet. *Journal of Anatomy*, **113**: 433-455, 1972.

[4] Lewis, T., Pickering, G. W., and Rothschild, P. Centripetal paralysis arising out of arrested bloodflow to the limb, including notes on a form of tingling. *Heart*, **16**: 1-32, 1931.

[5] Denny-Brown, D., and Brenner, C. Paralysis of nerve induced by direct pressure and by tourniquet. *Archives of Neurology and Psychiatry*, **51**: 1-26, 1944.

[6] Grundfest, H. Effects of hydrostatic pressures upon the excitability, the recovery, and the potential sequence of frog nerve. *Cold Spring Harbor Symposia on Quantitative Biology*, **4**: 179-187, 1936.

[7] Ochoa, J., Danta, G., Fowler, T. J., and Gilliatt, R. W. Nature of the nerve lesion caused by a pneumatic tourniquet. *Nature, London*, **233**: 265-266, 1971.

[8] McEwen, J. A., and Auchinleck, G. F. Advances in surgical tourniquets. *AORN Journal*, **36**: 889-896, 1982.

[9] Arenson, D. J., and Weil, L. S. The uses and abuses of tourniquets in bloodless field foot surgery. *Journal of American Podiatry Association*, **66**: 854-861, 1976.

[10] Klenerman, L. Tourniquet paralysis. *The Journal of Bone and Joint Surgery*, **65-B**: 374-375, 1983.

[11] Kalisman, M., and Millendorf, J. B. Use and abuse of the tourniquet. *Infections in Surgery*, **2**: 197-204, 1983.

[12] Fletcher, I. R., and Healy, T. E. The arterial tourniquet. *Annals of the Royal College of Surgeons of England*, **65**: 409-417, 1983.

[13] Klenerman, L. The tourniquet in surgery. *The Journal of Bone and Joint Surgery*, **44-B**: 937-953, 1962.

[14] McGraw, R. W., McEwen, J. A., and Wachsmuth, M.A. A new pneumatic tourniquet. *American Society for Surgery of the Hand*, **63B**: 459, 1981.

[15] McEwen, J. A., and McGraw, R. W. An adaptive tourniquet for improved safety in surgery. *IEEE Transactions on Bio-Medical Engineering*, **BME-29**: 122-128, 1982.

[16] Johnson, T. L., Wright, S. C., and Segall, A. Filtering of muscle artifact from the electroencephalogram. *IEEE Transactions on Bio-Medical Engineering*, **BME-26**: 556-563, 1975.

[17] Shaw, J. A., and Murray, D. G. The relationship between tourniquet pressure and underlying soft-tissue pressure in the thigh. *The Journal of Bone and Joint Surgery*, **64-A**: 1148-1152, 1982.

[18] Bruner, J. M. Time, pressure, and temperature factors in the safe use of the tourniquet. *The Hand*, **2**: 39-42, 1970.

[19] Griffiths, J. C., and Heywood, O. B. Bio-mechanical aspects of the tourniquet. *The Hand*, **5**: 113-118, 1973.

[20] Moore, M. R., Garfin, S. R., and Hargens, A. R. Wide tourniquets eliminate blood flow at low inflation pressures. *The Journal of Hand Surgery*, **12A**: 1006-1011, 1987.

[21] Fowler, T. J., Danta, G., and Gilliatt, R. W. Recovery of nerve conduction after a pneumatic tourniquet: observations on the hind-limb of the baboon. *Journal of Neurology, Neurosurgery, and Psychiatry*, **35**: 638-647, 1972.

[22] Klenerman, L. Tourniquet time — how long? *The Hand*, **12**: 231-234, 1980.

[23] Patterson, S., and Klenerman, L. The effect of pneumatic tourniquets on the ultrastructure of skeletal muscle. *The Journal of Bone and Joint Surgery*, **61-B**: 178-183, 1979.

[24] Sy, W. P. Ulnar nerve palsy possibly related to use of automatically cycled blood pressure cuff. *Anaesthesia and Analgesia*, **60**: 687-688, 1981.

[25] Fahmy, N. R., and Patel, D. G. Hemostatic changes and post-operative deep-vein thrombosis associated with use of a pneumatic tourniquet. *The Journal of Bone and Joint Surgery*, **63-A**: 461-465, 1981.

[26] Hofmann, A. A., and Wyatt, R. W. B. Fatal pulmonary embolism following tourniquet inflation. *The Journal of Bone and Joint Surgery*, **67-E**: 633-634, 1985.

[27] Wells, H. S., Joumans, J. B., and Miller, D. G. Tissue pressure (intracutaneous, subcutaneous, and intramuscular) as related to venous pressure, capillary filtration, and other factors. *Journal of Clinical Investigation*, **17** : 489-499, 1938.

[28] Stein, R. E. Use of the tourniquet during surgery in patients with sickle cell hemoglobinapothies. *Clinical Orthopaedics*, **151**: 231-233, 1980.

[29] Arenson, J., Steer, M. D., and Joffe, N. Edema of the pipilla of water stimulating retained common duct stone. *Surgery*, **817**: 712-713, 1980.

[30] Kaufman, R. D. Tourniquet induced hypertension. *British Journal of Anesthesiology*, **54**: 333-336, 1982.

[31] Griffiths, J. C., and Sankarankutty, M. Bone marrow pressure changes under an inflatable tourniquet. *The Hand*, **15**: 3-8, 1983.

[32] Gilliatt, R. W., McDonald, W. I., and Rudge, P. The site of conduction block in peripheral nerves compressed by a pneumatic tourniquet. *Journal of Physiology*, **238**: 31p-32p, 1974.

[33] Bentley, F. H., and Schlapp, W. The effects of pressure on conduction in peripheral nerve. *Journal of Physiology*, **102**: 72-82, 1943.

[34] McEwen, J. A. Complications of and improvements in pneumatic tourniquets used in surgery. *Medical Instrumentation*, **15**: 253-257, 1981.

[35] Yamada, H. *Strength of Biological Materials*. Evans, Williams & Wilkins Co., Baltimore, 1970.

[36] Sinclair, D. C. Observations on sensory paralysis produced by compression of a human limb. *Journal of Neurophysiology*, **11**: 75-92, 1947.

[37] Eckhoff, N. L. Tourniquet paralysis: a plea for the extended use of the pneumatic tourniquet. *Lancet*, **2**: 343-345, 1931.

[38] Berliner, K., Fujiy, H., Ho Lee, D., Yildiz, M., and Garnier, B. The accuracy of blood pressure determinations. A comparison of direct and indirect measurements. *Cardiologia*, **37**: 118-128, 1960.

[39] McLaren, A. C., and Rorabeck, C. H. The pressure distribution under tourniquets. *The Journal of Bone and Joint Surgery*, **67-A**: 433-438, 1985.

[40] Breault, M. J. *A Biomedical Investigation of Blood Flow Occlusion Achieved with the Use of Surgical Pneumatic Tourniquets*. University of British Columbia, Department of Mechanical Engineering. Thesis, M.A.Sc., 1988.

[41] Thomson, A. E., and Doupe, J. Some factors affecting the auscultatory measurement of arterial blood pressures. *Canadian Journal of Research*, **27E**, 72-80, 1949.

[42] Auerbach, S. M. Axisymmetric finite element analysis of tourniquet application on limb. *Journal of Biomechanics*, **17**: 861-866, 1984.

[43] Chow, W. W., and Odell, E. I. Deformations and stresses in soft body tissues of a sitting person. *Journal of Biomechanical Engineering*, **100**: 79-87, 1978.

[44] Hodgson, A. J. *A Parametric Study of the Axisymmetric Loading of an Anisotropically Elastic Limb Model by a Tourniquet.* University of British Columbia, Department of Mechanical Engineering. Thesis, M.A.Sc., 1986.

[45] Gallagher, R. H., Simon, B., Johnson, P., and Gross, J. *Finite elements in Biomechanics.* John Wiley & Sons, New York, 1982.

[46] Williams, P. L., and Warmick, R. *Gray's Anatomy (36th edition).* W. B. Saunders Co., Philadelphia, 1980.

[47] Advani, S. H., Martin, R. B., and Powell, W. R. Mechanical properties and constitutive equations of anatomical materials. *Applied Physiological Mechanics*, 31-103. Hardwood Academic Publishers, New York, 1979.

[48] Hill, A. V. The mechanics of active muscle. *Proceedings of the Royal Society of London*, **B141**: 104-117, 1953.

[49] Husain, T. An experimental study of some pressure effects on tissues, with reference to the bed-sore problem. *Journal of Pathology and Bacteriology*, **66**: 347-358, 1953.

[50] Timoshenko, S. P., and Goodier, J. N. *Theory of Elasticity* (3rd edition). McGraw-Hill, New York, 1970.

[51] Tickner, E. G., and Sacks, A. H. A theory for the static elastic behavior of blood vessels. *Biorheology*, **4**: 151-168, 1967.

[52] Peterson, L. H., Jensen, R. E., and Parnell, J. Mechanical properties of arteries in vivo. *Circulation Research*, **8**: 622-639, 1960.

[53] Moreno, A. H., Katz, A. I., Gold, L. D., and Reddy, R. V. Mechanics of distension of dog veins and other very thin-walled tubular structures. *Circulation Research*, **27**: 1069-1080, 1970.

[54] Evans, F. G. *Mechanical Properties of Bone.* Charles C. Thomas, Springfield (Illinois), 1973.

[55] Spence, A. P. *Basic Human Anatomy* (2nd edition). The Benjamin/Cummings Publishing Company Inc., Menlo Park (California), 1986.

[56] Cushing, H. Pneumatic tourniquets: with especial reference to their use in craniotomies. *Medical News*, **84**: 577-580, 1904.

[57] Holt, J. P. Flow through collapsible tubes and through *in situ* veins. *IEEE Transactions on Bio-Medical Engineering*, **BME-16**: 274-283, 1969.

[58] Rubinow, S. I., and Keller, J. B. Flow of a viscous fluid through an elastic tube with applications to blood flow. *Journal of Theoretical Biology*, **35**: 299-313, 1972.

[59] Oates, G. C. Fluid flow in soft-walled tubes. Part 1: steady flow. *Medical and Biological Engineering*, **13**: 773-779, 1975.

[60] Oates, G. C. Fluid flow in soft-walled tubes. Part 2: behaviour of finite waves. *Medical and Biological Engineering*, **13**: 780-784, 1975.

[61] Griffiths, D. J. Negative-resistance effects in flow through collapsible tubes: 1 relaxation oscillations. *Medical and Biological Engineering*, **13**: 785-790, 1975.

[62] Griffiths, D. J. Negative-resistance effects in flow through collapsible tubes: 2 two-dimensional theory of flow near an elastic constriction. *Medical and Biological Engineering*, **13**: 791-796, 1975.

[63] Griffiths, D. J. Negative-resistance effects in flow through collapsible tubes: 3 two-dimensional treatment of the elastic properties of elastic constriction. *Medical and Biological Engineering*, **13**: 797-801, 1975.

[64] Shapiro, A. H. Steady flow in collapsible tubes. *Journal of Biomechanical Engineering*, **99**: 126-147, 1977.

[65] Kresch, E., and Noordergraaf, A. Cross-sectional shape of collapsible tubes. *Biophysical Journal*, **12**: 274-294, 1972.

[66] Wild, R., Pedley, T. J., and Riley, D. S. Viscous flow in collapsible tubes of slowly varying elliptical cross-section. *Journal of Fluid Mechanics*, **81**: 273-294, 1977.

[67] Hall, P., and Parker, K. H. The stability of the decaying flow in a suddenly blocked channel. *Journal of Fluid Mechanics*, **75**: 305-314, 1976.

[68] Lambert, R. K., and Wilson, T. A. Flow limitation in a collapsible tube. *Journal of Applied Physiology*, **33**: 150-153, 1972.

[69] Conrad, W. A. Pressure-flow relationships in collapsible tubes. *IEEE Transactions on Bio-Medical Engineering*, **BME-16**: 284-295, 1969.

[70] Katz, A. I., Chen, Y., and Moreno, A. H. Flow through a collapsible tube. Experimental analysis and mathematical model. *Biophysical Journal*, **9**: 1261-1279, 1969.

[71] Reddy, J. N. *An Introduction to the Finite Element Method.* McGraw Hill, New York, 1984.

[72] Zienkiewicz, O. C., and Morgan, K. *Finite Elements and Approximation.* John Wiley & Sons, New York, 1983.

[73] Ghista, D. N., Kobayashi, A. S., and Davids, N. Analyses of some biomechanical structures and flows by computer-based finite element method. *Computers in Biology and Medecine*, **5**: 119-161, 1975.

[74] Attinger, E. O. Wall properties of veins. *IEEE Transactions on Bio-Medical Engineering*, **BME-16**: 253-261, 1969.

Table 3.1: **Mechanical properties of muscles**

Ref.	Muscle	Method Description	Young's Modulus (kPa)	Poisson Ratio
[47]	variety	tensile	5 - 21	-
[43]	buttocks	finite element	15	0.49
[35]	variety	tensile	8 - 30	-
[44]	arm	analytical	15	0.45
[42]	arm	finite element	15	0.49

Table 3.2: **Mechanical properties of blood vessels**

Ref.	Vessel	Method Description	Young's Modulus (kPa)	Poisson Ratio
[51]	brachial	axial tension and internal pressure	1 000 - 4 000 (E_θ) 200 - 500 (E_r) 400 - 2 500 (E_z)	0.0 ($\nu_{r\theta}$) 0.20 - 0.45 (ν_{rz}) 0.40 - 0.80 ($\nu_{\theta z}$)
[53]	dog vena cava	relaxed	50 (E_θ)	-
[73]	arterioles	relaxed	500 - 5 000 (collagen) 50 (smooth muscle)	-
[74]	veins	relaxed	10 000 - 100 000 (collagen) 600 (elastin)	-
[52]	veins and arteries	relaxed	300 (elastin) 3 000 (collagen) 6 - 6 000 (smooth muscle)	-
[66]	veins	relaxed	300 - 800 (elastin) 1 000 000 (collagen) 2 100 (rubber) 700 (vein)	-
[35]	femoral and brachial	tensile	500 - 2 200 (E_θ) 300 - 1 300 (E_z)	-

Table 3.3: **Mechanical properties of bone**

Ref.	Bone	Method Description	Young's Modulus (GPa)	Poisson Ratio
[54]	femur	tensile	12.4	-
[54]	tibia	tensile	13.7	-
[54]	femur	tensile	8.9	0.30
[54]	cranial	tensile	8.9	0.28
[54]	femur	tensile	11.0	-
[54]	tibia	tensile	11.0	-
[54]	fibula	tensile	10.3	-
[35]	femur	tensile	13.7	-
[35]	humerus	tensile	12.4	-

Table 5.1: **Model properties used for the thick-walled cylinder analysis**

Figures	r_b (cm)	r_l (cm)	E_θ & E_r (Pa)	E_z (Pa)	ν_{rz} & $\nu_{\theta z}$	$\nu_{r\theta}$
5.6	1.5	5.0	15 000	7 500	0.45	0.49
5.6	1.5	5.0	15 000	10 000	0.45	0.49
5.6	1.5	5.0	15 000	12 500	0.45	0.49
5.6	1.5	5.0	15 000	15 000	0.45	0.49
5.7	1.5	5.0	15 000	7 500	0.10	0.49
5.7	1.5	5.0	15 000	7 500	0.20	0.49
5.7	1.5	5.0	15 000	7 500	0.30	0.49
5.7	1.5	5.0	15 000	7 500	0.40	0.49
5.7	1.5	5.0	15 000	7 500	0.45	0.49
5.8 - 5.9	1.5	5.0	15 000	7 500	0.45	0.10
5.8 - 5.9	1.5	5.0	15 000	7 500	0.45	0.20
5.8 - 5.9	1.5	5.0	15 000	7 500	0.45	0.30
5.8 - 5.9	1.5	5.0	15 000	7 500	0.45	0.40
5.8 - 5.9	1.5	5.0	15 000	7 500	0.45	0.49

Table 5.2: **Model properties used for replicating Hodgson's model**

Figures	r_b (cm)	r_l (cm)	E_θ & E_r (Pa)	E_z (Pa)	ν_{rz} & $\nu_{\theta z}$	$\nu_{r\theta}$	PD
5.12	1.0	3.5	15 000	15 000	0.45	0.45	sin
5.13	1.0	3.5	15 000	15 000	0.45	0.45	rec
5.14	1.0	2.5	15 000	15 000	0.45	0.45	sin
5.15	1.0	5.0	15 000	15 000	0.45	0.45	sin

Table 5.3: **Model properties of the artery compression model**

Figures	r_0 (mm)	h (mm)	l (cm)	E_r (kPa)	E_θ (kPa)	E_z (kPa)	ν_{rz} & $\nu_{\theta z}$	$\nu_{r\theta}$
5.69	2.65	0.50	15.0	200	550	200	0.35	0.45
5.69	2.65	0.50	17.5	200	550	200	0.35	0.45
5.69	2.65	0.50	22.5	200	550	200	0.35	0.45
5.70	2.65	0.50	15.0	100	550	200	0.35	0.45
5.70	2.65	0.50	15.0	200	550	200	0.35	0.45
5.70	2.65	0.50	15.0	300	550	200	0.35	0.45
5.71	2.65	0.50	15.0	200	275	200	0.35	0.45
5.71	2.65	0.50	15.0	200	550	200	0.35	0.45
5.71	2.65	0.50	15.0	200	825	200	0.35	0.45
5.72	2.65	0.50	15.0	200	550	100	0.35	0.45
5.72	2.65	0.50	15.0	200	550	200	0.35	0.45
5.72	2.65	0.50	15.0	200	550	300	0.35	0.45

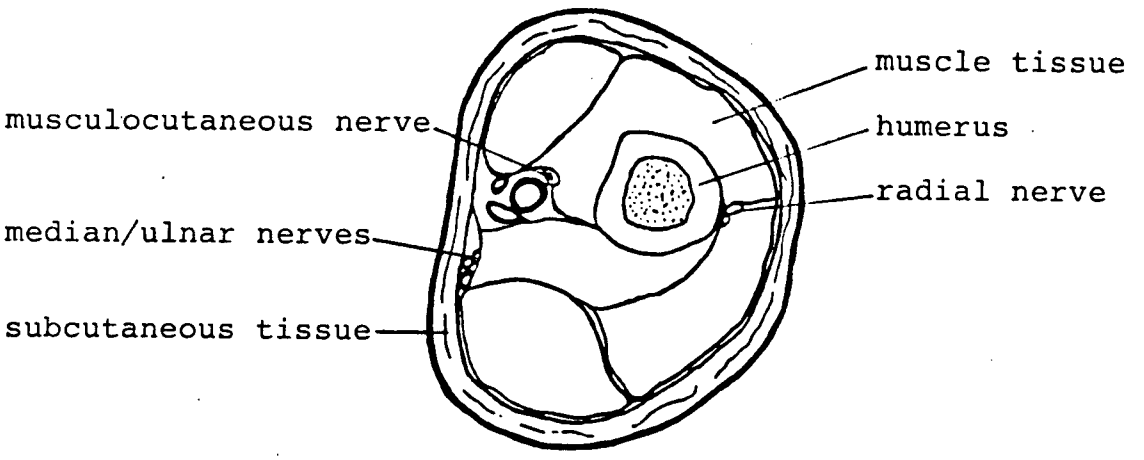

a. Cross-section of a human upper arm

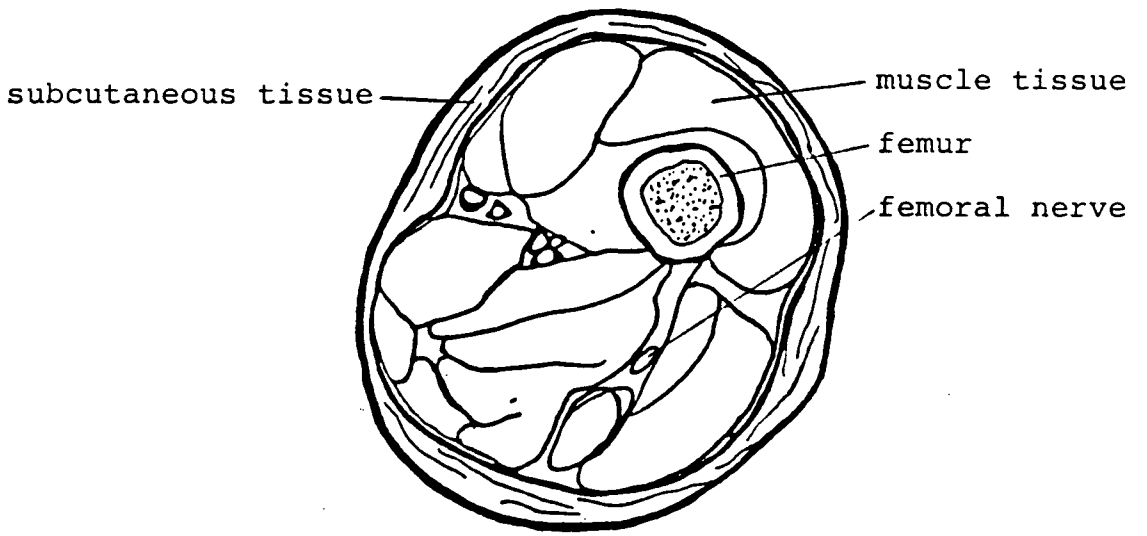

b. Cross-section of a human thigh

Figure 2.1: Limb cross-sections [40]

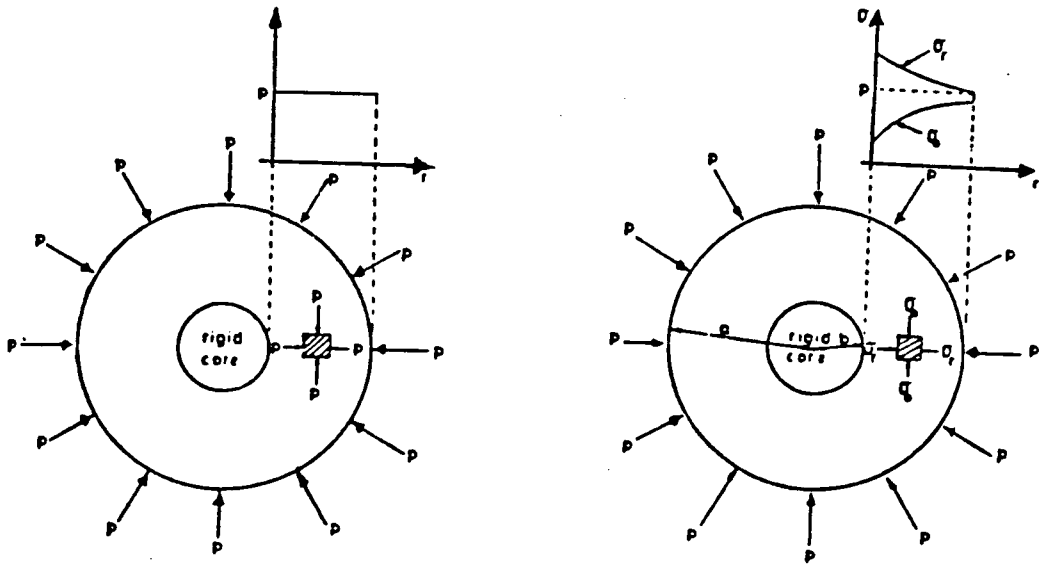

a. Fluid tissue model

b. Elastic solid tissue model

Figure 2.2: **Griffiths' and Heywood's models [19]**

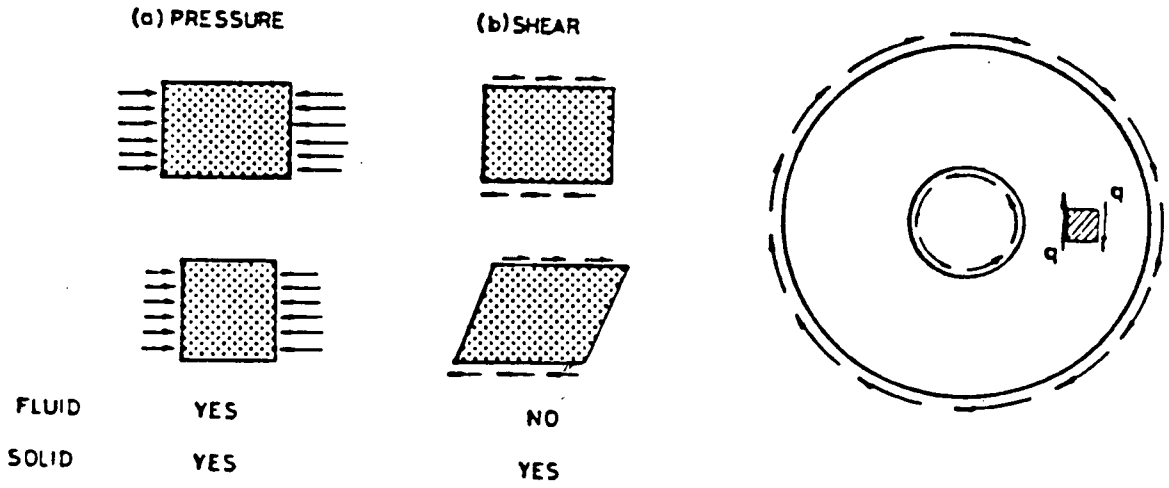

Figure 2.3: **Griffiths' and Heywood's models subjected to a twisting force [19]**

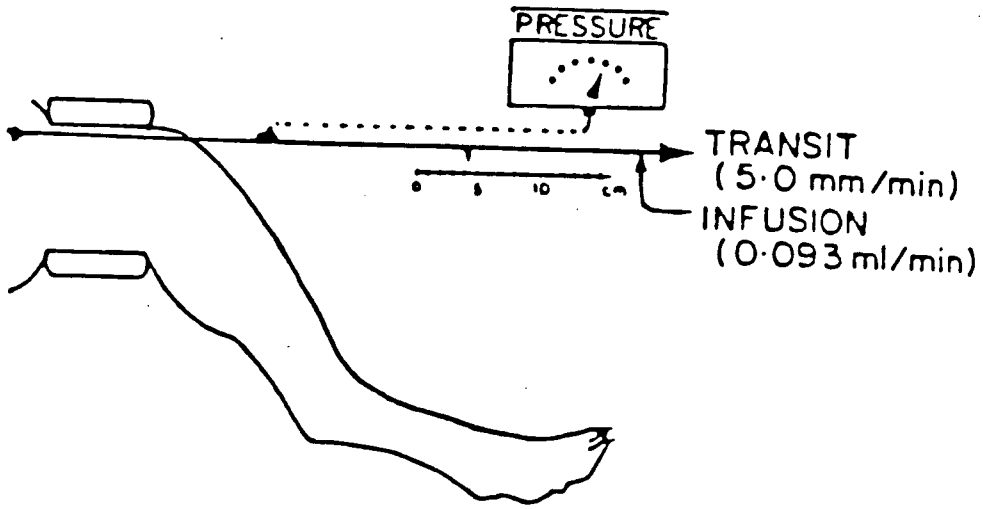

a. Experimental setup

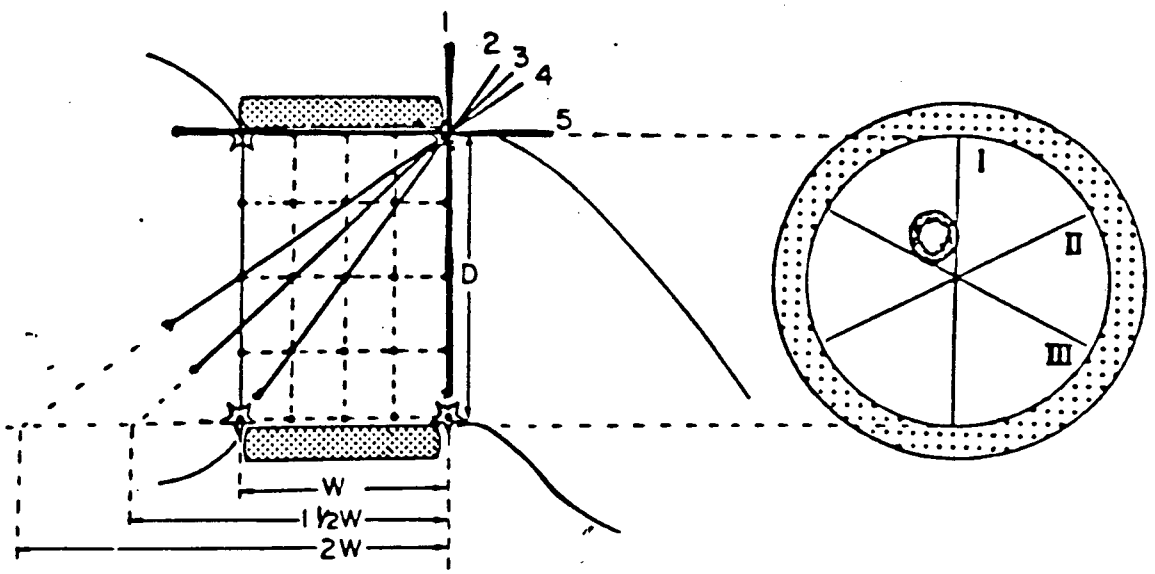

b. Paths taken by the slit catheter including entry and recording points

c. Longitudinal planes of the limb

Figure 2.4: **McLaren's and Rorabeck's experiments [39]**

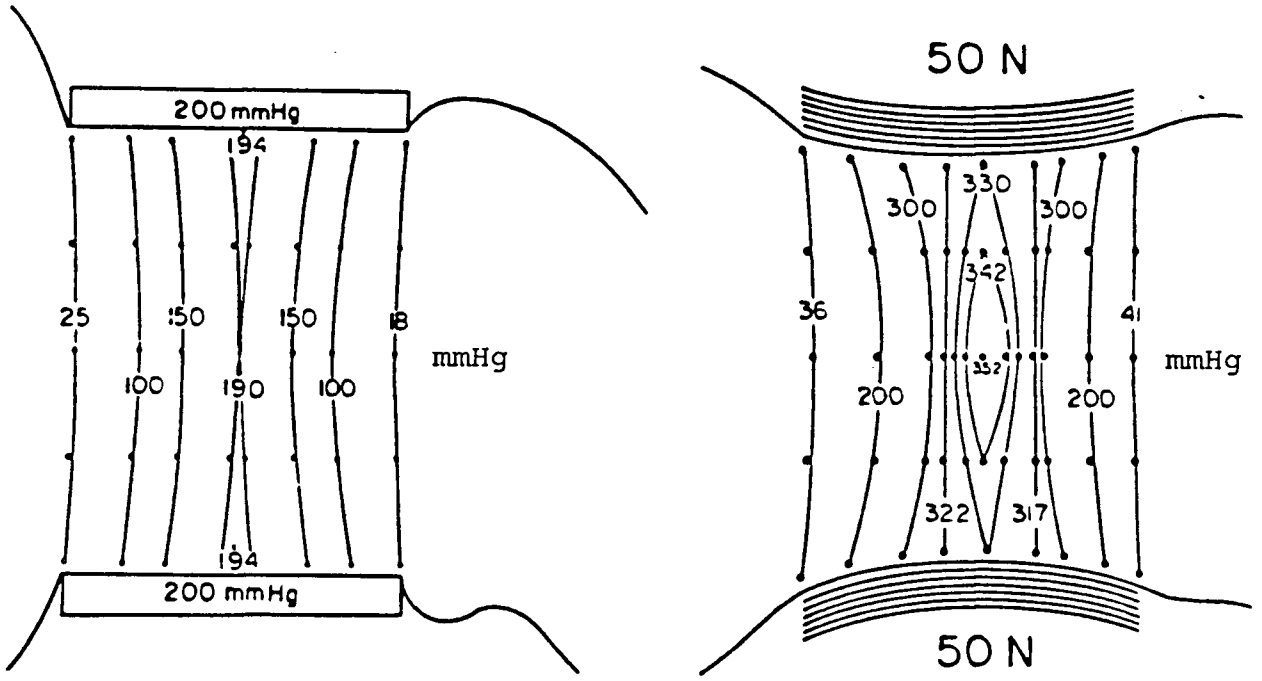

a. Beneath a pneumatic tourniquet b. Beneath an Esmarch bandage

Figure 2.5: **Pressure profiles recorded by McLaren and Rorabeck [39]**

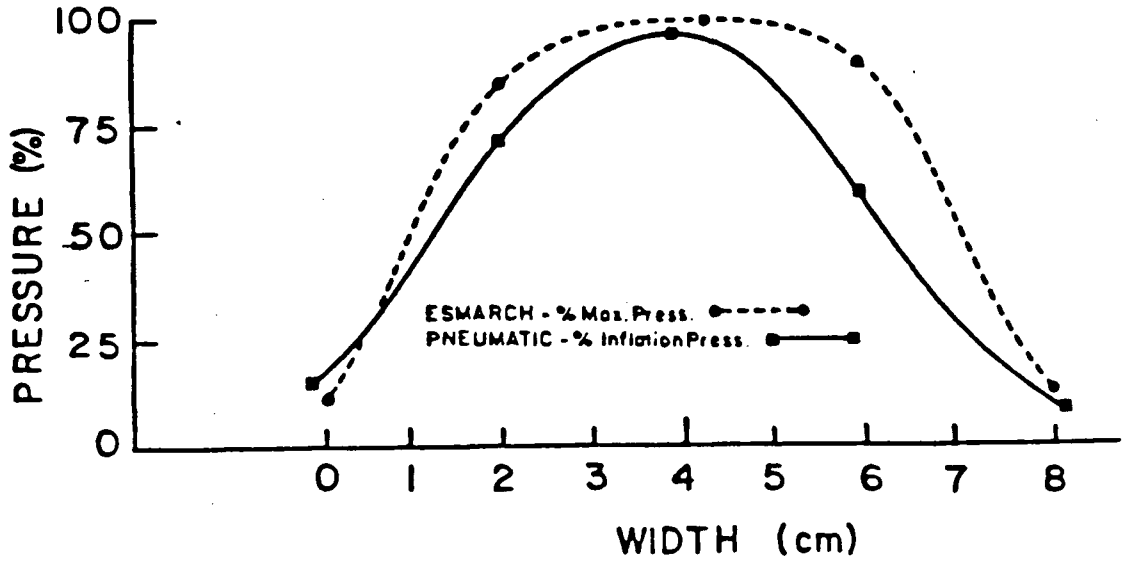

Figure 2.6: **Surface pressure profiles for the pneumatic tourniquet and the Esmarch bandage [39]**

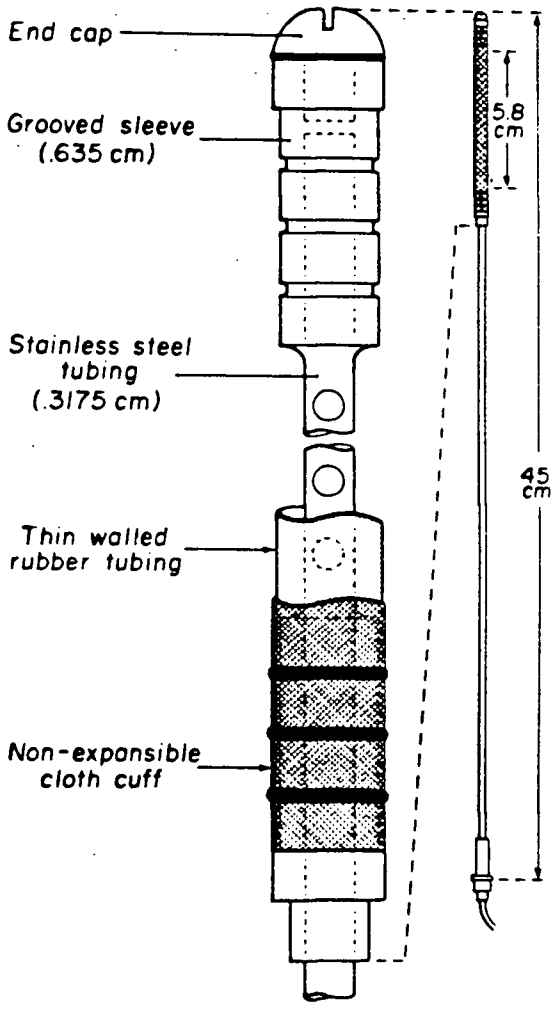

Figure 2.7: **Pressure probe used by Shaw and Murray [17]**

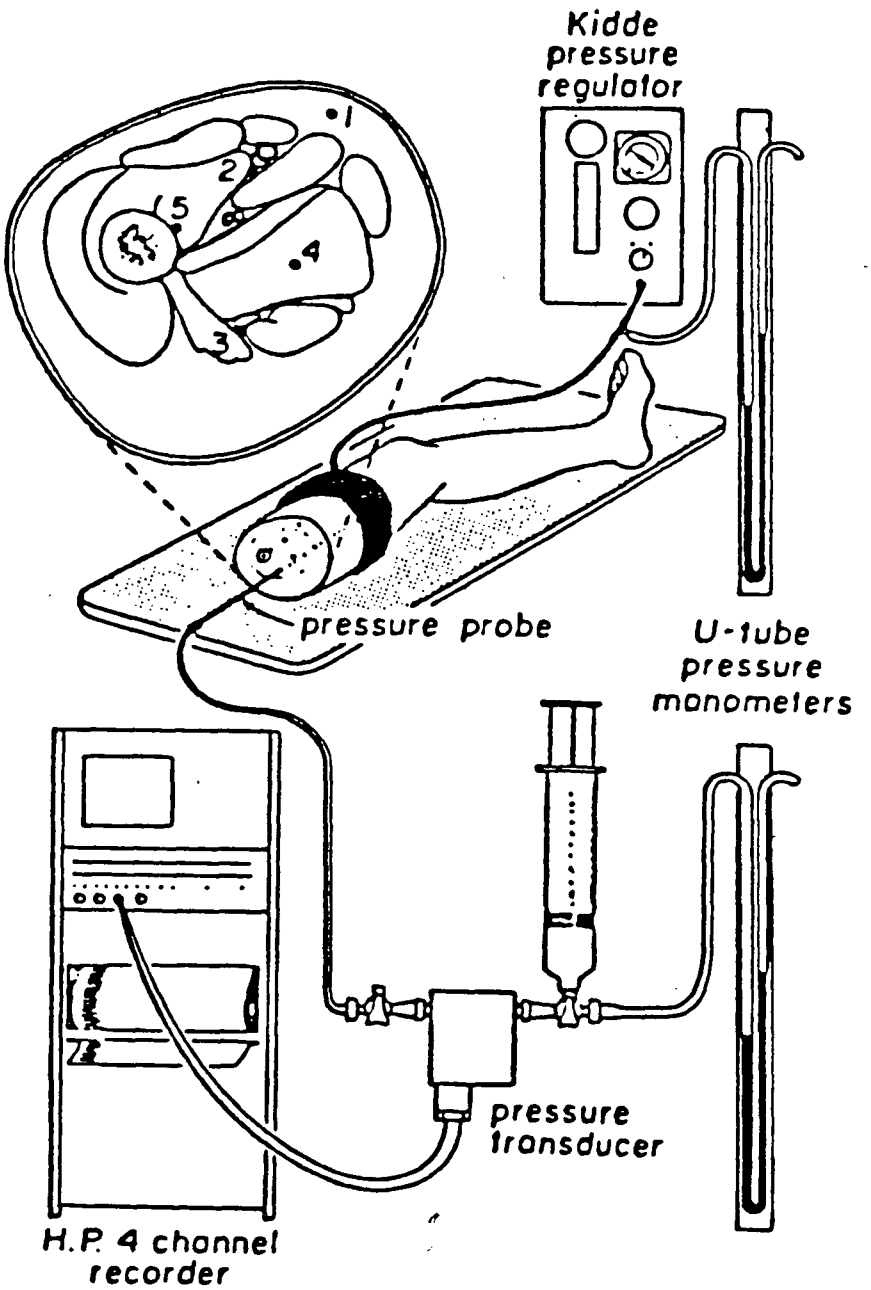

Figure 2.8: **Shaw's and Murray's experimental setup [17]**

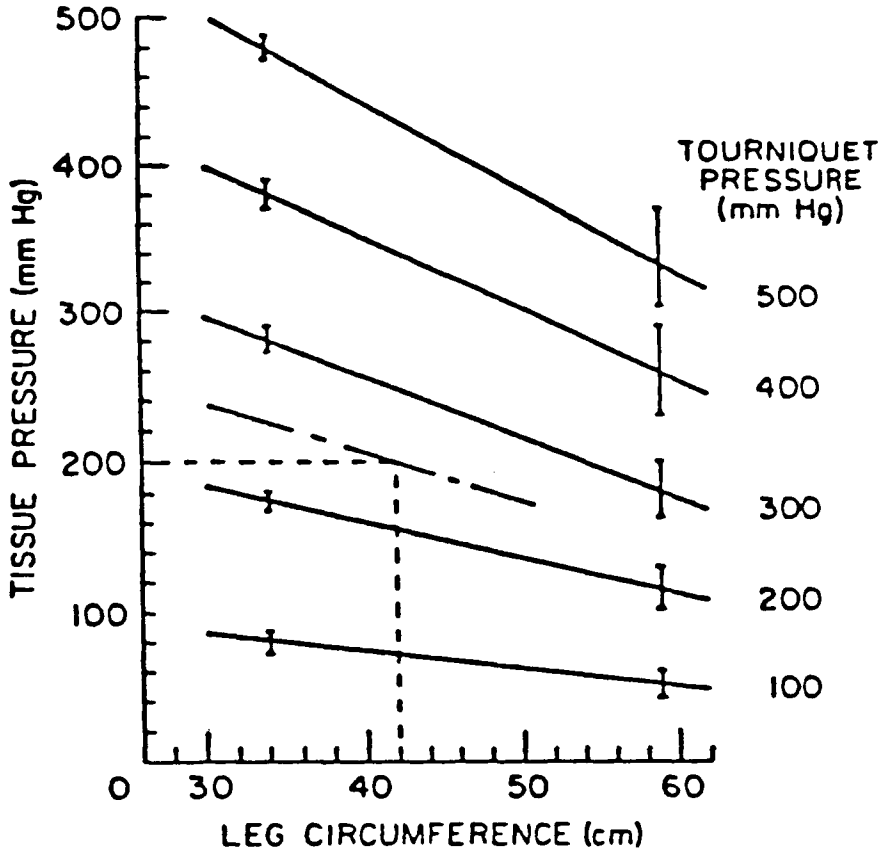

Figure 2.9: **Nomogram relating leg circumference, tissue pressure and tourniquet pressure [17]**

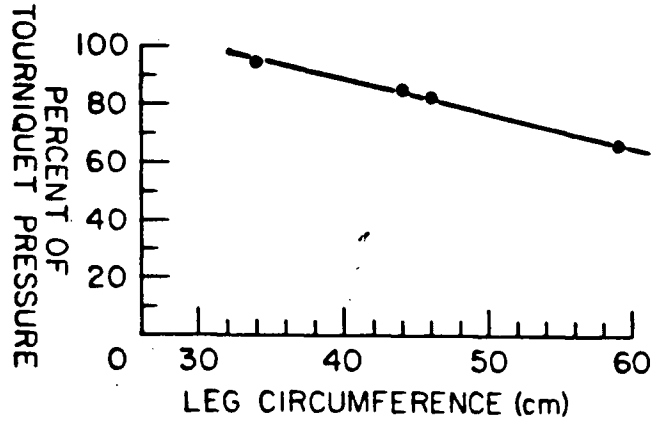

Figure 2.10: **Relationship between leg circumference and average tissue pressure [17]**

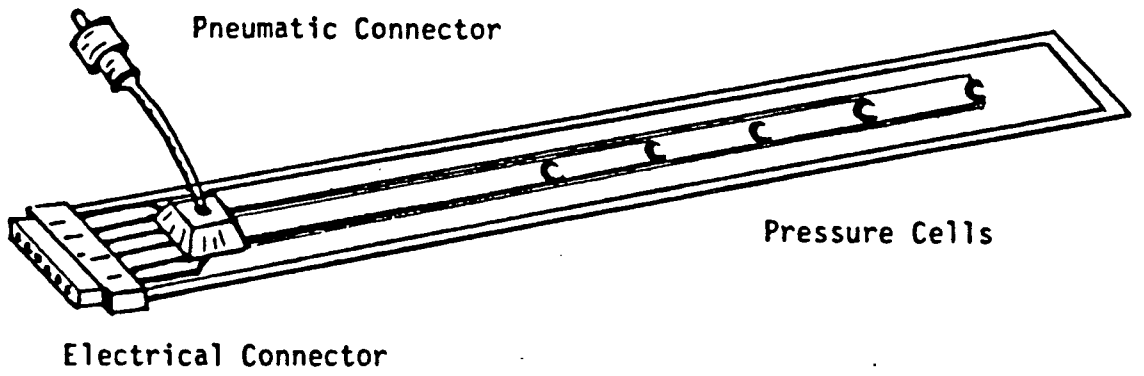

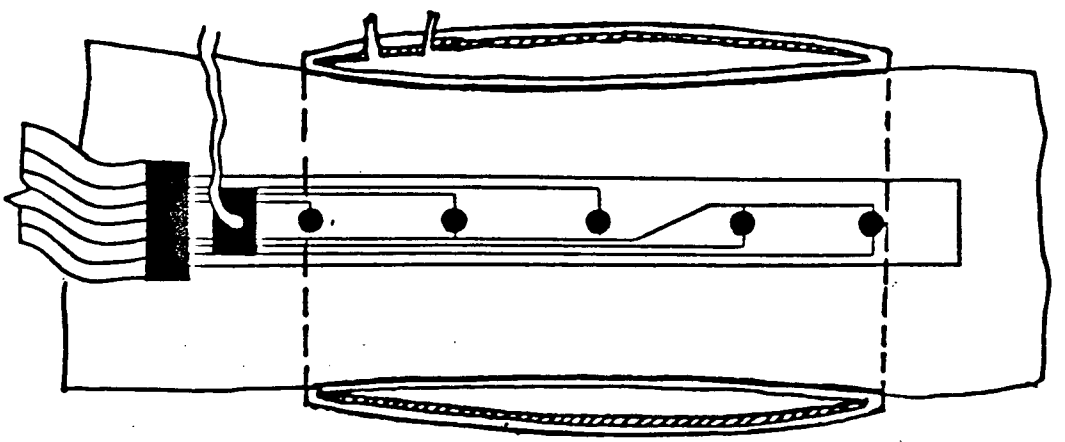

Figure 2.11: **Pressure probe used by Breault [40]**

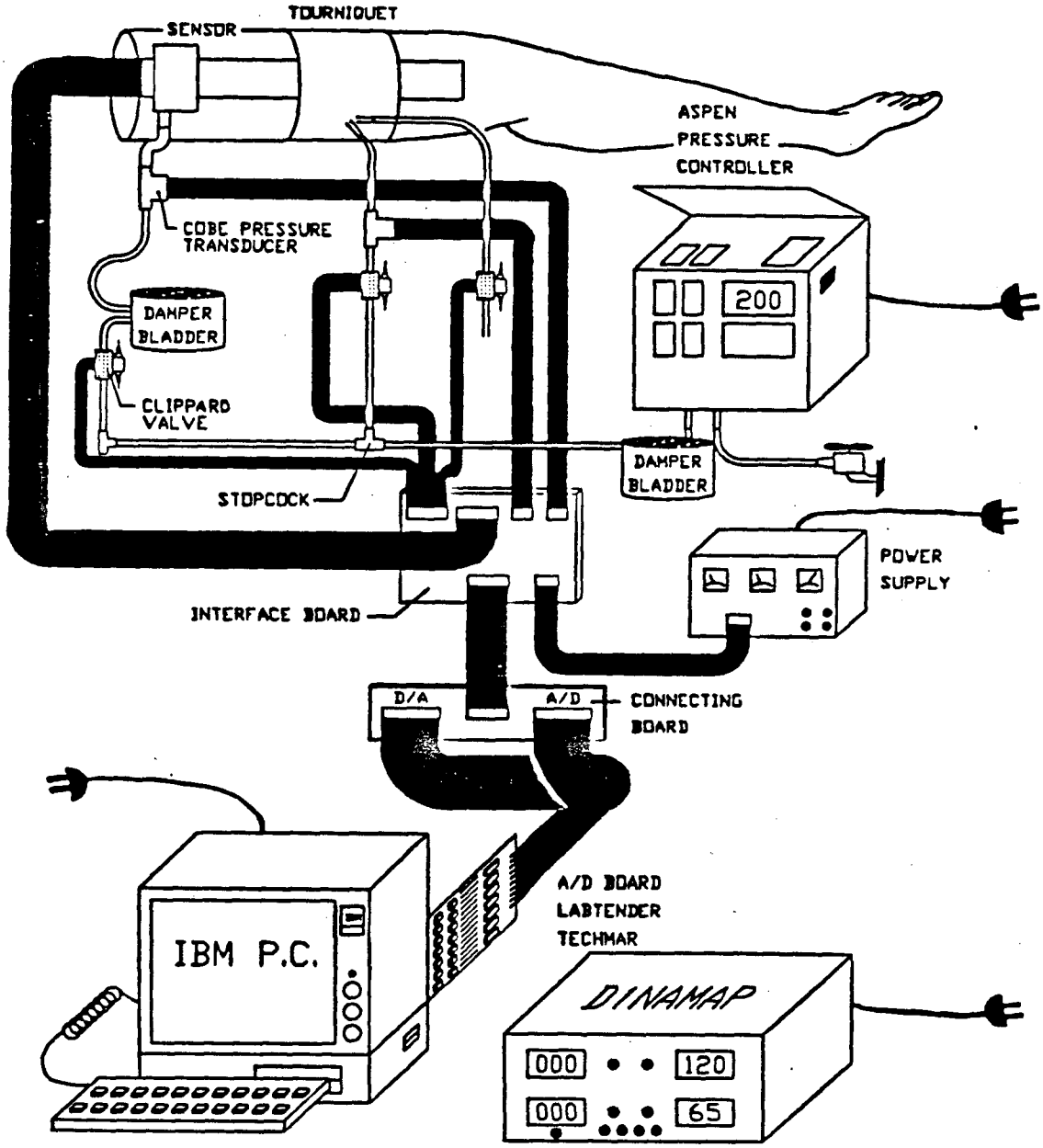

Figure 2.12: **Breault's experimental setup [40]**

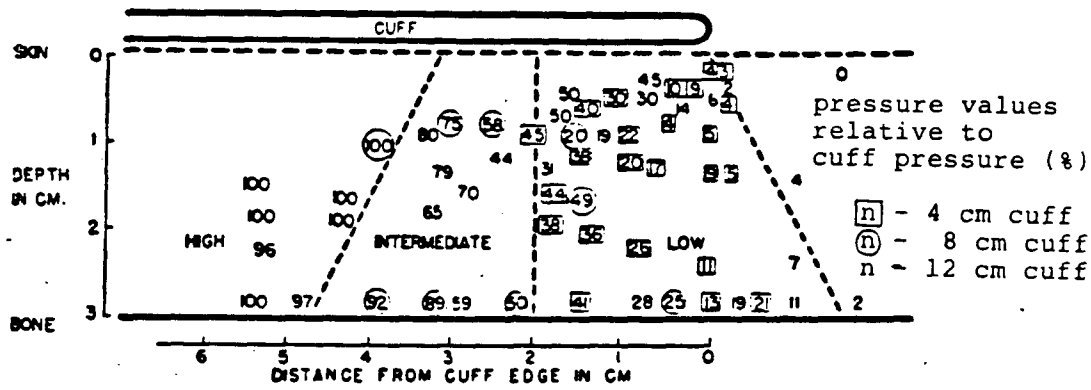

Figure 2.13: **Thomson's and Doupe's experimental results [41]**

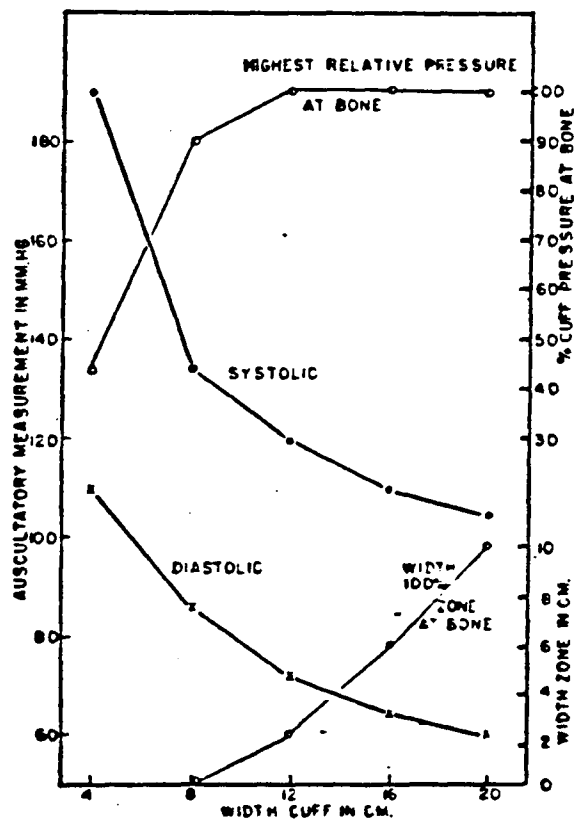

Figure 2.14: **Effect of cuff width on recorded arterial pressure [41]**

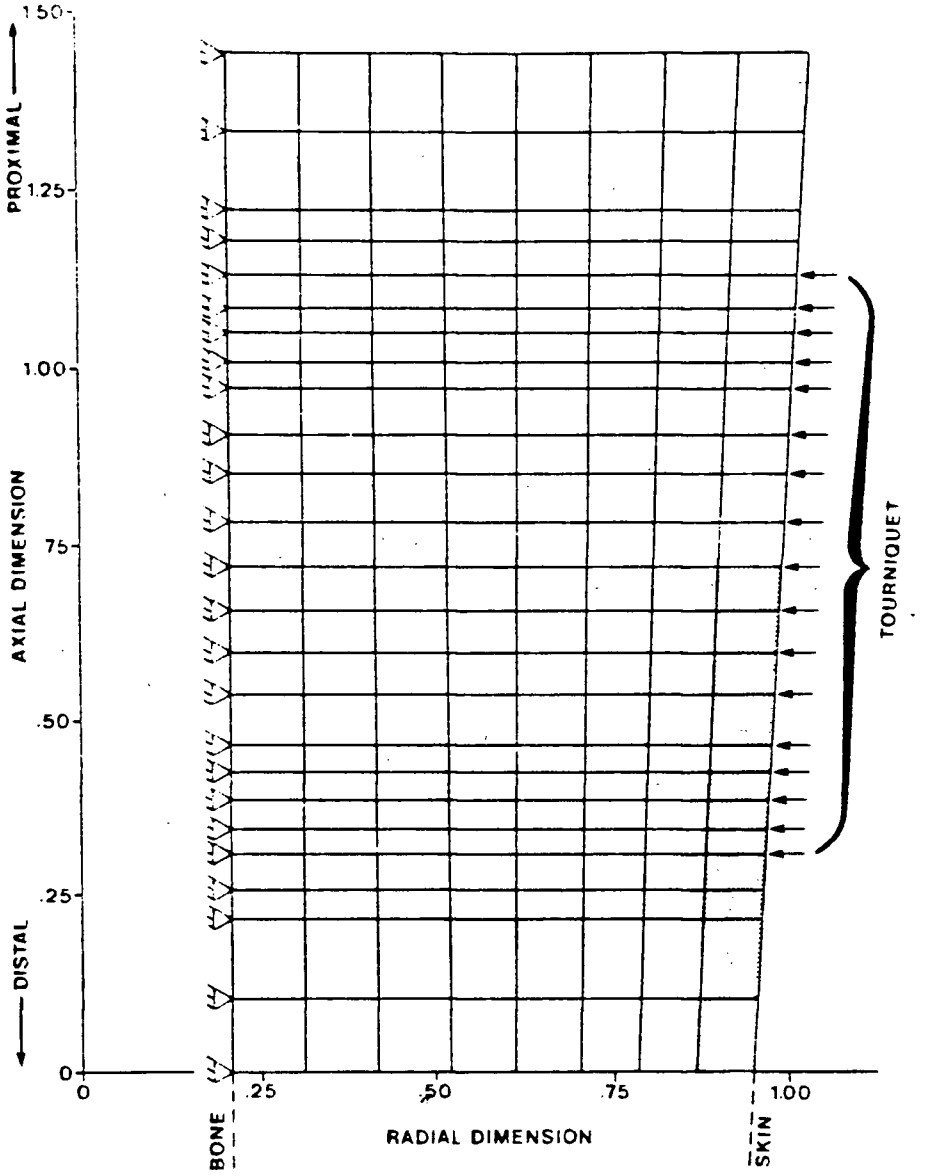

Figure 2.15: **Auerbach's finite element mesh of the analyzed limb section [42]**

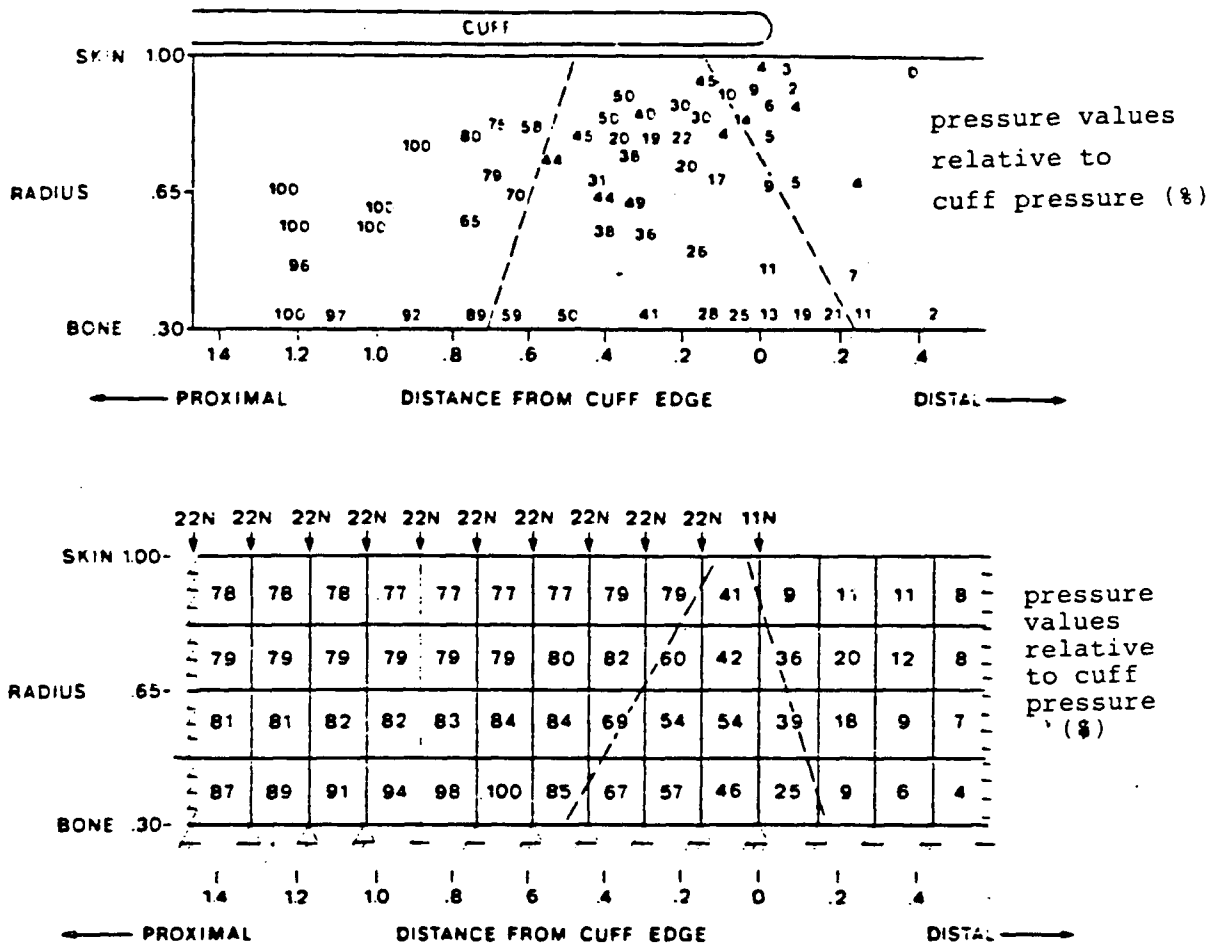

Figure 2.16: **Hydrostatic pressure distribution numerically evaluated by Auerbach compared to Thomson's and Doupe's experimental results [42]**

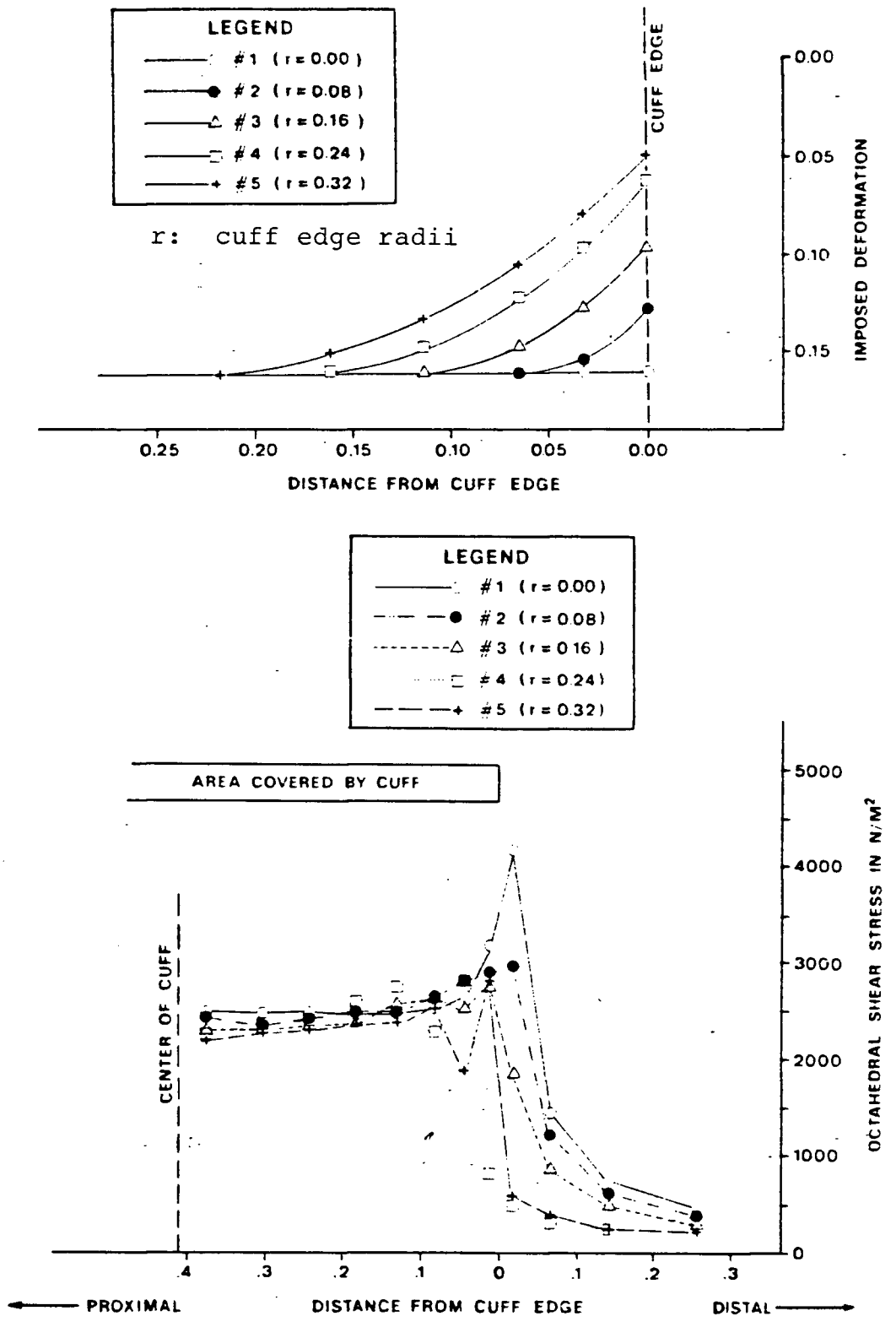

Figure 2.17: **Octahedral shear stress profiles as computed by Auerbach [42]**

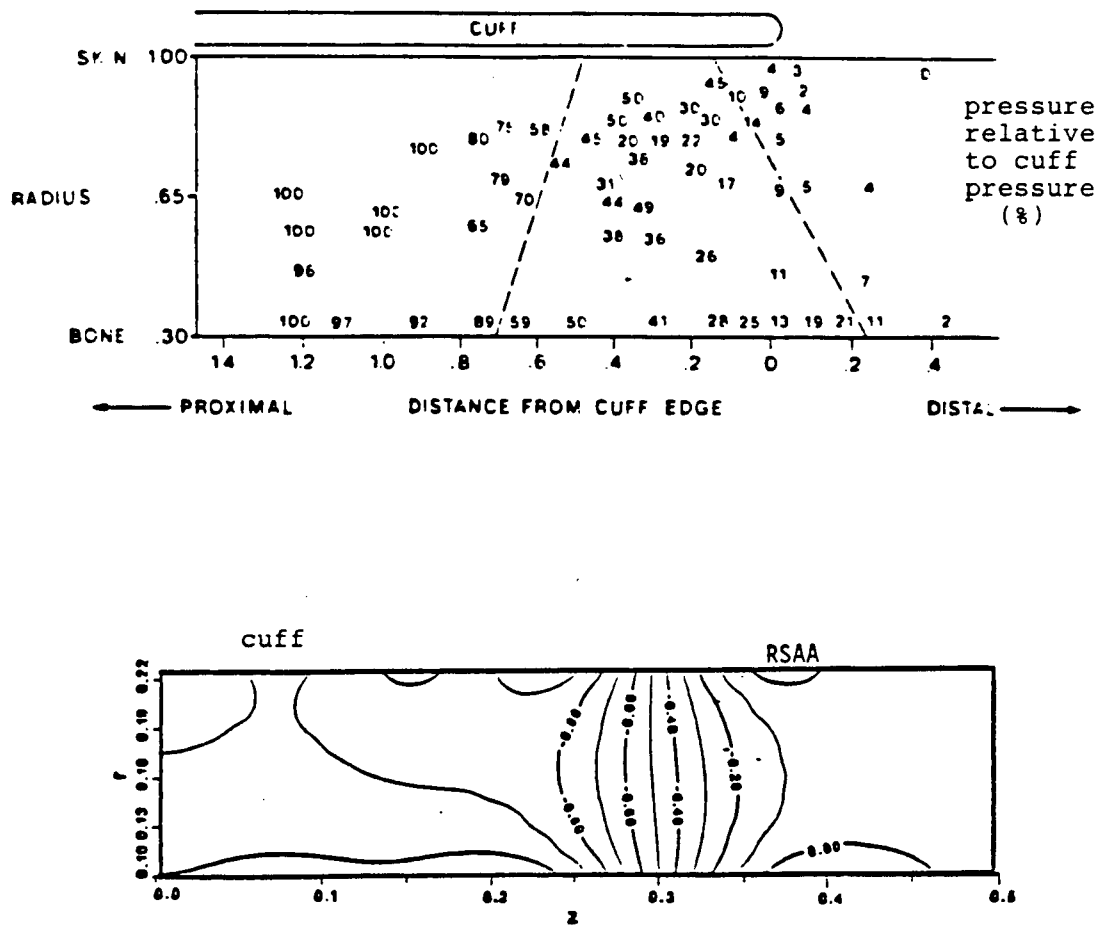

Figure 2.18: **Hydrostatic pressure distribution analytically calculated by Hodgson compared to Thomson's and Doupe's experimental results [44]**

a. Normal node of Ranvier showing a nodal gap 1.2 μm wide

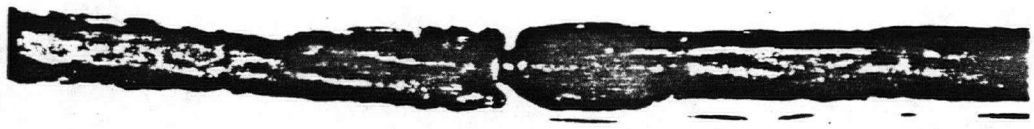

b. Abnormal node of Ranvier, four days after compression, showing minimal invagination of the paranode on the left by the one on the right, with obliteration of the nodal gap

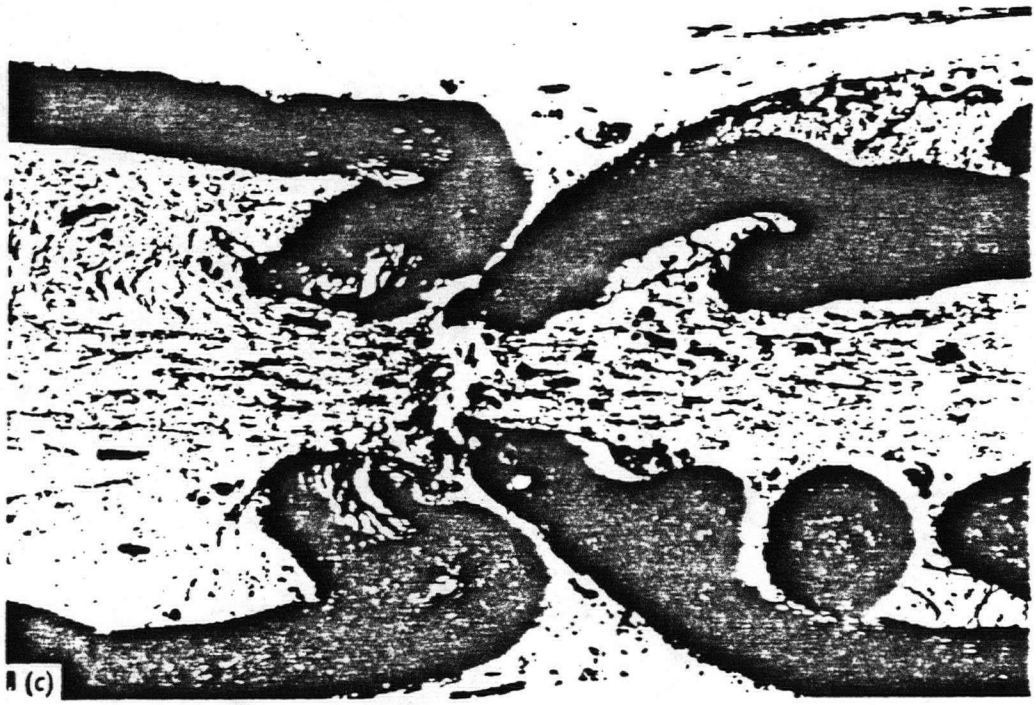

c. Enlargement of b. showing a more detailed account of the invagination phenomenon

Figure 2.19: **Invagination phenomenon observed by Ochoa et al. [3]**

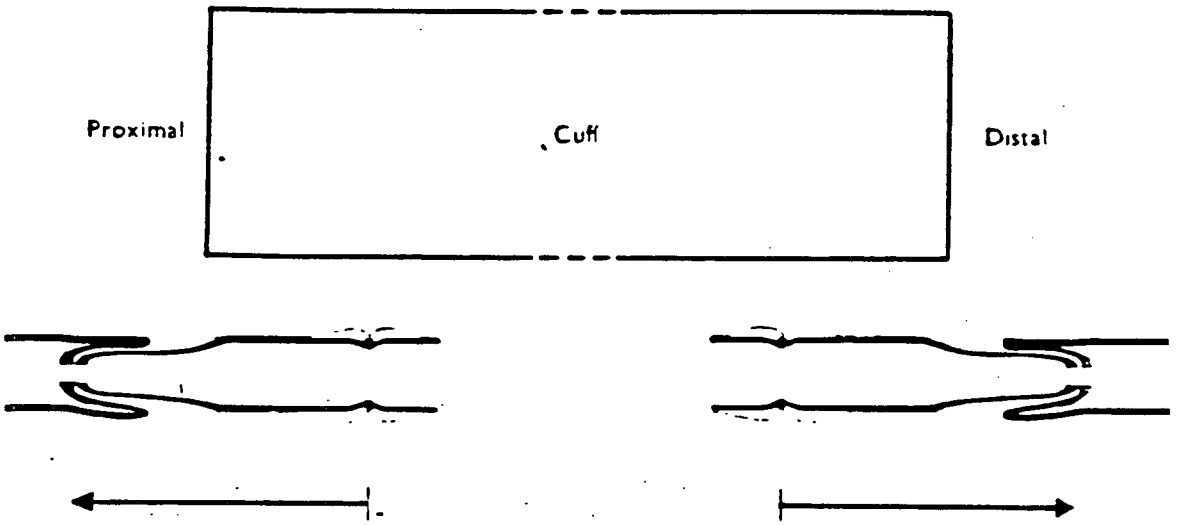

Figure 2.20: **Direction of displacement of the nodes of Ranvier with respect to cuff position [3]**

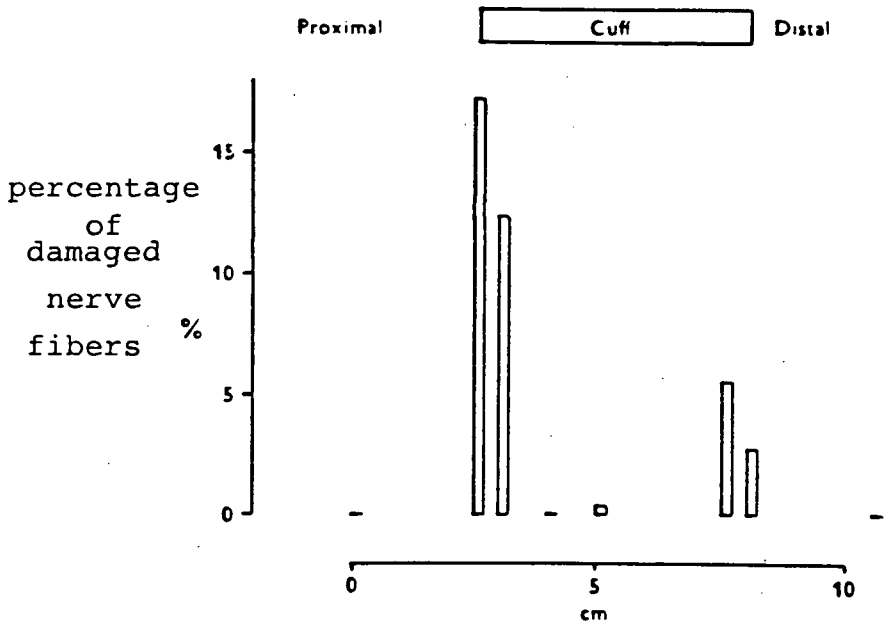

Figure 2.21: **Histogram illustrating the distribution of nerve lesions relative to cuff site [3]**

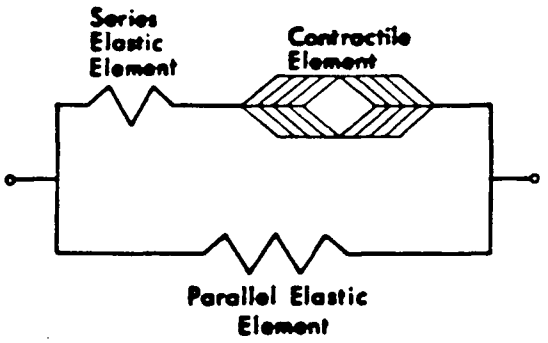

Figure 3.1: **Hill's three element muscle model** [48]

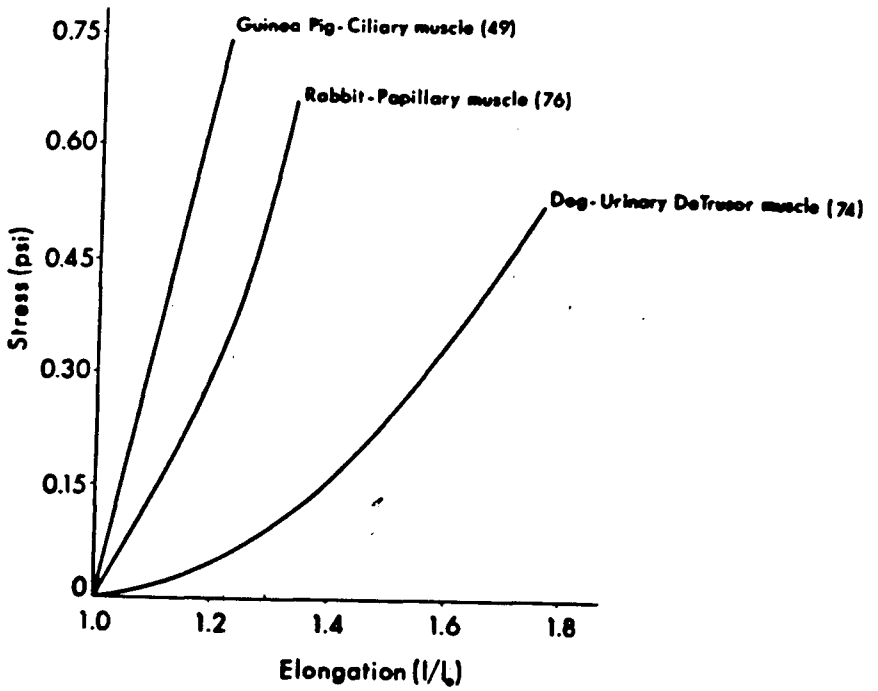

Figure 3.2: **Stress-strain curves for three muscle samples** [47]

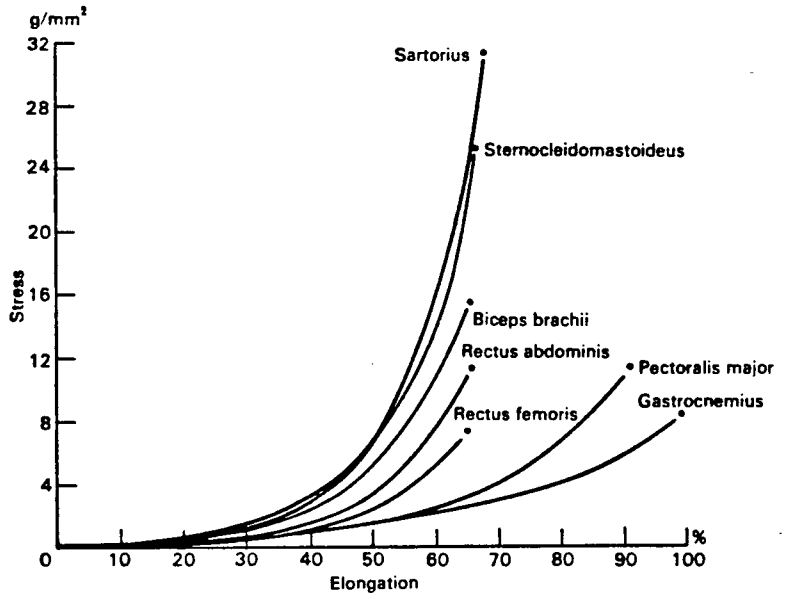

Figure 3.3: **Stress-strain curves for different human squeletal muscles [35]**

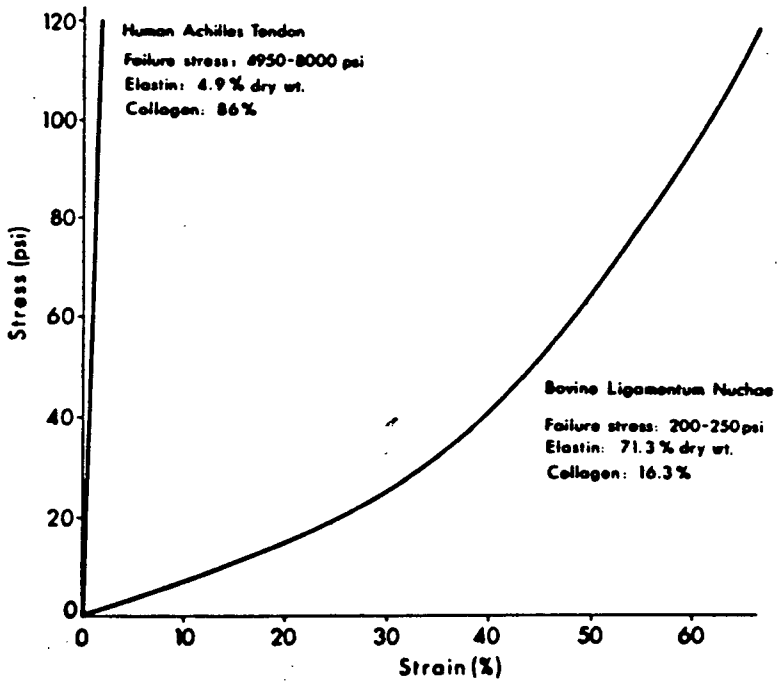

Figure 3.4: **Stress-strain curves for elastin and collagen [48]**

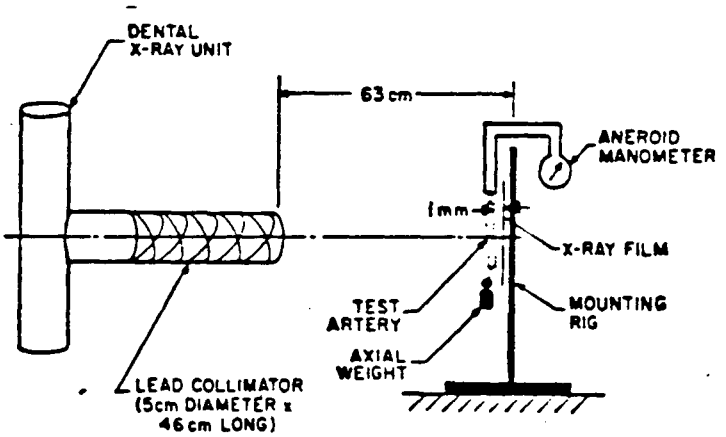

Figure 3.5: **Setup to load arteries in axial tension and internal compression [51]**

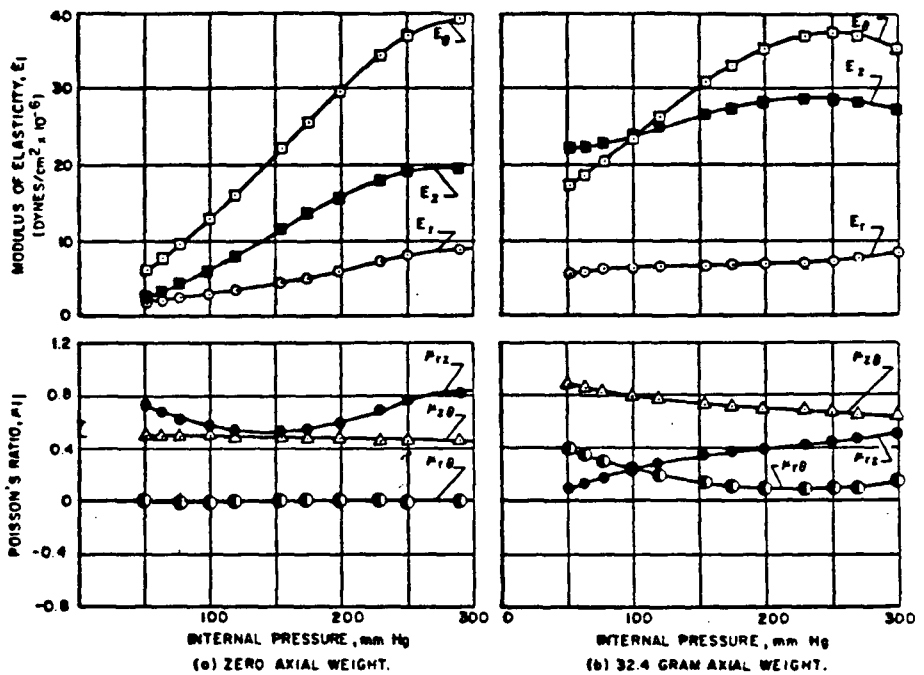

Figure 3.6: **Material properties of a human brachial artery [51]**

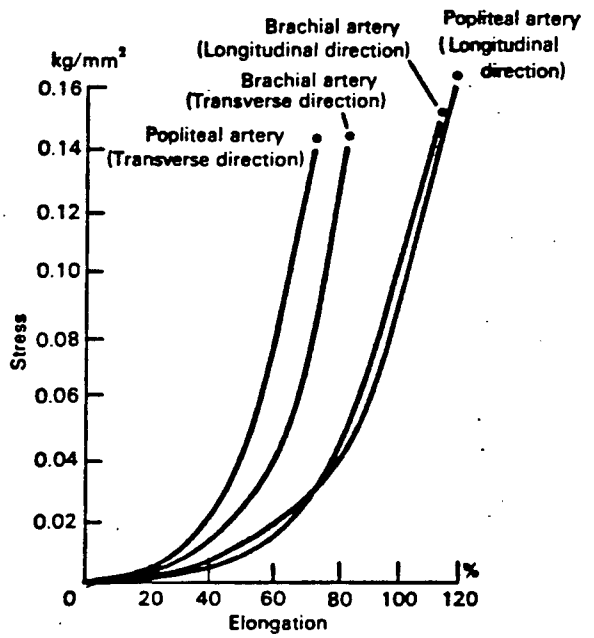

Figure 3.7: **Stress-strain curves for arteries [35]**

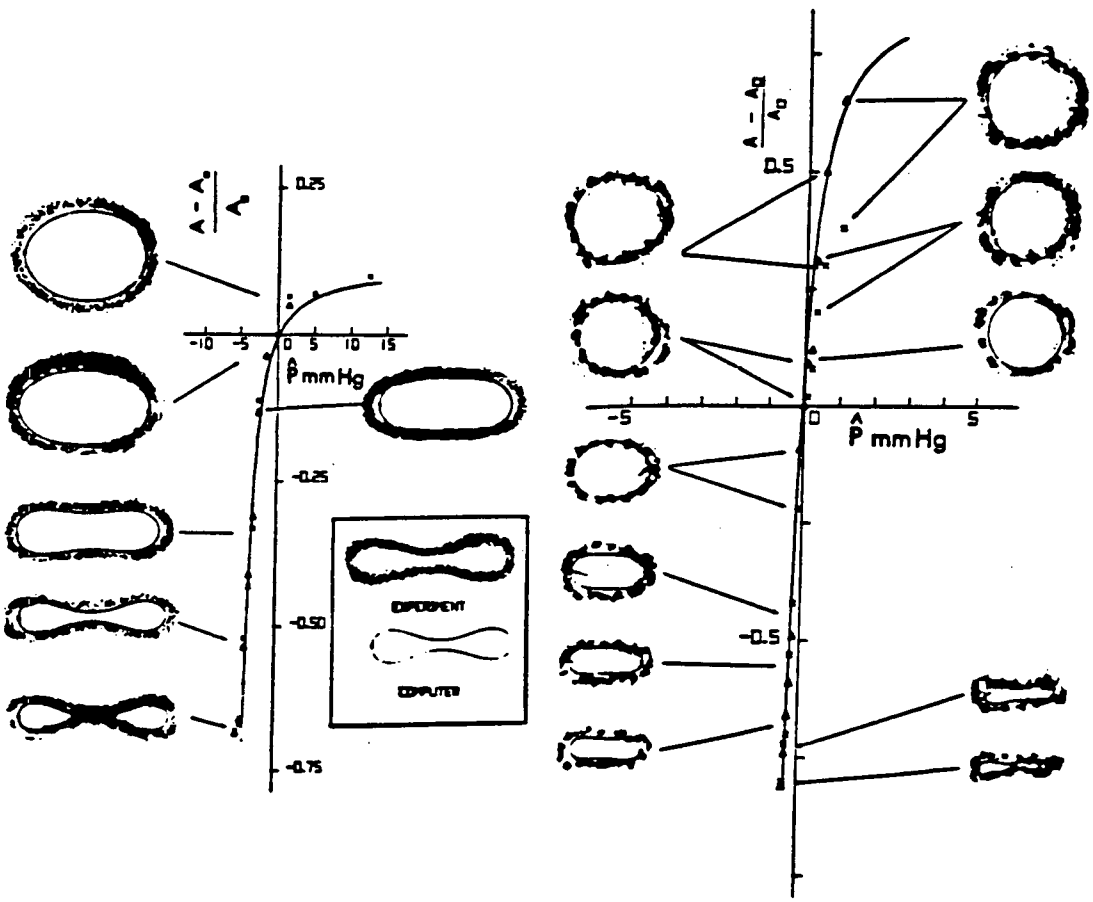

a. For a latex tube b. For a vein

Figure 3.8: **Collapsing process [53]**

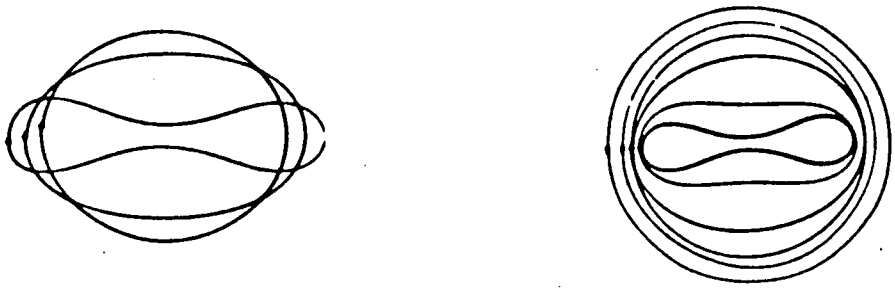

a. Of a collapsing latex tube b. Of a collapsing vein

Figure 3.9: **Cross-sections [53]**

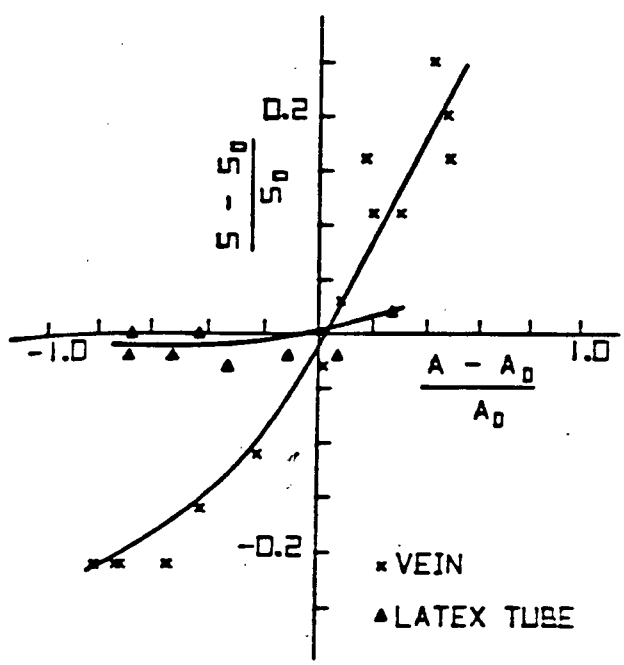

Figure 3.10: **Area-perimeter relationship for latex tubes and arteries [53]**

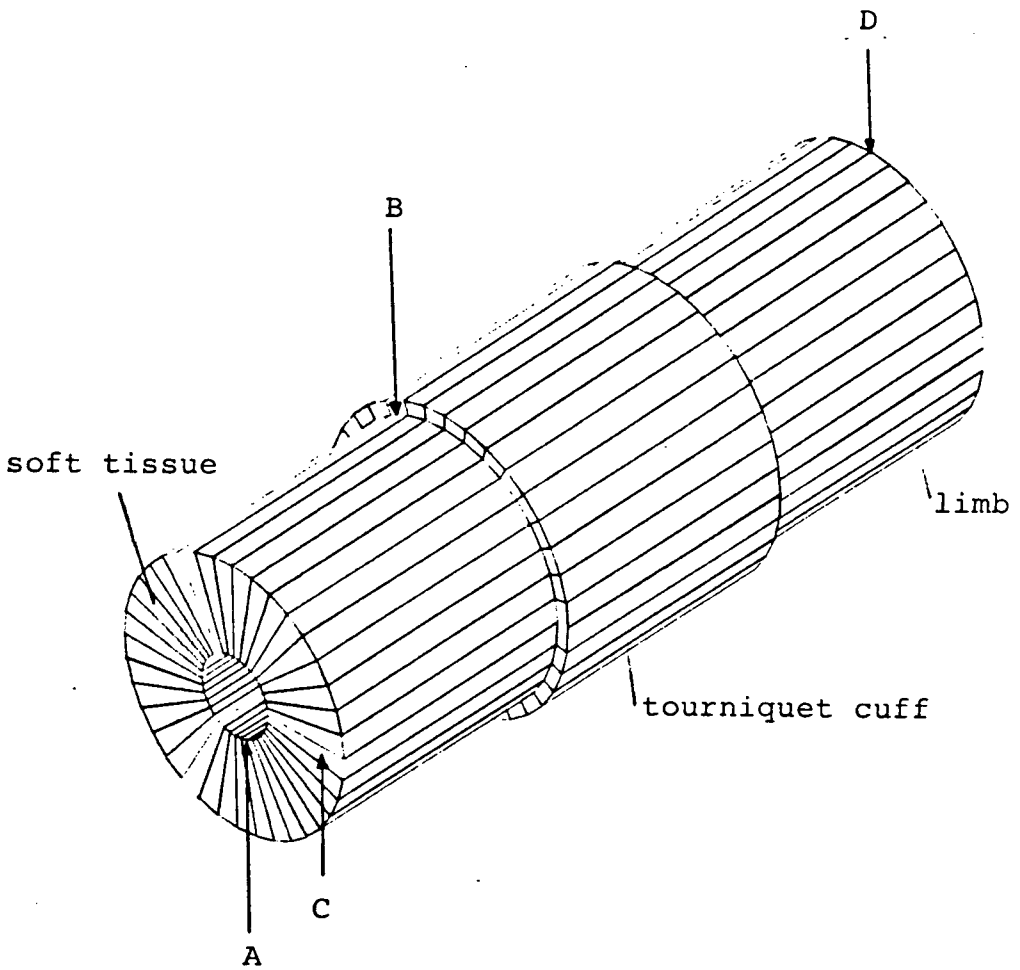

Figure 3.11: **Limb model showing the three main boundaries**

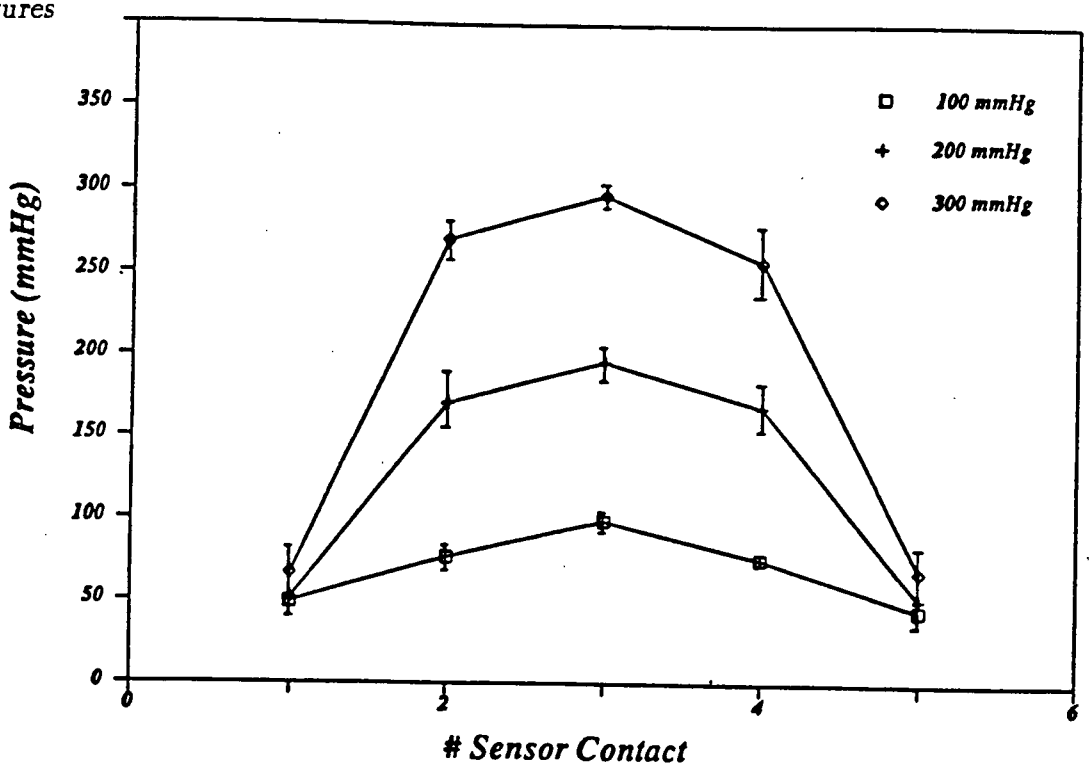

Figure 3.12: **Experimental parabolic surface pressure profile measured by Breault [40]**

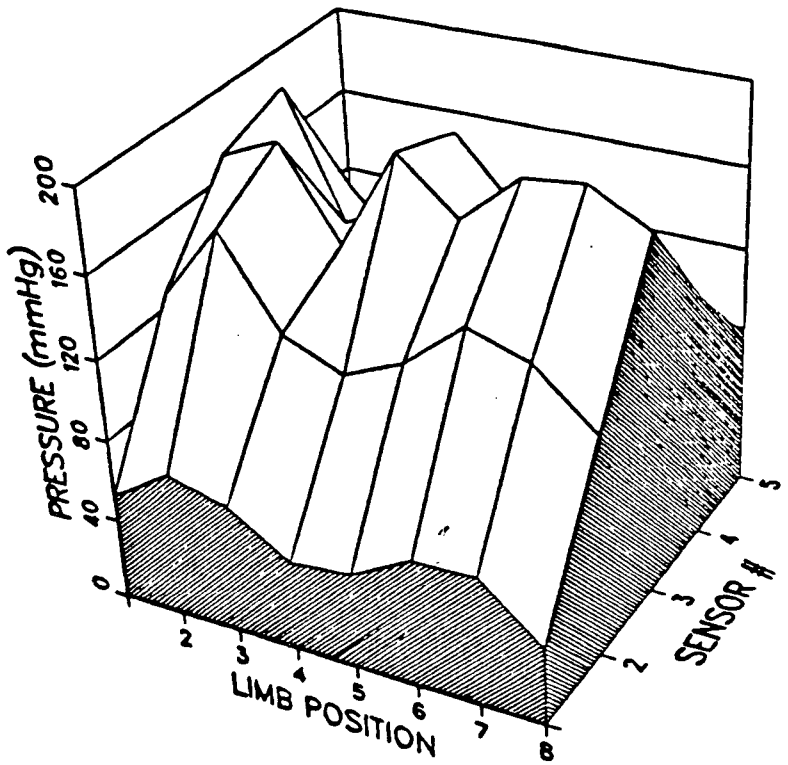

Figure 3.13: **Three-dimensional view of the surface pressure profile under a pneumatic tourniquet [40]**

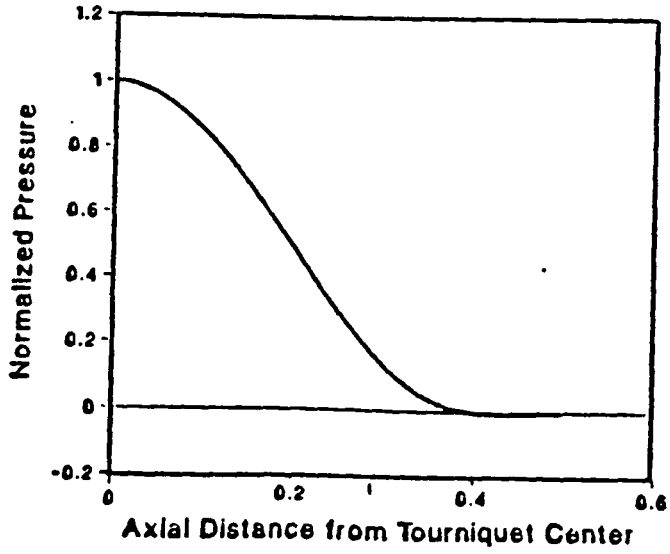

a. Sinusoidal

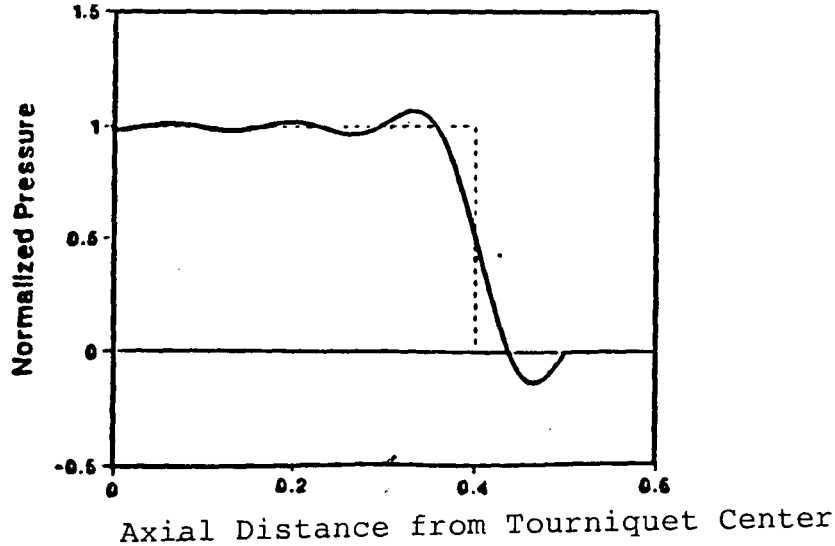

b. Rectangular

Figure 3.14: **Hodgson's surface pressure profiles [44]**

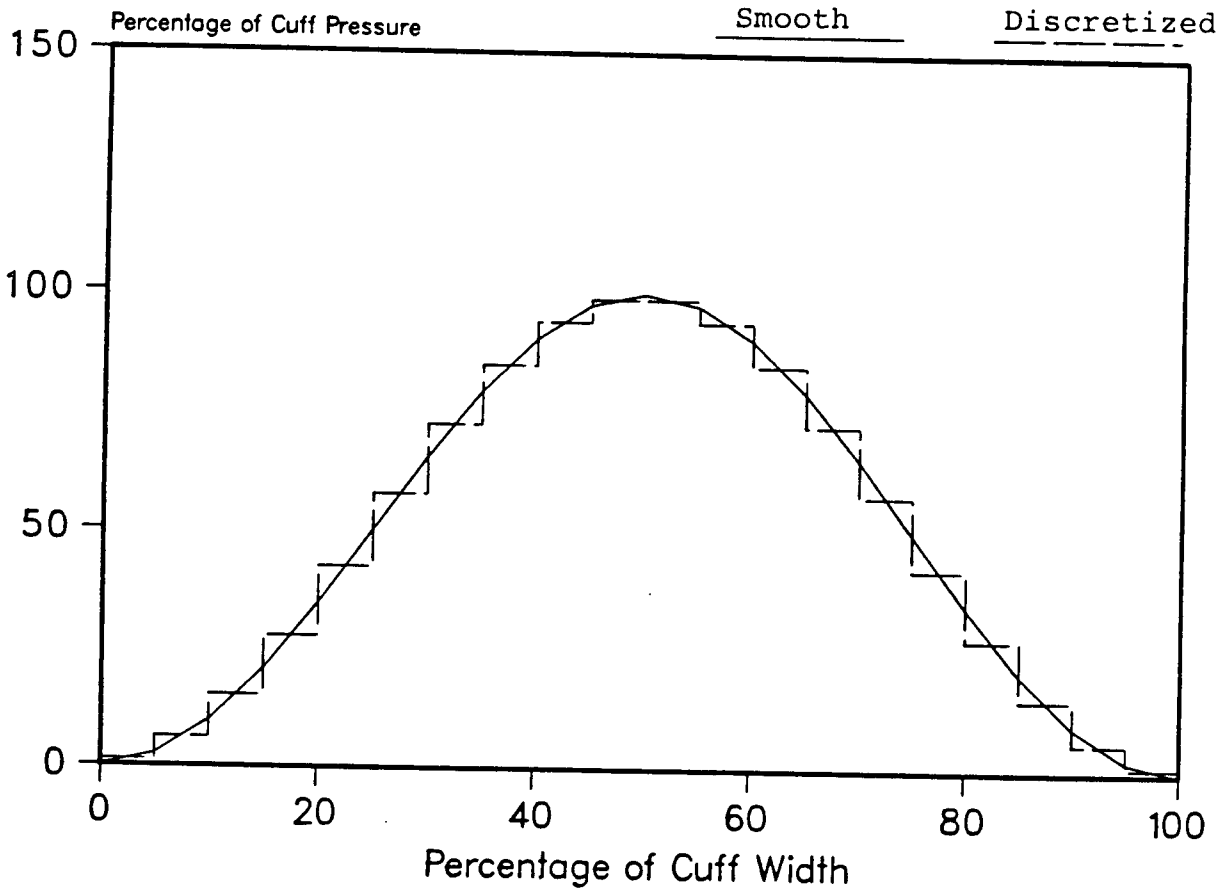

Figure 3.15: **Comparison between smooth and discretized surface pressure profiles**

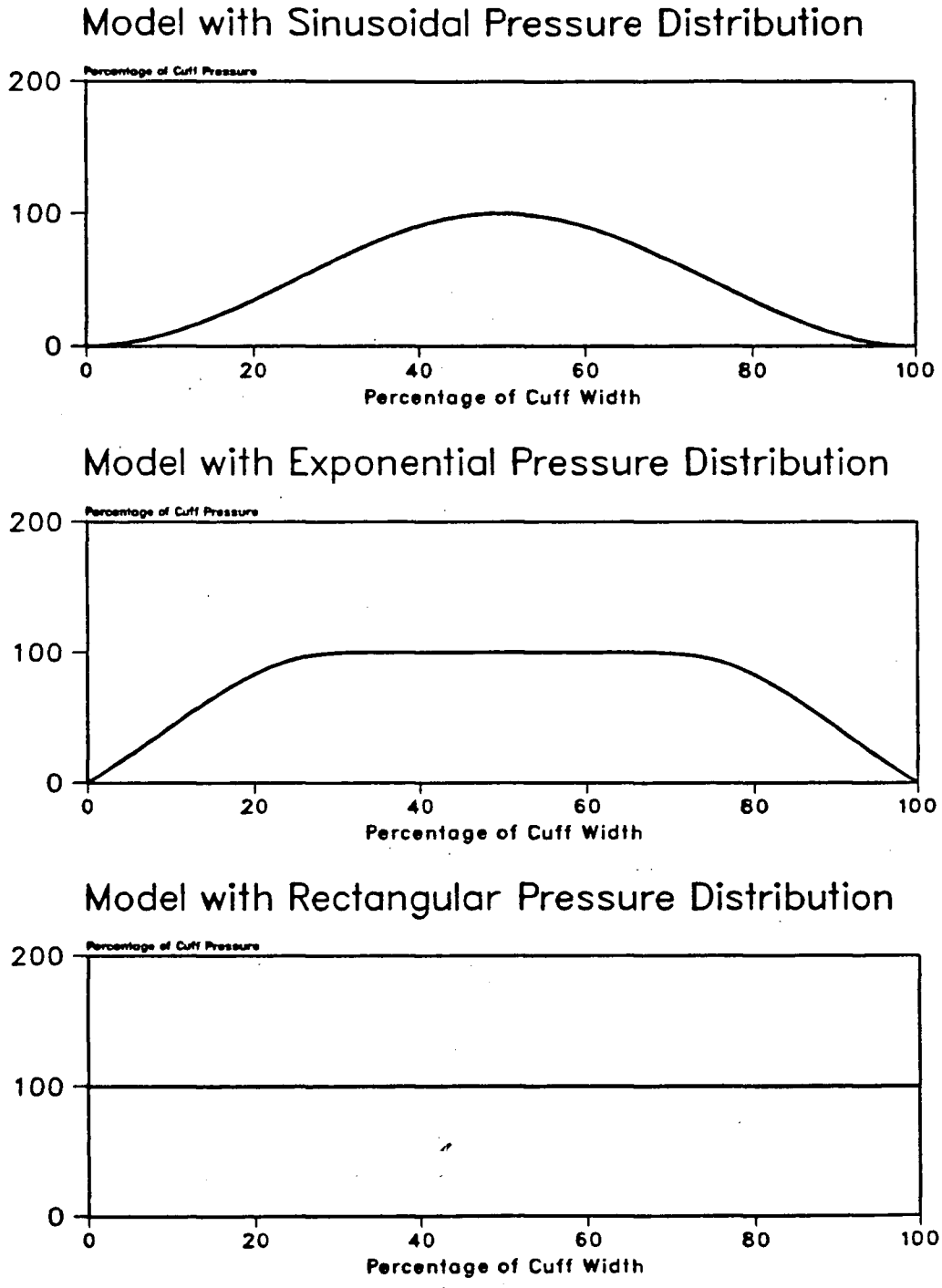

Figure 3.16: **Three main pressure profiles applied to the limb model**

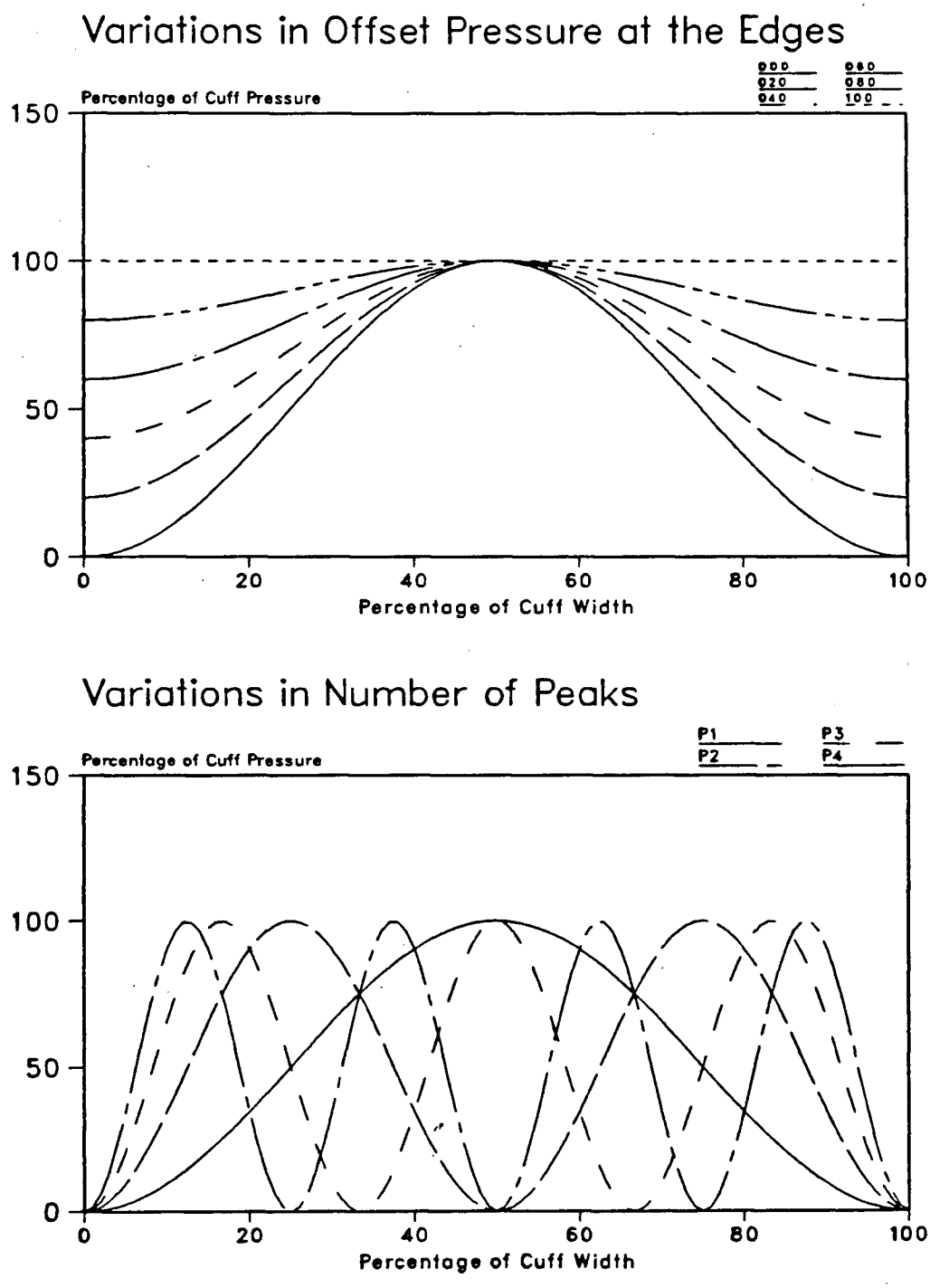

Figure 3.17: **Varying offset and multiple peak characteristics of the sinusoidal pressure profile**

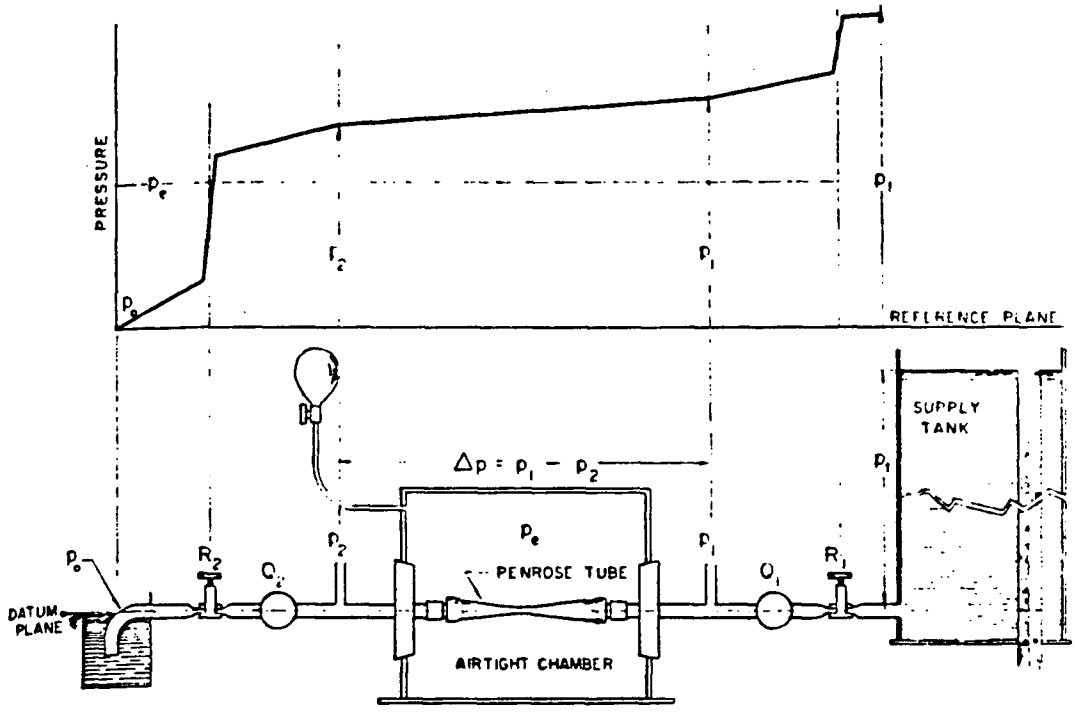

Figure 3.18: **Setup to simulate blood flow through the arteries** [67]

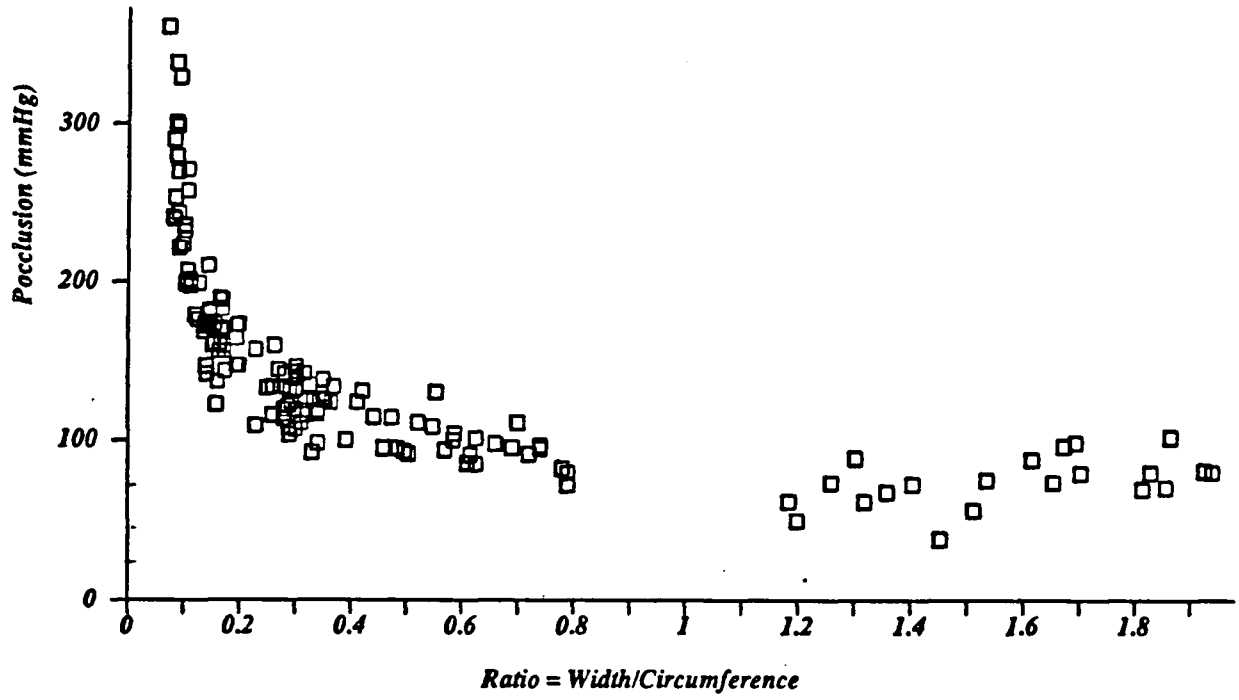

Figure 3.19: **Experimental results of occlusion pressure vs the ratio of cuff width to arm circumference [40]**

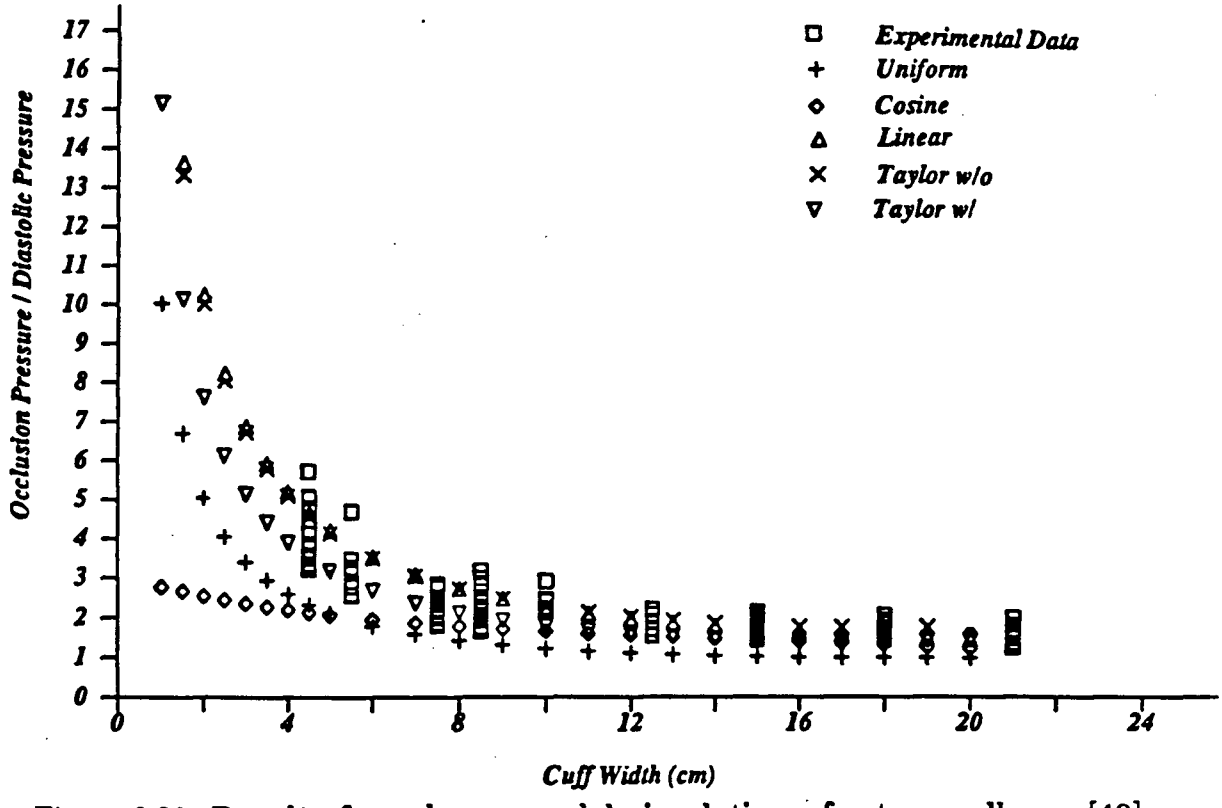

Figure 3.20: **Results from beam model simulation of artery collapse [40]**

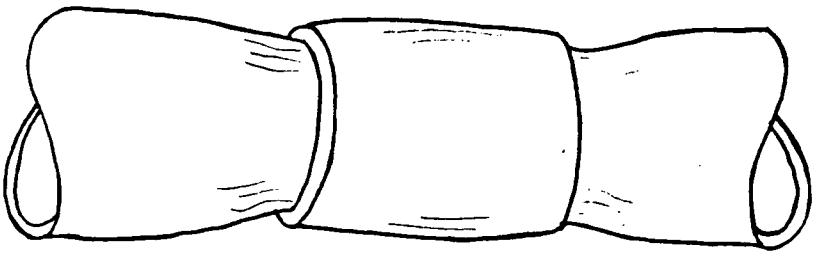

a. Schematic representation of a surgical tourniquet around a limb

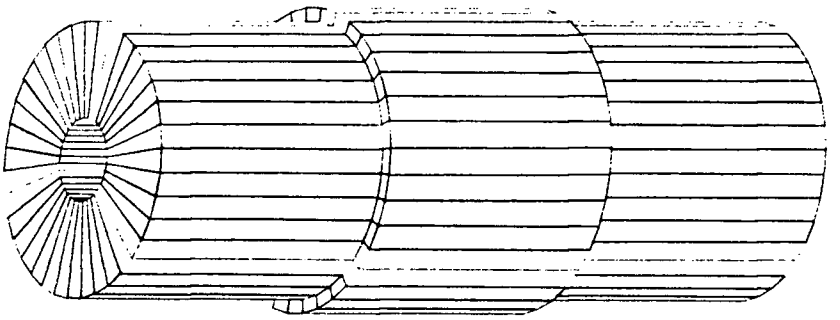

b. Three-dimensional simplification of the limb compression model

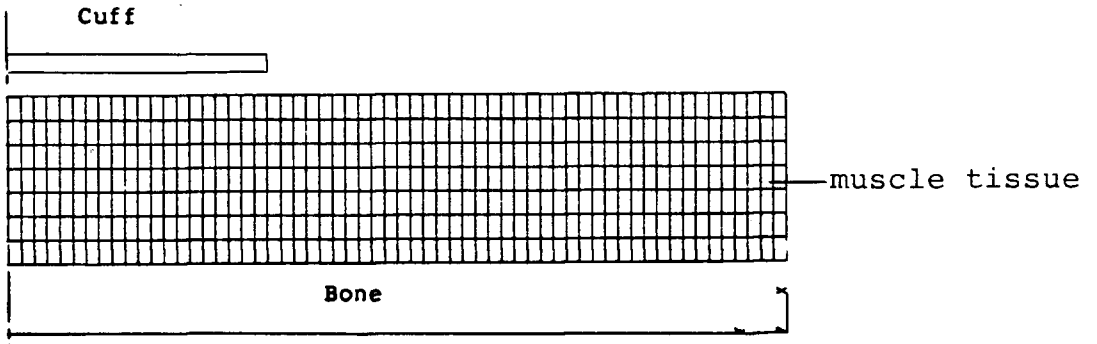

c. Axisymmetric view of the single-layer limb compression model

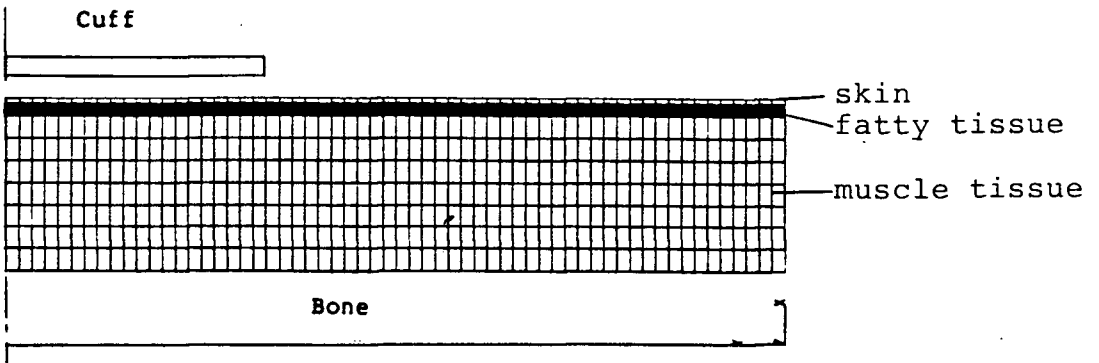

d. Axisymmetric view of the multi-layer limb compression model

Figure 4.1: **Steps performed to obtain the limb compression model**

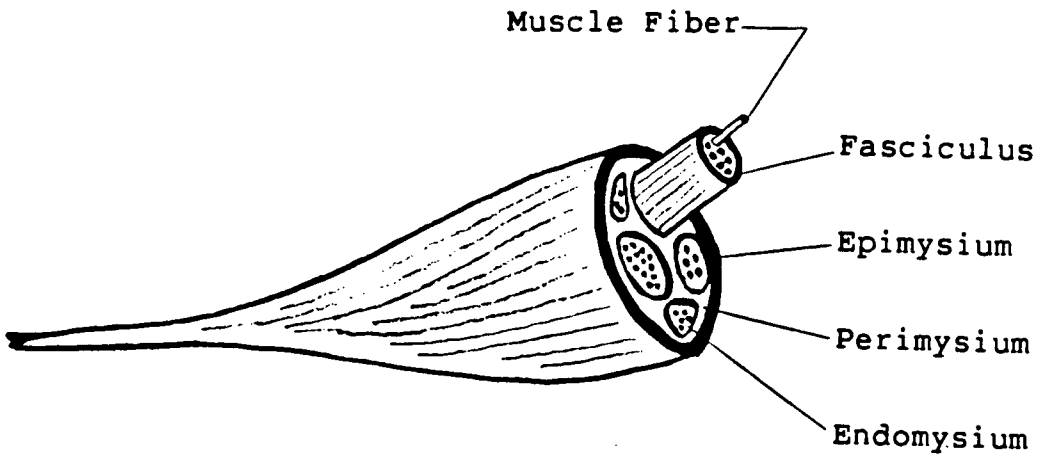

a. Schematic representation of a muscle

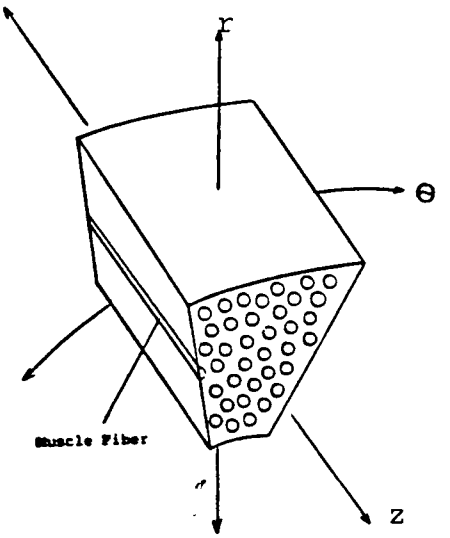

b. Example of the finite element structure of a muscle with the following mechanical properties: $E_r = E_\theta = 15\,000\,Pa$, $E_z = x\,E_r = 0.5\,E_r = 7\,500\,Pa$, $\nu_{rz} = \nu_{\theta z} = 0.49$, and $\nu_{r\theta} = 0.45$

Figure 4.2: **Muscle structure**

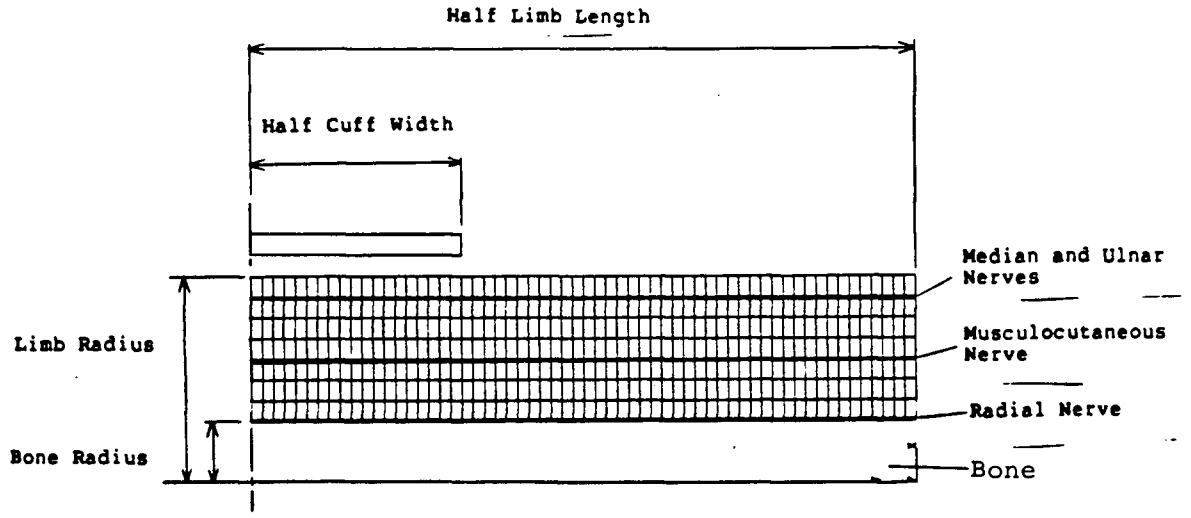

a. Geometric features of the single-layer limb compression model

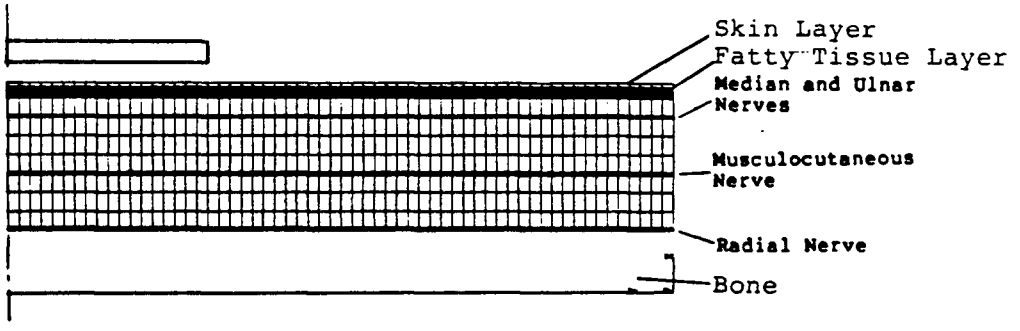

b. Geometric features of the multi-layer limb compression model

Figure 4.3: **Finite element models of an axisymmetric limb**

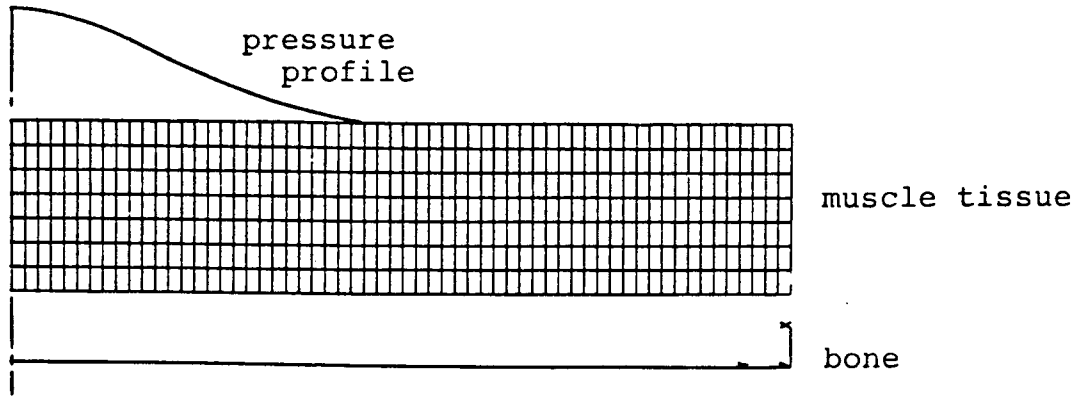

a. Single-layer limb compression model with sinusoidal surface pressure distribution

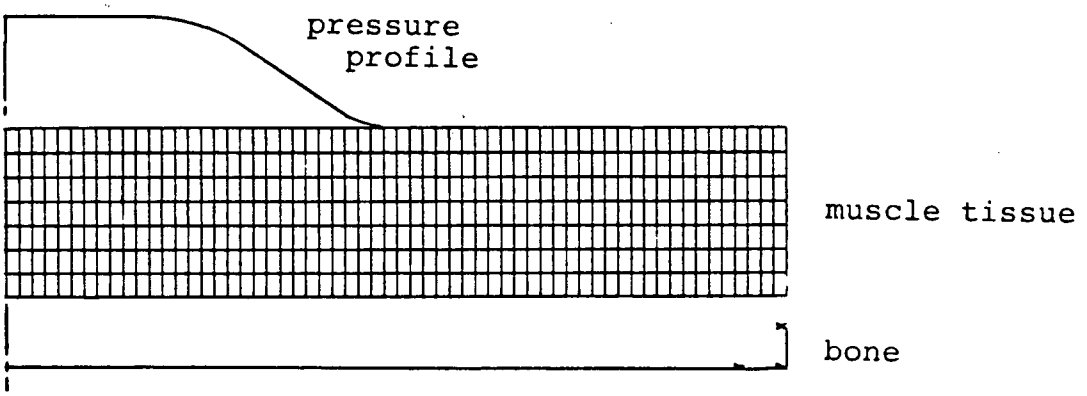

b. Single-layer limb compression model with exponential surface pressure distribution

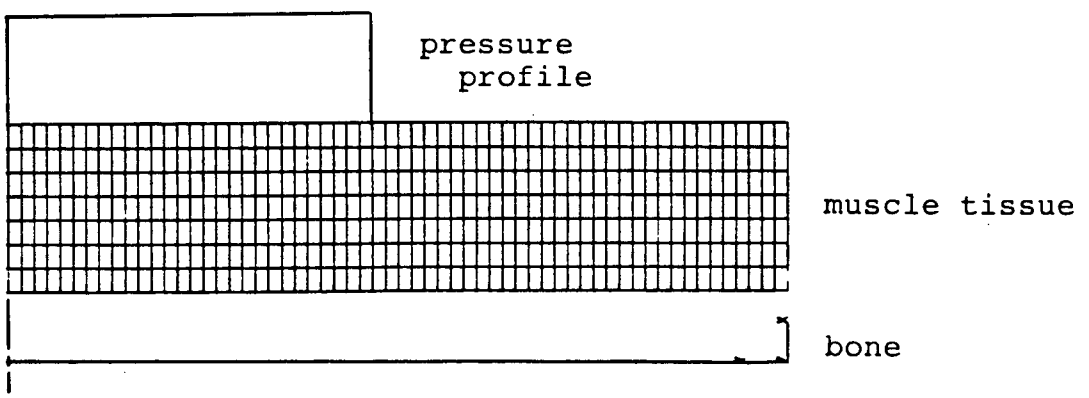

c. Single-layer limb compression model with rectangular surface pressure distribution

Figure 4.4: **Loading conditions imposed**

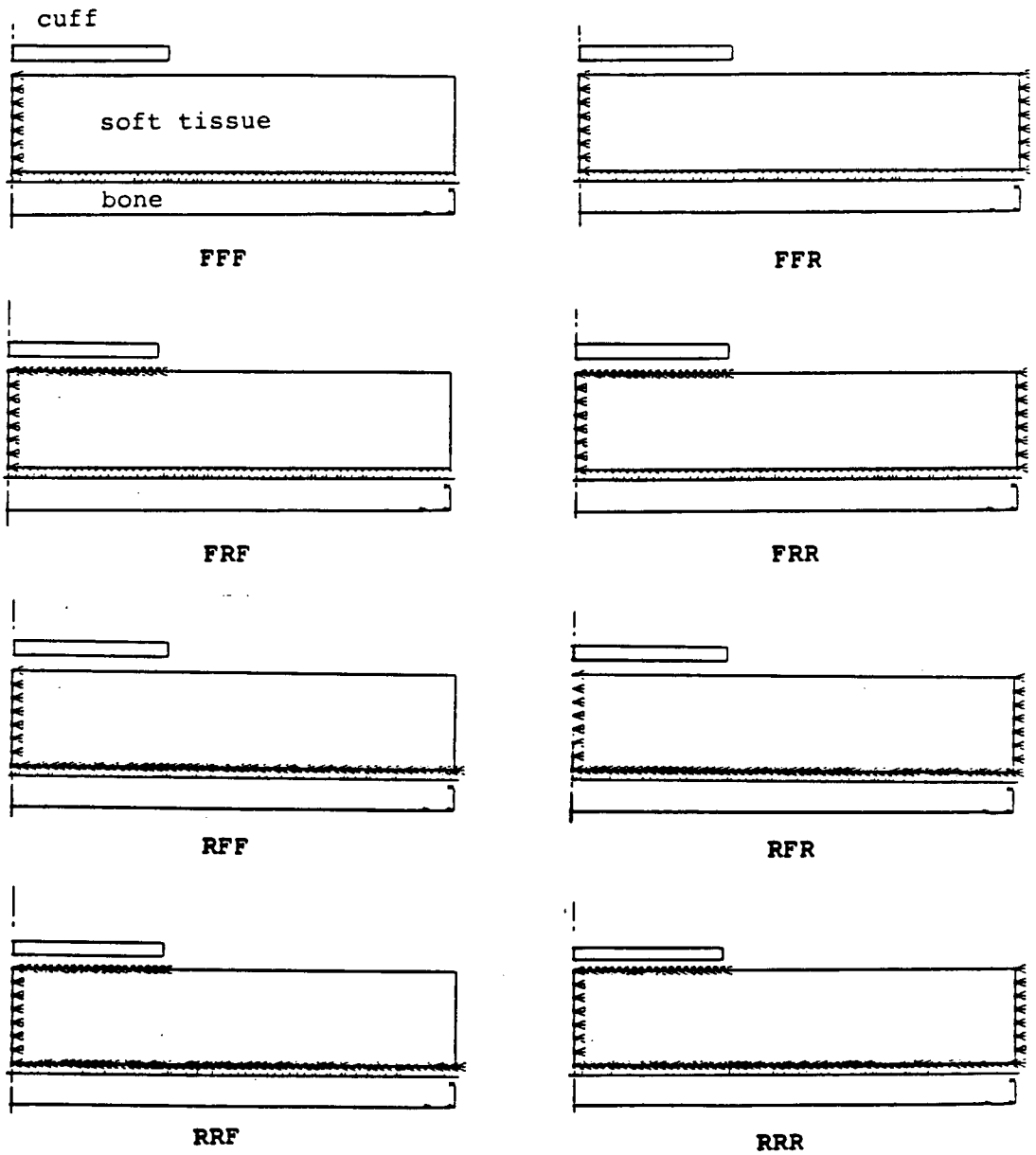

Figure 4.5: **Boundary conditions as applicable to the limb compression model**

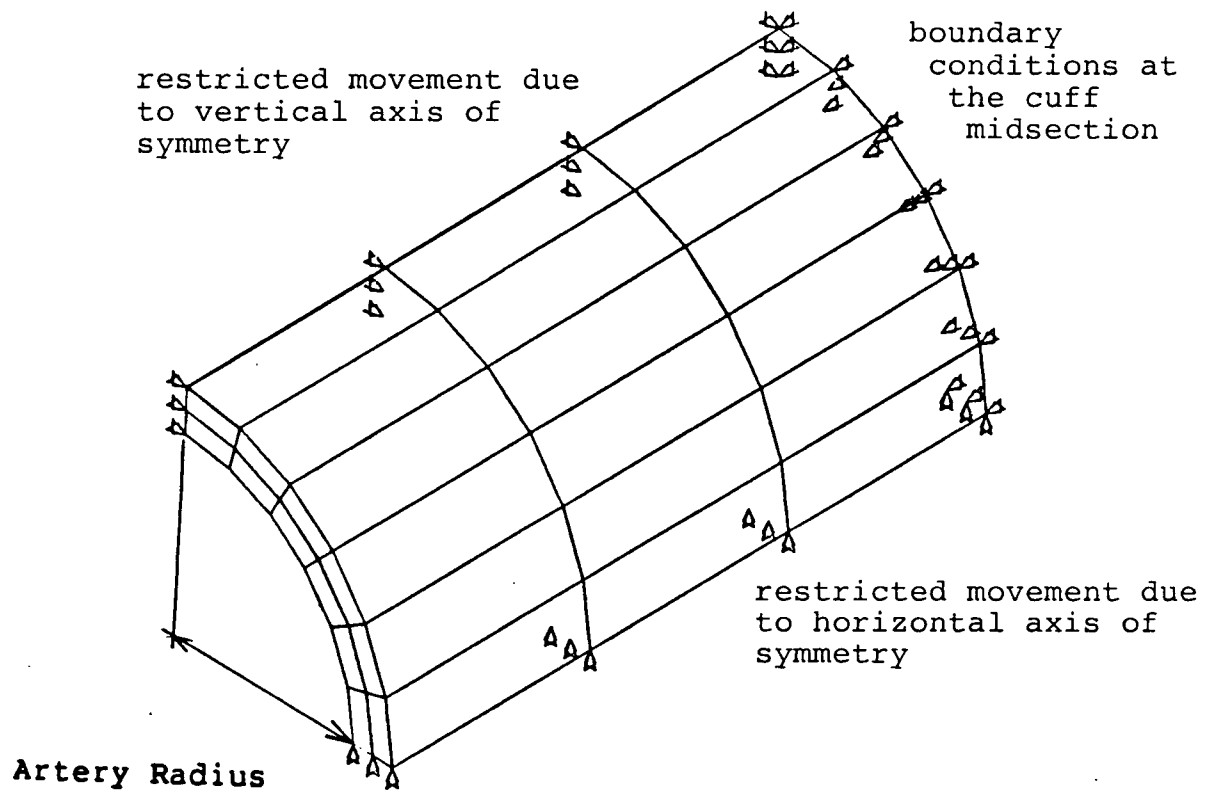

Figure 4.6: **Boundary conditions as applicable to the artery model**

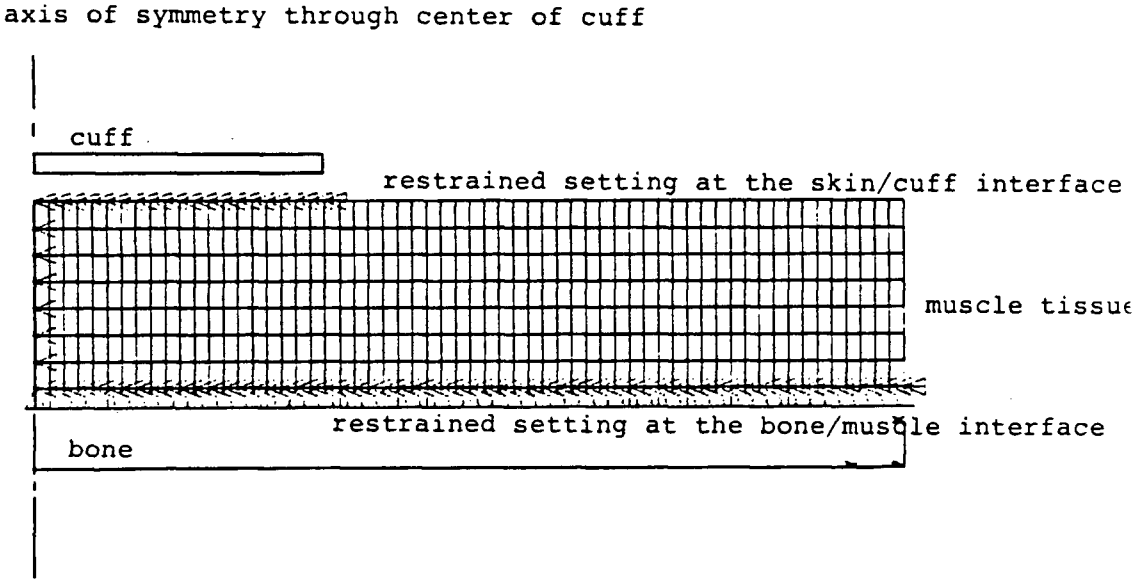

Figure 4.7: **Single-layer limb compression model**

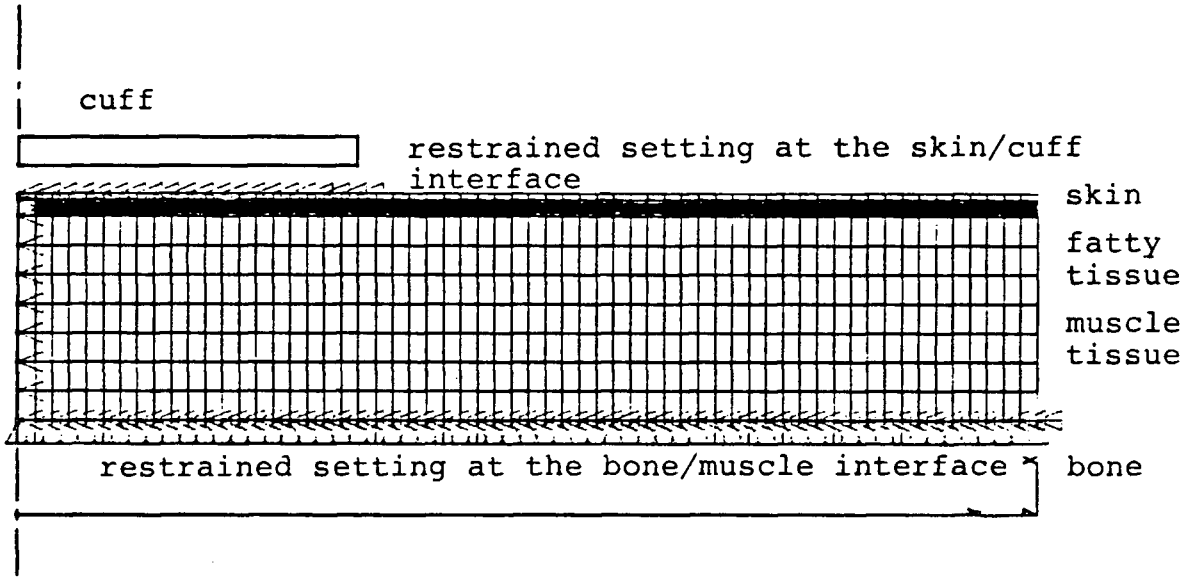

Figure 4.8: **Multi-layer limb compression model**

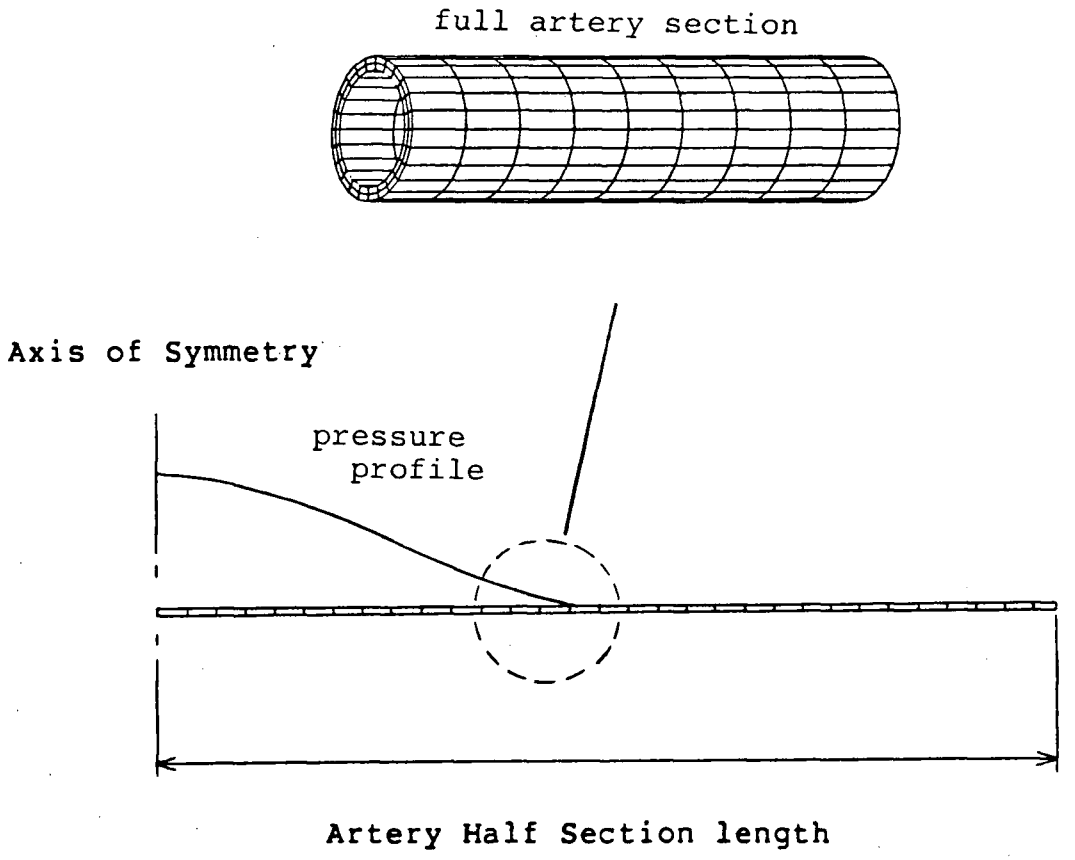

Figure 4.9: **Full section of the finite element artery model**

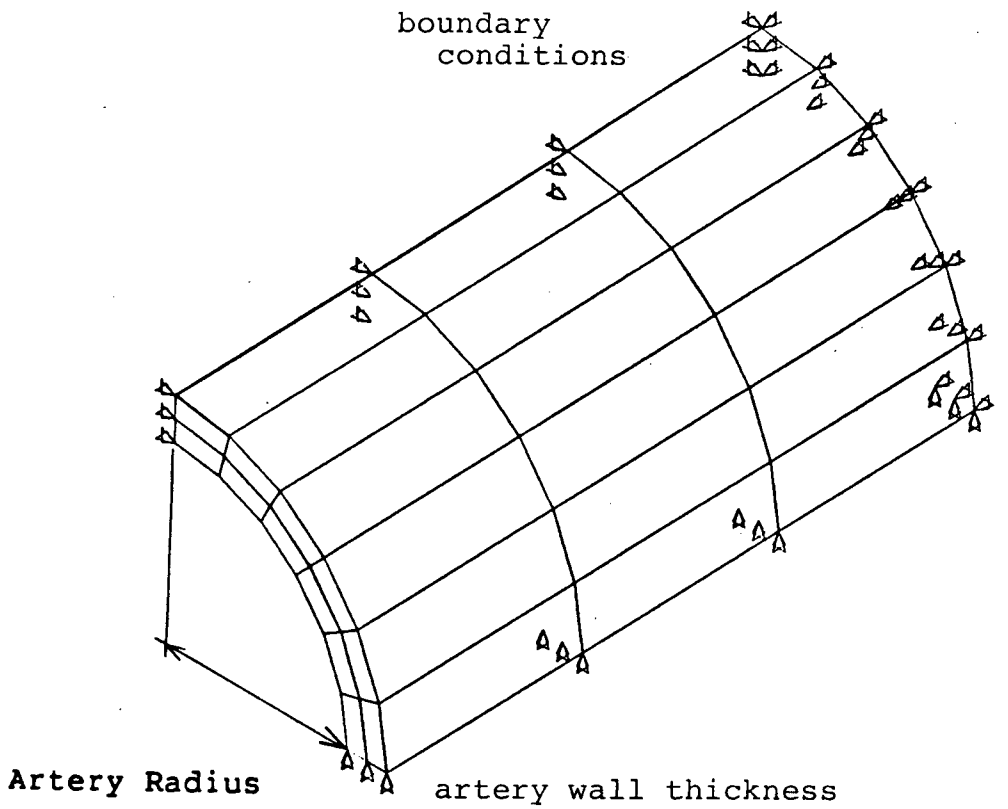

Figure 4.10: **Quarter section of the finite element artery model**

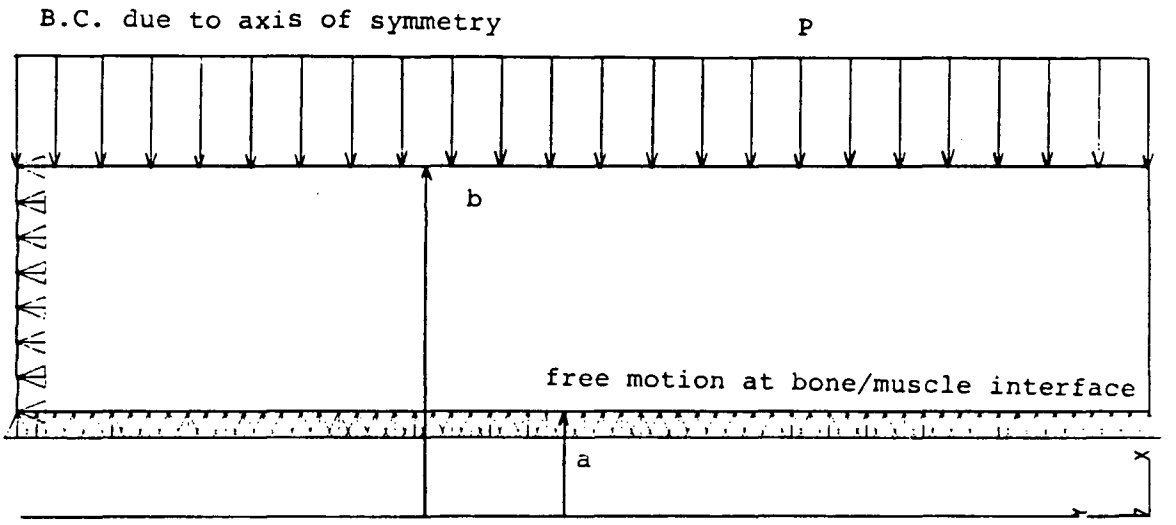

Figure 5.1: **Single-layer finite element limb compression model subjected to thick-walled cylinder conditions**

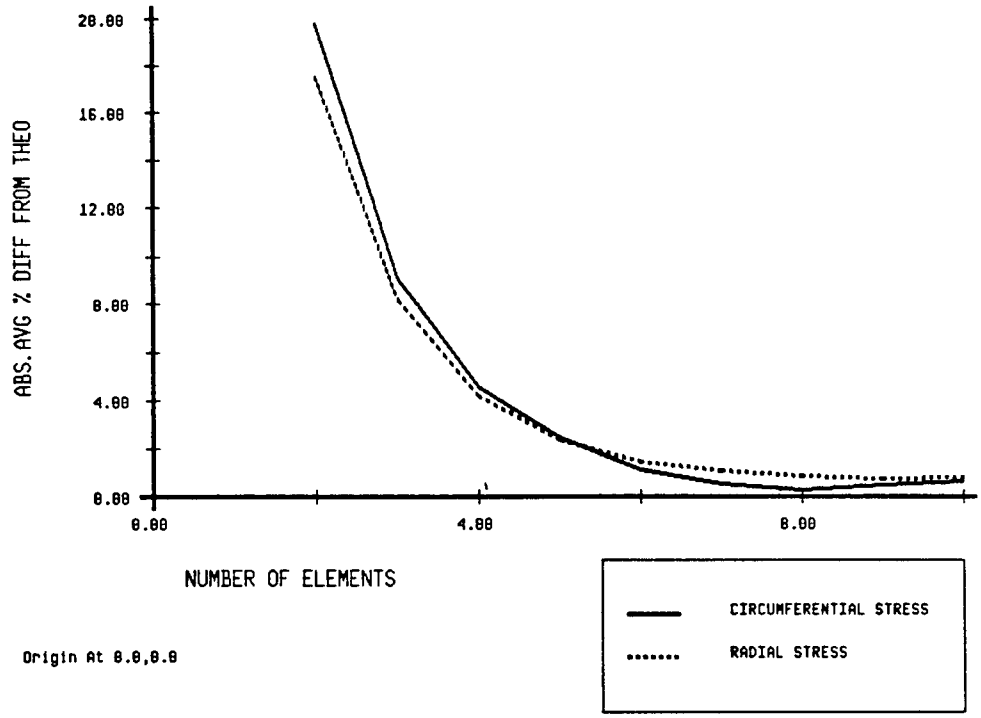

Figure 5.2: **Influence of radial mesh on the model's accuracy (absolute average percentage difference)**

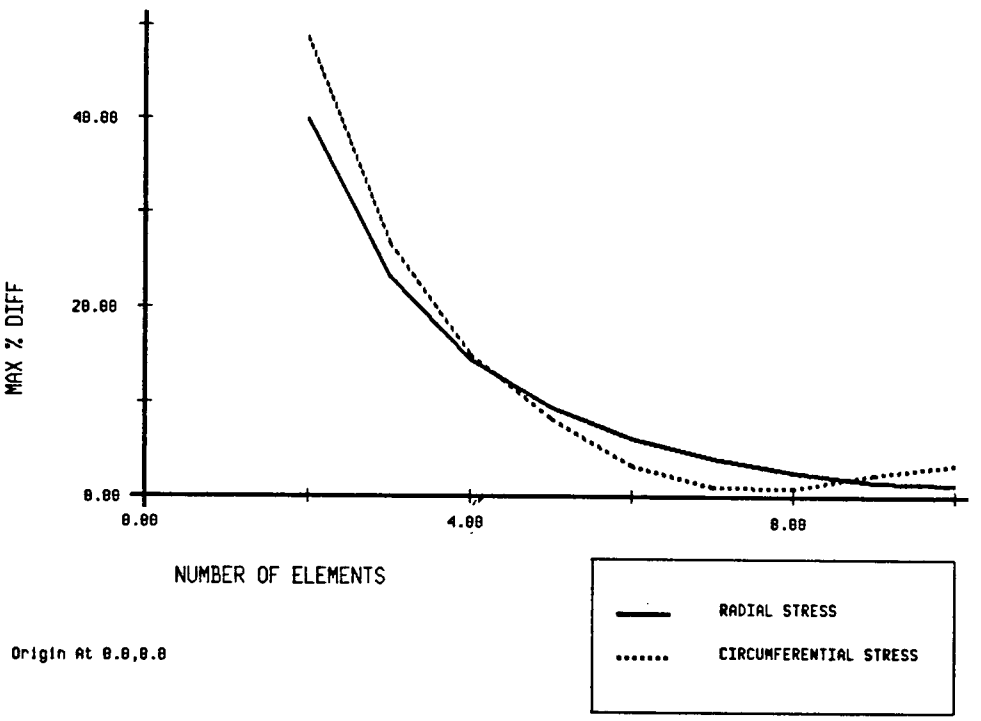

Figure 5.3: **Influence of radial mesh on the model's accuracy (maximum percentage difference)**

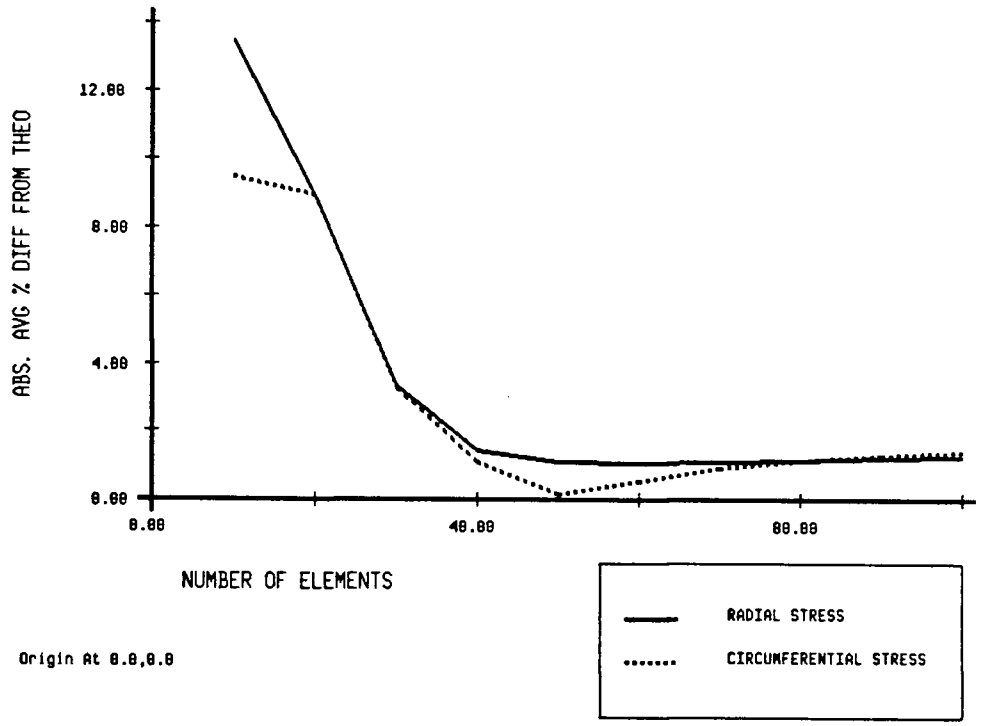

Figure 5.4: **Influence of axial mesh on the model's accuracy (absolute average percentage difference)**

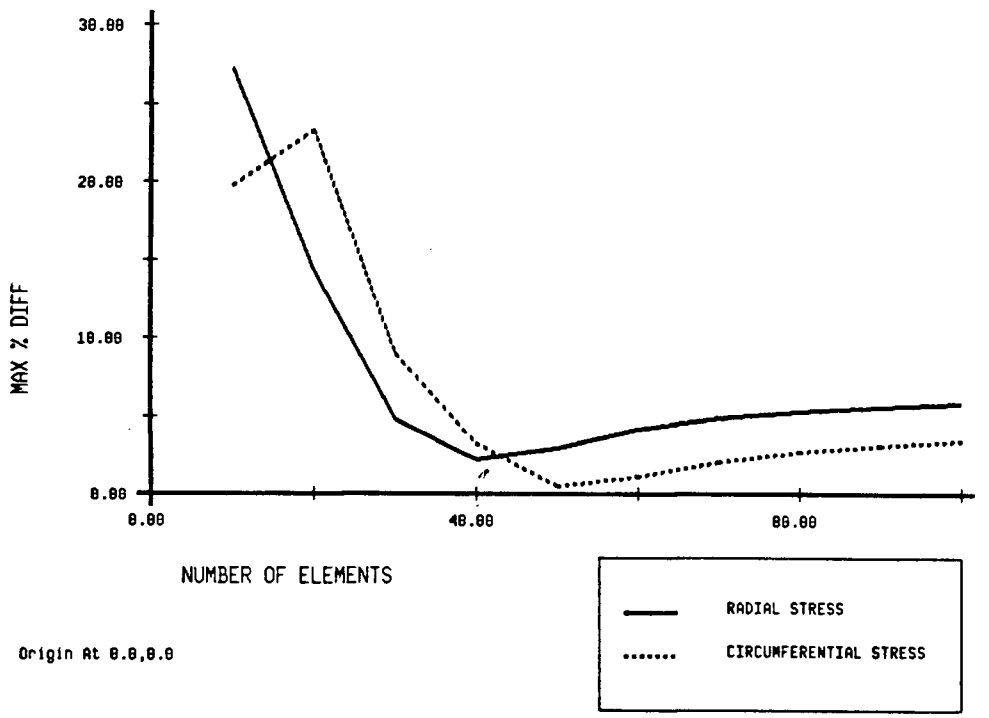

Figure 5.5: **Influence of axial mesh on the model's accuracy (maximum percentage difference)**

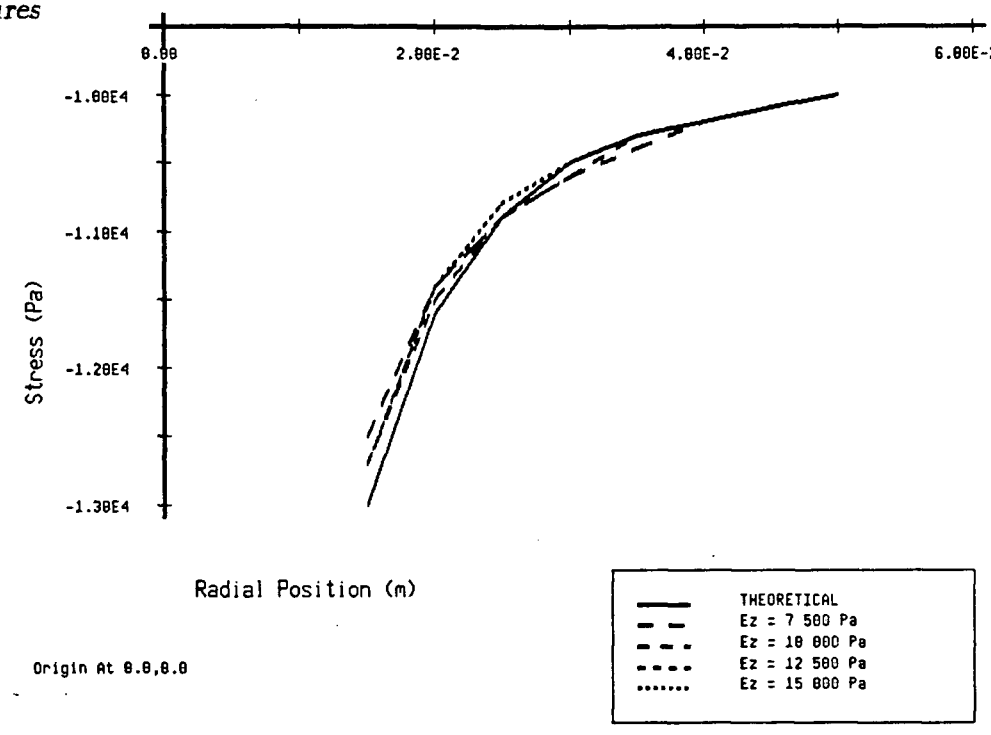

a. Radial stress profiles

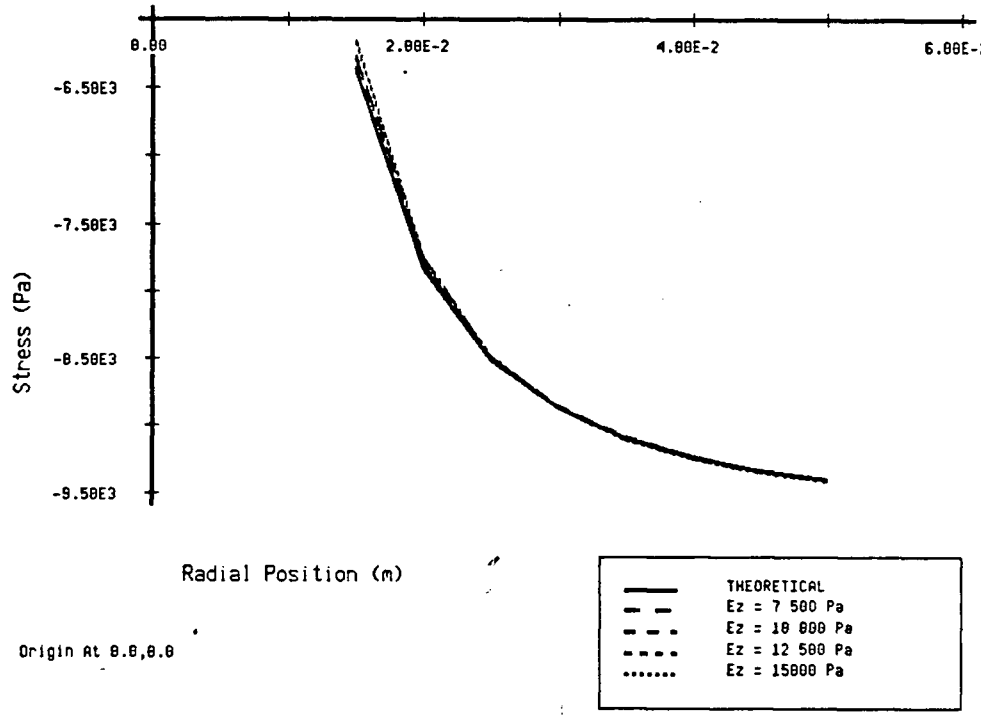

b. Circumferential stress profiles

Figure 5.6: **Comparison of stress profiles for varying E_z**

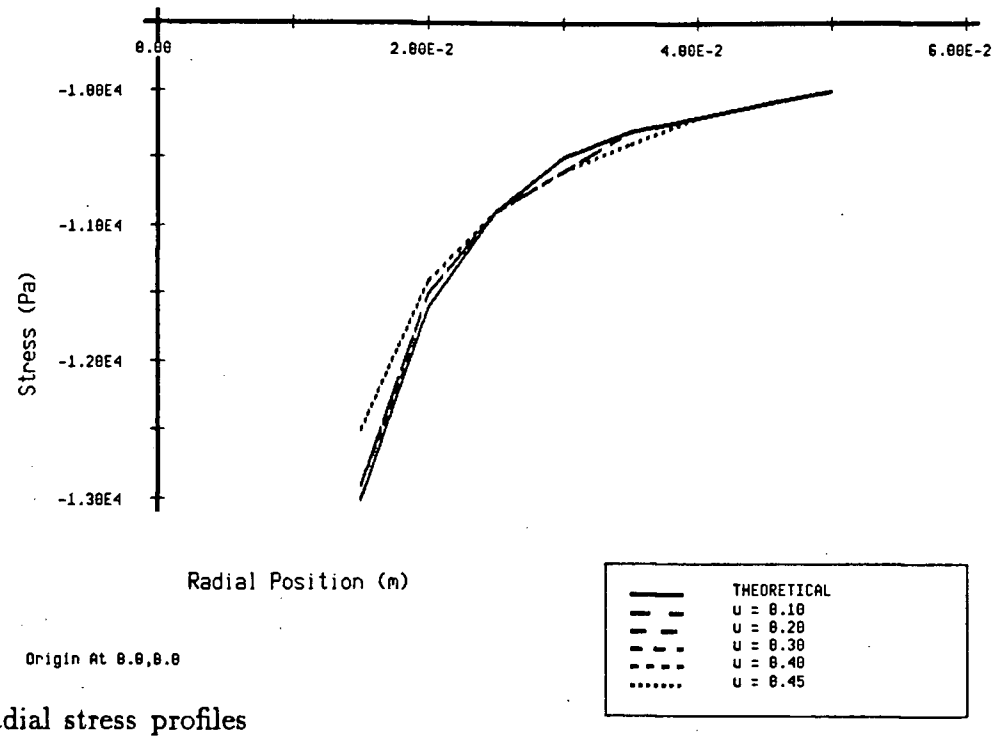

a. Radial stress profiles

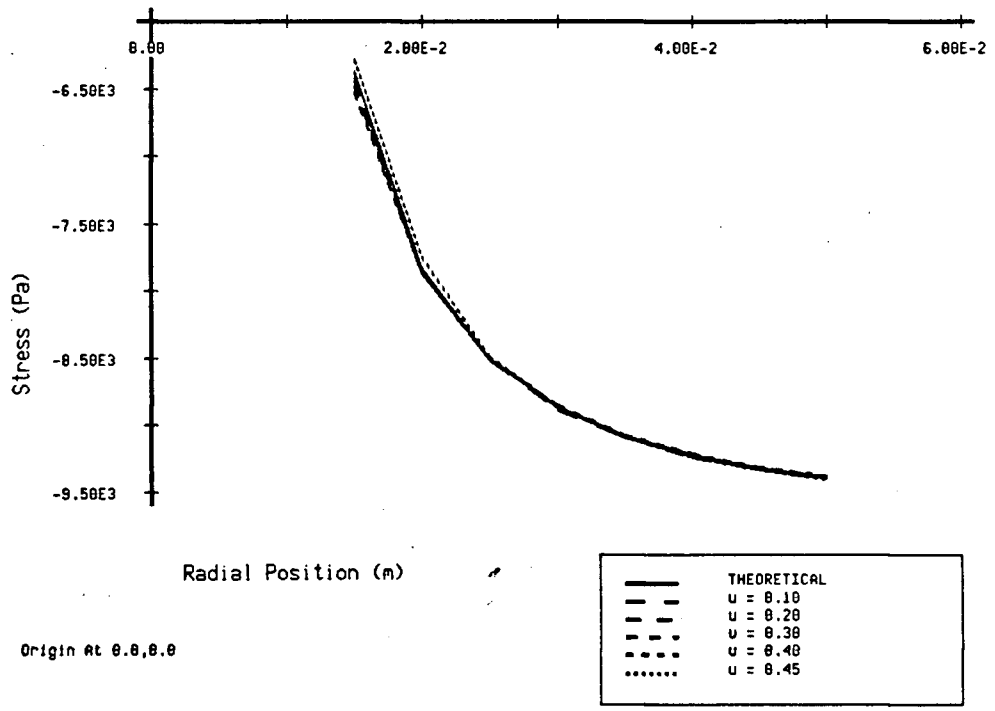

b. Circumferential stress profiles

Figure 5.7: **Comparison of stress profiles for varying ν_{rz} and $\nu_{\theta z}$**

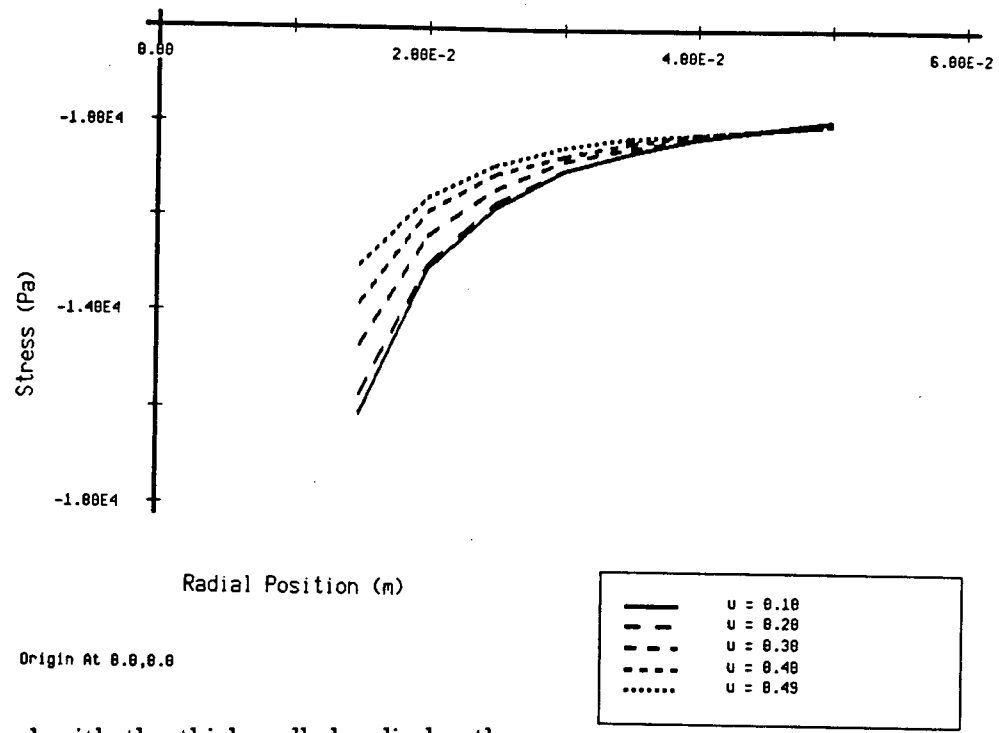

a. Obtained with the thick-walled cylinder theory

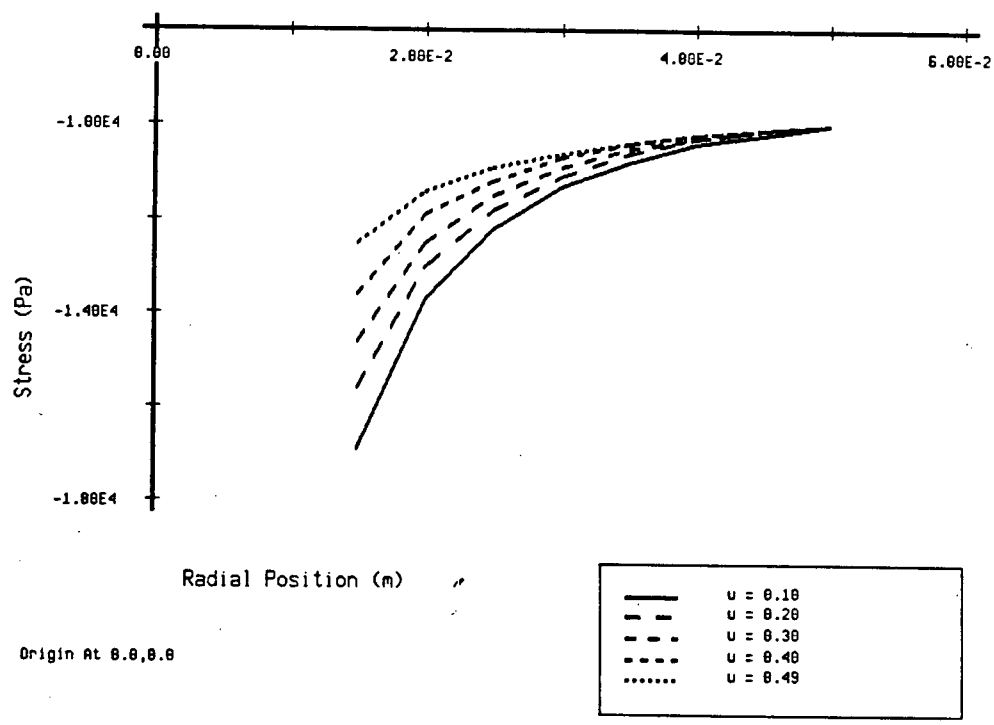

b. Obtained with the finite element method

Figure 5.8: **Radial stress profiles for varying $\nu_{r\theta}$**

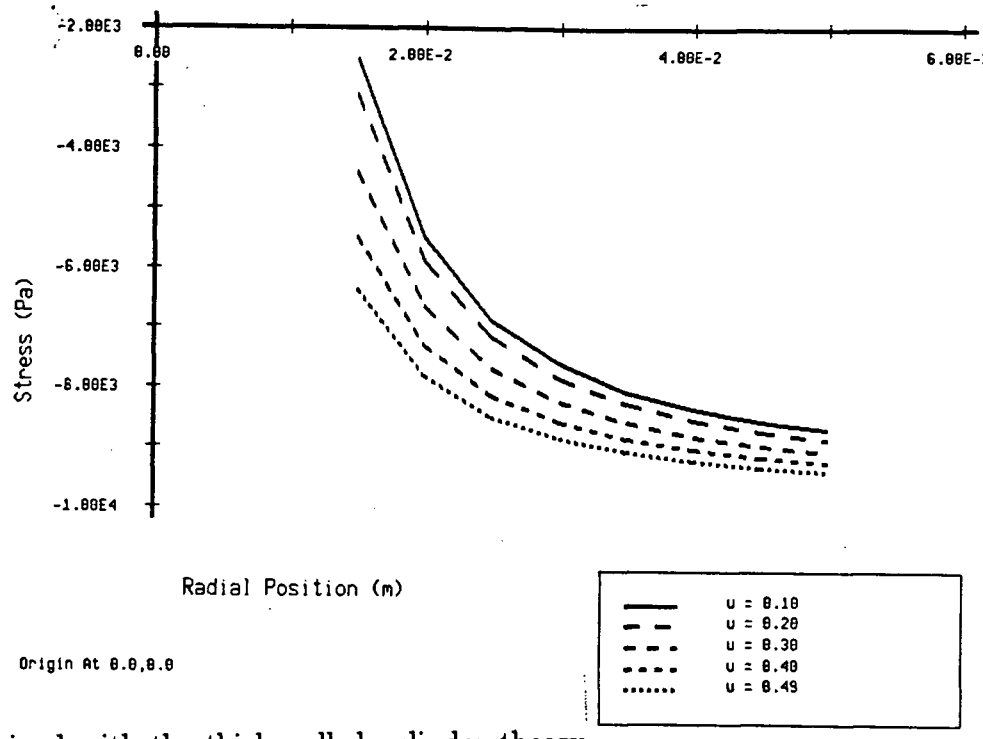

a. Obtained with the thick-walled cylinder theory

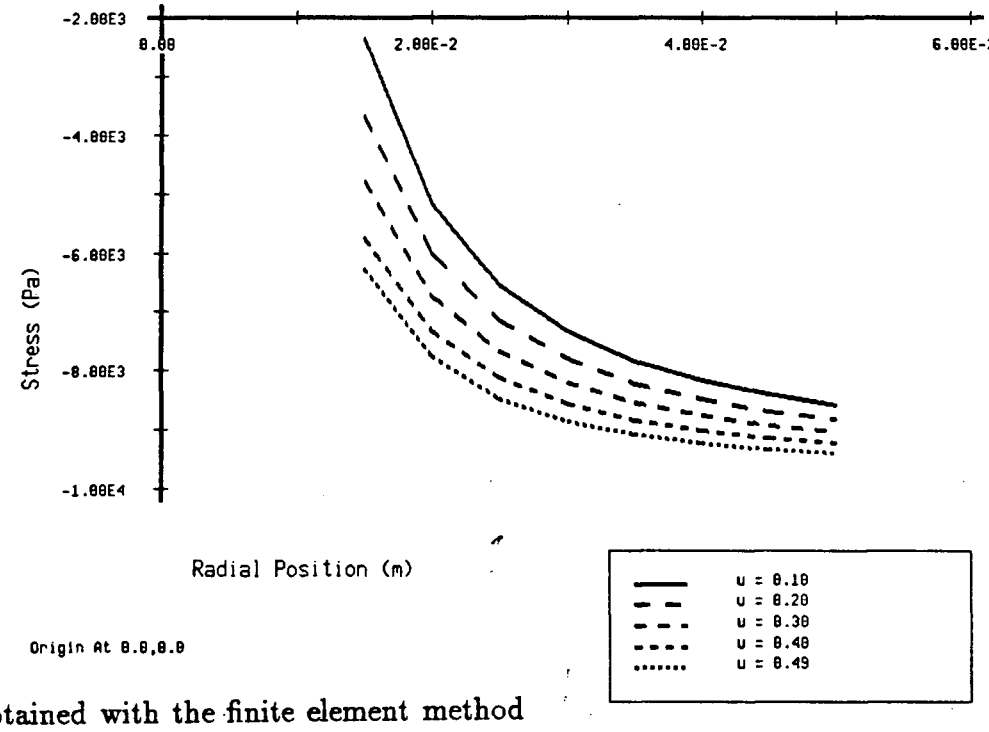

b. Obtained with the finite element method

Figure 5.9: **Circumferential stress profiles for varying $\nu_{r\theta}$**

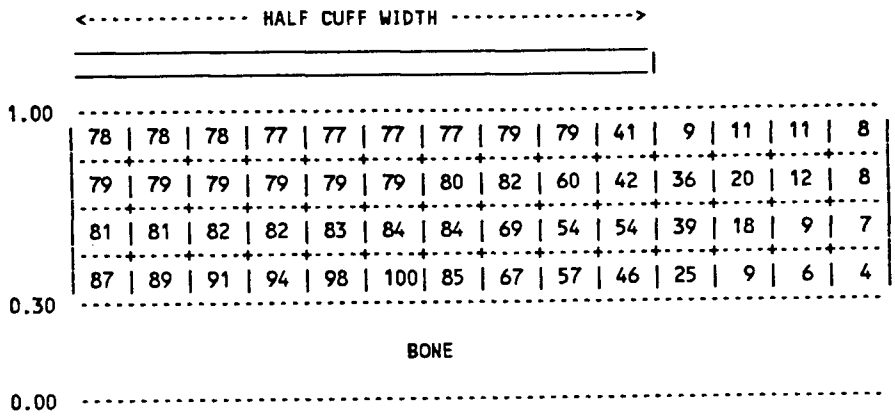

a. Obtained by Auerbach

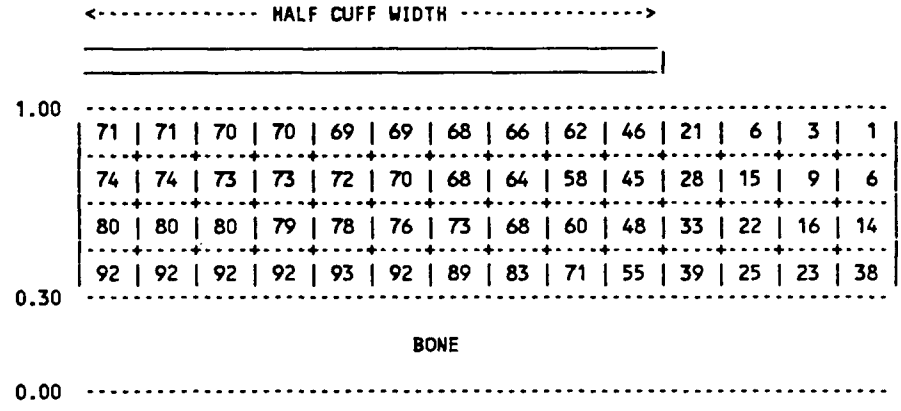

b. Obtained by ANSYS

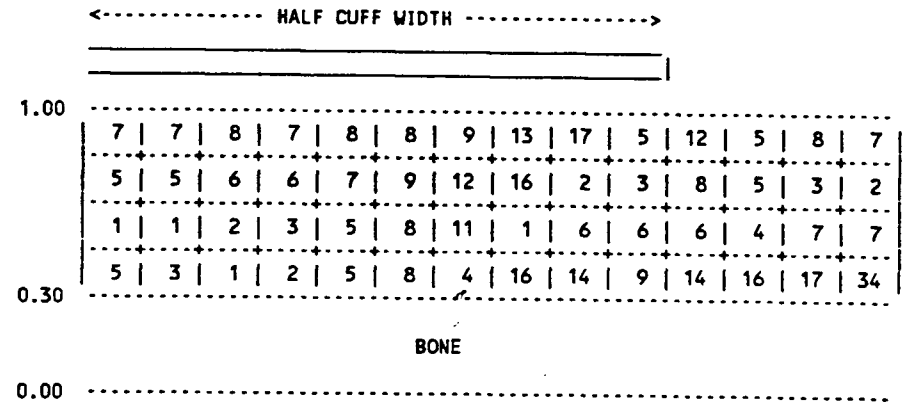

c. Difference between Auerbach and ANSYS

Figure 5.10: **Hydrostatic pressure distributions (14 elements)**

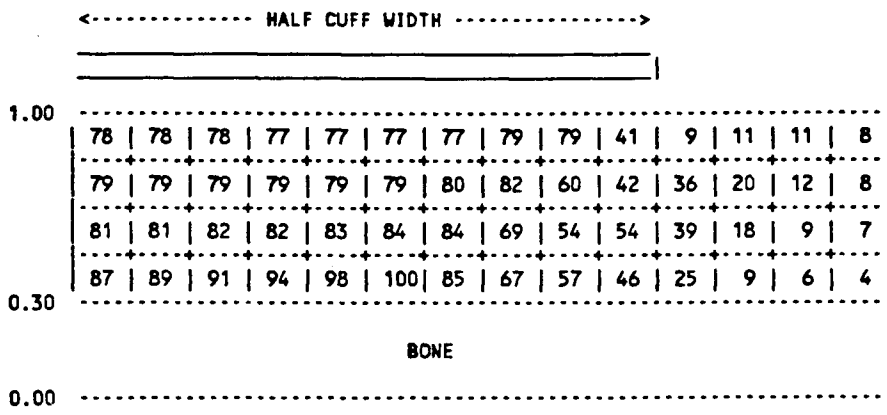

a. Obtained by Auerbach

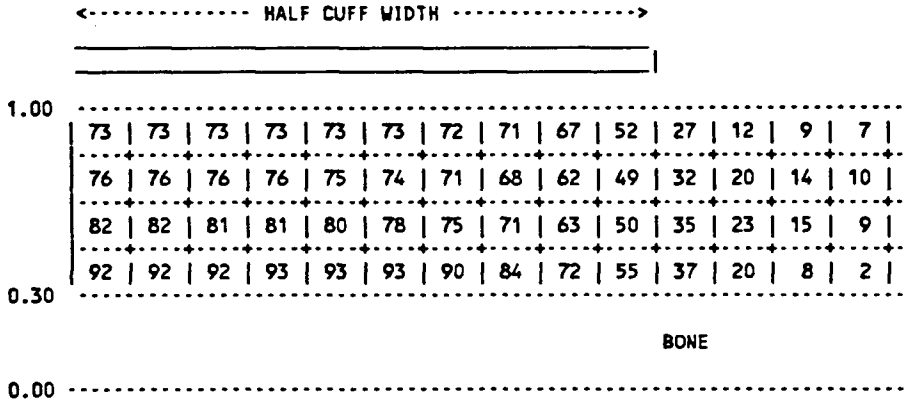

b. Obtained by ANSYS

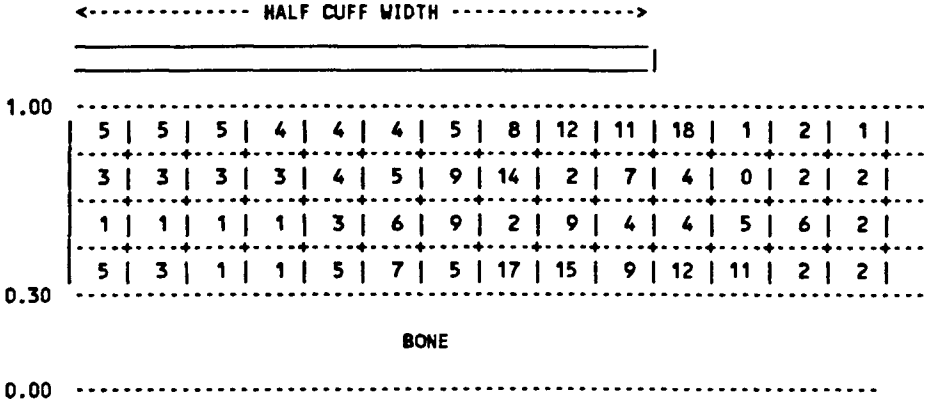

c. Difference between Auerbach and ANSYS

Figure 5.11: **Hydrostatic pressure distributions (24 elements)**

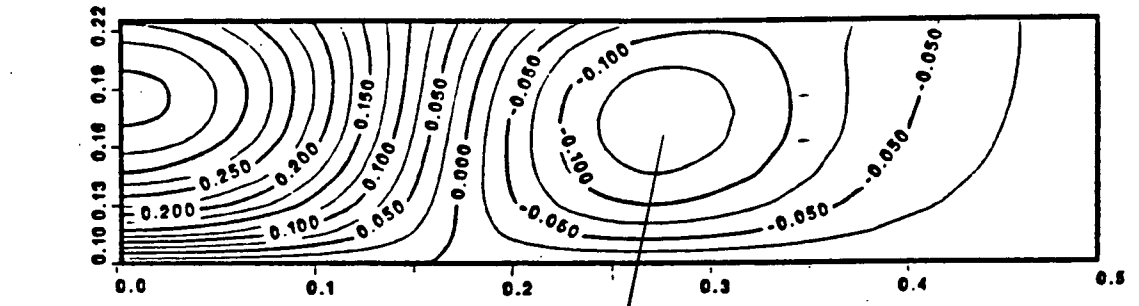

a. Obtained by Hodgson

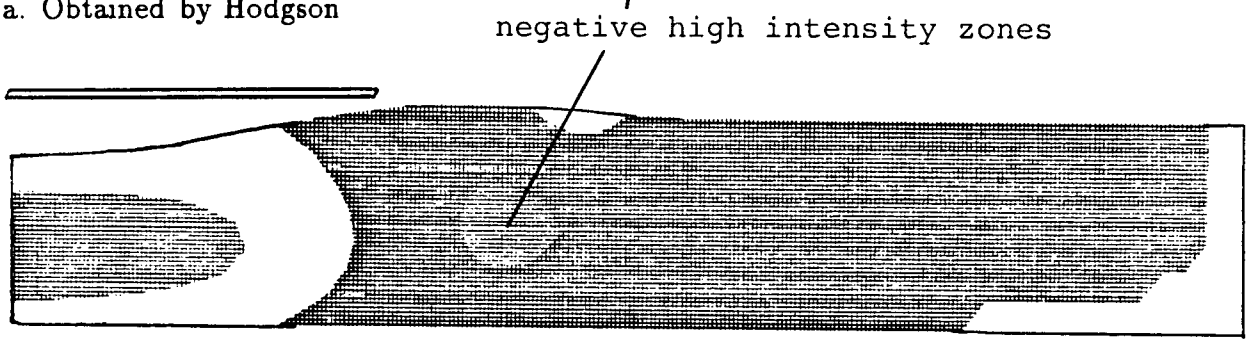

b. Obtained by ANSYS

Figure 5.12: **Axial strain distributions for a sinusoidal surface pressure profile**

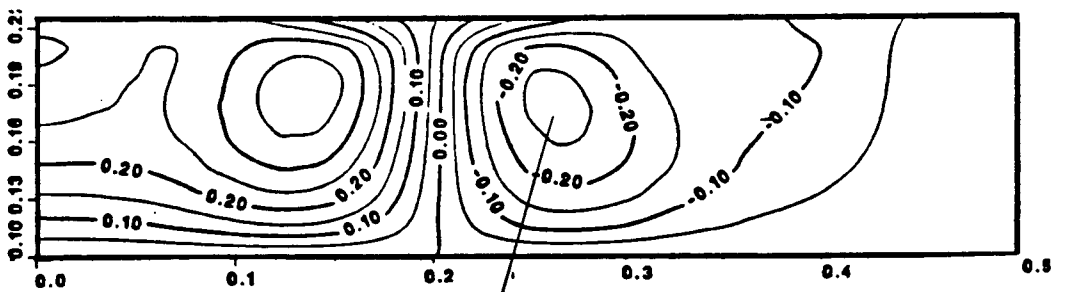

a. Obtained by Hodgson

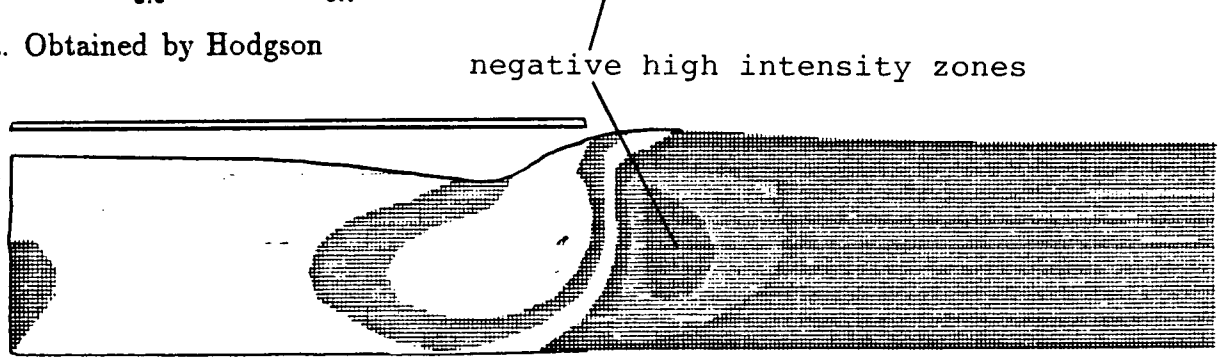

b. Obtained by ANSYS

Figure 5.13: **Axial strain distributions for a rectangular surface pressure profile**

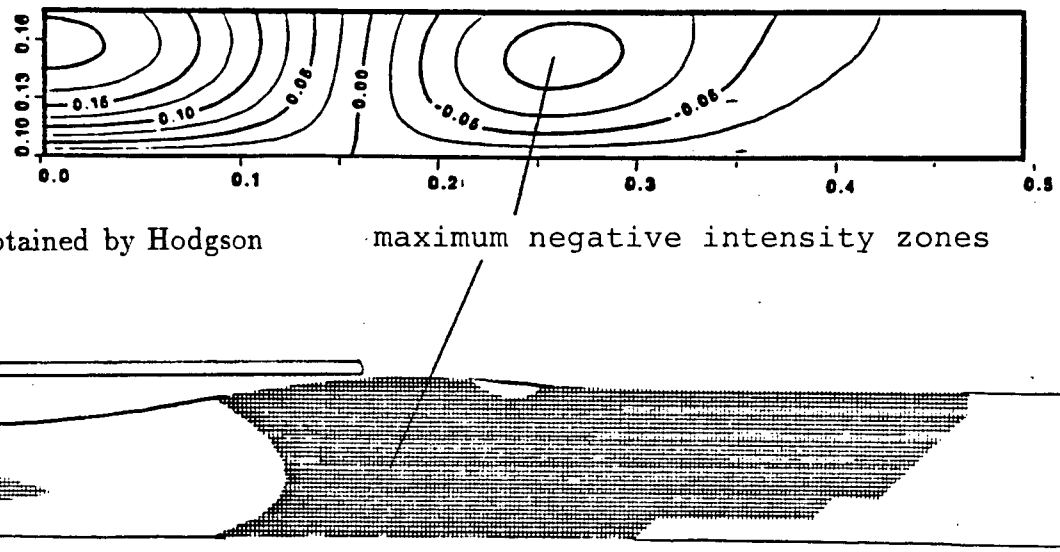

a. Obtained by Hodgson

b. Obtained by ANSYS

Figure 5.14: **Axial strain distributions when the smallest arm radius considered in Hodgson's study is assumed**

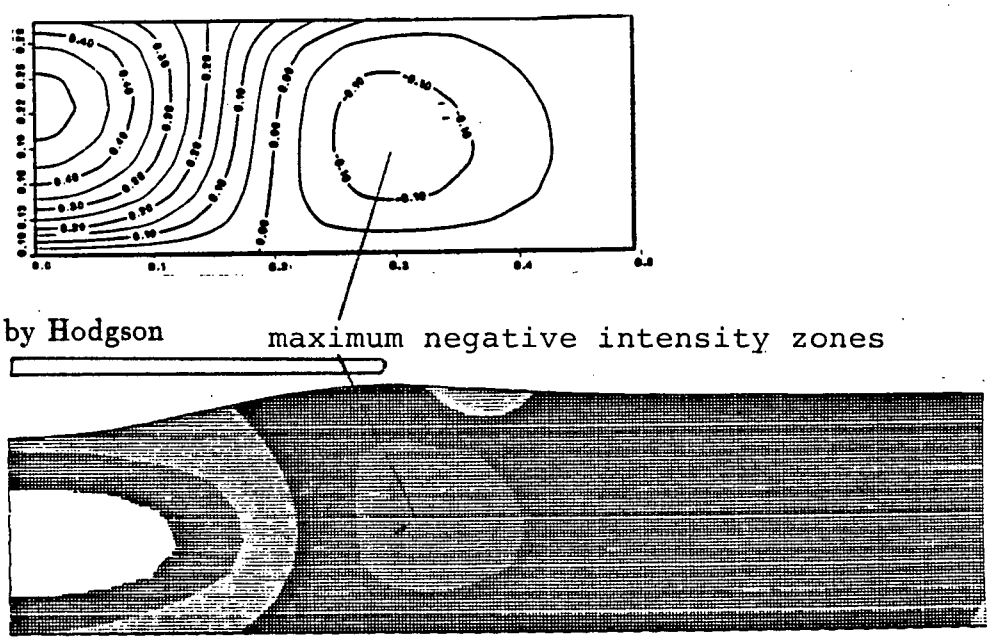

a. Obtained by Hodgson

b. Obtained by ANSYS

Figure 5.15: **Axial strain distributions when the largest arm radius considered in Hodgson's study is assumed**

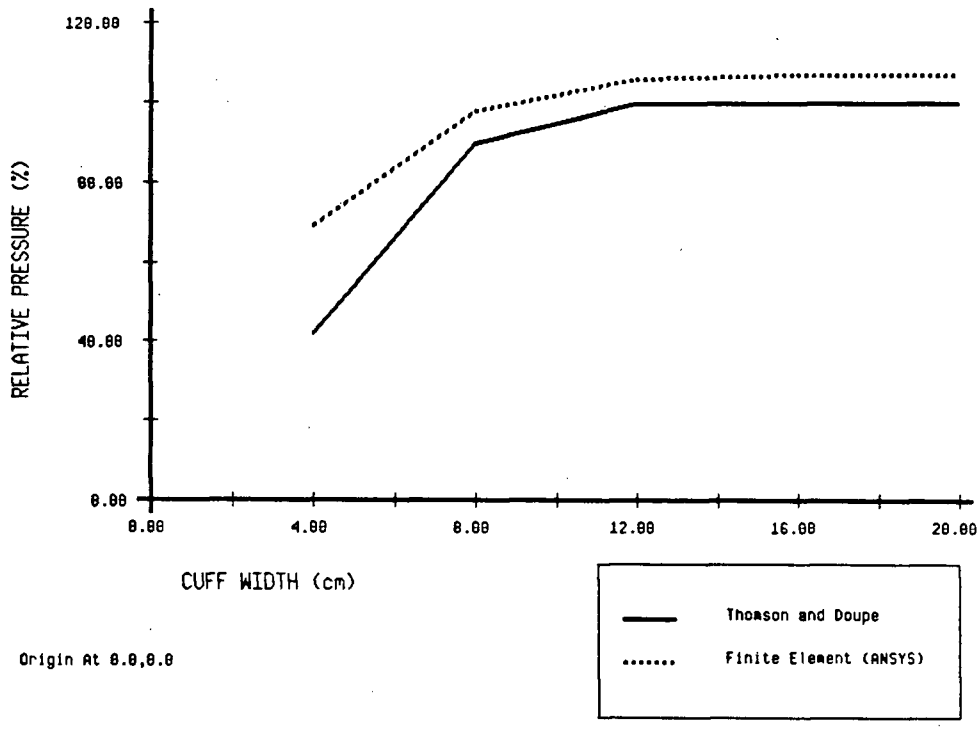

Figure 5.16: **Comparison of the maximum relative pressure at the bone level**

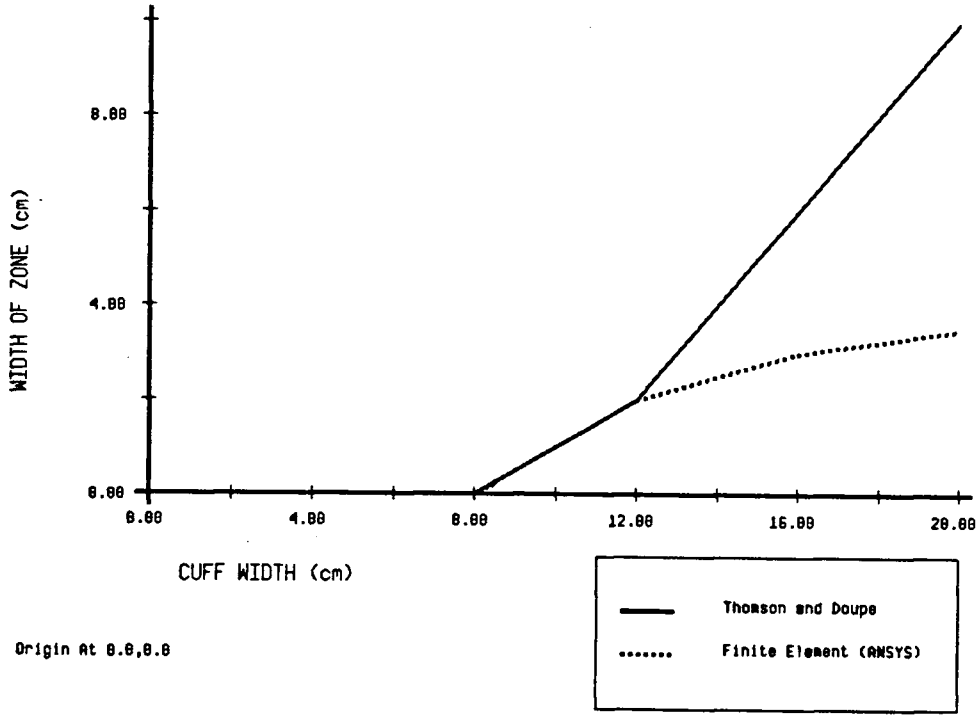

Figure 5.17: **Comparison of the width of the 100% pressure zone at the bone**

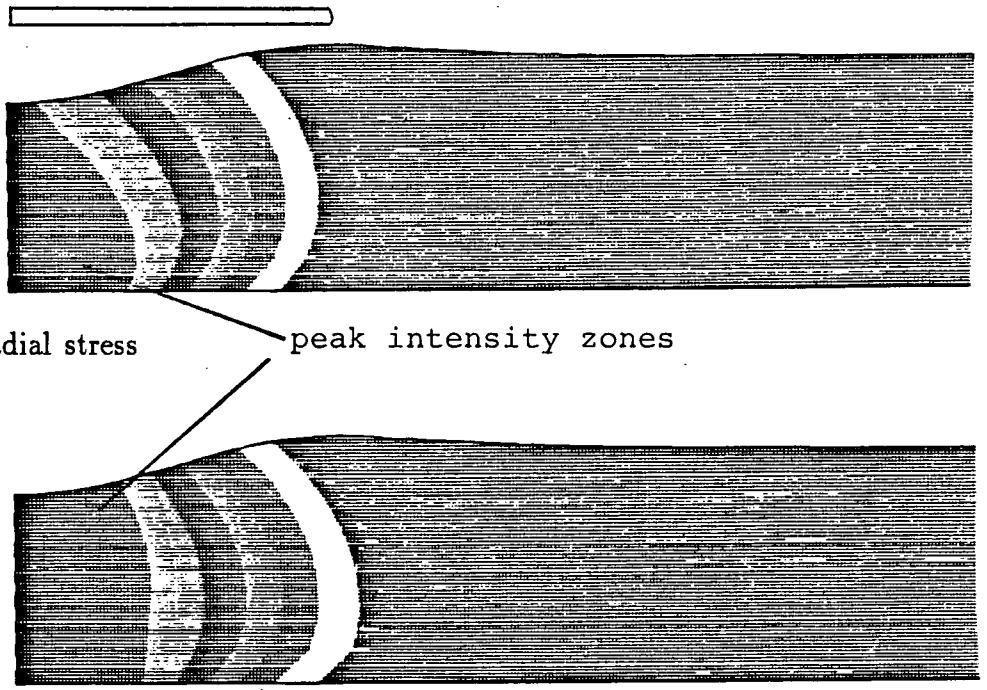

a. Radial stress

b. Circumferential stress

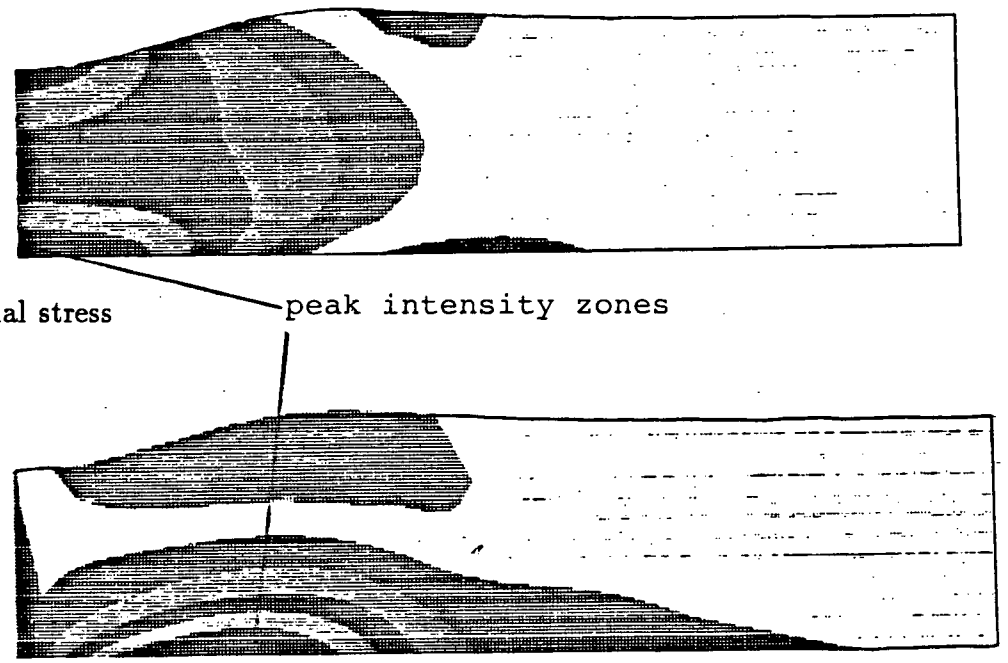

c. Axial stress

d. Shear stress

Figure 5.18: **Component stress profiles**

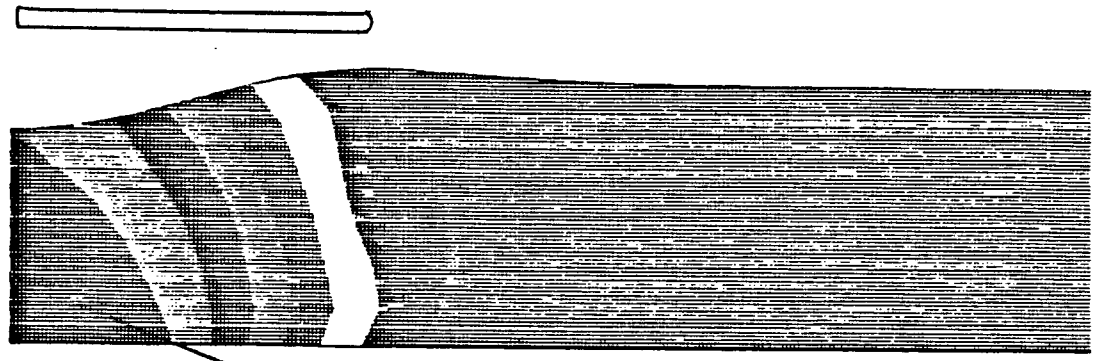

a. High intensity peak intensity zones

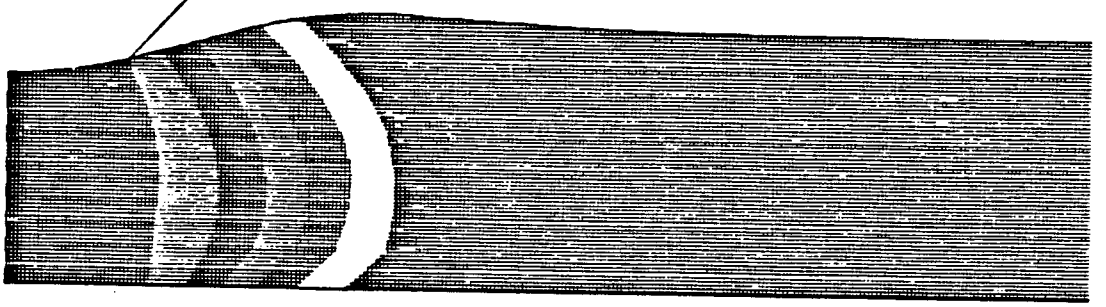

b. Medium intensity

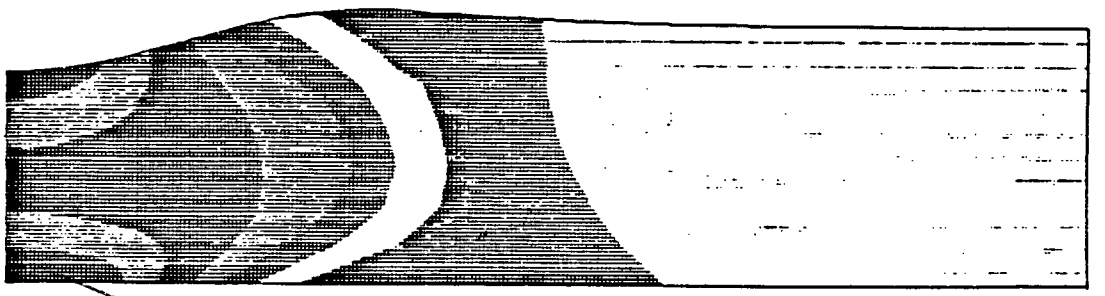

c. Low intensity peak intensity zone

Figure 5.19: **Principal stress profiles**

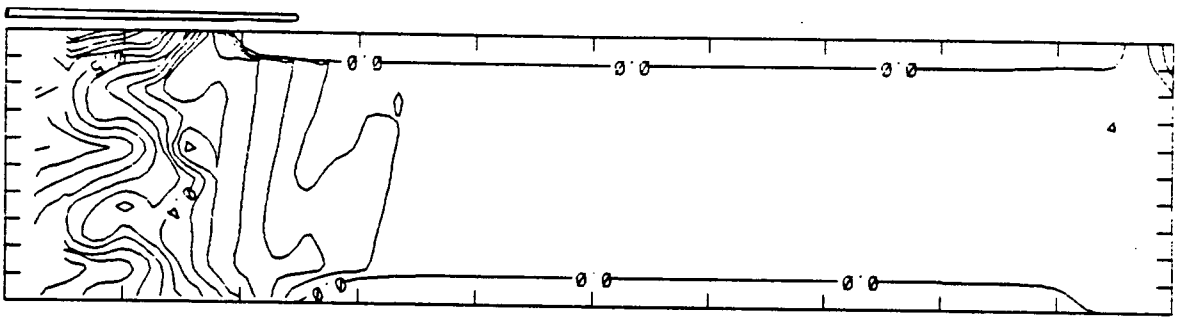

a. Hydrostatic stress

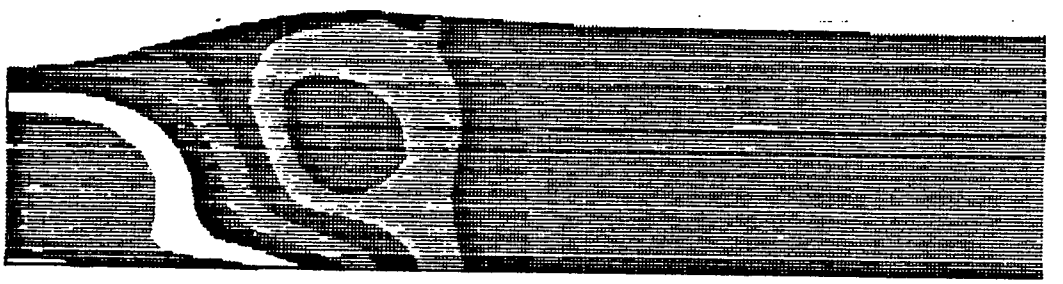

b. Octahedral stress

Figure 5.20: **Combination stress profiles**

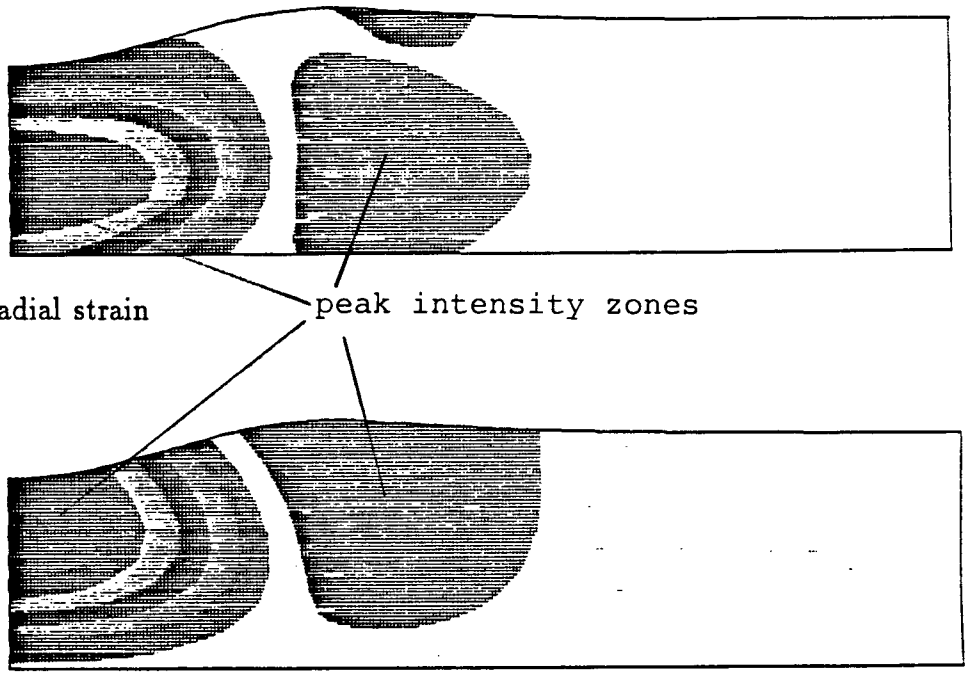

a. Radial strain

b. Circumferential strain

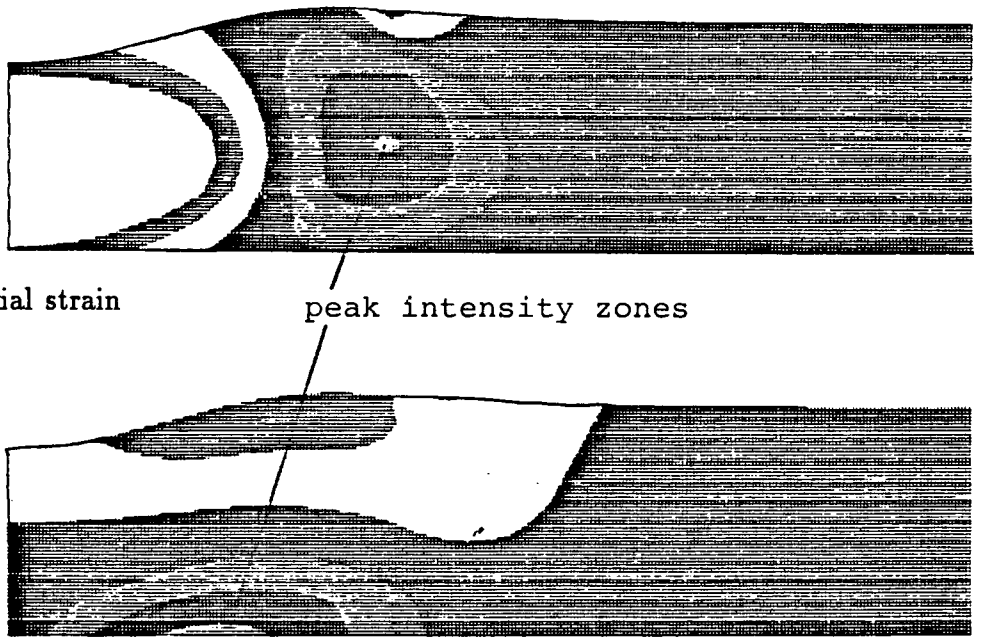

c. Axial strain

d. Shear strain

Figure 5.21: **Component strain profiles**

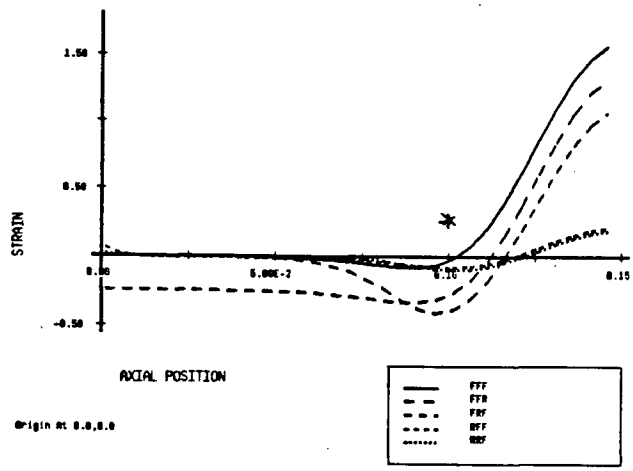

*: indicates the edge of the cuff on each curve

a. Radial nerve

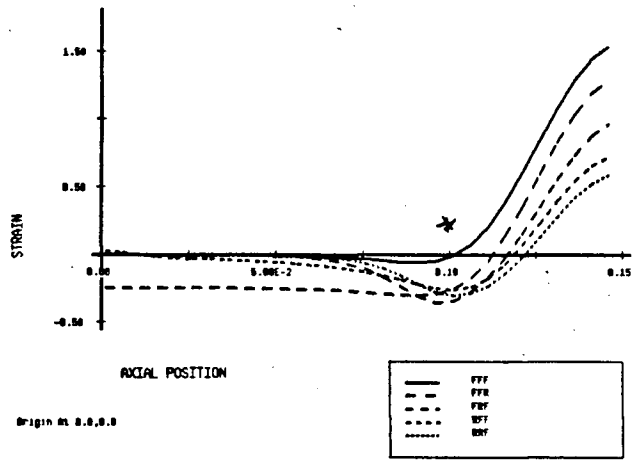

b. Musculocutaneous nerve

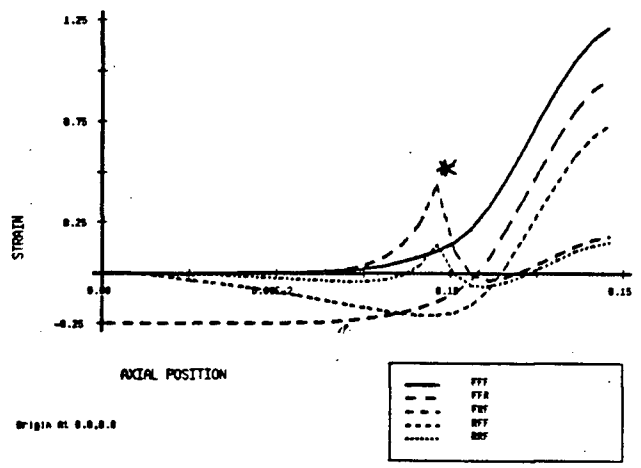

c. Median/ulnar nerves

Figure 5.22: **Predicted axial strain profiles for varying boundary condition setting at each nerve location (single-layer model)**

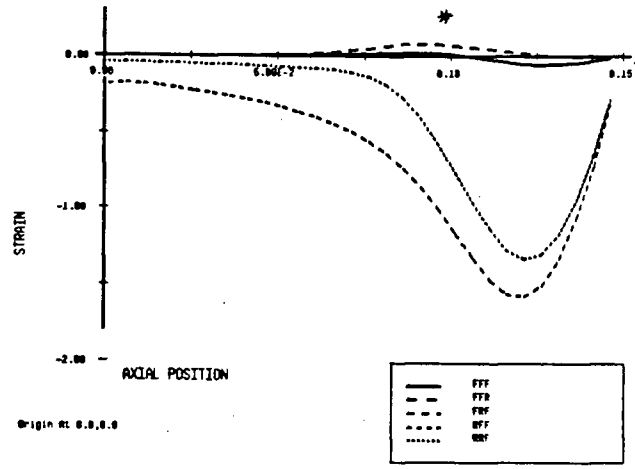

*: indicates the edge of the cuff on each curve

a. Radial nerve

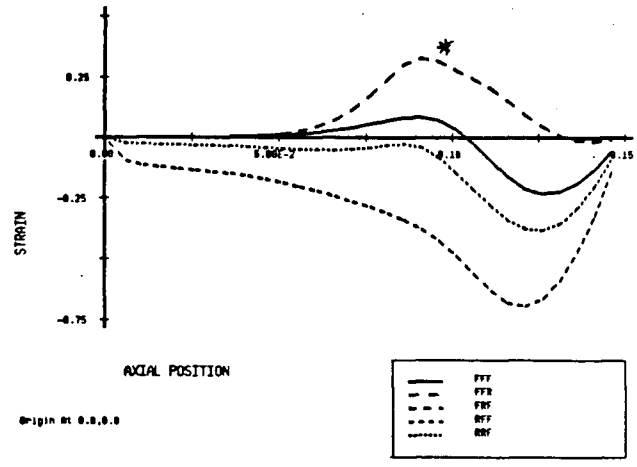

b. Musculocutaneous nerve

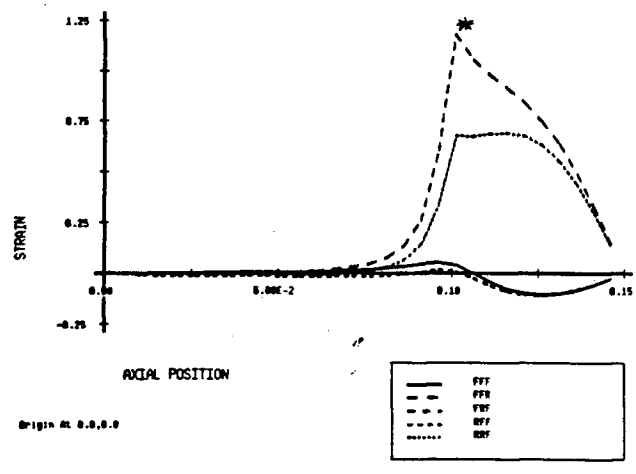

c. Median/ulnar nerves

Figure 5.23: **Predicted shear strain profiles for varying boundary condition setting at each nerve location (single-layer model)**

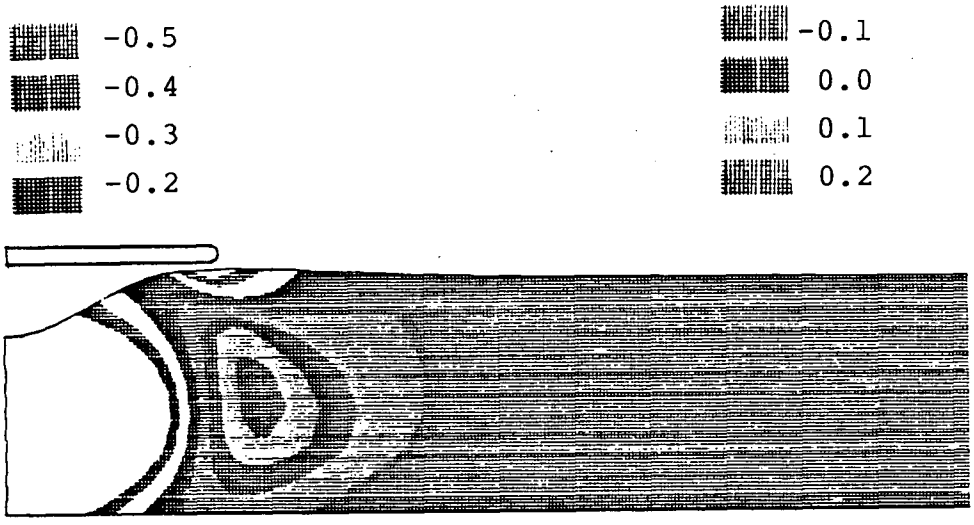

a. 5.0 cm cuff width

b. 10.0 cm cuff width

c. 15.0 cm cuff width

d. 20.0 cm cuff width

Figure 5.24: **Predicted axial strain profiles for varying cuff width (single-layer model)**

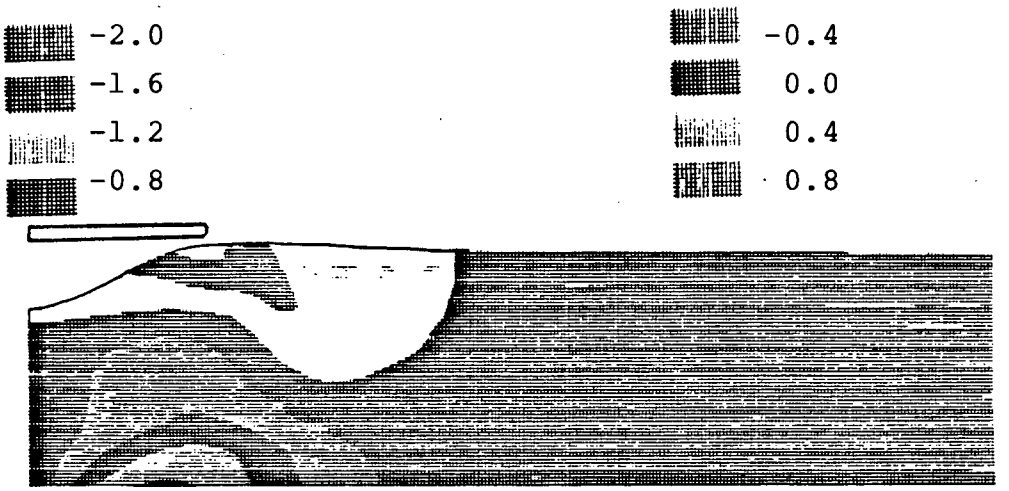

a. 5.0 cm cuff width

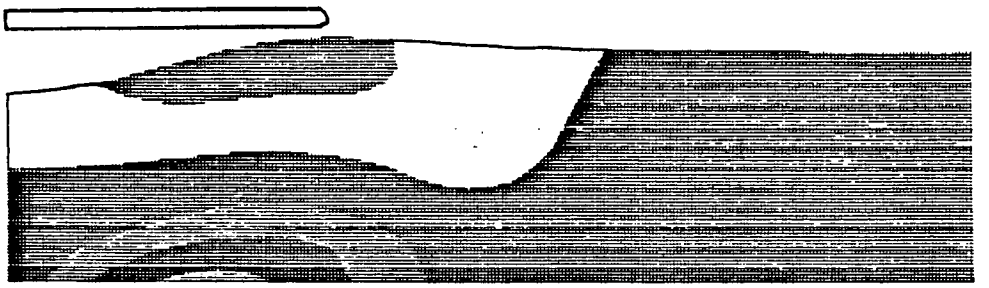

b. 10.0 cm cuff width

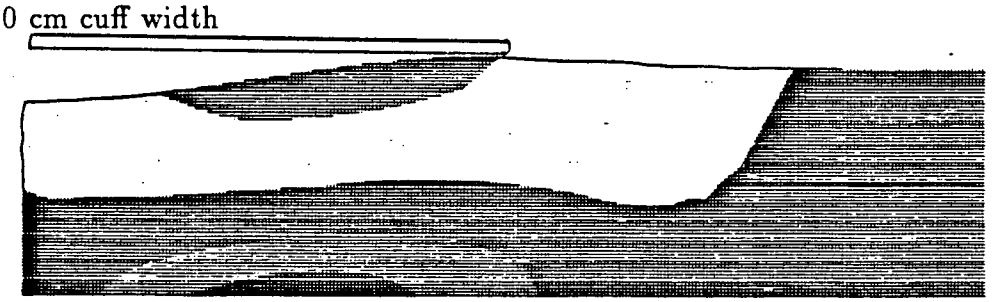

c. 15.0 cm cuff width

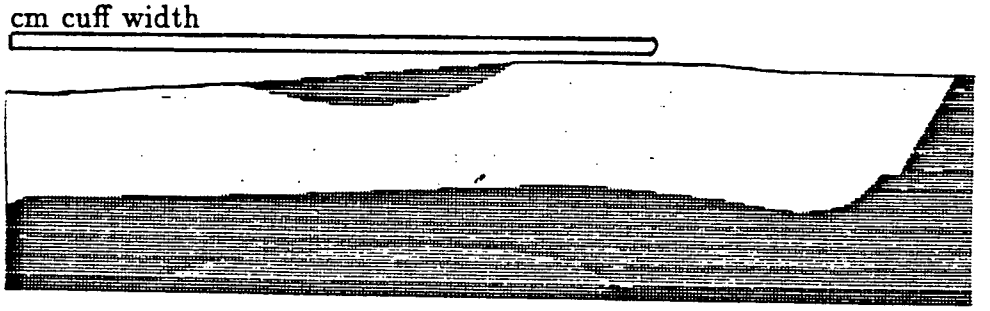

d. 20.0 cm cuff width

Figure 5.25: **Predicted shear strain profiles for varying cuff width (single-layer model)**

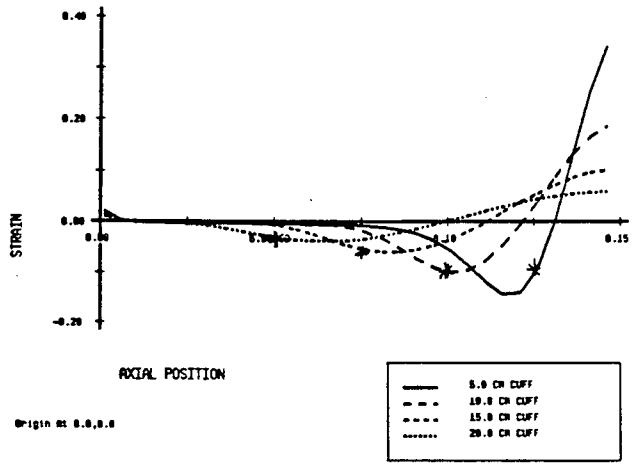

*: indicates the edge of the cuff on each curve

a. Radial nerve

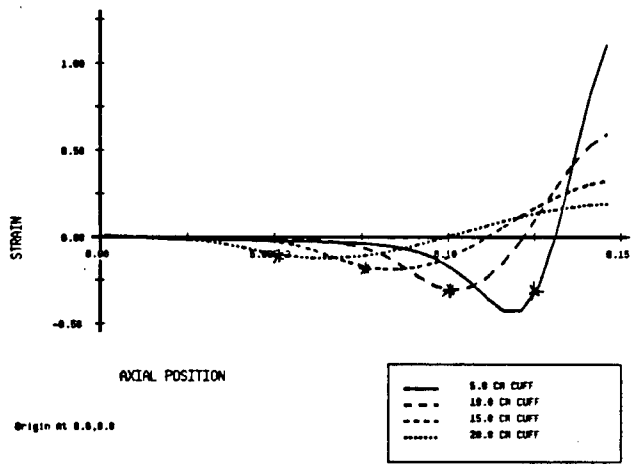

b. Musculocutaneous nerve

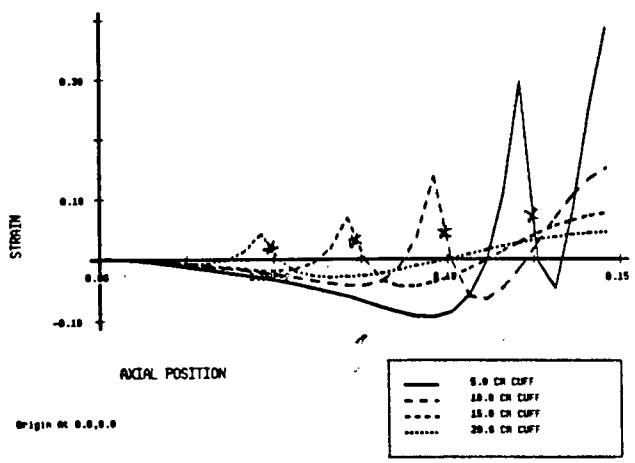

c. Median/ulnar nerves

Figure 5.26: **Predicted axial strain profiles for varying cuff width at each nerve location (single-layer model)**

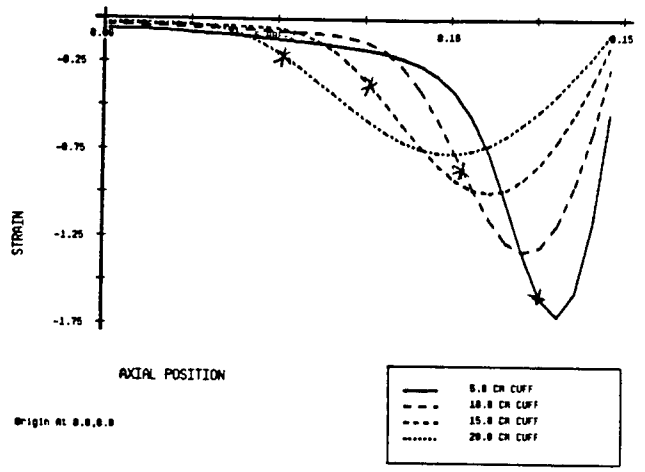

*: indicates the edge of the cuff on each curve

a. Radial nerve

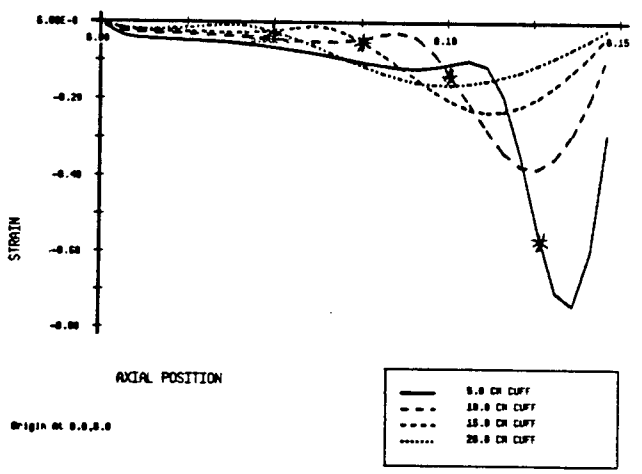

b. Musculocutaneous nerve

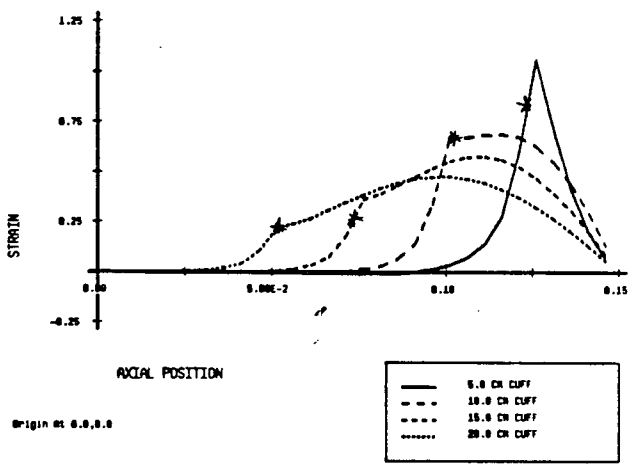

c. Median/ulnar nerves

Figure 5.27: **Predicted shear strain profiles for varying cuff width at each nerve location (single-layer model)**

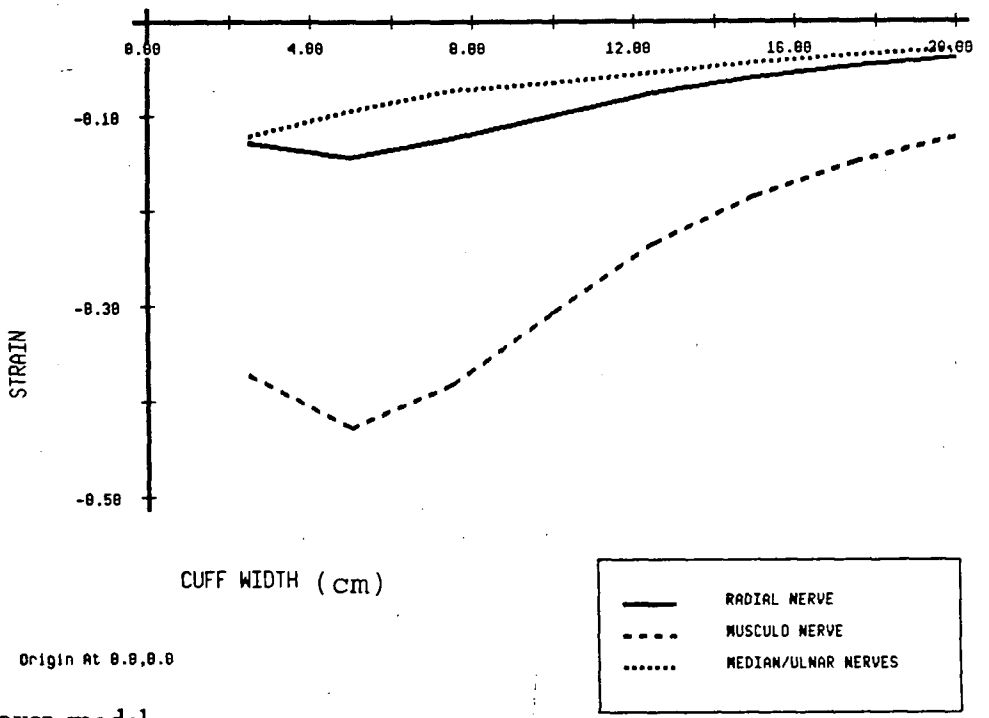

a. Single-layer model

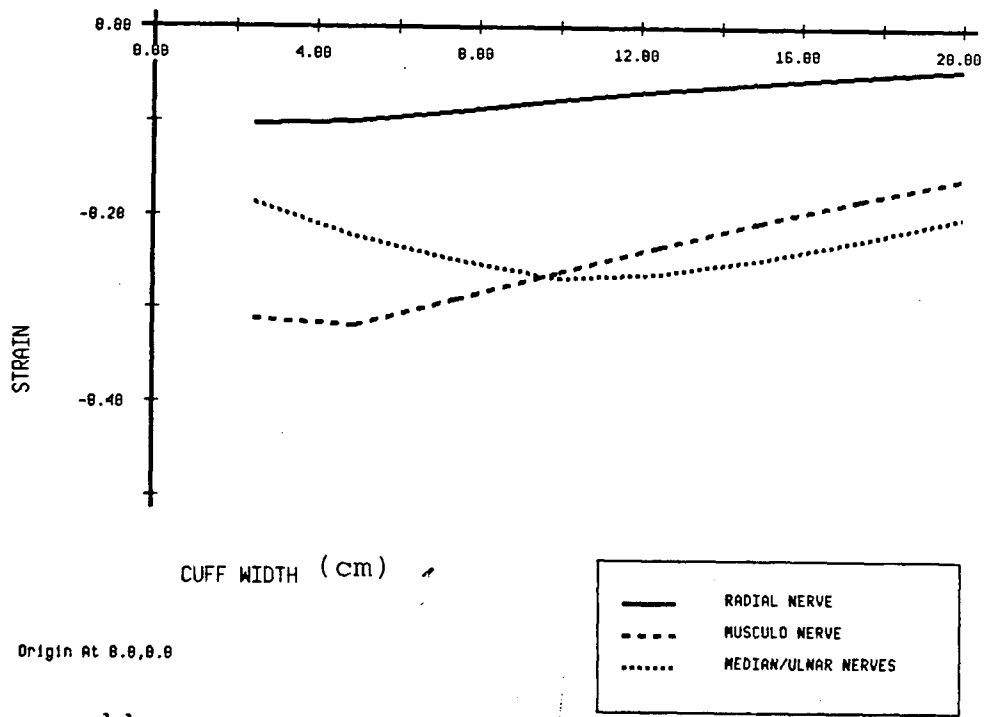

b. Multi-layer model

Figure 5.28: **Maximum axial strain intensities for varying cuff width**

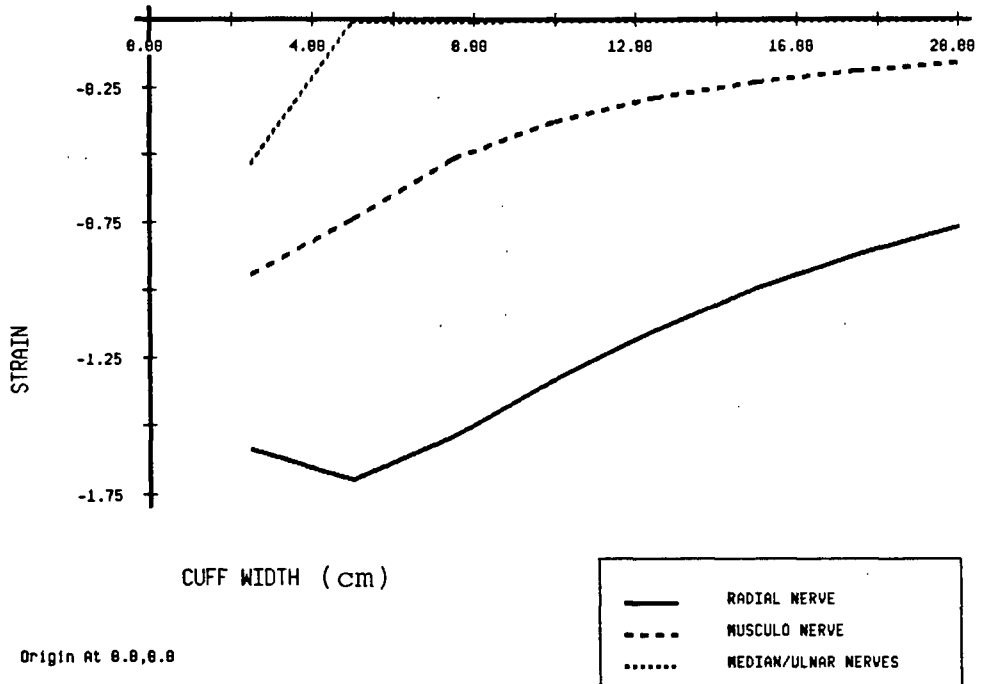

a. Single-layer model

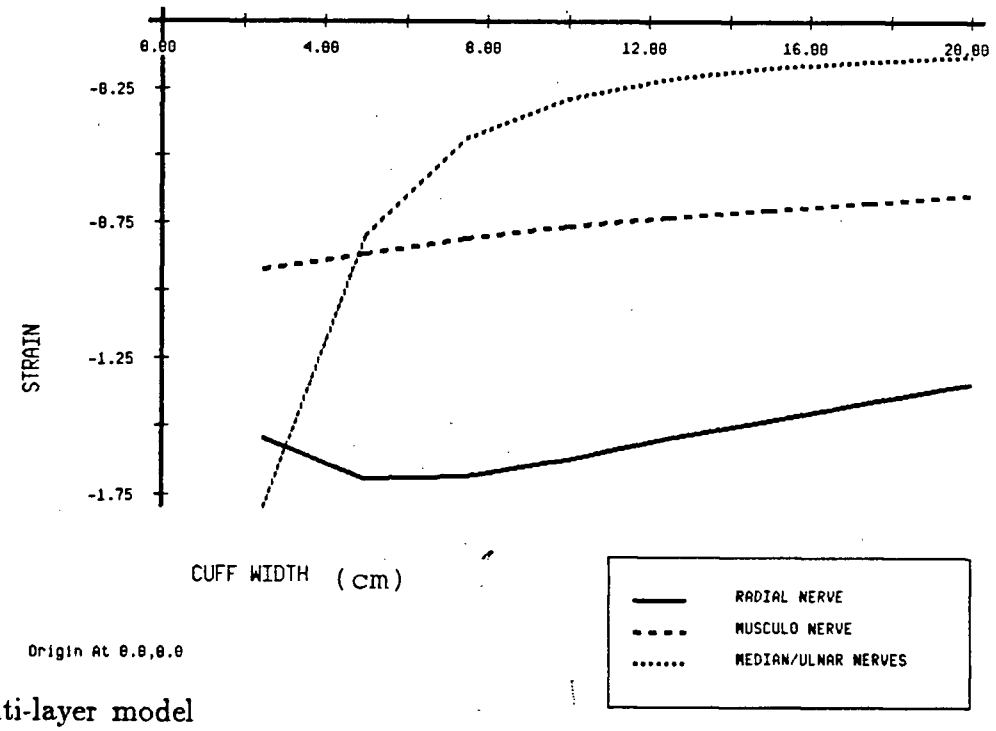

b. Multi-layer model

Figure 5.29: **Maximum shear strain intensities for varying cuff width**

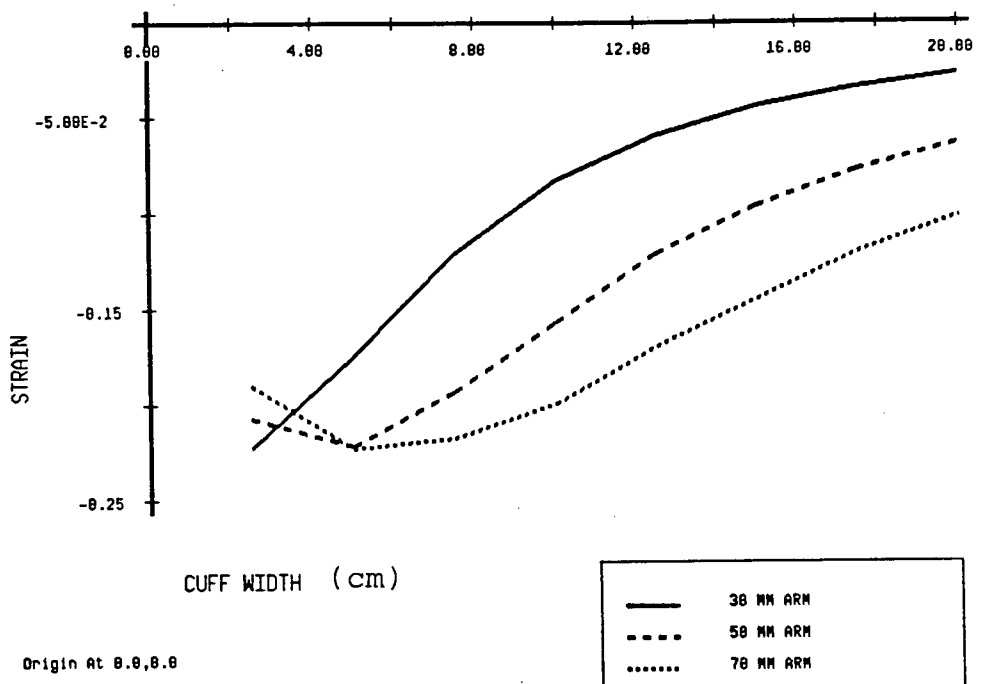

a. Single-layer model

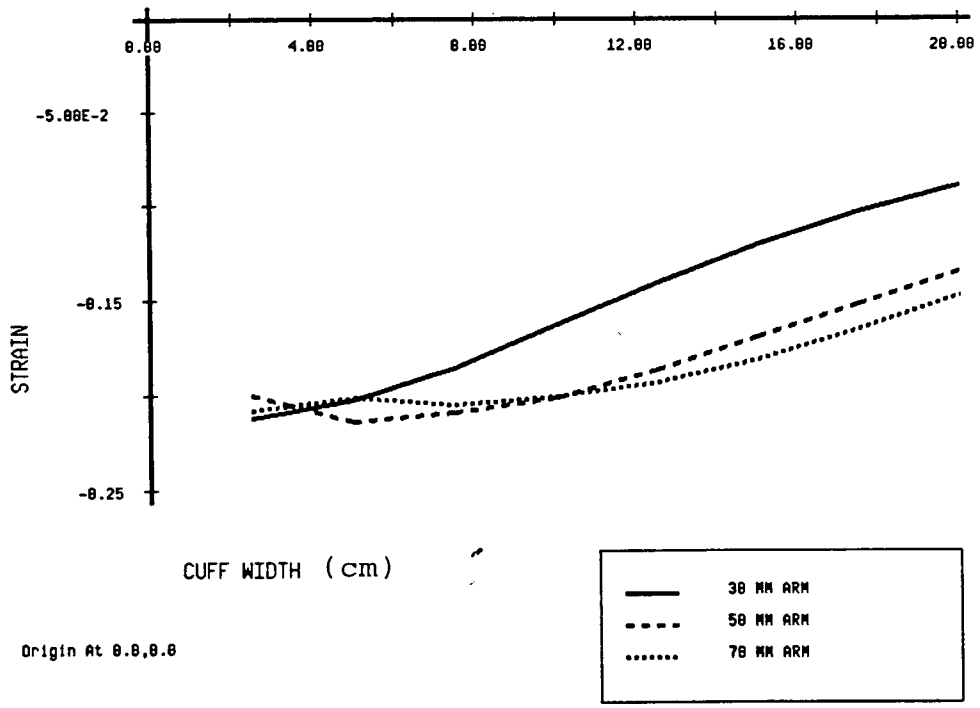

b. Multi-layer model

Figure 5.30: **Average maximum axial strain intensities for varying cuff width and limb radius**

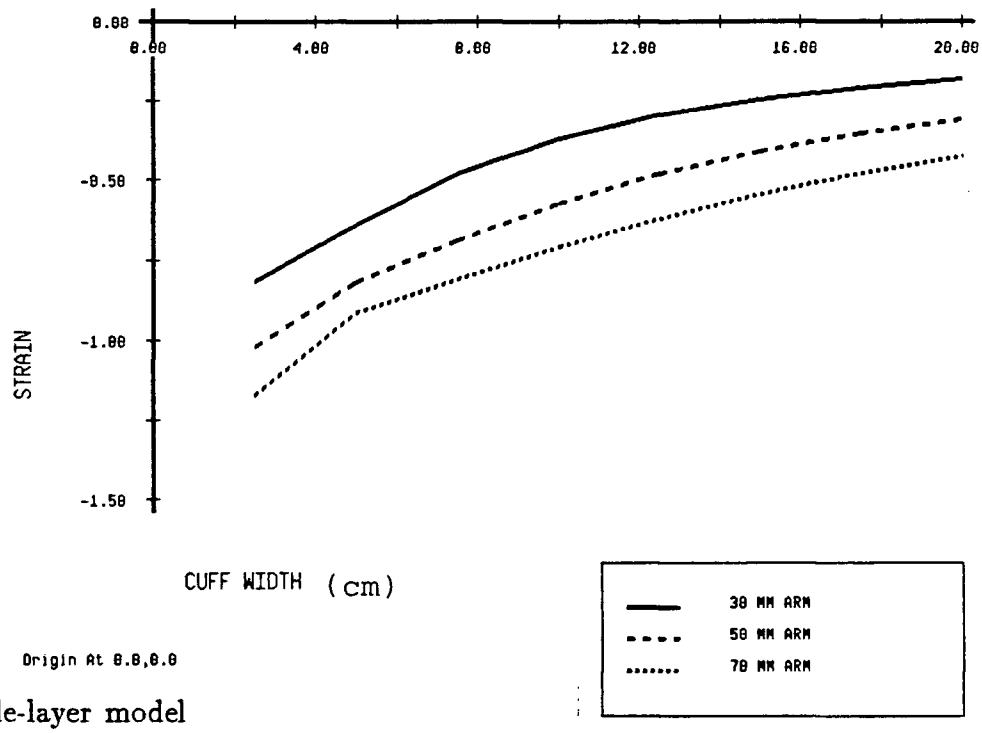

a. Single-layer model

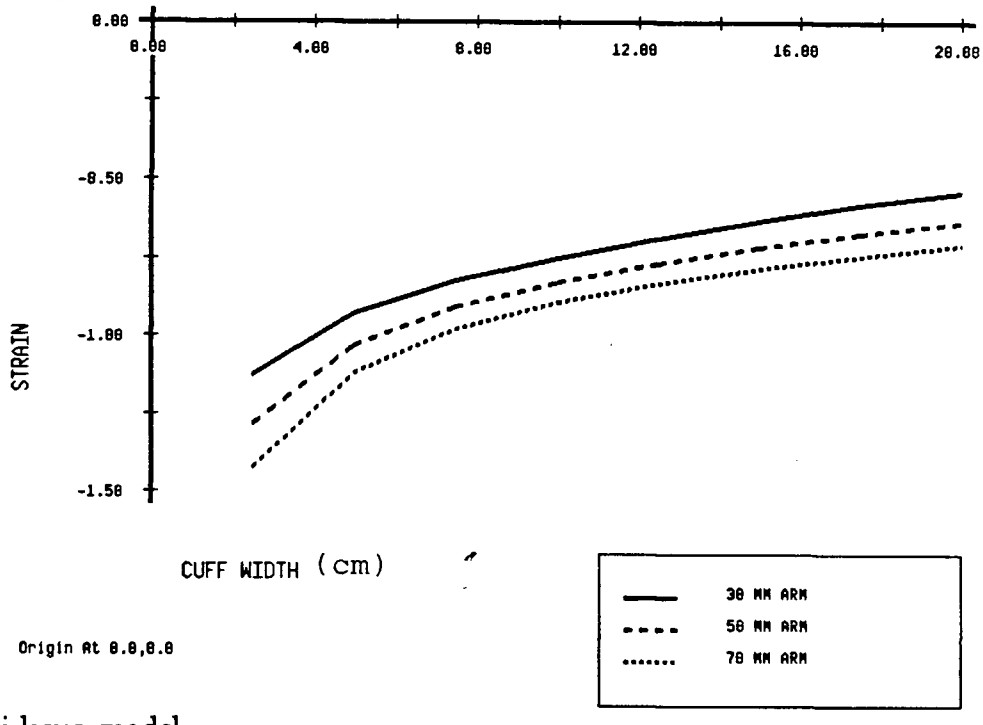

b. Multi-layer model

Figure 5.31: **Average maximum shear strain intensities for varying cuff width and limb radius**

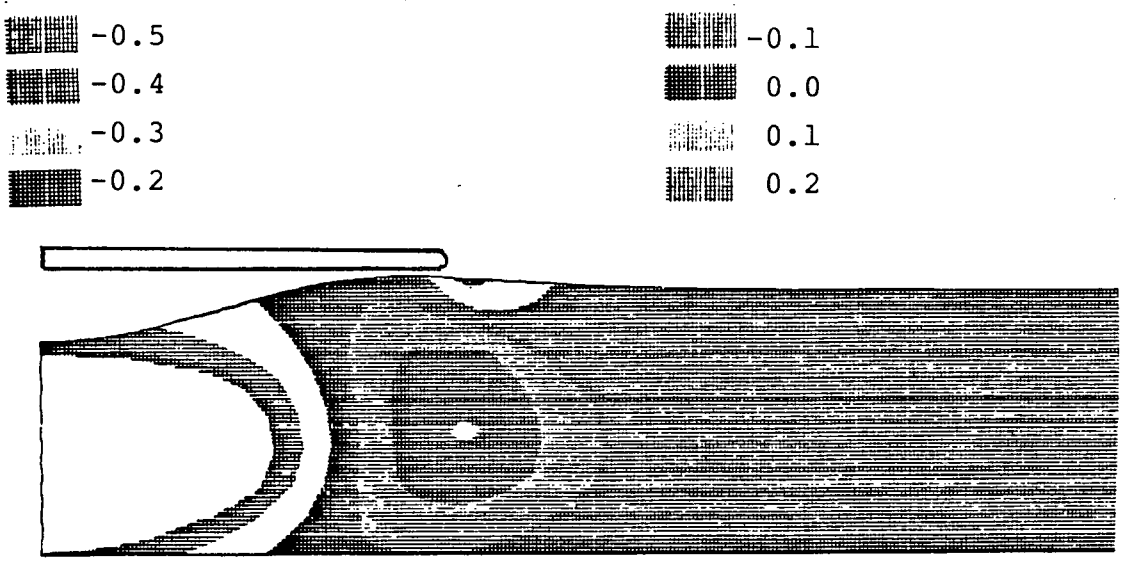

a. Sinusoidal pressure profile

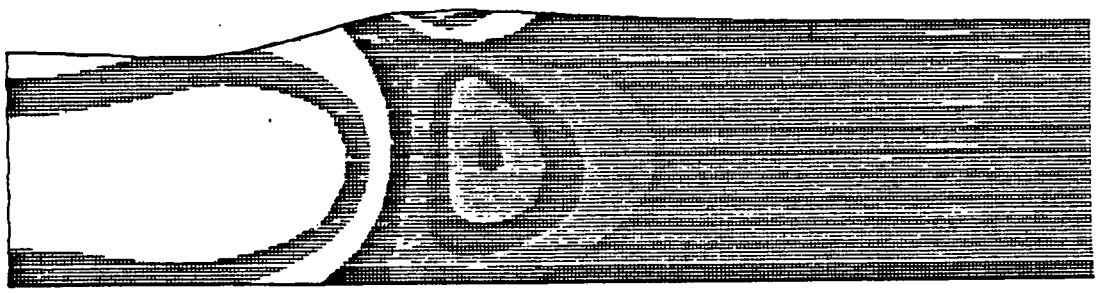

b. Exponential pressure profile

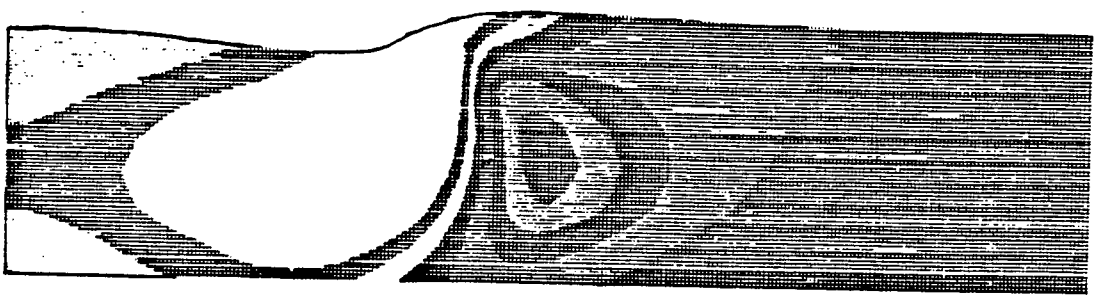

c. Rectangular pressure profile

Figure 5.32: **Predicted axial strain profiles for varying surface pressure profile (single-layer model)**

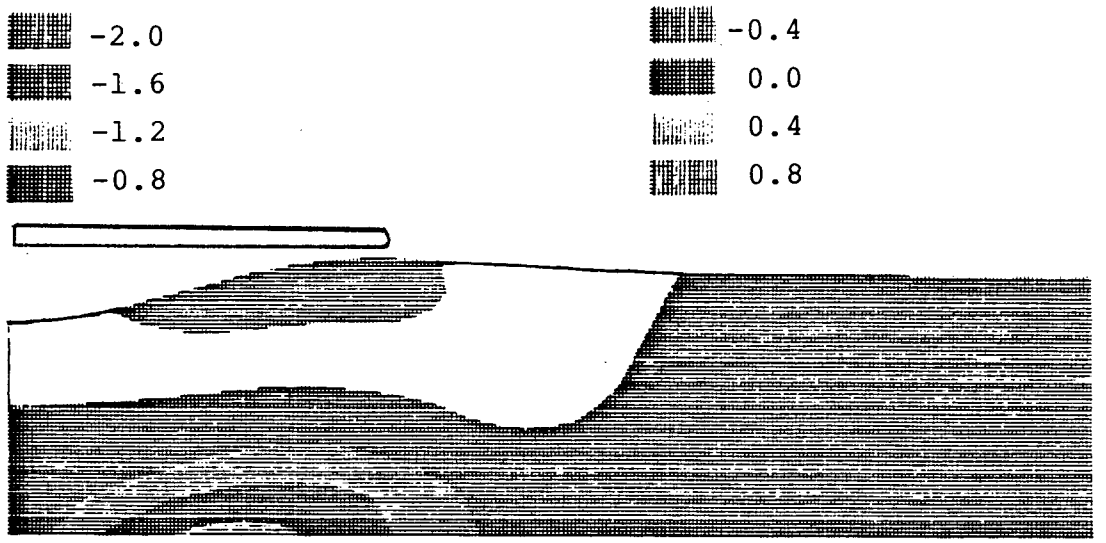

a. Sinusoidal pressure profile

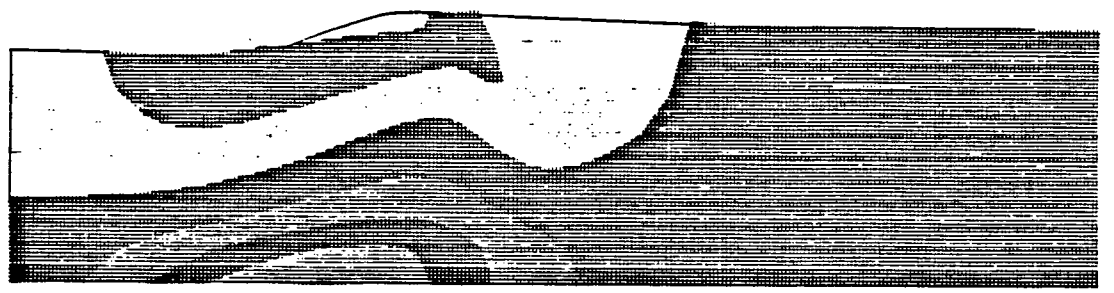

b. Exponential pressure profile

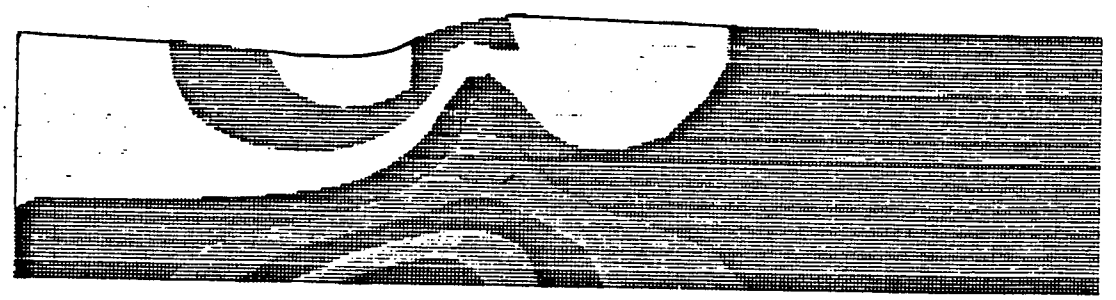

c. Rectangular pressure profile

Figure 5.33: **Predicted shear strain profiles for varying surface pressure profile (single-layer model)**

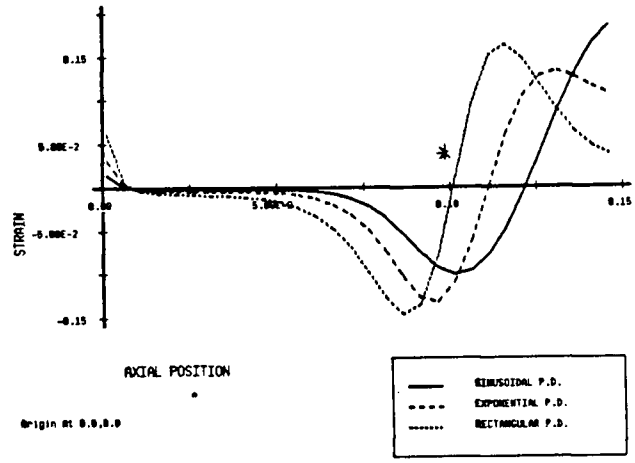

*: indicates the edge of the cuff on each curve

a. Radial nerve

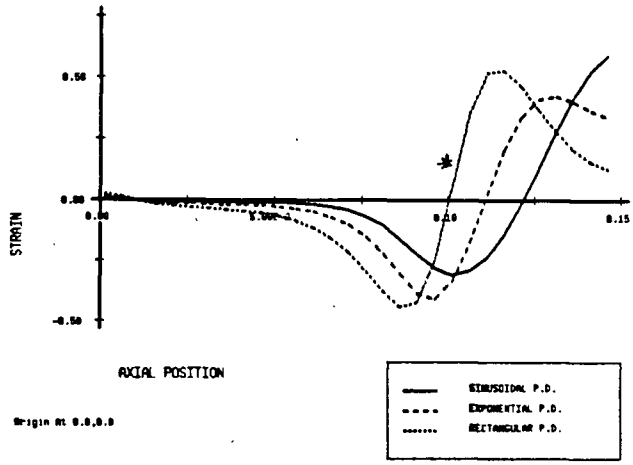

b. Musculocutaneous nerve

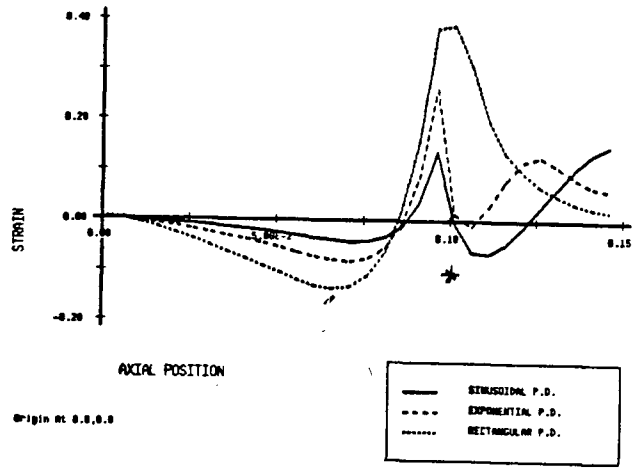

c. Median/ulnar nerves

Figure 5.34: **Predicted axial strain profiles for varying surface pressure profile at each nerve location (single-layer model)**

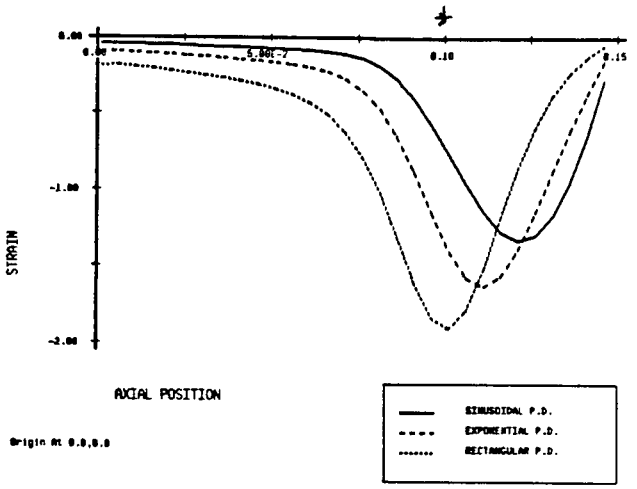

*: indicates the edge of the cuff on each curve

a. Radial nerve

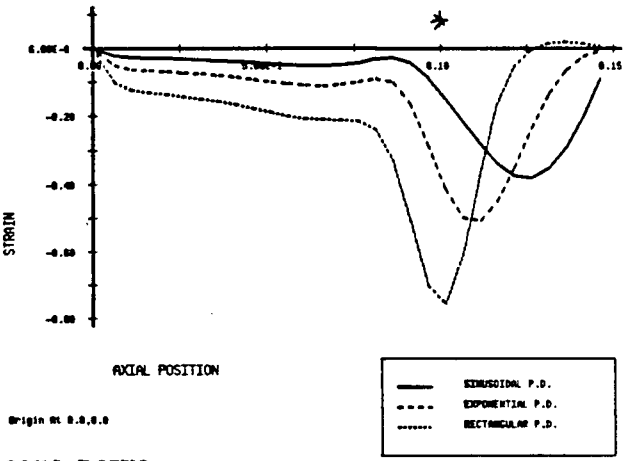

b. Musculocutaneous nerve

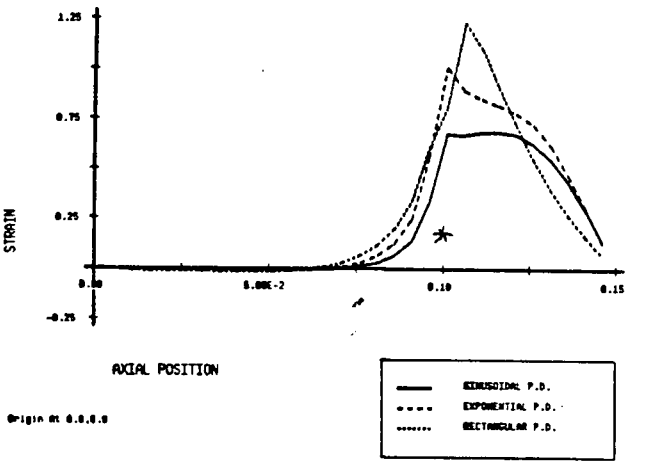

c. Median/ulnar nerves

Figure 5.35: **Predicted shear strain profiles for varying surface pressure profile at each nerve location single-layer model)**

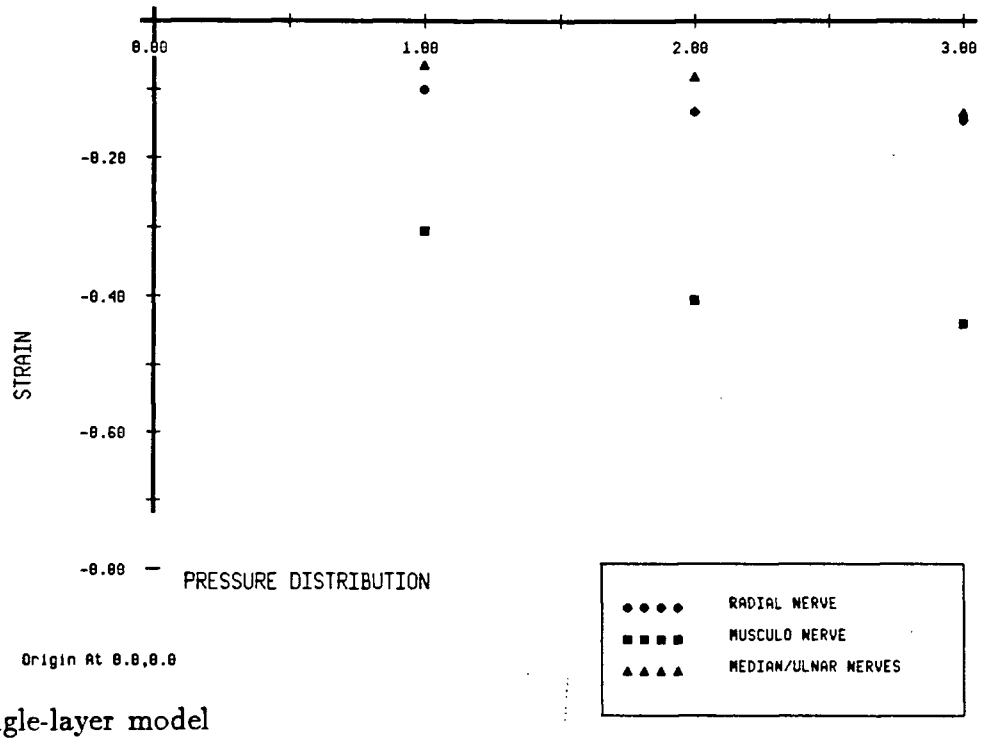

a. Single-layer model

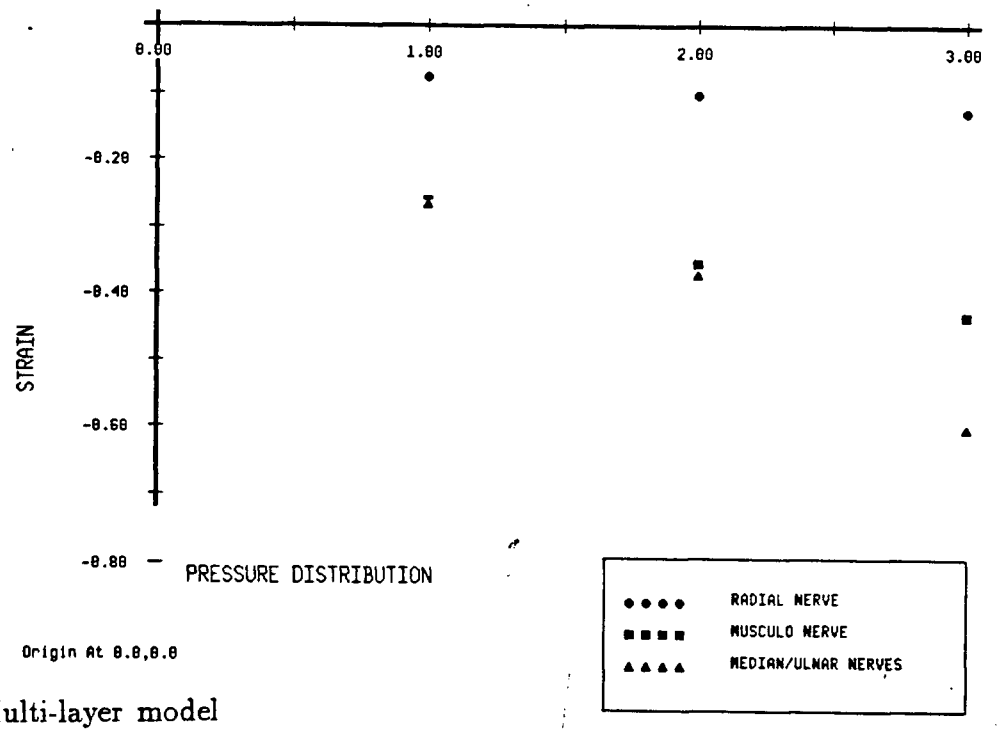

b. Multi-layer model

Figure 5.36: **Maximum axial strain intensities for varying surface pressure distribution**

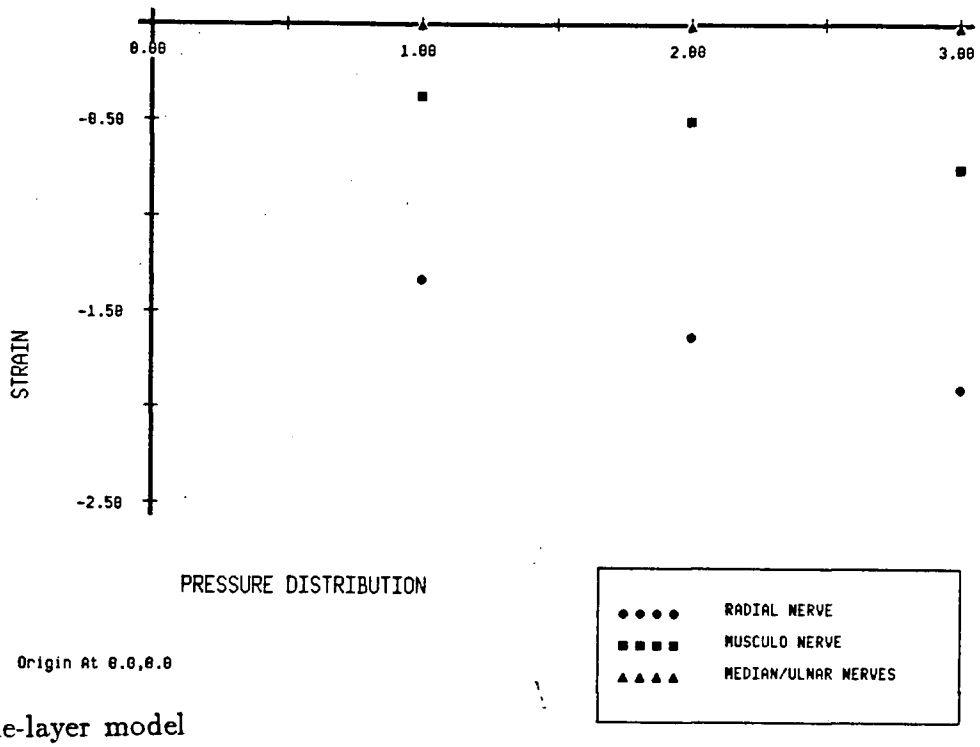

a. Single-layer model

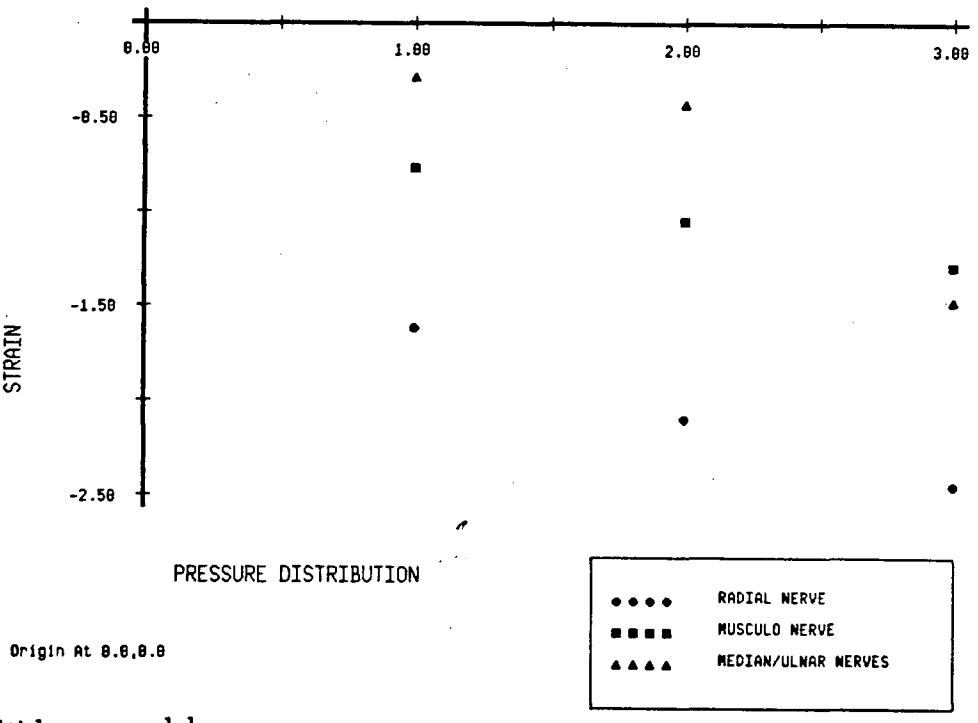

b. Multi-layer model

Figure 5.37: **Maximum shear strain intensities for varying surface pressure distribution**

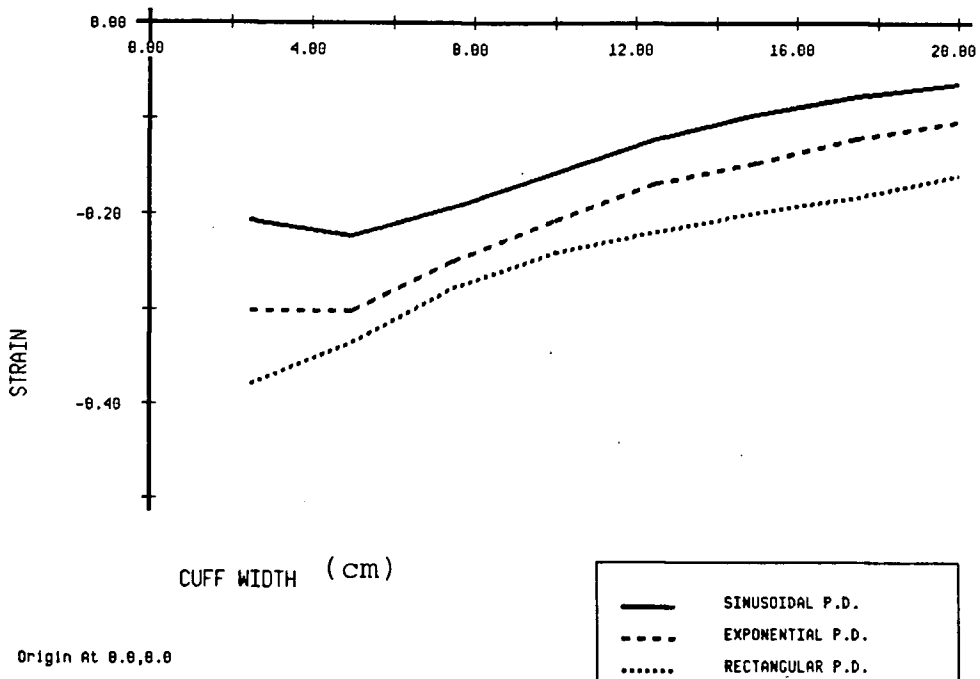

a. Single-layer model

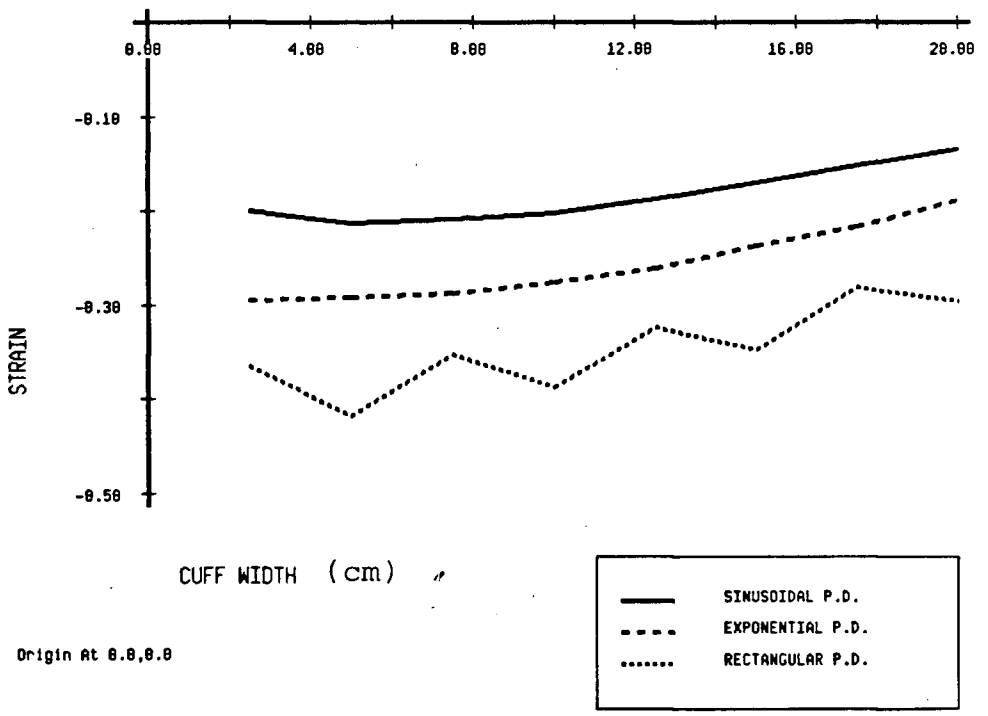

b. Multi-layer model

Figure 5.38: **Average maximum axial strain intensities for varying surface pressure distribution and cuff width**

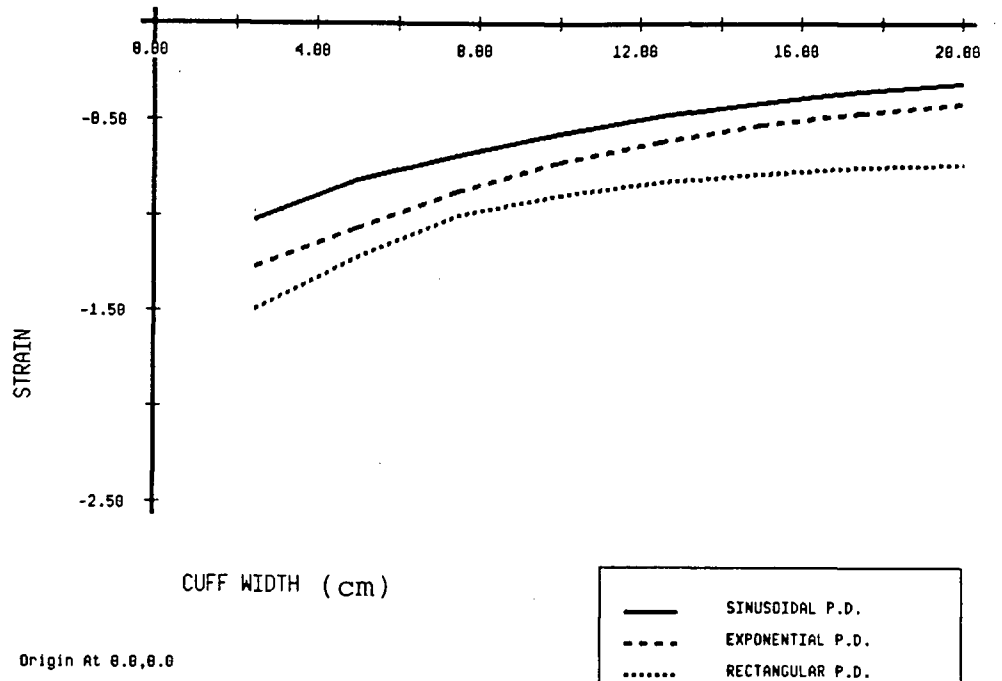

a. Single-layer model

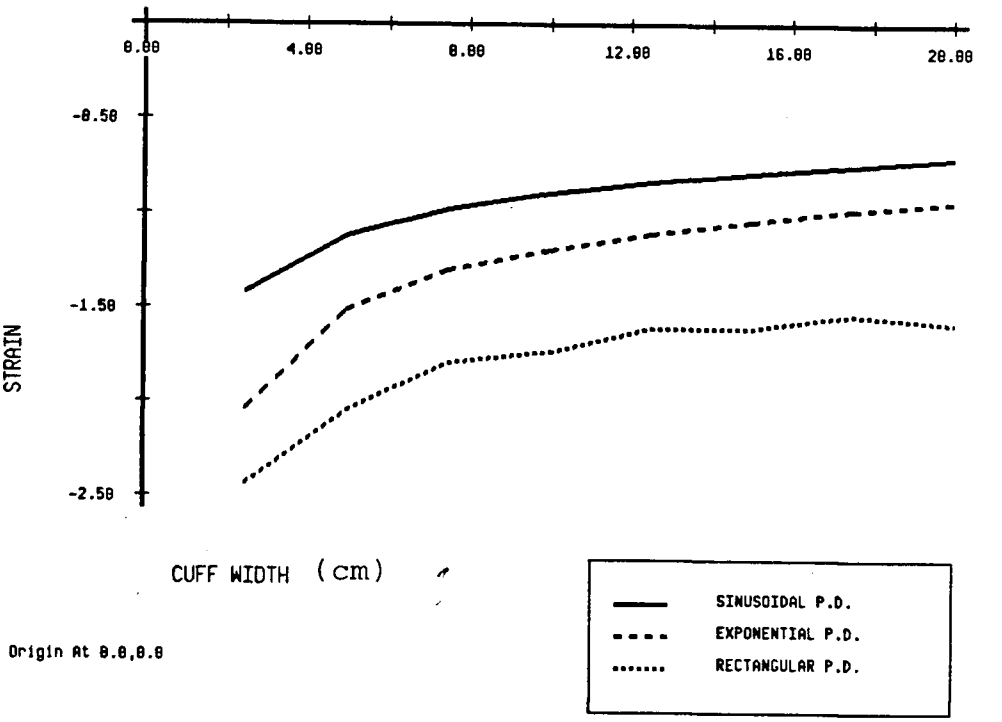

b. Multi-layer model

Figure 5.39: **Average maximum shear strain intensities for varying surface pressure distribution and cuff width**

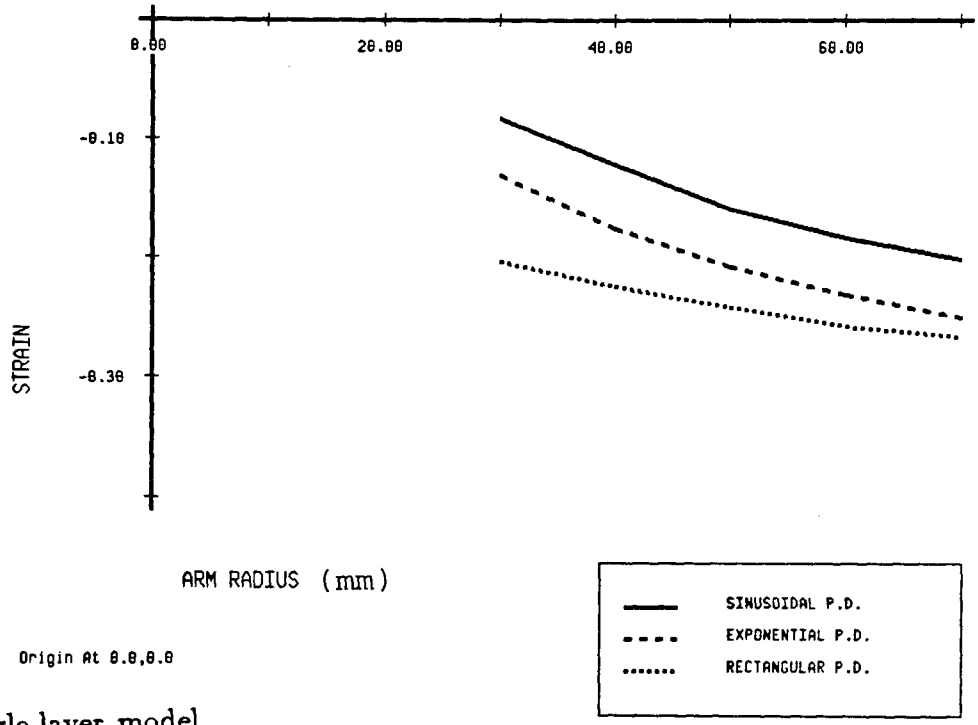

a. Single-layer model

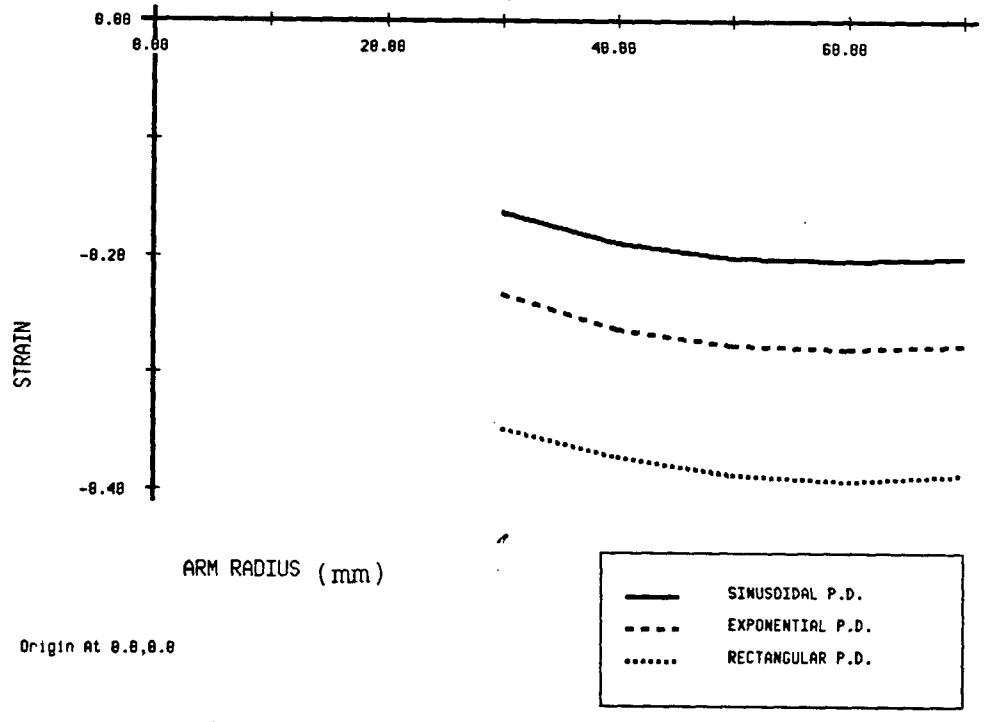

b. Multi-layer model

Figure 5.40: **Average maximum axial strain intensities for varying surface pressure distribution and limb radius**

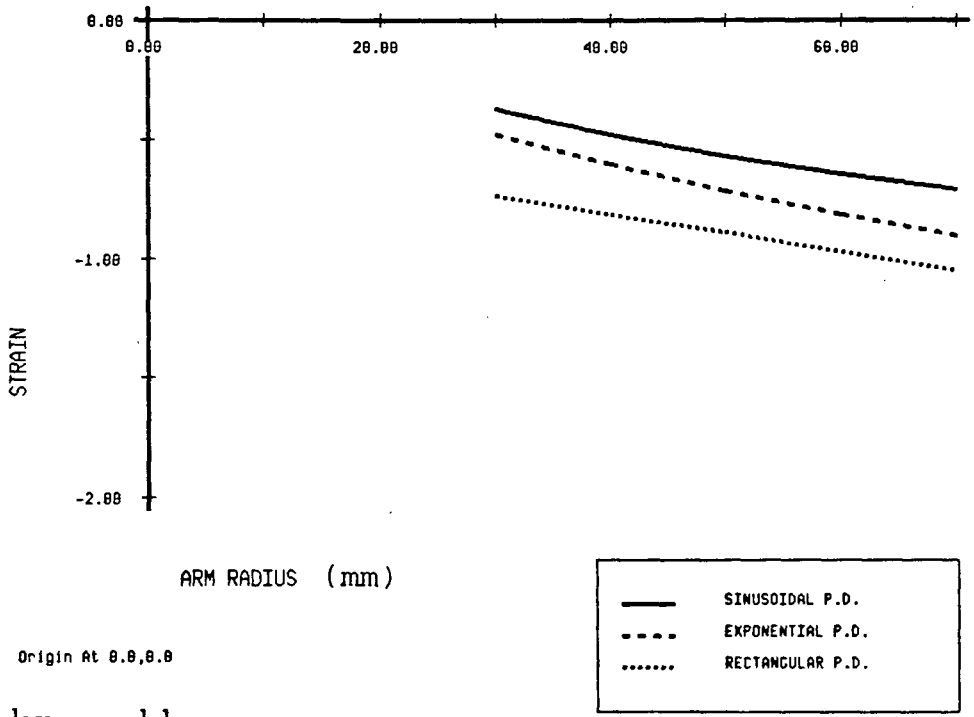

a. Single-layer model

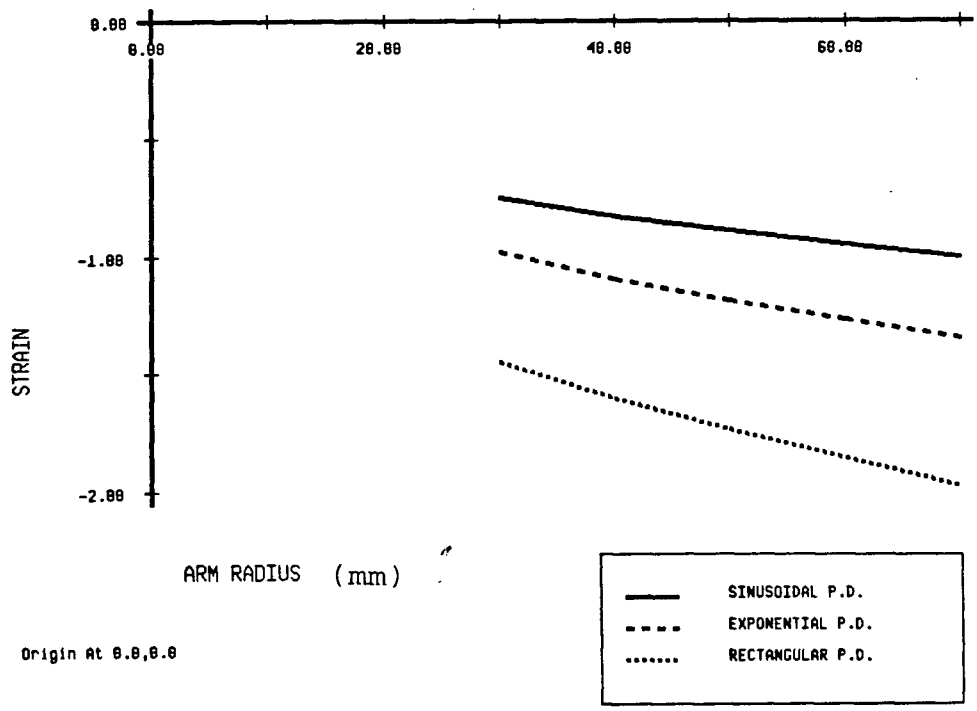

b. Multi-layer model

Figure 5.41: **Average maximum shear strain intensities for varying surface pressure distribution and limb radius**

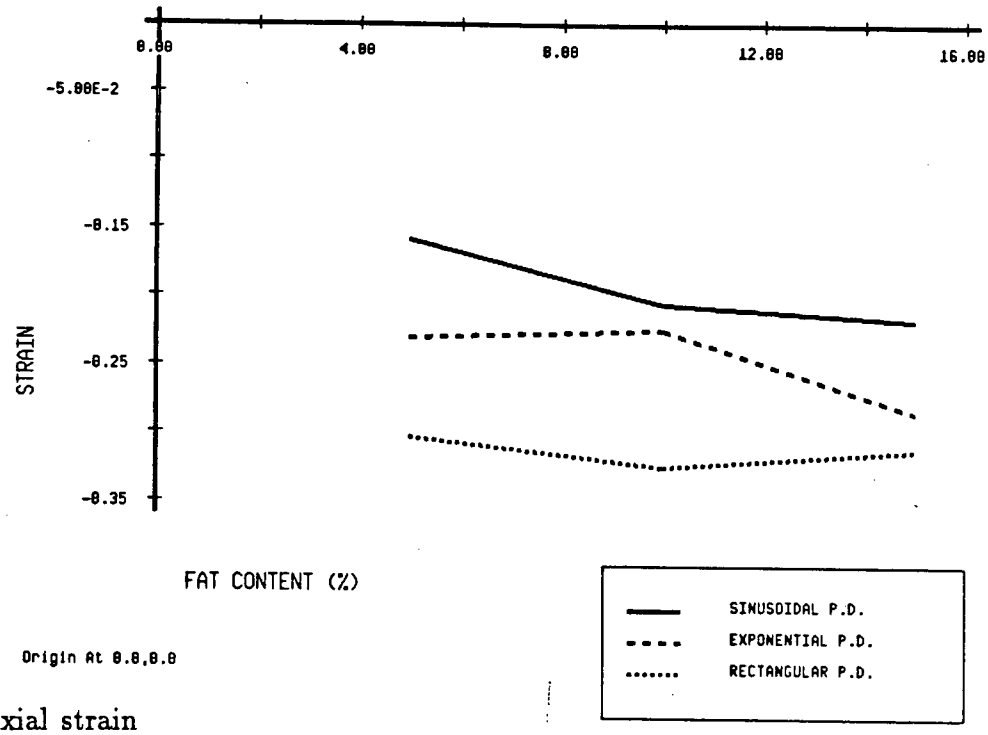

a. Axial strain

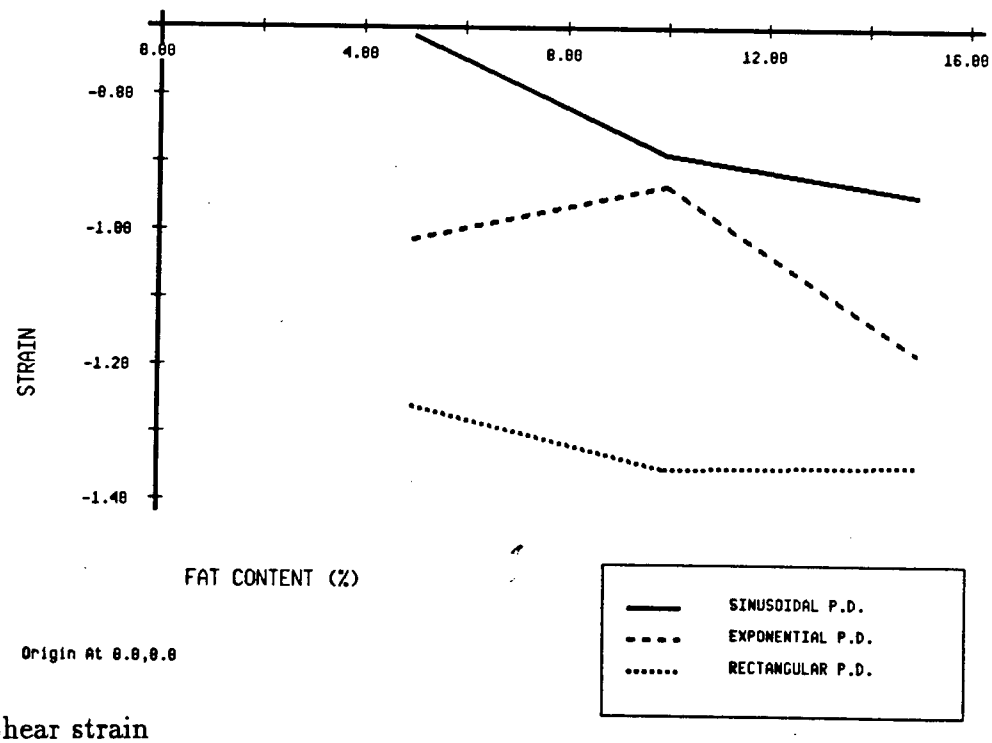

b. Shear strain

Figure 5.42: **Average maximum strain intensities for varying surface pressure distribution and fat content (multi-layer model)**

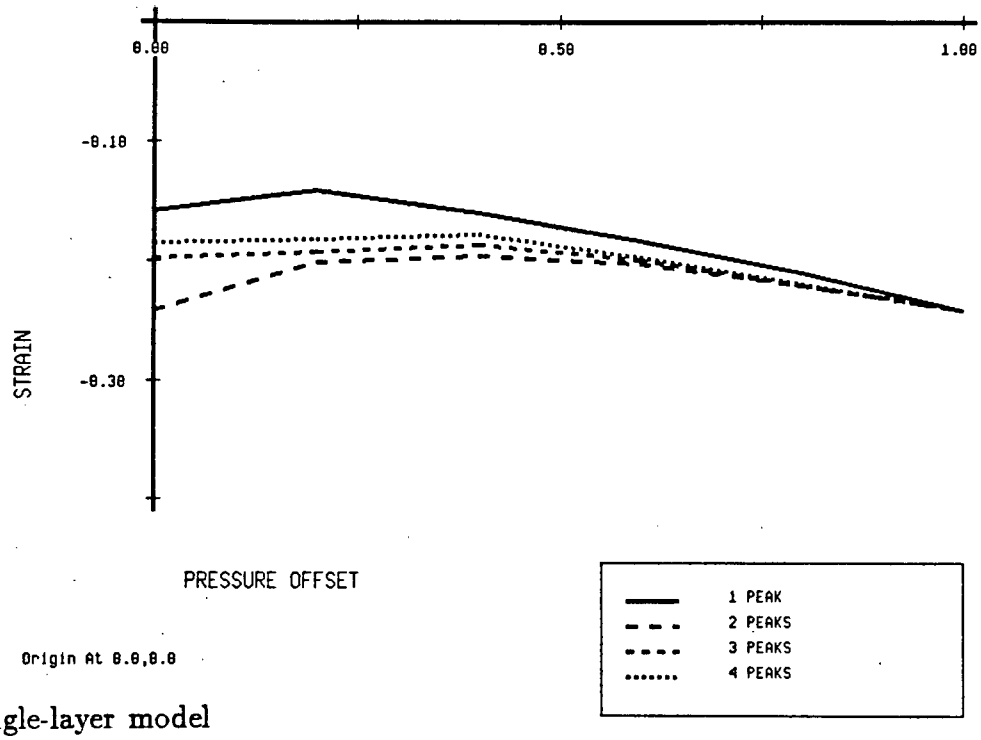

a. Single-layer model

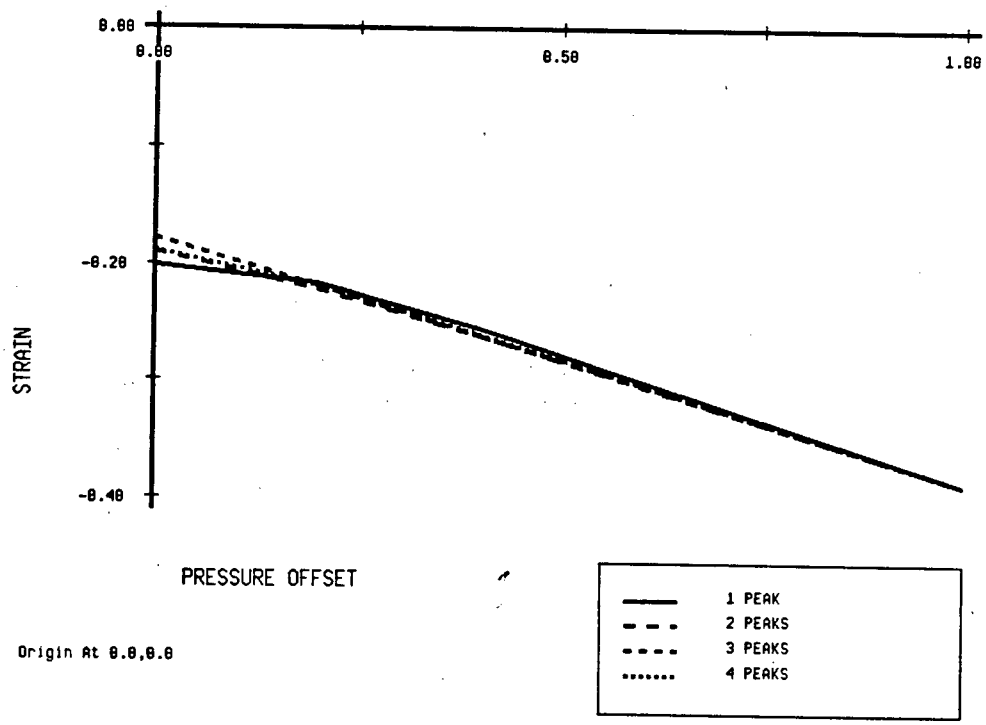

b. Multi-layer model

Figure 5.43: **Average maximum axial strain intensities for varying pressure offset (sinusoidal pressure distribution)**

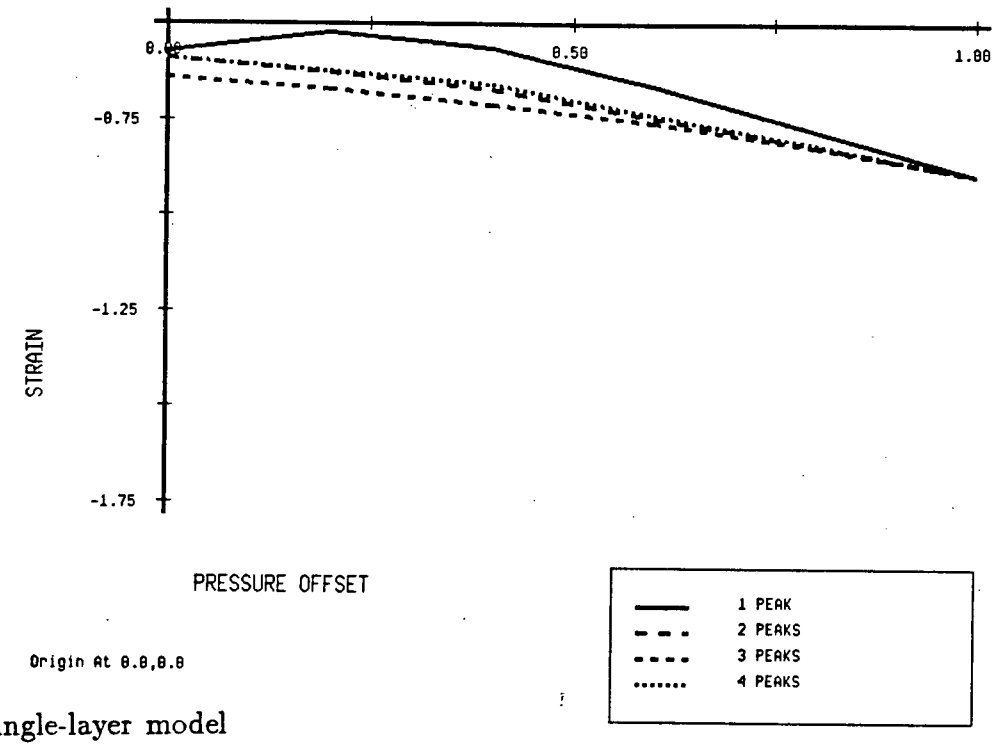

a. Single-layer model

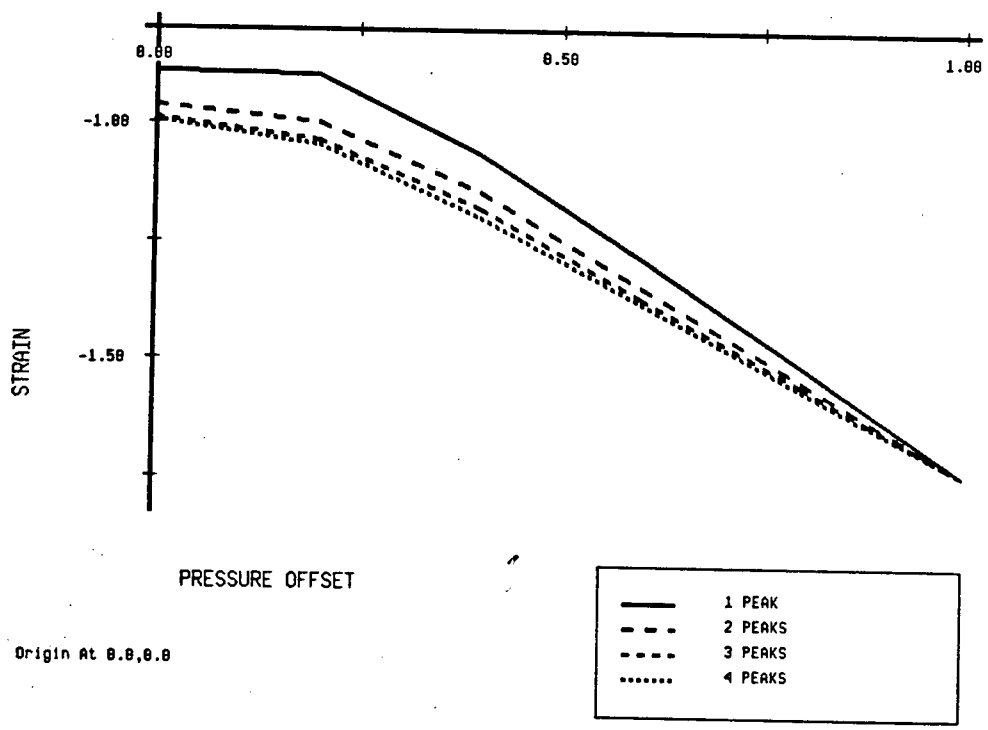

b. Multi-layer model

Figure 5.44: **Average maximum shear strain intensities for varying pressure offset (sinusoidal pressure distribution)**

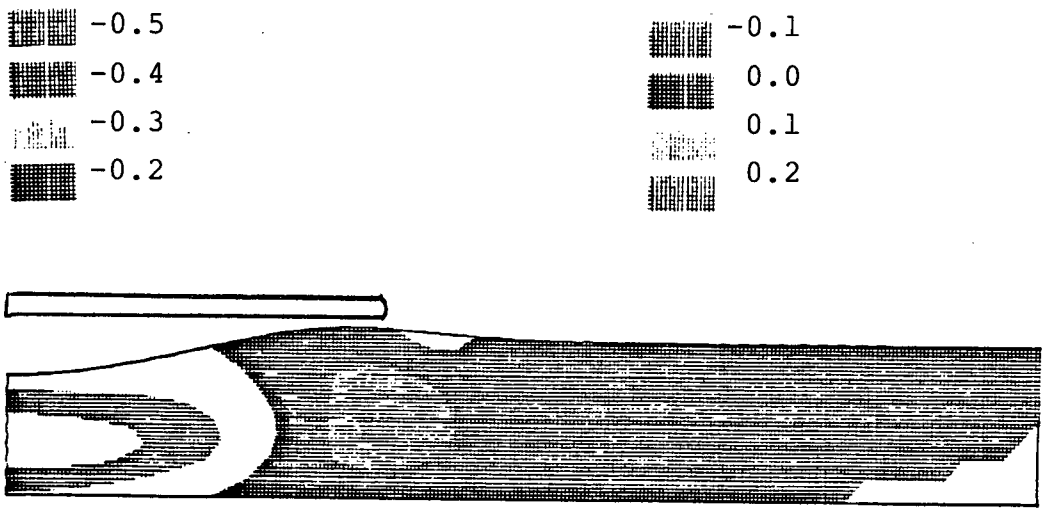

a. 30 mm limb radius

b. 50 mm limb radius

c. 70 mm limb radius

Figure 5.45: **Predicted axial strain profiles for varying limb radius (single-layer model)**

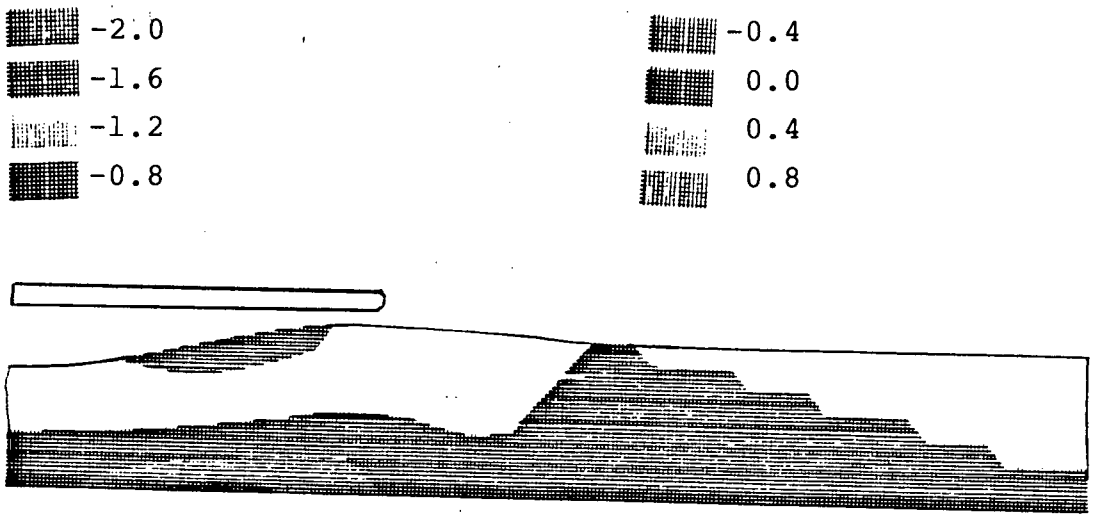

a. 30 mm limb radius

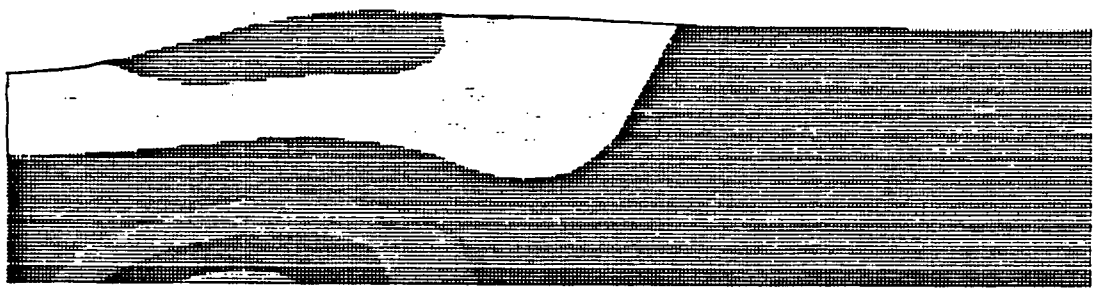

b. 50 mm limb radius

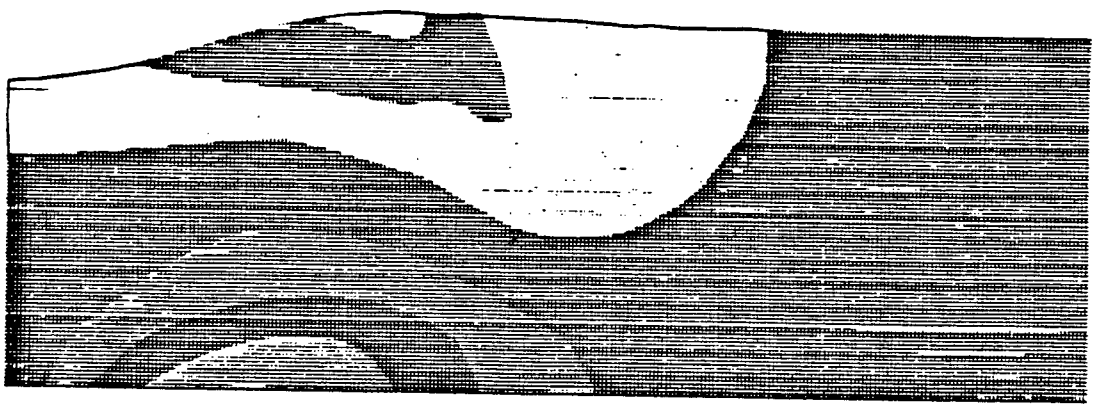

c. 70 mm limb radius

Figure 5.46: **Predicted shear strain profiles for varying limb radius (single-layer model)**

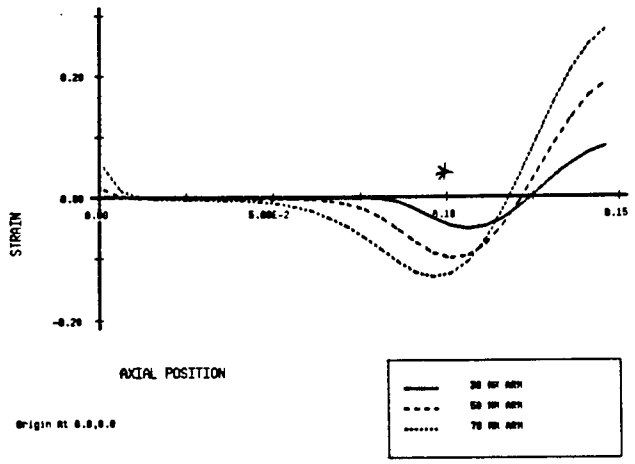

*: indicates the edge of the cuff on each curve

a. Radial nerve

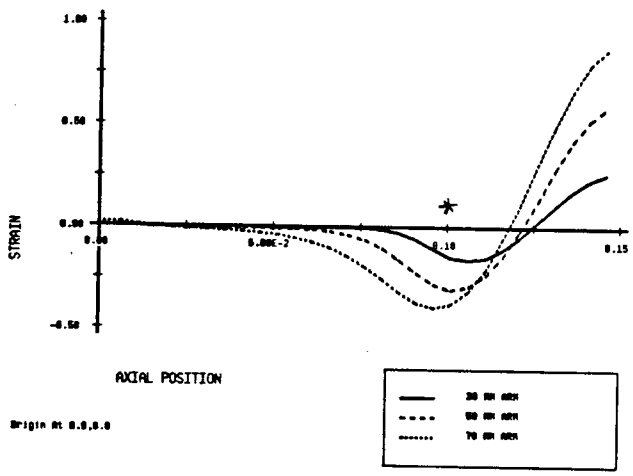

b. Musculocutaneous nerve

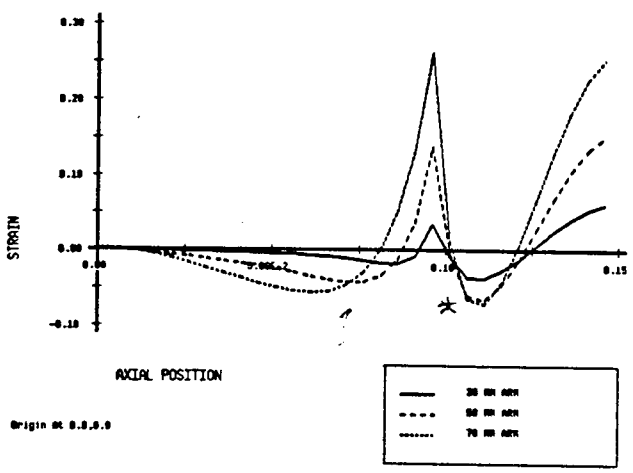

c. Median/ulnar nerves

Figure 5.47: **Predicted axial strain profiles for varying limb radius at each nerve location (single-layer model)**

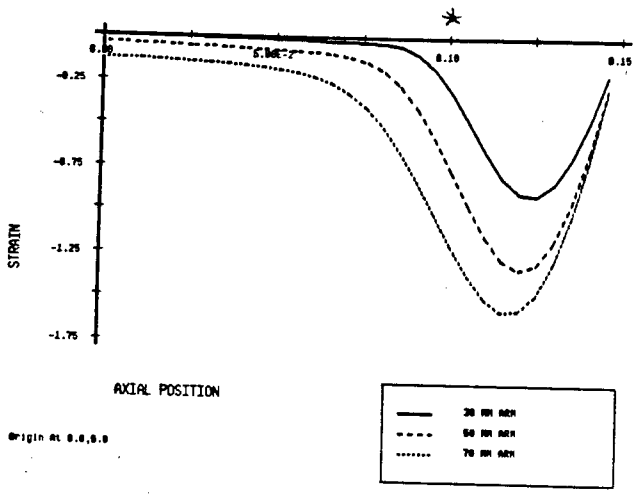

*: indicates the edge of the cuff on each curve

a. Radial nerve

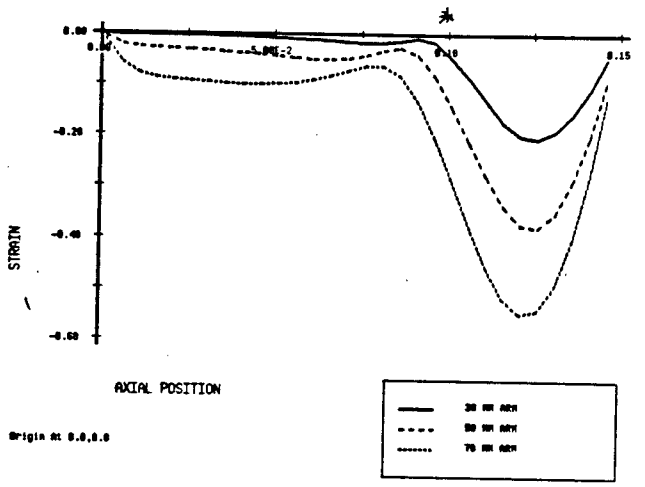

b. Musculocutaneous nerve

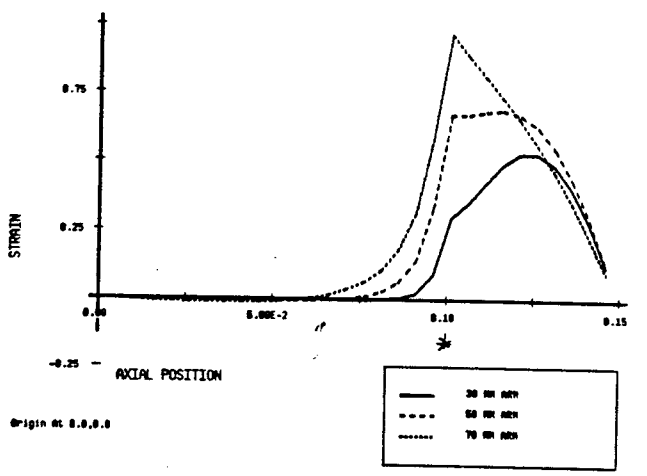

c. Median/ulnar nerves

Figure 5.48: **Predicted shear strain profiles for varying limb radius at each nerve location (single-layer model)**

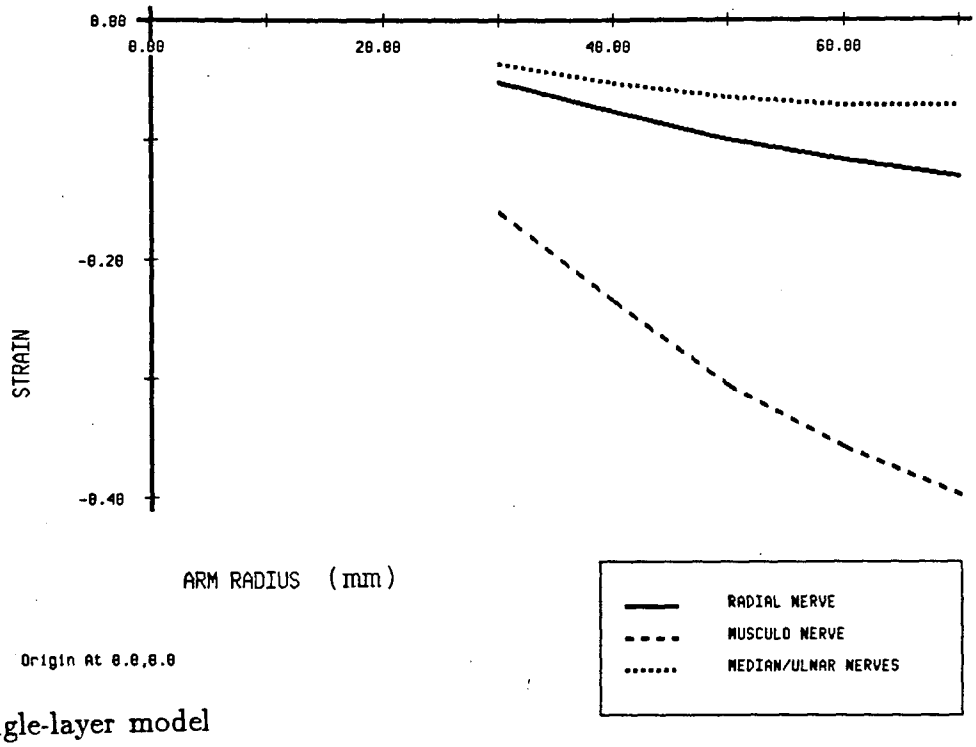

a. Single-layer model

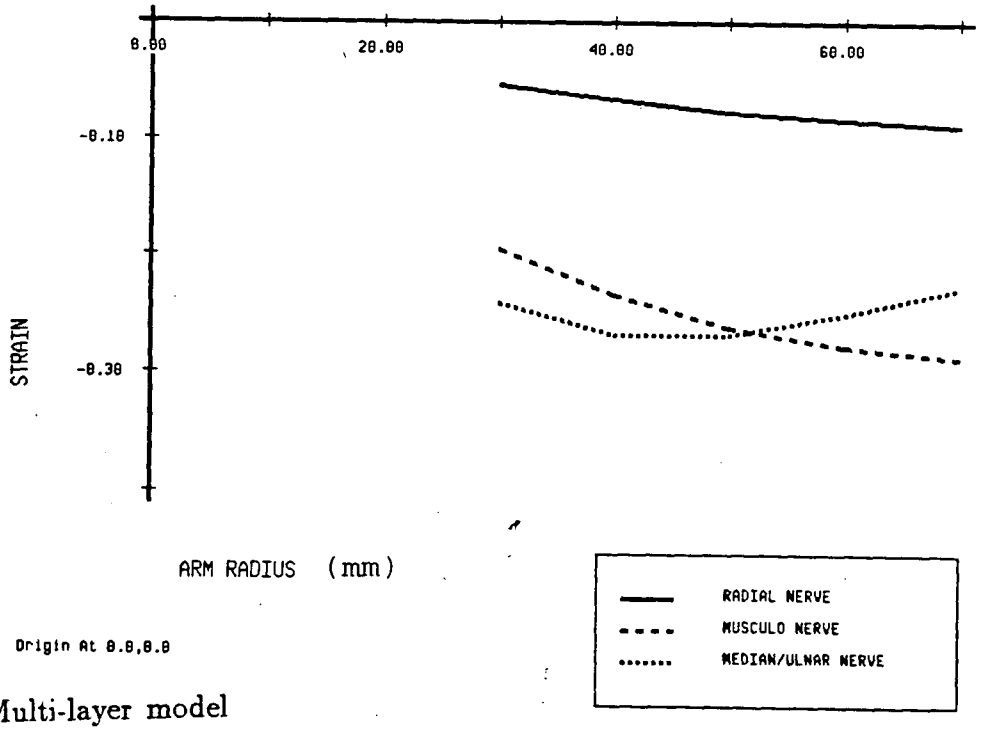

b. Multi-layer model

Figure 5.49: **Maximum axial strain intensities for varying limb radius**

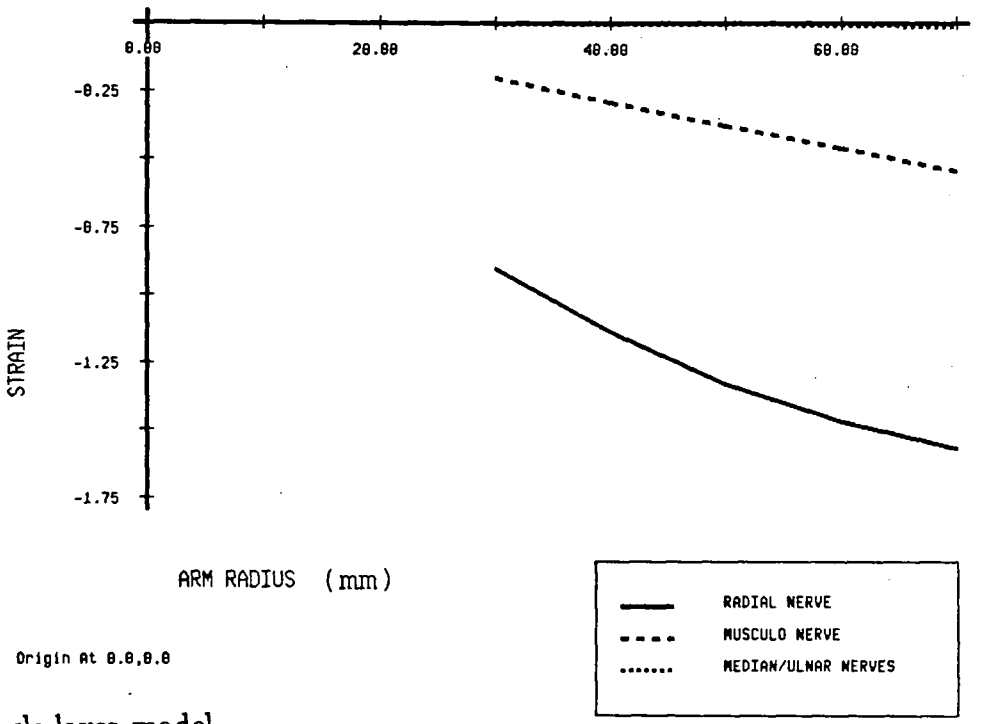

a. Single-layer model

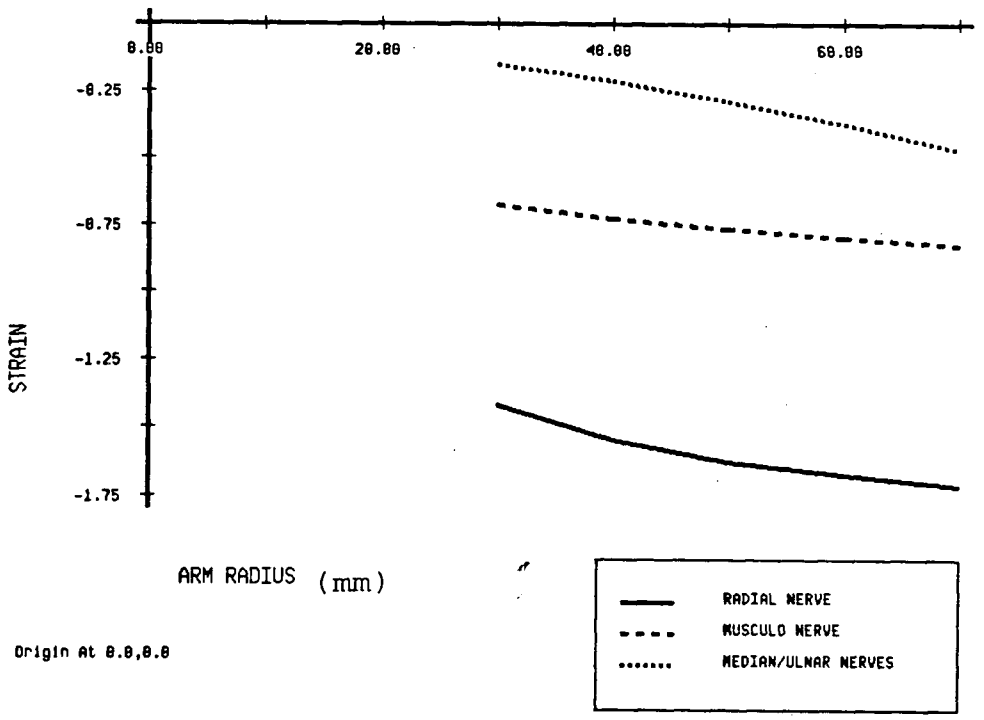

b. Multi-layer model

Figure 5.50: **Maximum shear strain intensities for varying limb radius**

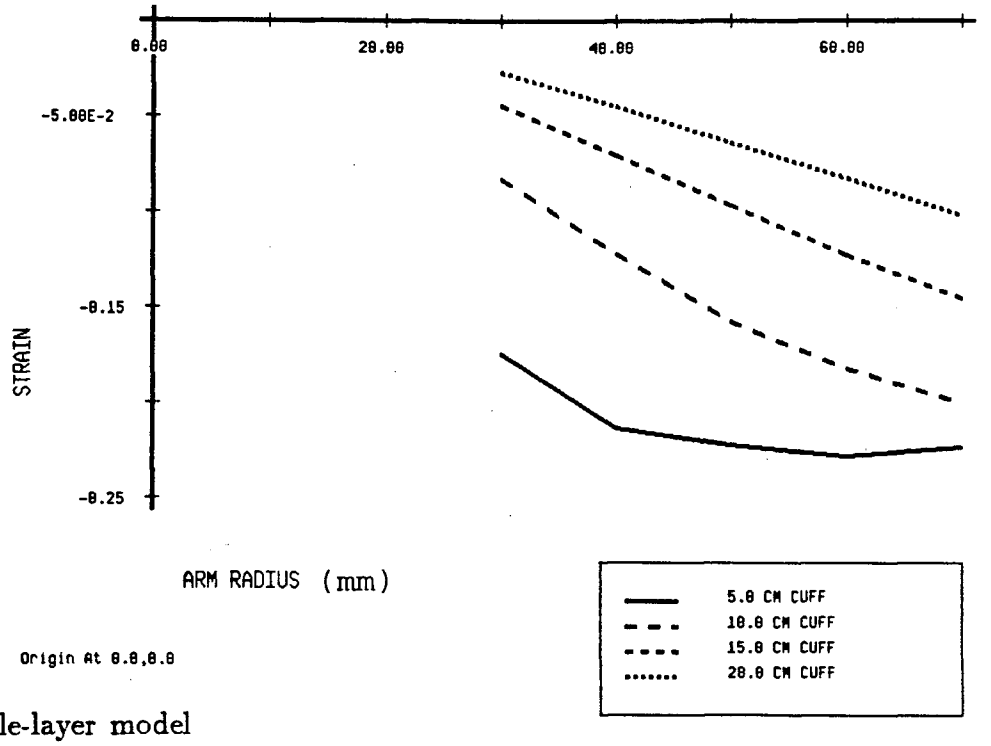

a. Single-layer model

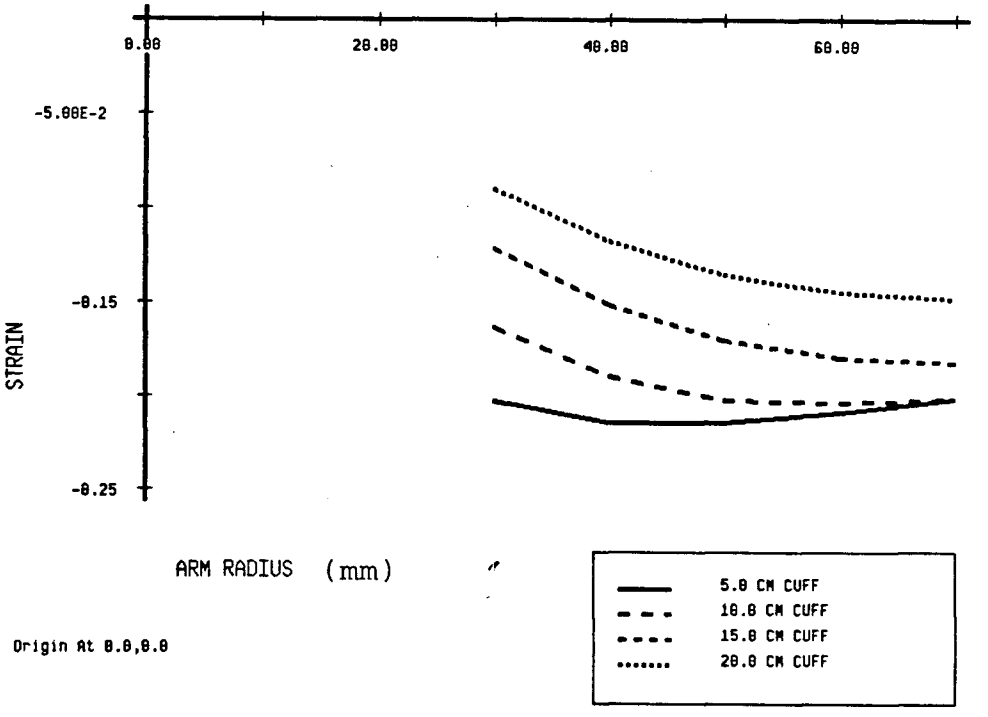

b. Multi-layer model

Figure 5.51: **Average maximum axial strain intensities for varying limb radius and cuff width**

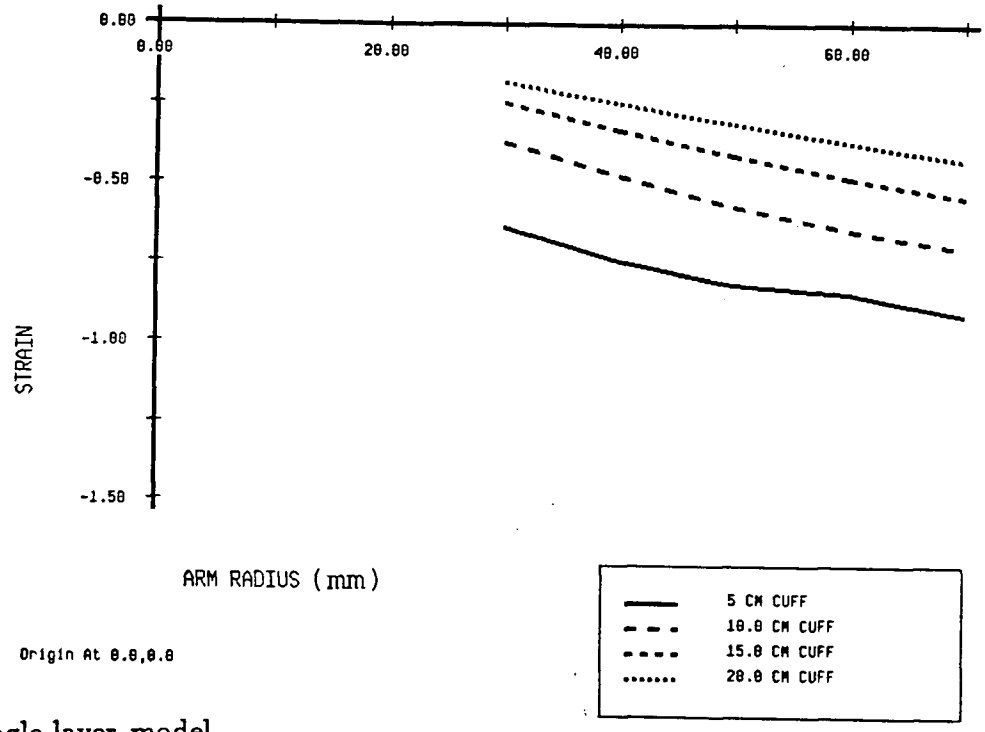

a. Single-layer model

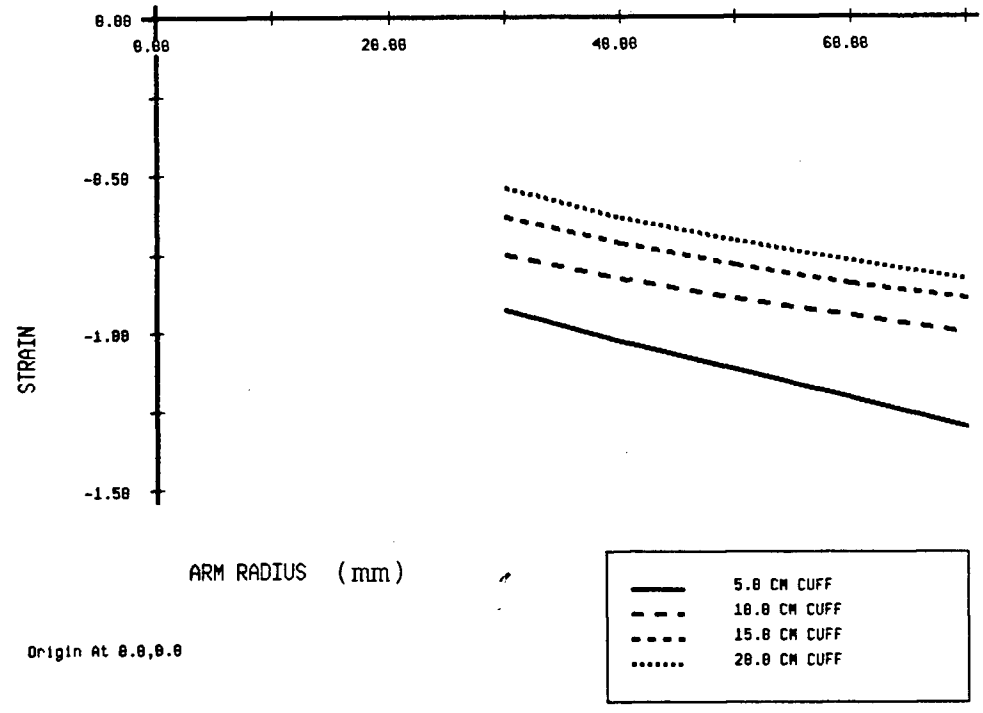

b. Multi-layer model

Figure 5.52: **Average maximum shear strain intensities for varying limb radius and cuff width**

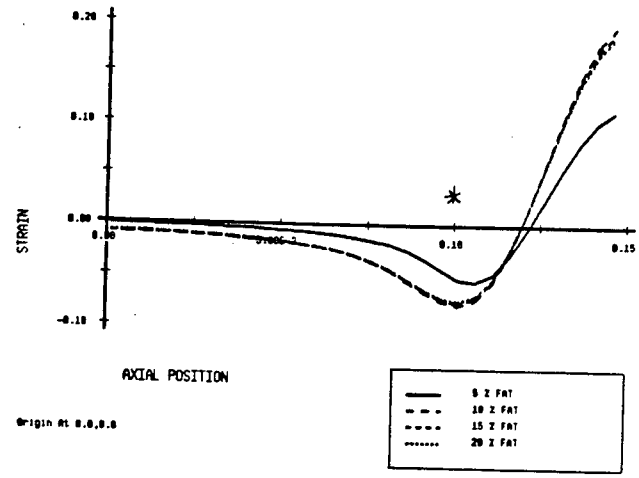

*: indicates the edge of the cuff on each curve

a. Radial nerve

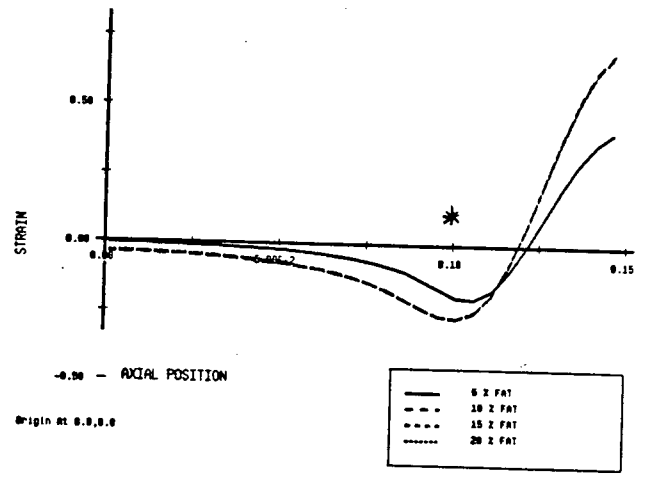

b. Musculocutaneous nerve

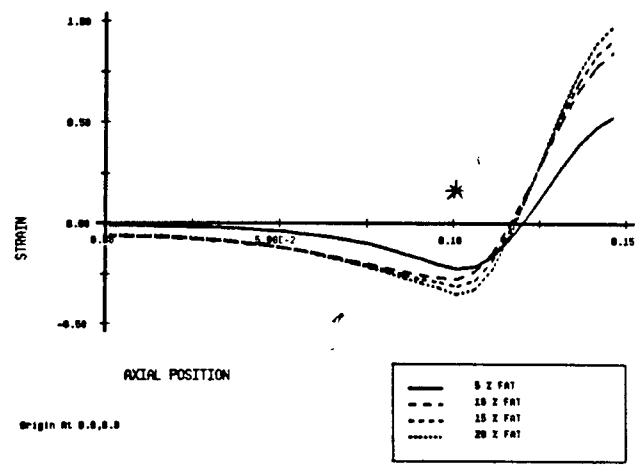

c. Median/ulnar nerves

Figure 5.53: **Predicted axial strain profiles for varying fat content at each nerve location (multi-layer model)**

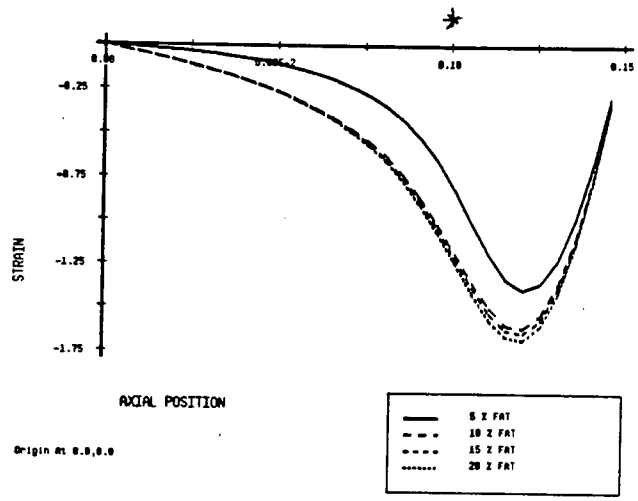

*: indicates the edge of the cuff on each curve

a. Radial nerve

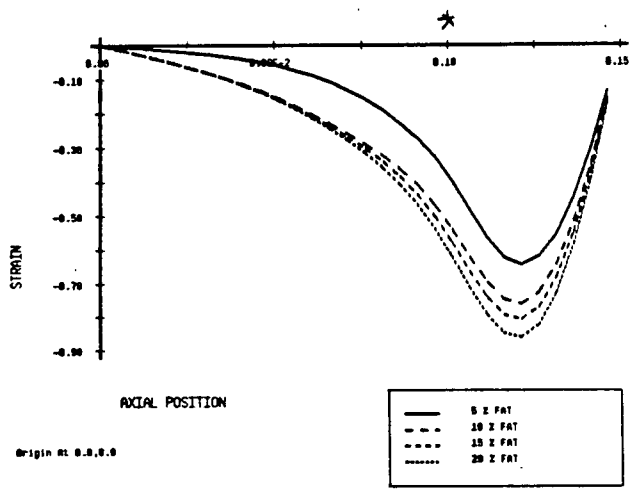

b. Musculocutaneous nerve

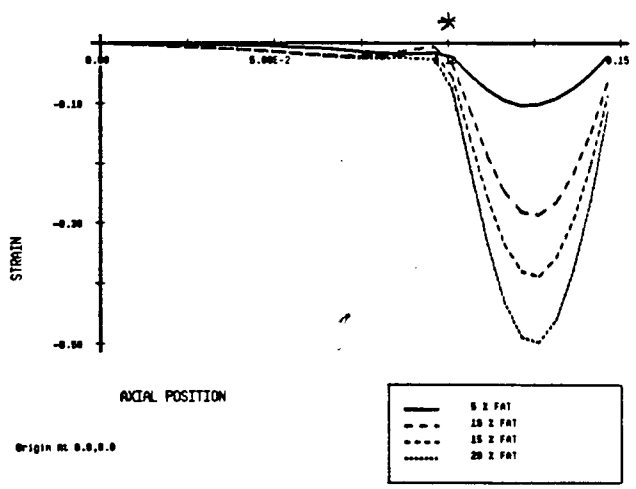

c. Median/ulnar nerves

Figure 5.54: **Predicted shear strain profiles for varying fat content at each nerve location (multi-layer model)**

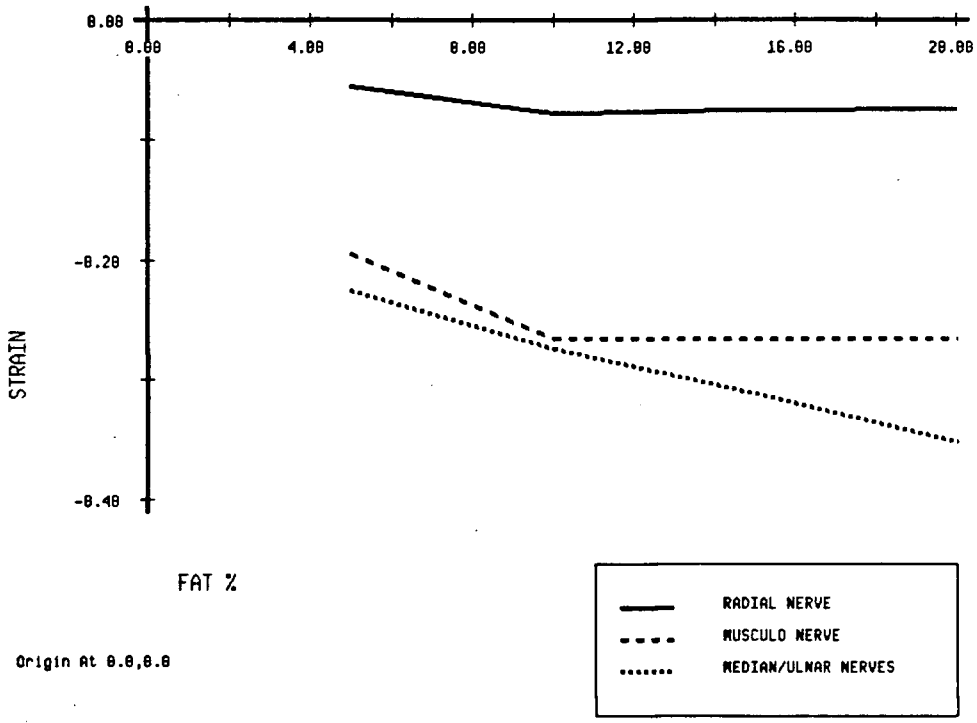

Figure 5.55: **Maximum axial strain intensities for varying fat content (multi-layer model)**

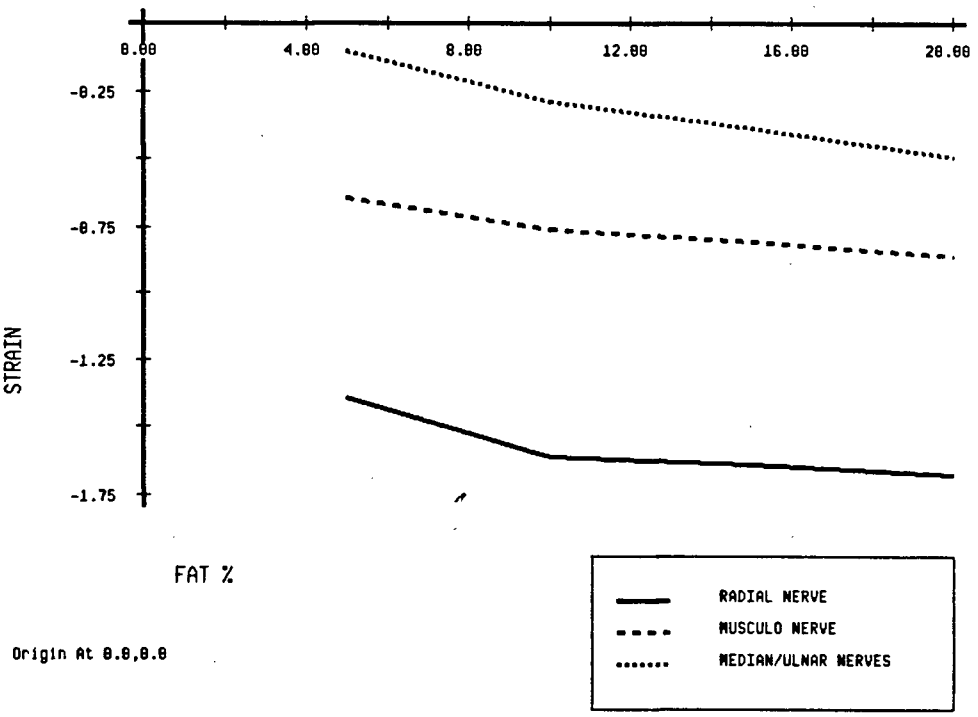

Figure 5.56: **Maximum shear strain intensities for varying fat content (multi-layer model)**

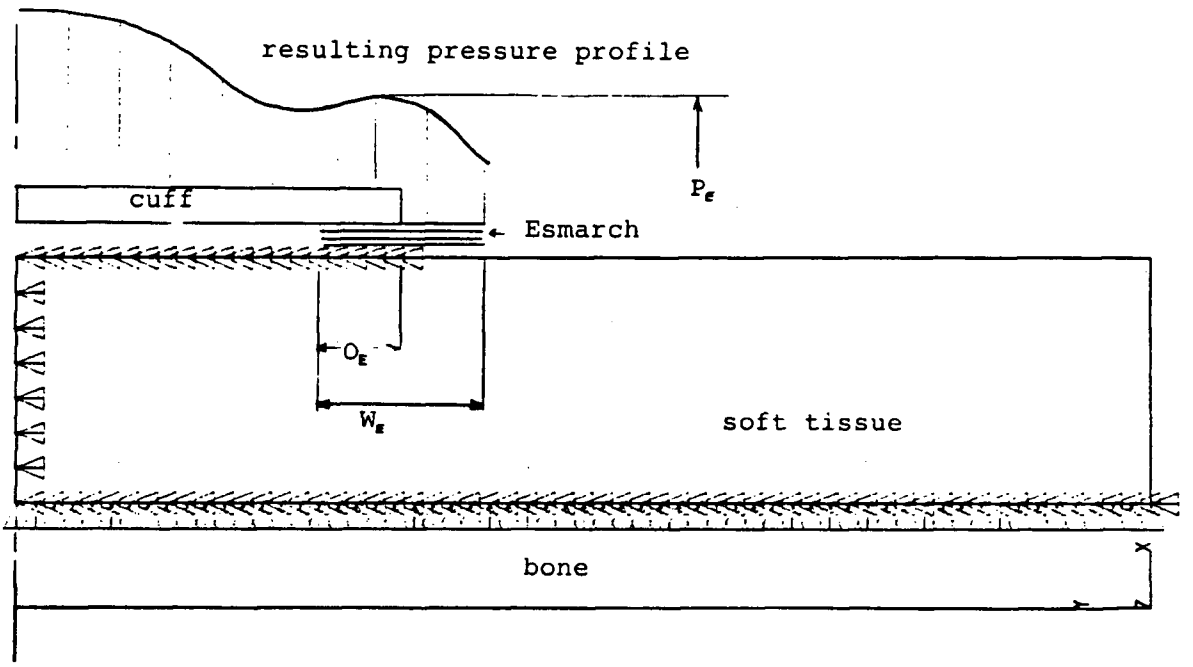

Figure 5.57: **Proposed Esmarch/tourniquet combination and its resulting pressure profile**

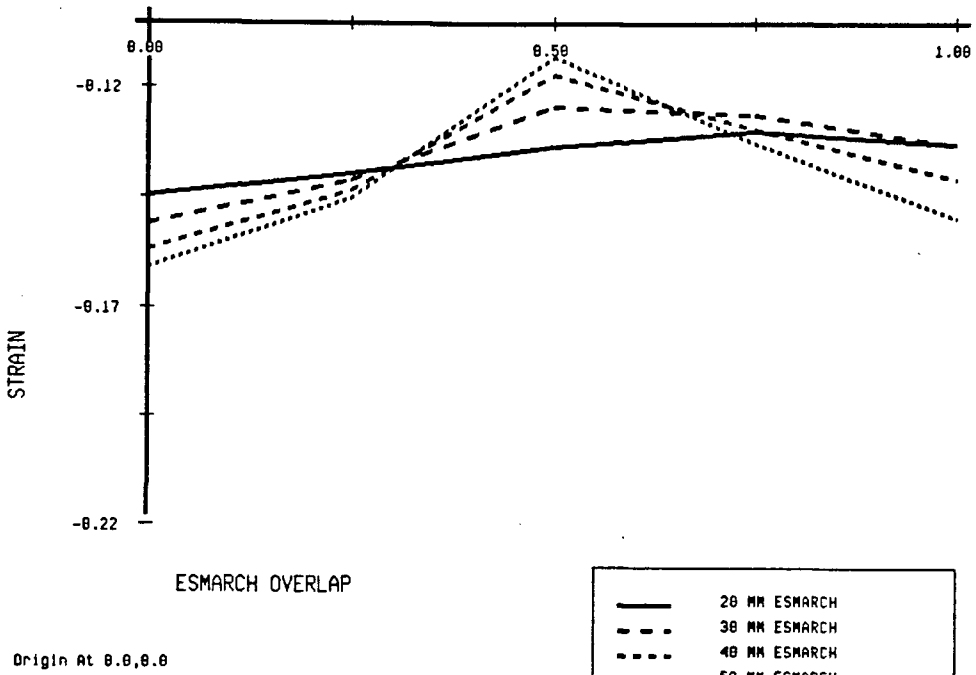

a. Single-layer model

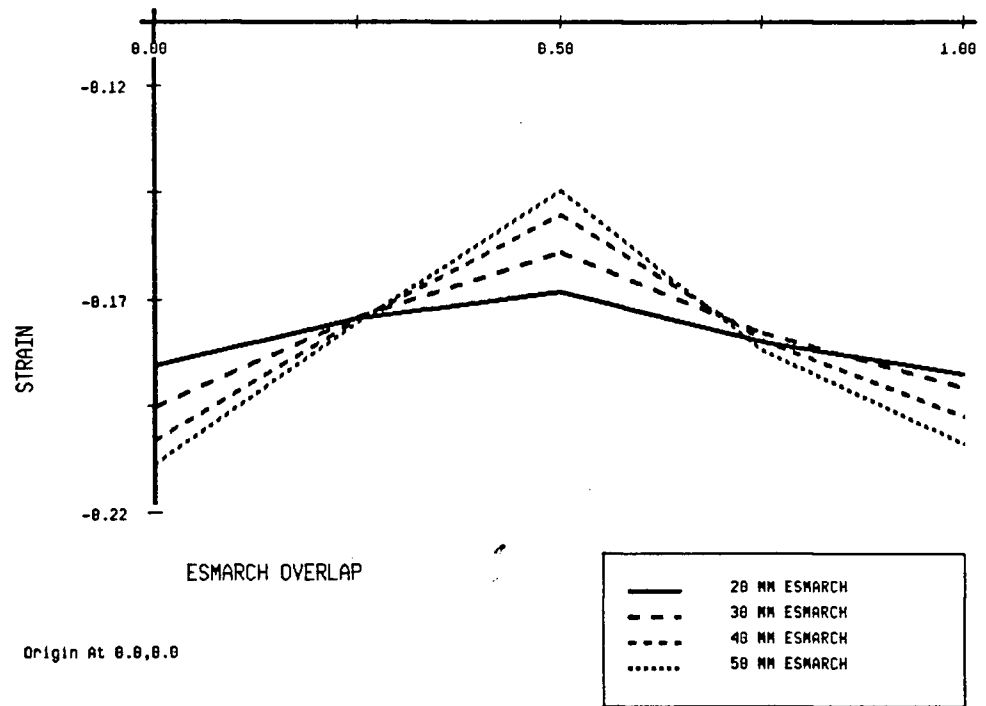

b. Multi-layer model

Figure 5.58: **Average maximum axial strain intensities for varying Esmarch overlap and width**

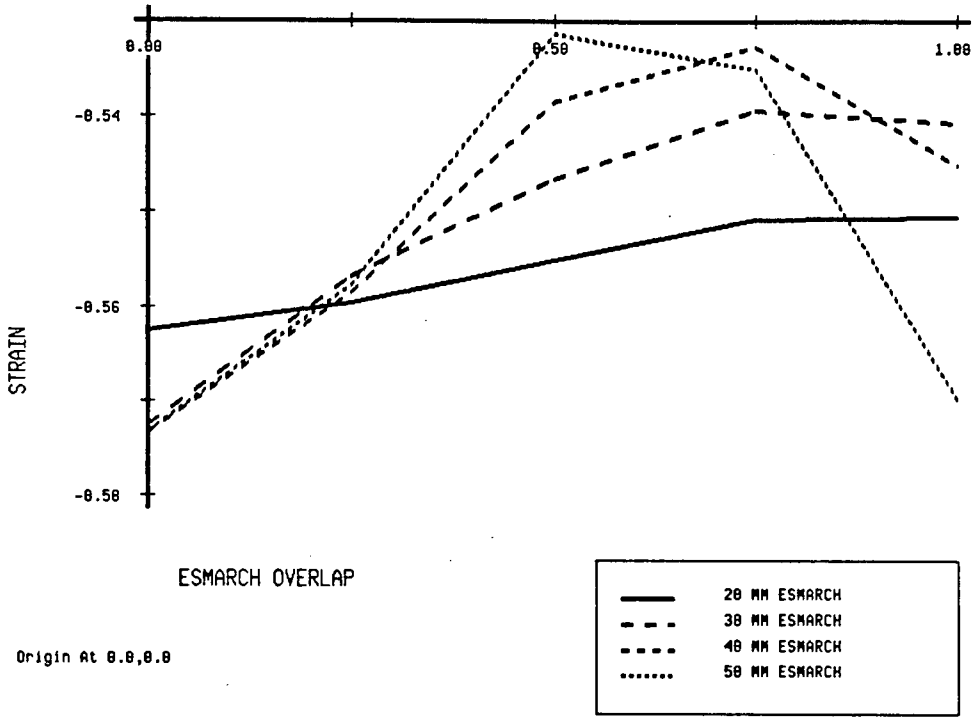

a. Single-layer model

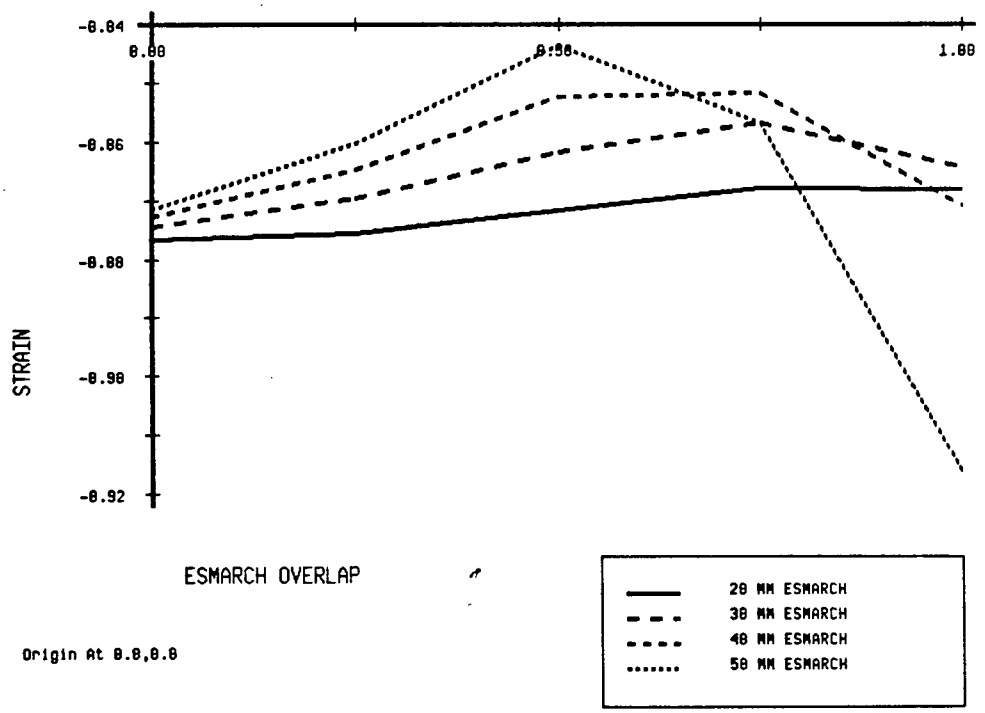

b. Multi-layer model

Figure 5.59: **Average maximum shear strain intensities for varying Esmarch overlap and width**

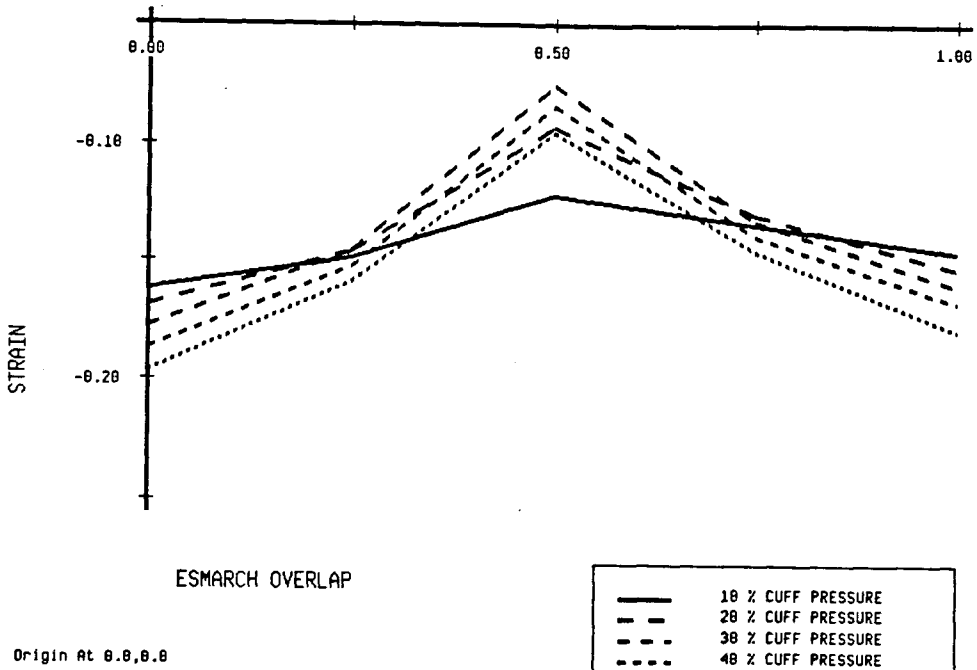

a. Single-layer model

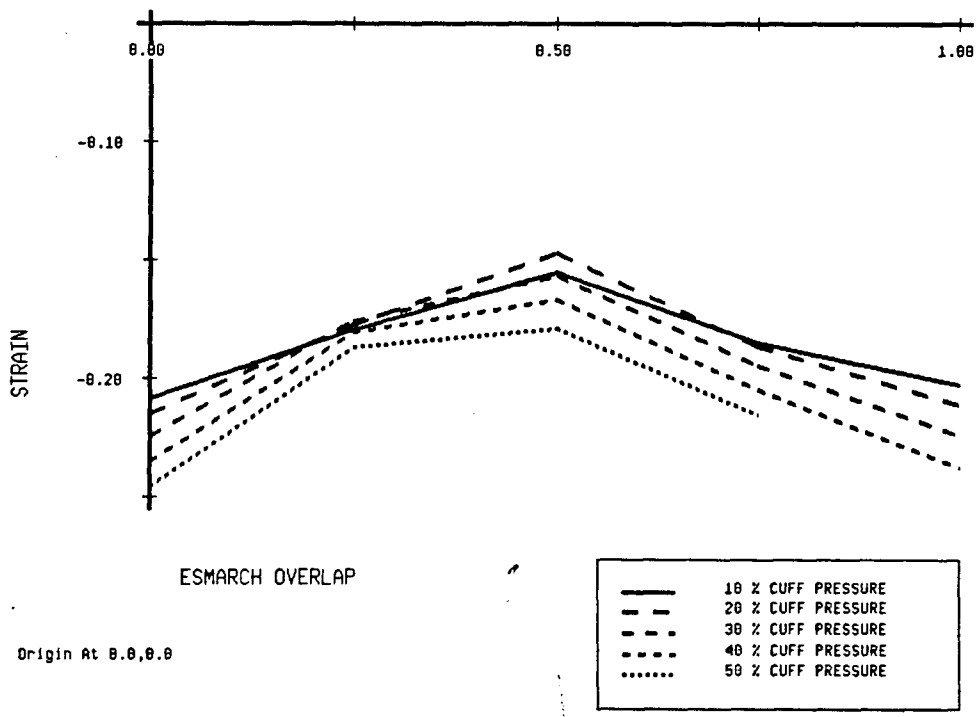

b. Multi-layer model

Figure 5.60: **Average maximum axial strain intensities for varying Esmarch overlap and cuff pressure**

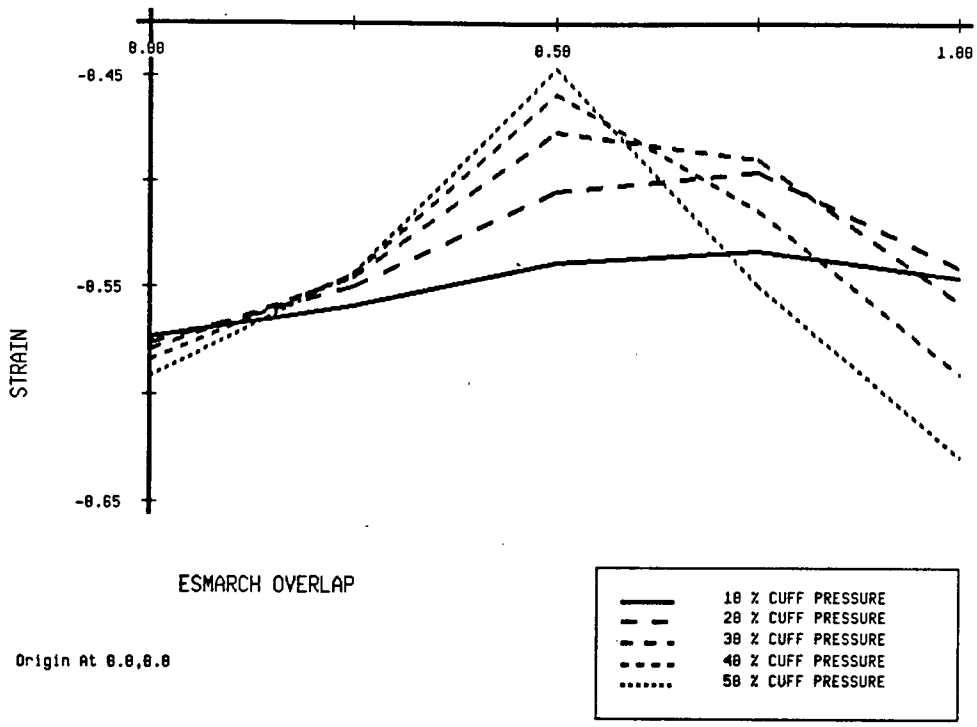

a. Single-layer model

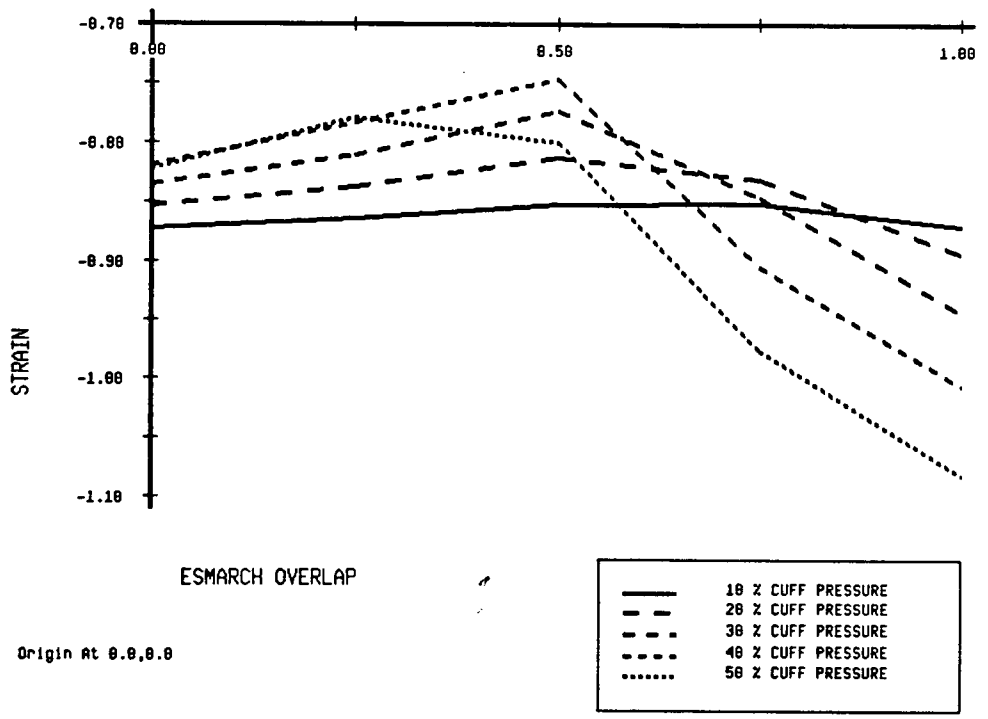

b. Multi-layer model

Figure 5.61: **Average maximum shear strain intensities for varying Esmarch overlap and cuff pressure**

Figures

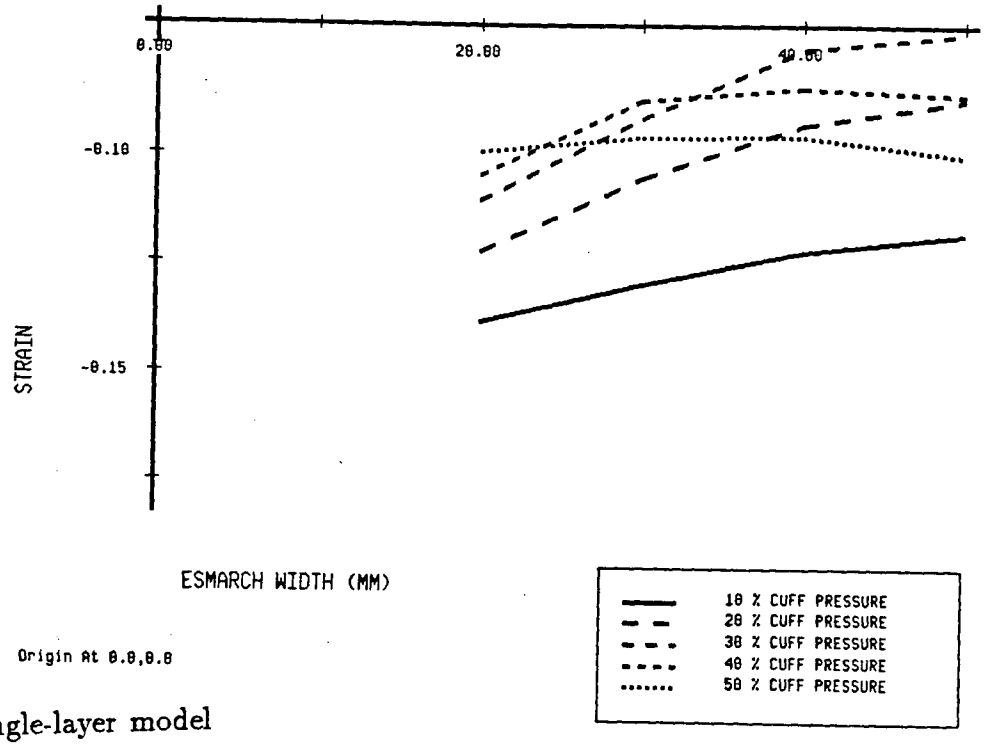

a. Single-layer model

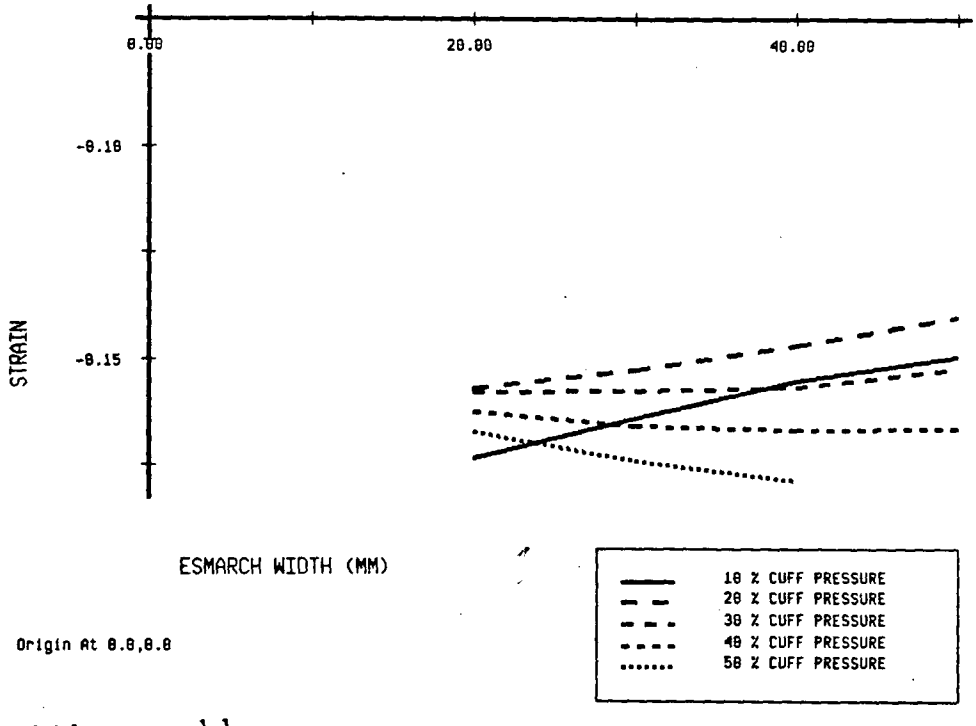

b. Multi-layer model

Figure 5.62: **Average maximum axial strain intensities for varying Esmarch width and cuff pressure**

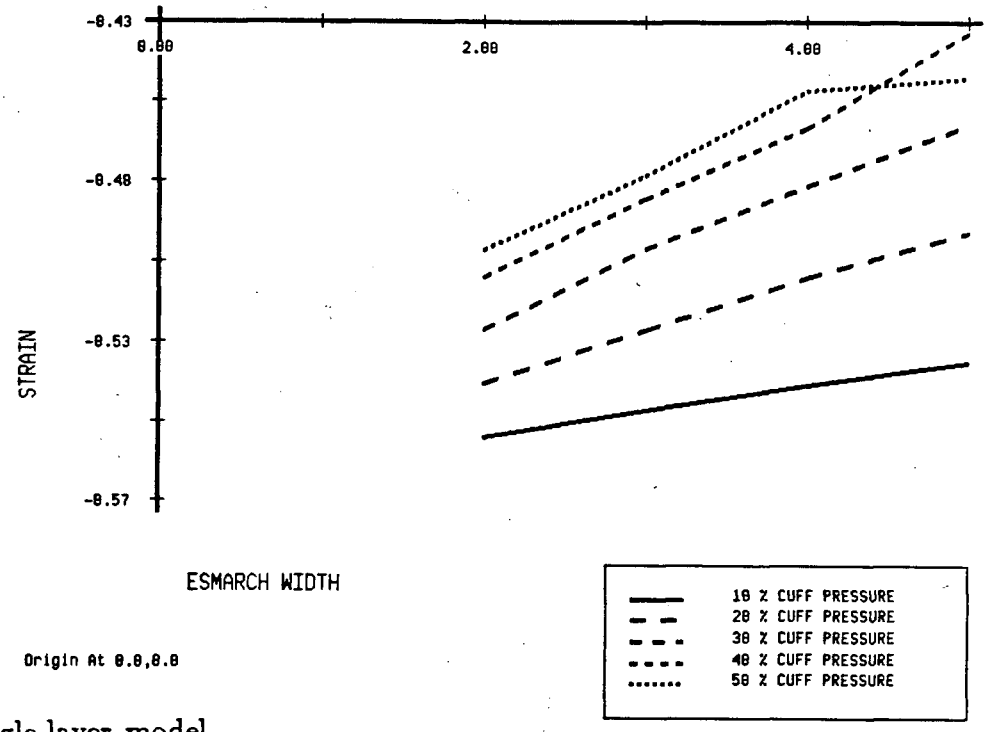

a. Single-layer model

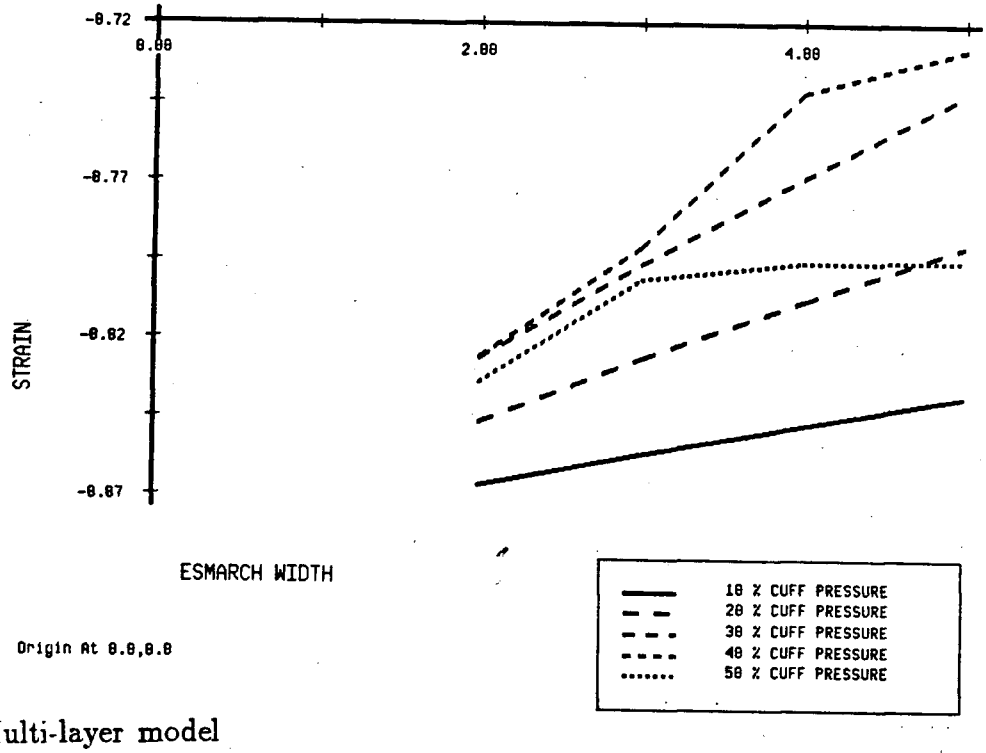

b. Multi-layer model

Figure 5.63: **Average maximum shear strain intensities for varying Esmarch width and cuff pressure**

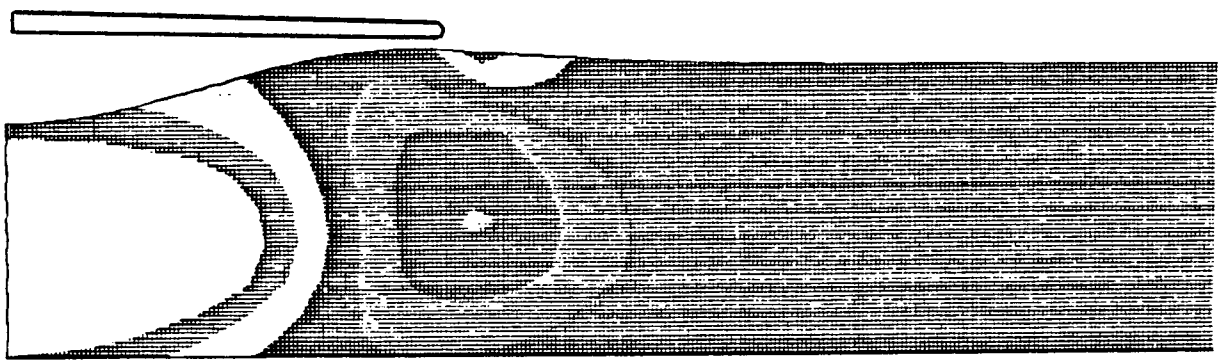

a. Conventional pneumatic tourniquet

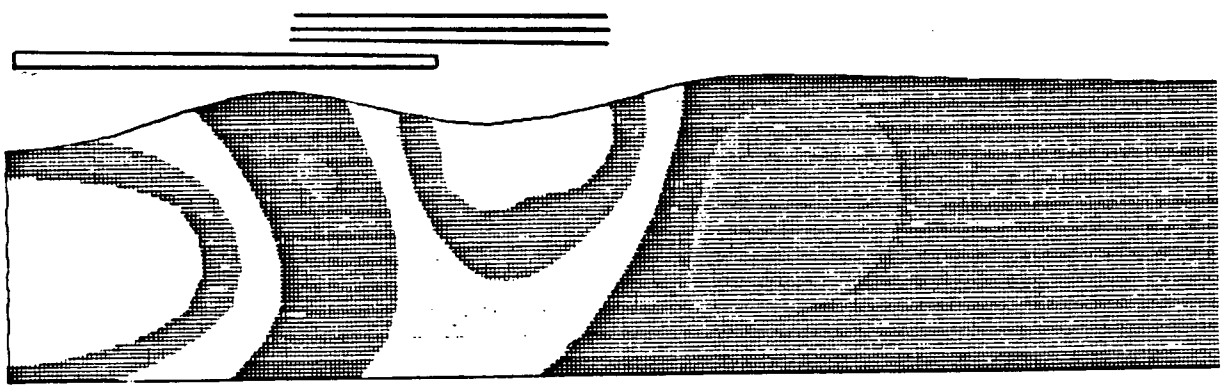

b. Optimal Esmarch/tourniquet configuration

Figure 5.64: **Comparison of predicted axial strain profiles (single-layer model)**

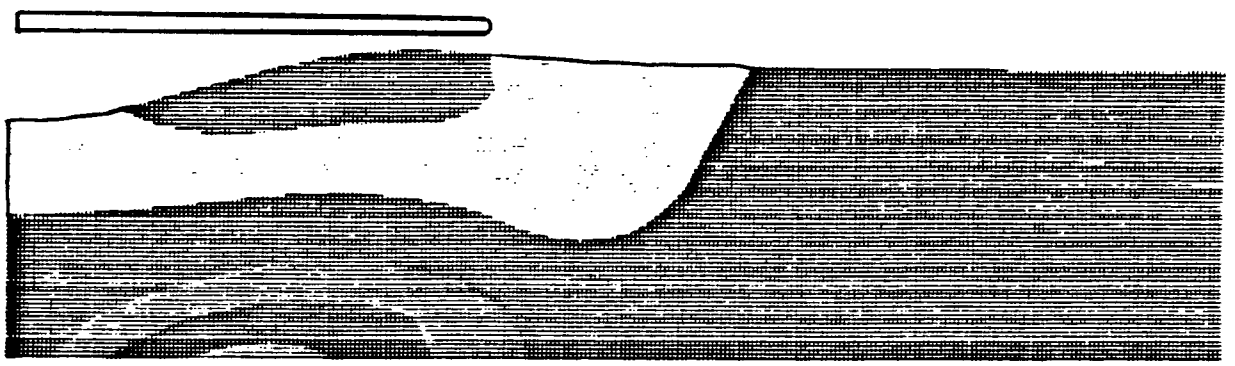

a. Conventional pneumatic tourniquet

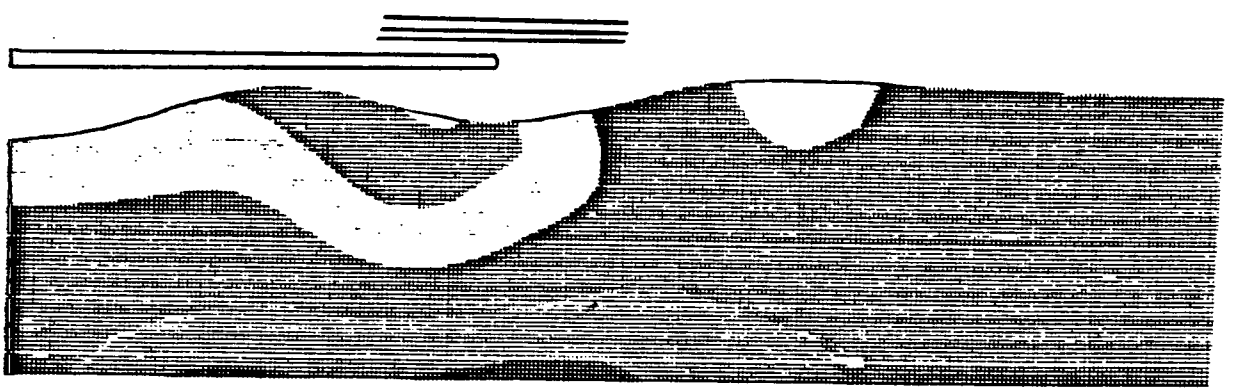

b. Optimal Esmarch/tourniquet configuration

Figure 5.65: **Comparison of predicted shear strain profiles (single-layer model)**

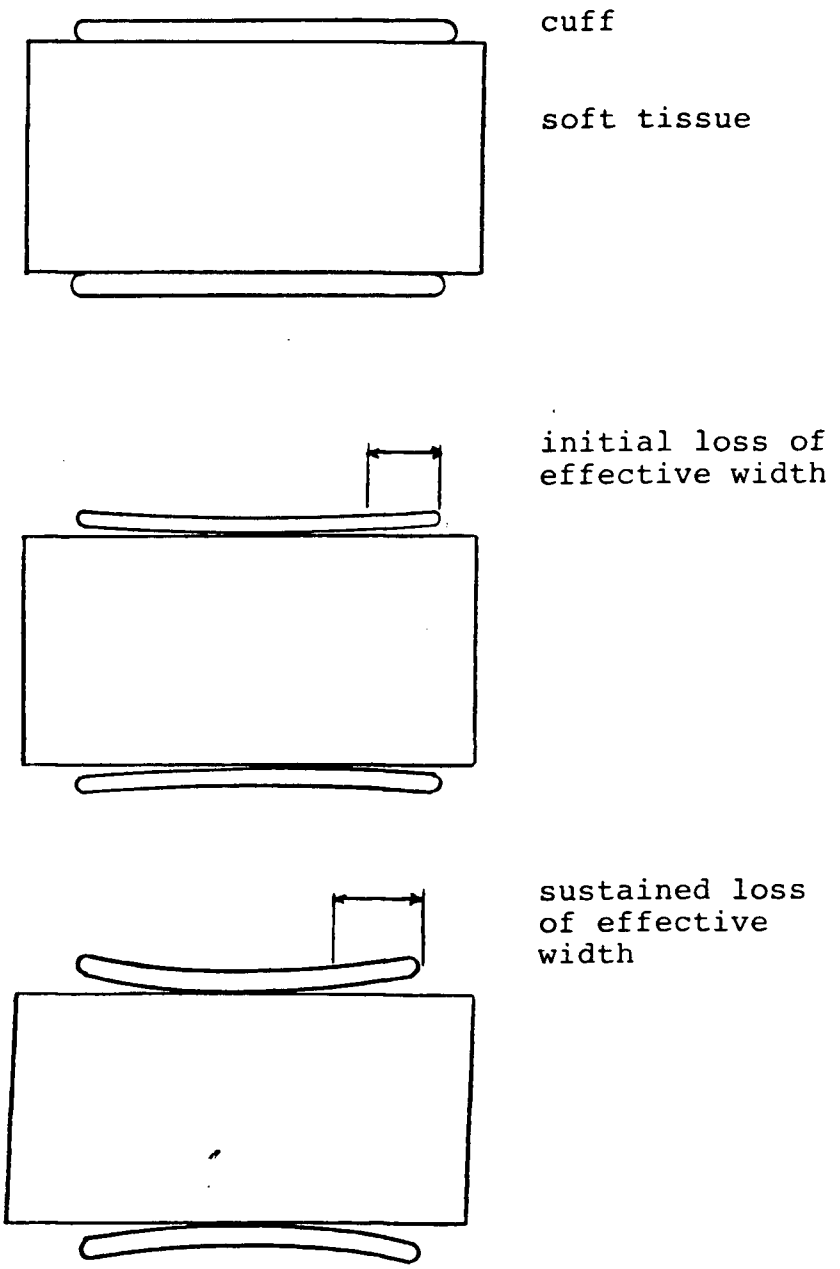

Figure 5.66: **Schematic representation of the pneumatic tourniquet as it is inflated**

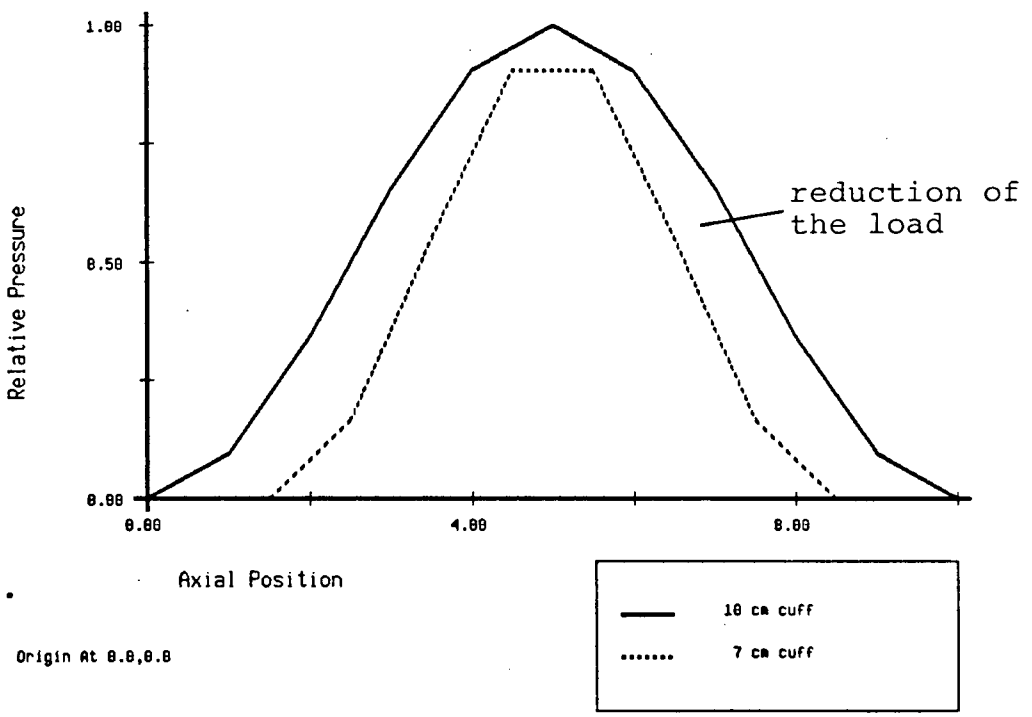

Figure 5.67: **Load reduction induced by upward-curving of the cuff edges**

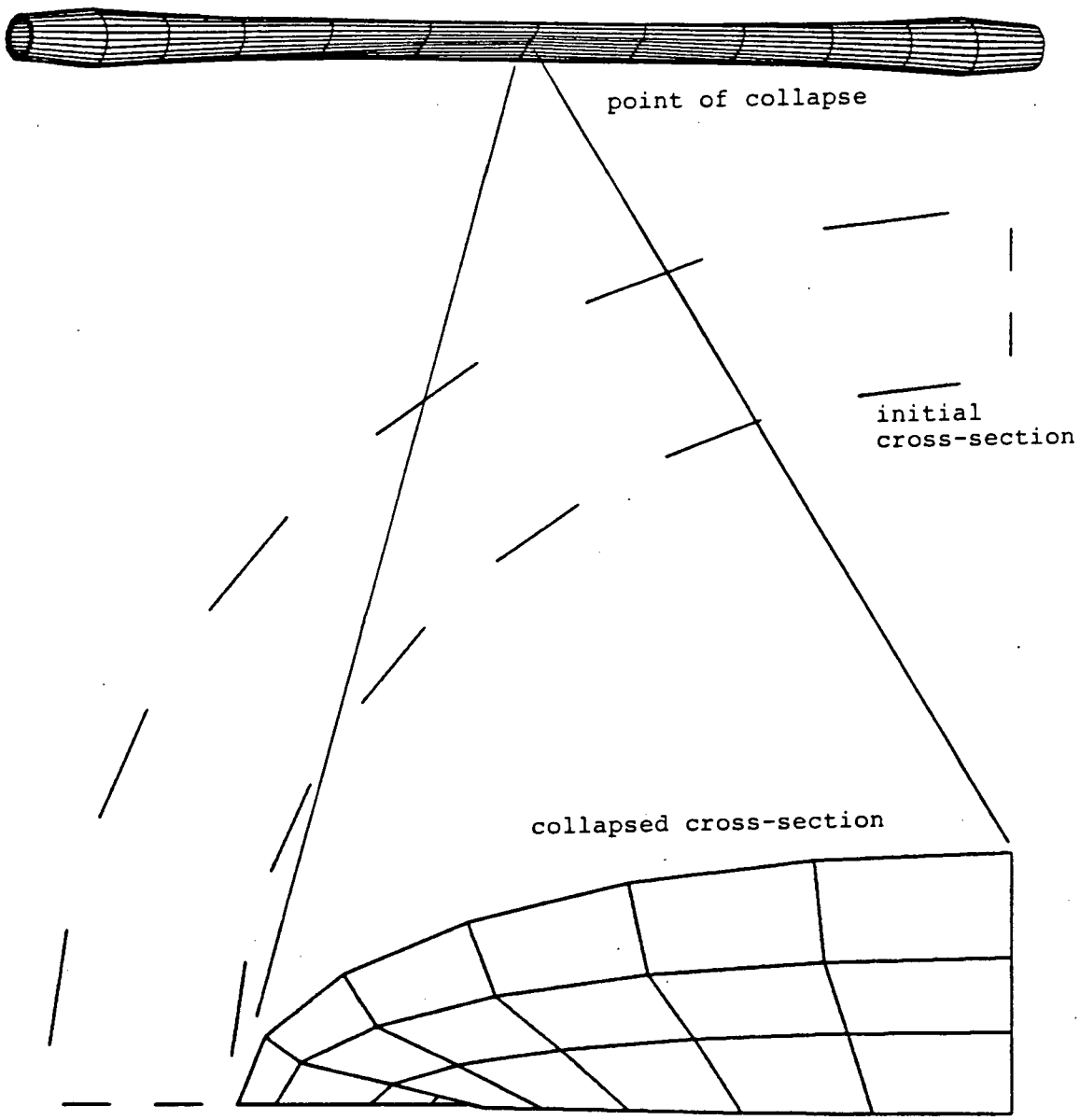

Figure 5.68: **Cross-section of the collapsed artery**

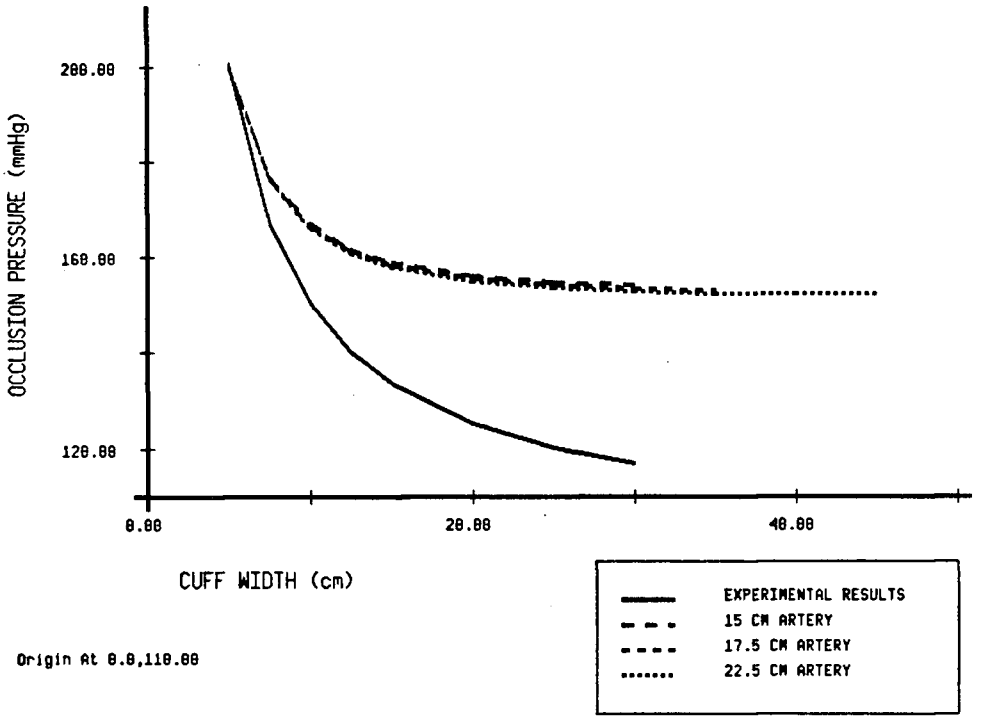

Figure 5.69: **Predicted occlusion pressures for varying cuff width and artery length**

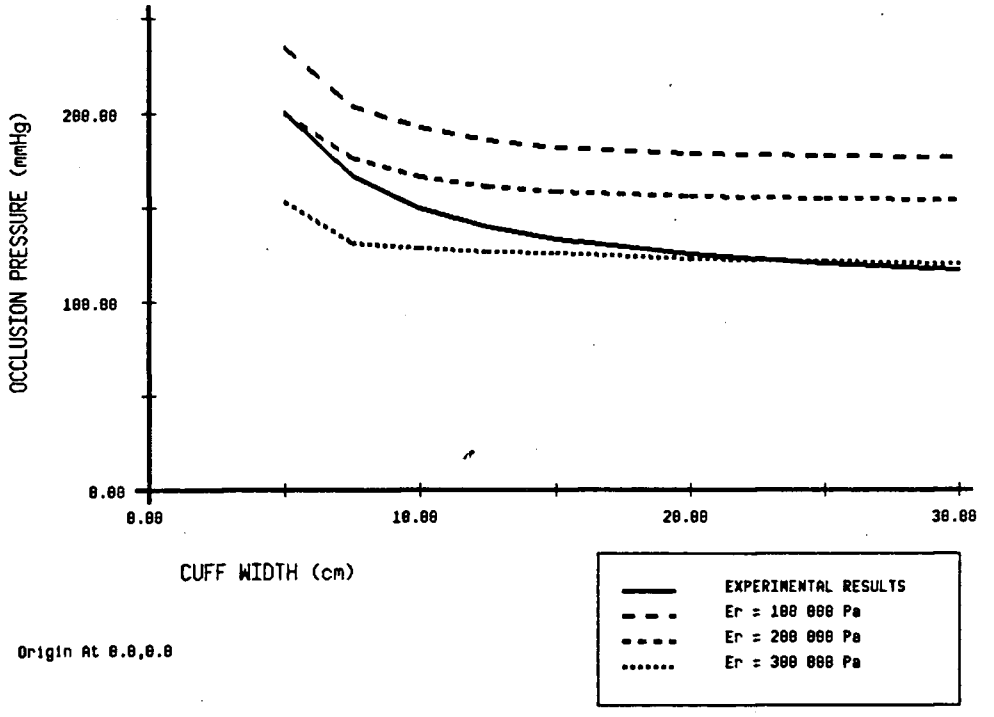

Figure 5.70: **Predicted occlusion pressures for varying cuff width and E_r**

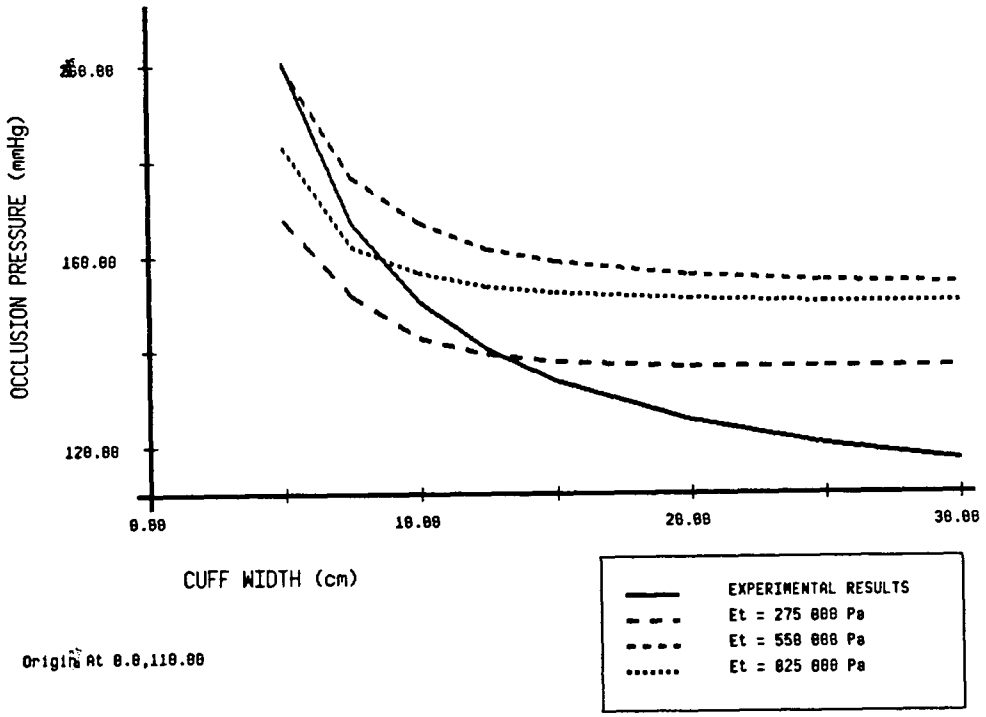

Figure 5.71: **Predicted occlusion pressures for varying cuff width and E_θ**

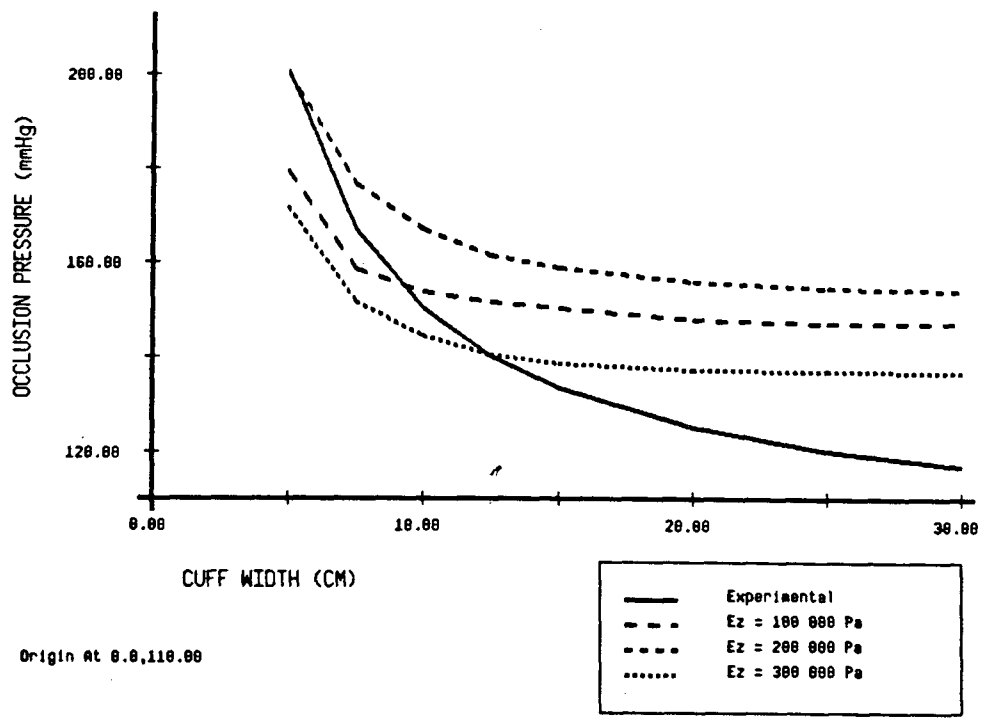

Figure 5.72: **Predicted occlusion pressures for varying cuff width and E_z**

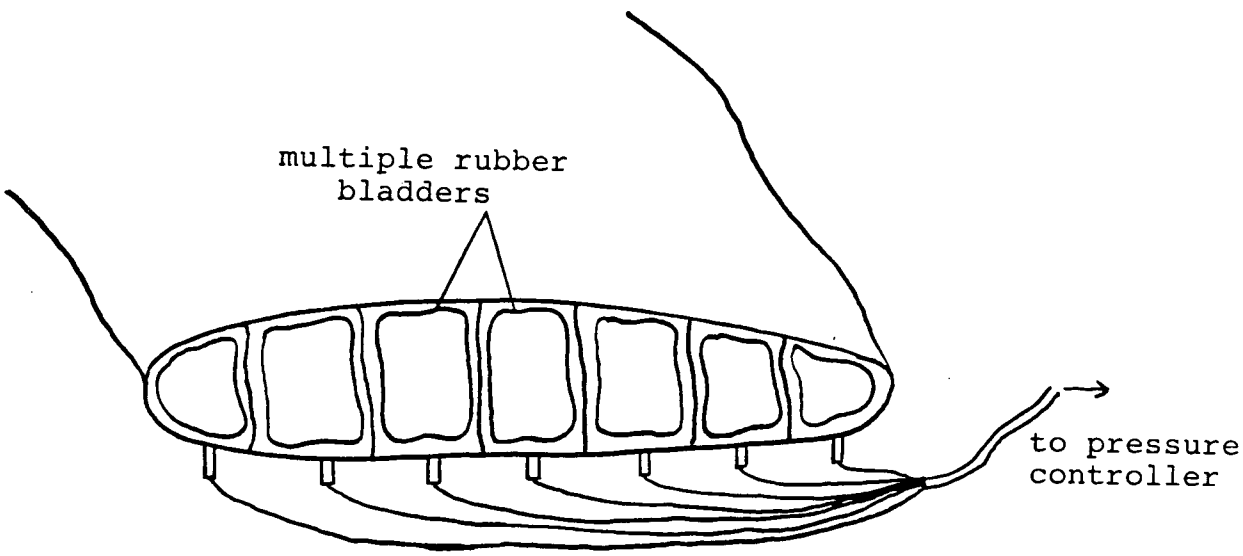

Figure 6.1: **Proposed multi-bladder tourniquet**

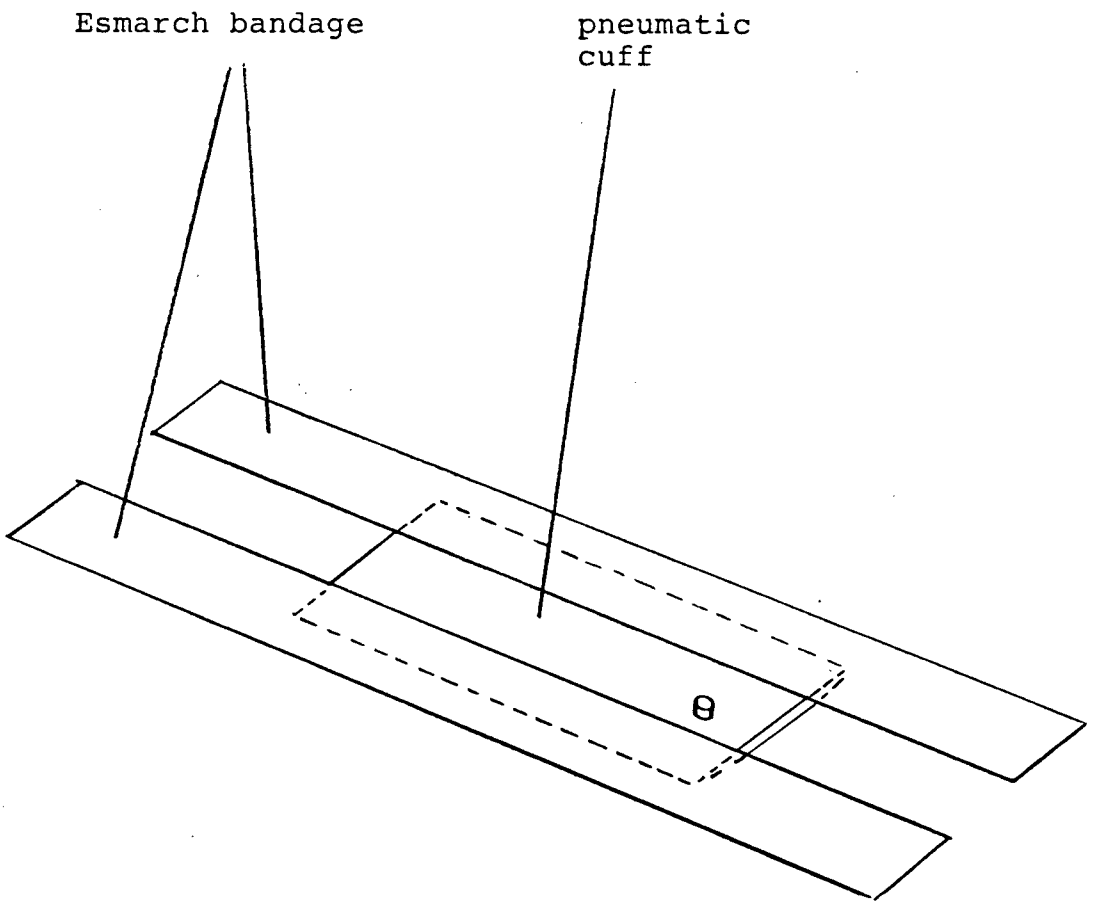

Figure 6.2: **Proposed Esmarch/tourniquet configuration**

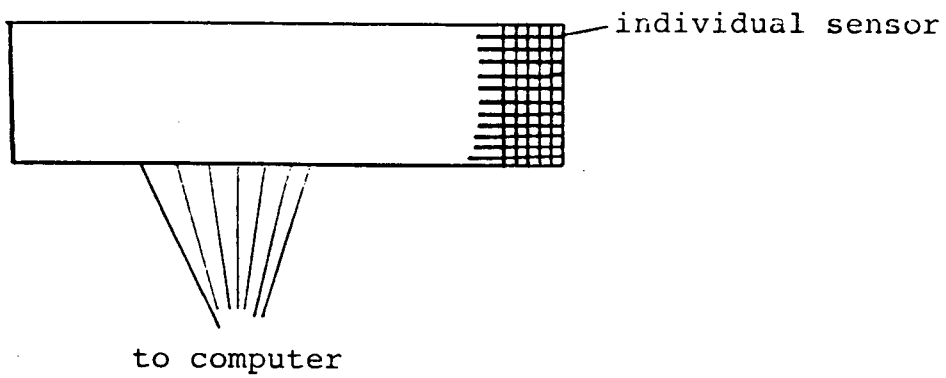

a. Piezoelectric sensor

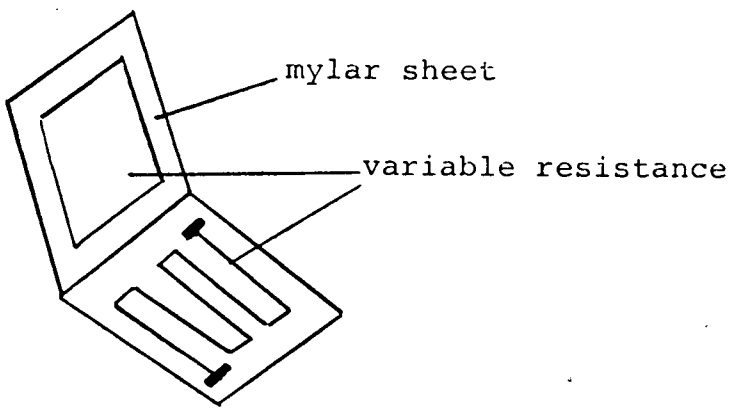

b. Potentiometer style sensor

Figure 6.3: **Examples of pressure sensors**

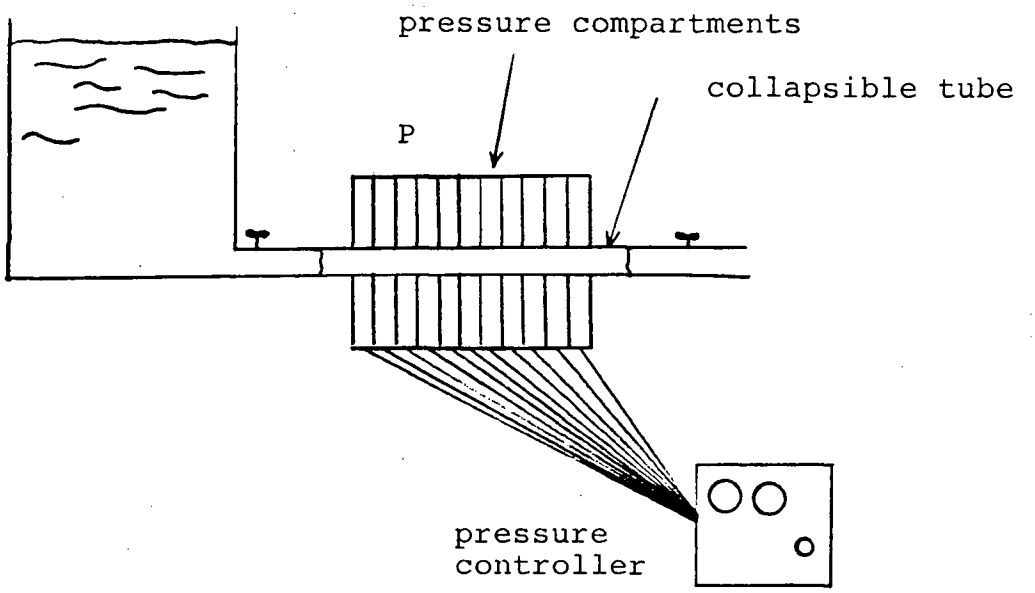

Figure 6.4: **Example of experimental setup to investigate blood flow occlusion**

Appendix A

NERVE ANATOMY

The structural features of peripheral nerves are shown in Figure A.1. The nerve trunk (bottom left) has been cut away to expose a single fasciculus, on which three fibers are indicated in detail. These include two myelinated axons, one on each side of a group of non-myelinated axons enclosed within a Schwann cell sheath. The myelinated fiber on the bottom has been cut away at various points to demonstrate the relationship between the axon, the Schwann cell, and its sheath of myelin.

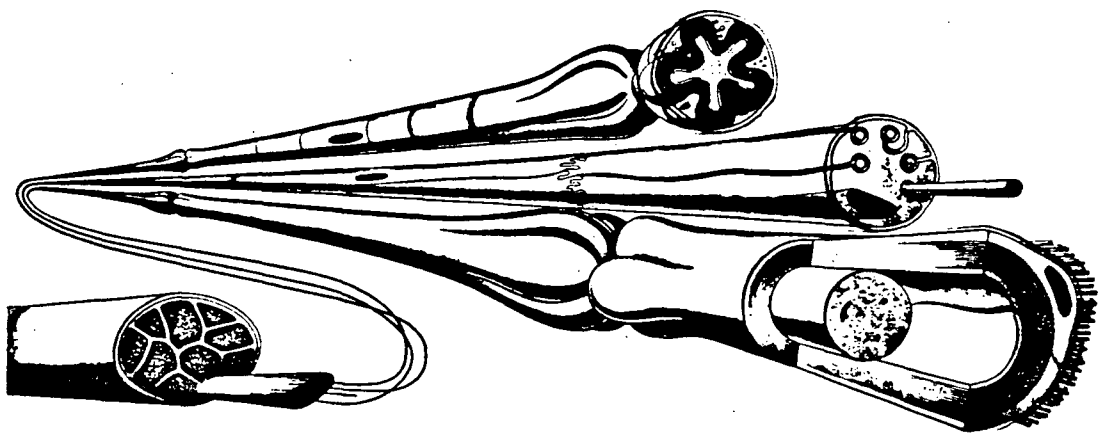

Figure A.1: **Structural features of a peripheral nerve [46]**

The general plan of a myelinated nerve fiber in longitudinal section including one complete internodal segment and two adjacent paranodal bulbs is shown in Figure A.2. Figure A.2a shows a transverse section through the center of a node of Ranvier, while Figure A.2b shows the arrangement of the axon, myelin sheath and Schwann cell cytoplasm at the node of Ranvier in the paranodal bulb.

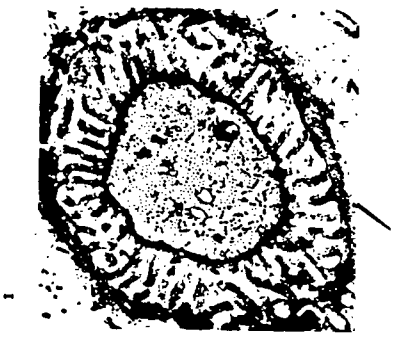

a. Transverse section through the node of Ranvier

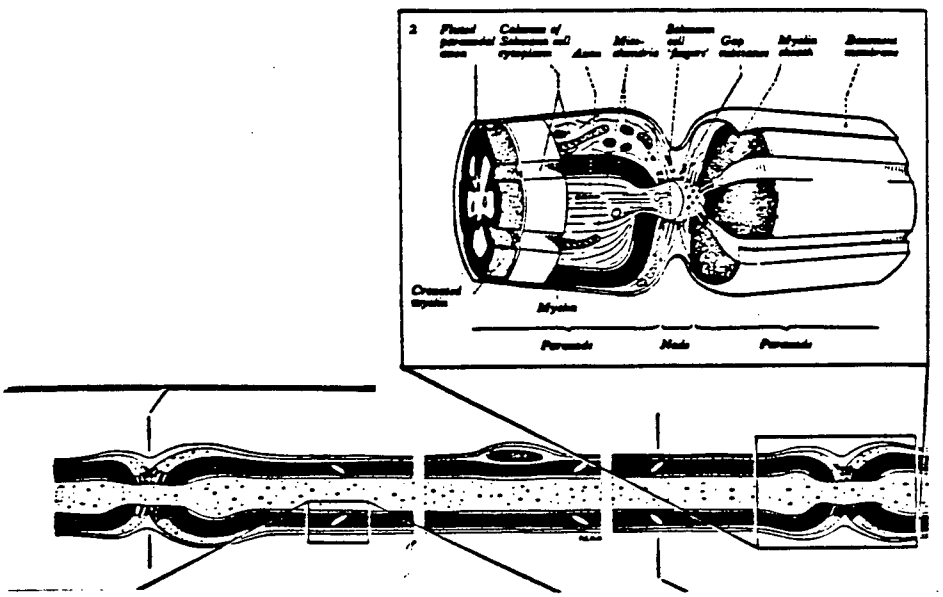

b. Arragement of the axon

Figure A.2: **General plan of a myelinated nerve fiber [46]**

Appendix B

FINITE ELEMENT THEORY

Using first order shape functions associated with rectangular elements possessing four nodes, a stiffness matrix is constructed to reflect the properties of a single finite element under plane stress conditions. This is followed by a demonstration of the assembly of a global stiffness matrix. Figure B.1 shows the finite element to be used in this development.

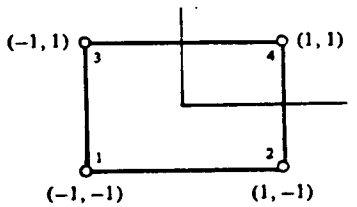

Figure B.1: **Single finite element [71]**

Equation B.1 lists the linear functions associated with each node of the element.

$$\left.\begin{aligned} N_1 &= (1-x)(1-y)/4 \\ N_2 &= (1+x)(1-y)/4 \\ N_3 &= (1+x)(1+y)/4 \\ N_4 &= (1-x)(1+y)/4 \end{aligned}\right\} \tag{B.1}$$

Note that the displacements at any given coordinate (x, y) are calculated using Equation B.2 where u signifies displacement in the x direction while v is in the y direction.

$$\{\Psi\} = \begin{Bmatrix} u \\ v \end{Bmatrix} = \begin{bmatrix} N_1 & N_2 & N_3 & N_4 & 0 & 0 & 0 & 0 \\ 0 & 0 & 0 & 0 & N_1 & N_2 & N_3 & N_4 \end{bmatrix} \begin{Bmatrix} a_1 \\ a_2 \\ a_3 \\ a_4 \\ a_5 \\ a_6 \\ a_7 \\ a_8 \end{Bmatrix} \tag{B.2}$$

In Equation B.2, $a_1 ... a_4$ represent the displacements at each of the corner nodes in the x direction, while $a_5 ... a_8$ represent the displacements in the y direction.

The strain relationship is given by:

$$\{\varepsilon\} = [L][N]\{a\} \tag{B.3}$$

where:

$$[L] = \begin{bmatrix} \frac{\partial}{\partial x} & 0 \\ 0 & \frac{\partial}{\partial y} \\ \frac{\partial}{\partial y} & \frac{\partial}{\partial x} \end{bmatrix}$$

Furthermore, stresses at each element can be evaluated by incorporating the material properties into the problem. Assuming a homogeneous isotropic material, Equation B.4 reflects the stresses at each element.

$$\{\sigma\} = \begin{Bmatrix} \sigma_x \\ \sigma_y \\ \tau_{xy} \end{Bmatrix} = [D]\{\varepsilon\} \tag{B.4}$$

where

$$[D] = \frac{E}{(1-\nu^2)} \begin{bmatrix} 1 & \nu & 0 \\ \nu & 1 & 0 \\ 0 & 0 & \frac{(1-\nu)}{2} \end{bmatrix}$$

The finite element method requires that the total energy be defined for each element (this implies strain and potential energies). Equations B.5 through B.7 show the development of the strain energy relationship.

$$U = \frac{1}{2}\int_V \{\sigma\}^T\{\varepsilon\}dV \tag{B.5}$$

$$U = \frac{t}{2}\int_A \{\sigma\}^T\{\varepsilon\}dA \tag{B.6}$$

$$U = \frac{t}{2}\int_A \{a\}^T[N]^T[L]^T[D][L][N]\{a\}dA \tag{B.7}$$

The potential energy of the internal and external loads is given by the negative of the body forces and surface tractions times the displacements. Equations B.8 and B.9 show the potential energy relationship.

$$PE = -\int_V \{F\}^T\{\Psi\}dV - \int_\Gamma \{T\}^T\{\Psi\}d\Gamma \tag{B.8}$$

$$PE = -t\int_A \{F\}^T[N]dA\{a\} - \int_\Gamma \{T\}^T[N]d\Gamma\{a\} \tag{B.9}$$

By combining the strain and potential energy equations and applying Lagrange's theorem, the stiffness equation is set up. Equations B.10 through B.12 below show this development.

$$W = U + PE = \frac{t}{2}\{a\}^T \int_A [N]^T[L]^T[D][L][N]dA\{a\} - t\int_A \{F\}^T[N]dA\{a\} - \int_\Gamma \{T\}^T[N]d\Gamma\{a\} \tag{B.10}$$

$$\frac{\partial W}{\partial a} = t\int_A [N]^T[L]^T[D][L][N]dA\{a\} - t\int_A \{F\}^T[N]dA - \int_\Gamma \{T\}^T[N]d\Gamma = 0 \tag{B.11}$$

$$[k]_1\{a\} = \{f\}_1 \tag{B.12}$$

where

$[k]_1 = \int_A [N]^T[L]^T[D][L][N]dA$ stiffness matrix

$\{f\}_1 = t\int_A \{F\}^T[N]dA$ for each element with body forces

$+ \int_\Gamma \{T\}^T[N]d\Gamma$ along the boundary of elements having edge loads

Solving these equations results in an 8 by 8 stiffness matrix and an 8 term force vector (i.e. 8 degrees of freedom, two at each of the four nodes).

From this development a stiffness matrix and force vector can be established for a single element. The next step is to combine all the individual stiffness matrices and force vectors into one global stiffness equation. Figure B.2 represents a simple two element structure along with the associated degrees of freedom. (Each of the two elements exhibit the same individual stiffness matrix.)

As before, each element possesses eight degrees of freedom while the combined structure has twelve (6 x 2 D.O.F/node). Remembering that $a_1 ... a_4$ represent displacements in the x direction and that $a_5 ... a_8$ represent displacements in the y direction, the locator matrix of Equation B.13 can be constructed by associating the individual degrees of freedom of each element with the global degrees of freedom of the combined structure.

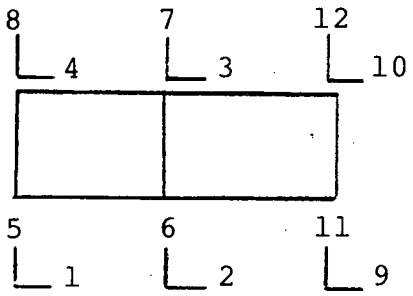

Figure B.2: **Simple two element structure**

element	a_1	a_2	a_3	a_4	a_5	a_6	a_7	a_8
1	1	2	3	4	5	6	7	8
2	2	9	10	3	6	11	12	7

(B.13)

Using Equation B.13 the global stiffness matrix can be assembed element by element as follows:

$$
\begin{aligned}
(1,1) \text{ of } [k]_1 &\longrightarrow (1,1) \text{ of } [K] \\
(1,2) \text{ of } [k]_1 &\longrightarrow (1,2) \text{ of } [K] \\
&\vdots \\
(1,1) \text{ of } [k]_2 &\longrightarrow (2,2) \text{ of } [K] \\
(1,2) \text{ of } [k]_2 &\longrightarrow (2,9) \text{ of } [K] \\
&\vdots
\end{aligned}
$$

Finally, a similar technique is used to assemble the global force vector as well as to incorporate the boundary conditions.

Appendix C

ANSYS PROGRAM LISTINGS

```
C*************************************************************
C***
C***    ROOT FILE TO SET THE PARAMETERS OF THE
C***    HOMOGENEOUS ESMARCH/CUFF LIMB COMPRESSION MODEL
C***
/PREP7
/TITLE ARM SECTION - ****
*SET,RADI,.05                          *  LIMB RADIUS
*SET,CUFF,.10                          *  CUFF WIDTH
*SET,OFFS,0.00                         *  OFFSET OF PRESSURE PROFILE
*SET,PEAK,1                            *  NUMBER OF PEAKS
*SET,BONN,1                            *  BONE/MUSCLE INTERFACE SETTING
*SET,SKIN,1                            *  SKIN/CUFF INTERFACE SETTING
*SET,ENDS,0                            *  AXIAL ENDS SETTING
*SET,MESH,7                            *  RADIAL MESH
*SET,ESMW,0.02                         *  ESMARCH WIDTH
*SET,ESMO,0.50                         *  ESMARCH OVERLAP
*SET,ESMP,0.1                          *  ESMARCH PRESSURE
*SET,ESMU,0.0                          *  ESMARCH OFFSET PRESSURE
/INPUT,MODEL                           *  CALL THE PROGRAM TO BUILD THE MODEL
AFWRIT                                 *  COMPILE THE PROGRAM
FINISH
/EXE                                   *  EXECUTE THE PROGRAM
/INPUT,27
FINISH
/POST1
/INPUT,OUTPUT                          *  PERFORM ANALISYS ON OUTPUT
FINISH
```

```
C*************************************************************
C***
C***   THIS PROGRAM CONSTRUCTS THE HOMOGENEOUS
C***   ESMARCH/CUFF LIMB COMPRESSION MODEL
C***
ET,1,25                                  *  CHOOSE ELEMENT TYPE
EX,1,15000                               *  SET MATERIAL PROPERTIES
EY,1,7500
EZ,1,15000
NUXY,1,0.45
NUYZ,1,0.45
NUXZ,1,0.49
C***
C***
C***   SET UP NODES AND ELEMENTS
C***
C***
EDELE,ALL                                *  ERASE AND COMPRESS ALL
NDELE,ALL                                *  NODES AND ELEMENTS
ECOMPR
NCOMPR
*SET,BONE,RADI*0.30                      *  SET PARAMETERS FOR
*SET,RINC,RADI-BONE                      *  CONSTRUCTION
*SET,RINC,RINC/MESH
*SET,AINC,0.0025
*SET,MES,MESH+1
*SET,X,BONE                              *  SET INITIAL CONDITIONS
*SET,NOD,1
*BEGIN,CONS                              *  LOOP TO PLACE NODES
N,NOD,X,0                                *  ON MODEL
NGEN,61,MES,NOD,NOD,1,,AINC
*SET,NOD,NOD+1
*SET,X,X+RINC
*END
*DO,CONS,1,MESH,1
E,1,2,MES+2,MES+1                        *  PLACE ELEMENTS ON MODEL
EGEN,MESH,1,1,1,1
EGEN,60,MES,1,MESH,1
WSORT,Y                                  *  SORT THE ELEMENTS IN THE
C***                                     *  AXIAL DIRECTION
C***
C***   SET THE BOUNDARY CONDITIONS
C***
C***
*SET,STAR,-CUFF/2
*SET,STAR,STAR+0.15
*IF,SKIN,EQ,0,HERE,10                    *  SET B.C. FOR CUFF/SKIN INTERFACE
NSEL,X,RADI-0.0001,RADI+0.0001           *  SKIN=0 : FREE TO SLIDE AXIALLY
DDELE,ALL                                *  SKIN=1 : RESTRAINED
NRSEL,Y,STAR-0.001,0.151
D,ALL,UY,0
NALL
EALL
*GO,HERE,5
NSEL,X,RADI-0.0001,RADI+0.0001
DDELE,ALL
NALL
EALL
*IF,BONN,EQ,0,HERE,7                     *  SET B.C. FOR BONE/MUSCLE INTERFACE
NSEL,X,BONE,BONE                         *  BONN=0 : FREE TO SLIDE AXIALLY
D,ALL,UX,0                               *  BONN=1 : RESTRAINED
D,ALL,UY,0
NALL
EALL
*GO,HERE,6
NSEL,X,BONE,BONE
DDELE,ALL
D,ALL,UX,0
NALL
EALL
*IF,ENDS,EQ,0,HERE,5                     *  SET B.C. FOR END OF MODEL
NSEL,Y,0,0                               *  ENDS=0 : FREE TO EXPAND AXIALLY
D,ALL,UY,0                               *  ENDS=1 : RESTRAINED
```

```
NALL
EALL
NSEL,Y,0.15,0.15                    *  SET B.C. AT SYMMETRY AXIS
D,ALL,UY,0
NALL
EALL
C***
C***
C***   SET THE PRESSURE DISTRIBUTION
C***
C***
*SET,CIRC,RADI*6.283185308          *  CALCULATE OCCLUSION PRESSURE
*SET,POCC,CIRC*16                   *  USING CUFF WIDTH AND LIMB RADIUS
*SET,POCC,POCC/CUFF
*SET,POCC,POCC*133.0
*SET,POCC,POCC+10000.0
PDELE,ALL
*SET,OVER,ESMW*ESMO                 *  SET INITIAL VALUES FOR
*SET,IOVE,ESMW-OVER                 *  ESMARCH P.D.
*SET,A,STAR-IOVE
*SET,OMEE,ESMW**-1
*SET,OMEE,OMEE*6.2832
*SET,LINC,0.0025
*SET,I,0
*SET,E,ESMU
*SET,EE,ESMU-1.0
*SET,EE,EE/2.0
*SET,FF,ESMU+1.0
*SET,FF,FF/2.0
*SET,DIV,IOVE/0.0025
*BEGIN,CONS                         *  BEGIN ESMARCH LOOP
*SET,B,A+LINC
*SET,I,I+LINC
*SET,F,COS(OMEE*I)
*SET,F,EE*F
*SET,F,F+FF
*SET,PPRF,E+F
*SET,PPRF,PPRF/2.0
*SET,PPRF,PPRF*ESMP
*SET,PPRF,PPRF*POCC
NSEL,Y,A-.001,B+.001
NRSEL,X,RADI-0.0001,RADI+0.002
PSF,0,0,RADI,PPRF
*SET,A,B
*SET,E,F
*END                                *  END ESMARCH LOOP
*DO,CONS,1,DIV-1,1
NALL
EALL
*SET,A,STAR                         *  SET INITIAL CONDITIONS FOR
*SET,OMEG,CUFF**-1                  *  ESMARCH/CUFF P.D.
*SET,OMEG,OMEG*PEAK
*SET,OMEG,OMEG*6.2832
*SET,LINC,0.0025
*SET,H,0
*SET,C,OFFS
*SET,CC,OFFS-1.0
*SET,CC,CC/2.0
*SET,DD,OFFS+1.0
*SET,DD,DD/2.0
*SET,DIV,OVER/0.0025
*BEGIN,CONS                         *  BEGIN ESMARCH/CUFF LOOP
*SET,B,A+LINC
*SET,H,H+LINC
*SET,D,COS(OMEG*H)
*SET,D,CC*D
*SET,D,D+DD
*SET,PPRE,C+D
*SET,PPRE,PPRE/2.0
*SET,I,I+LINC
*SET,F,COS(OMEE*I)
*SET,F,EE*F
*SET,F,F+FF
```

```
*SET,PPRF,E+F
*SET,PPRF,PPRF/2.0
*SET,PPRF,PPRF*ESMP
*SET,PPR,PPRF+PPRE
*SET,PPR,PPR*POCC
NSEL,Y,A-.001,B+.001
NRSEL,X,RADI-0.0001,RADI+0.002
PSF,0,0,RADI,PPR
*SET,A,B
*SET,C,D
*SET,E,F
*END                                    *  END ESMARCH/CUFF LOOP
*DO,CONS,1,DIV-1,1
*SET,DIST,STAR+OVER                     *  SET INITIAL CONDITIONS FOR
*SET,DIST,-DIST                         *  CUFF P.D.
*SET,DIST,DIST+0.15
*SET,DIV,DIST/0.0025
*BEGIN,CONS                             *  BEGIN CUFF LOOP
*SET,B,A+LINC
*SET,H,H+LINC
*SET,D,COS(OMEG*H)
*SET,D,CC*D
*SET,D,D+DD
*SET,PPRE,C+D
*SET,PPR,PPRE/2.0
*SET,PPR,PPR*POCC
NSEL,Y,A-.001,B+.001
NRSEL,X,RADI-0.0005,RADI+0.002
PSF,0,0,RADI,PPR
*SET,A,B
*SET,C,D
*END                                    *  END CUFF LOOP
*DO,CONS,1,DIV-1,1
NALL
EALL
C***
C***
C***   END OF PROGRAM
C***
C***
```

```
C*************************************************************************
C***
C***   THIS PROGRAM PRODUCES THE OUTPUT FROM
C***   HOMOGENEOUS ESMARCH/CUFF LIMB COMPRESSION MODEL
C***
C***
STRESS,EX,25,37                         *  DEFINE STRAINS
STRESS,EY,25,38
STRESS,EZ,25,39
STRESS,EXY,25,40
SET,1,1
*SET,EMAX,MESH*60
ESEL,ELEM,1,EMAX,MESH*2                 *  PRINT STRAINS FOR RADIAL NERVE
PRSTRS
ESEL,ELEM,3,EMAX,MESH*2                 *  PRINT STRAINS FOR MUSCULO NERVE
PRSTRS
ESEL,ELEM,MESH,EMAX,MESH*2              *  PRINT STRAINS FOR MEDIAN AND ULNAR NERVES
PRSTRS
EALL
NALL
NSEL,NODE,1,481,16                      *  PRINT STRESSES FOR RADIAL NERVE
PRNSTR
NSEL,NODE,4,484,16                      *  PRINT STRESSES FOR MUSCULO NERVE
PRNSTR
NSEL,NODE,7,487,16                      *  PRINT STRESSES FOR MEDIAN AND ULNAR NERVES
PRNSTR
EALL
NALL
```

```
C*************************************************************
C***
C***   ROOT FILE TO SET THE PARAMETERS OF THE
C***   NON HOMOGENEOUS ESMARCH/CUFF LIMB COMPRESSION MODEL
C***
/PREP7
/TITLE ARM SECTION - ****
*SET,RADI,.05                          *  LIMB RADIUS
*SET,CUFF,.10                          *  CUFF WIDTH
*SET,OFFS,0.00                         *  OFFSET OF PRESSURE PROFILE
*SET,PEAK,1                            *  NUMBER OF PEAKS
*SET,FAT,10                            *  FAT CONTENT
*SET,BONN,1                            *  BONE/MUSCLE INTERFACE SETTING
*SET,SKIN,1                            *  SKIN/CUFF INTERFACE SETTING
*SET,ENDS,0                            *  AXIAL ENDS SETTING
*SET,MESH,7                            *  RADIAL MESH
*SET,ESMW,0.02                         *  ESMARCH WIDTH
*SET,ESMO,0.0                          *  ESMARCH OVERLAP
*SET,ESMP,0.1                          *  ESMARCH PRESSURE
*SET,ESMU,0.0                          *  ESMARCH OFFSET PRESSURE
/INPUT,MODEL                           *  CALL THE PROGRAM TO BUILD THE MODEL
AFWRIT                                 *  COMPILE THE PROGRAM
FINISH
/EXE                                   *  EXECUTE THE PROGRAM
/INPUT,27
FINISH
/POST1                                 *  PERFORM ANALISYS ON OUTPUT
/INPUT,OUTPUT
FINISH
```

```
C*************************************************************
C***
C***   THIS PROGRAM CONSTRUCTS THE NON HOMOGENEOUS
C***   ESMARCH/CUFF LIMB COMPRESSION MODEL
C***
ET,1,25                                 *  CHOOSE ELEMENT TYPE FOR MUSCLE
EX,1,15000                              *  SET MATERIAL PROPERTIES
EY,1,7500
EZ,1,15000
NUXY,1,.45
NUYZ,1,.45
NUXZ,1,.49
ET,2,81                                 *  CHOOSE ELEM,ENT TYPE FOR FAT
EX,2,250000                             *  SET MATERIAL PROPERTIES
DENS,2,1000
C***
C***
C***   SET UP NODES AND ELEMENTS
C***
C***
EDELE,ALL                               *  ERASE AND COMPRESS ALL
NDELE,ALL                               *  NODES AND ELEMENTS
ECOMPR
NCOMPR
*SET,FAT,FAT/100
*SET,FAT,-FAT
*SET,FAT,FAT+1                          *  CALCULATE FAT THICKNESS
*SET,FAT,FAT**0.5                       *  FROM FAT %
*SET,FAT,-FAT
*SET,FAT,FAT+1
*SET,FAT,FAT*RADI
*SET,BONE,RADI*0.30                     *  SET PARAMETERS FOR
*SET,RINC,RADI-BONE                     *  CONSTRUCTION
*SET,RINC,RINC-FAT
*SET,RINC,RINC/MESH
*SET,AINC,0.0025
*SET,MES,MESH+3
*SET,X,BONE                             *  SET INITIAL CONDITIONS
*SET,NOD,1
*BEGIN,CONS                             *  LOOP TO PLACE NODES
N,NOD,X,0                               *  ON MODEL
NGEN,61,MES,NOD,NOD,1,,AINC
*SET,NOD,NOD+1
*SET,X,X+RINC
*END
*DO,CONS,1,MESH,1
*SET,X,X-RINC
N,NOD,X+FAT
NGEN,61,MES,NOD,NOD,1,,AINC
*SET,X,X+FAT
N,NOD+1,X+0.001                         *  DEFINE THE MUSCLE ELEMENTS
NGEN,61,MES,NOD+1,NOD+1,1,,AINC
MAT,1
TYPE,1
E,1,2,MES+2,MES+1
EGEN,MESH,1,1,1,1
EGEN,60,MES,1,MESH,1
MAT,2                                   *  DEFINE FATTY TISSUE ELEMENTS
TYPE,2
*SET,BB,MES+MESH
E,MESH+1,MESH+2,BB+2,BB+1
*SET,ELLI,MESH*60
*SET,ELLI,ELLI+1
EGEN,60,MES,ELLI,ELLI
MAT,1                                   *  DEFINE THE SKIN ELEMENTS
TYPE,1
*SET,ELL,MESH*60
*SET,ELL,ELL+61
*SET,CC,MES*2
E,MES-1,MES,CC,CC-1
EGEN,60,MES,ELL,ELL,1
WSORT,Y                                 *  SORT THE ELEMENTS IN THE
C***                                    *  AXIAL DIRECTION
```

```
C***
C***   SET THE BOUNDARY CONDITIONS
C***
C***
*SET,STAR,-CUFF/2
*SET,STAR,STAR+0.15
*IF,SKIN,EQ,0,HERE,10                  *  SET B.C. FOR CUFF/SKIN INTERFACE
NSEL,X,RADI+0.0005,RADI+0.002          *  SKIN=0 : FREE TO SLIDE AXIALLY
DDELE,ALL                              *  SKIN=1 : RESTRAINED
NRSEL,Y,STAR-0.001,0.151
D,ALL,UY,0
NALL
EALL
*GO,HERE,5
NSEL,X,RADI+0.0005,RADI+0.002
DDELE,ALL
NALL
EALL
*IF,BONN,EQ,0,HERE,7                   *  SET B.C. FOR BONE/MUSCLE INTERFACE
NSEL,X,BONE,BONE                       *  BONN=0 : FREE TO SLIDE AXIALLY
D,ALL,UX,0                             *  BONN=1 : RESTRAINED
D,ALL,UY,0
NALL
EALL
*GO,HERE,6
NSEL,X,BONE,BONE
DDELE,ALL
D,ALL,UX,0
NALL
EALL
*IF,ENDS,EQ,0,HERE,5                   *  SET B.C. FOR END OF MODEL
NSEL,Y,0,0                             *  ENDS=0 : FREE TO EXPAND AXIALLY
D,ALL,UY,0                             *  ENDS=1 : RESTRAINED
NALL
EALL
NSEL,Y,0.15,0.15                       *  SET B.C. AT SYMMETRY AXIS
D,ALL,UY,0
NALL
EALL
C***
C***
C***   SET THE PRESSURE DISTRIBUTION
C***
C***
*SET,CIRC,RADI*6.283185308             *  CALCULATE OCCLUSION PRESSURE
*SET,POCC,CIRC*16                      *  USING CUFF WIDTH AND LIMB RADIUS
*SET,POCC,POCC/CUFF
*SET,POCC,POCC*133.0
*SET,POCC,POCC+10000.0
PDELE,ALL
*SET,OVER,ESMW*ESMO                    *  SET INITIAL VALUES FOR
*SET,IOVE,ESMW-OVER                    *  ESMARCH P.D.
*SET,A,STAR-IOVE
*SET,OMEE,ESMW**-1
*SET,OMEE,OMEE*6.2832
*SET,LINC,0.0025
*SET,I,0
*SET,E,ESMU
*SET,EE,ESMU-1.0
*SET,EE,EE/2.0
*SET,FF,ESMU+1.0
*SET,FF,FF/2.0
*SET,DIV,IOVE/0.0025
*BEGIN,CONS                            *  BEGIN ESMARCH LOOP
*SET,B,A+LINC
*SET,I,I+LINC
*SET,F,COS(OMEE*I)
*SET,F,EE*F
*SET,F,F+FF
*SET,PPRF,E+F
*SET,PPRF,PPRF/2.0
*SET,PPRF,PPRF*ESMP
*SET,PPRF,PPRF*POCC
```

```
NSEL,Y,A-.001,B+.001
NRSEL,X,RADI+0.0005,RADI+0.002
PSF,0,0,RADI+0.001,PPRF
*SET,A,B
*SET,E,F
*END                                    *  END ESMARCH LOOP
*DO,CONS,1,DIV-1,1
NALL
EALL
*SET,A,STAR                             *  SET INITIAL CONDITIONS FOR
*SET,OMEG,CUFF**-1                      *  ESMARCH/CUFF P.D.
*SET,OMEG,OMEG*PEAK
*SET,OMEG,OMEG*6.2832
*SET,LINC,0.0025
*SET,H,0
*SET,C,OFFS
*SET,CC,OFFS-1.0
*SET,CC,CC/2.0
*SET,DD,OFFS+1.0
*SET,DD,DD/2.0
*SET,DIV,OVER/0.0025
*BEGIN,CONS                             *  BEGIN ESMARCH/CUFF LOOP
*SET,B,A+LINC
*SET,H,H+LINC
*SET,D,COS(OMEG*H)
*SET,D,CC*D
*SET,D,D+DD
*SET,PPRE,C+D
*SET,PPRE,PPRE/2.0
*SET,I,I+LINC
*SET,F,COS(OMEE*I)
*SET,F,EE*F
*SET,F,F+FF
*SET,PPRF,E+F
*SET,PPRF,PPRF/2.0
*SET,PPRF,PPRF*ESMP
*SET,PPR,PPRF+PPRE
*SET,PPR,PPR*POCC
NSEL,Y,A-.001,B+.001
NRSEL,X,RADI+0.0005,RADI+0.002
PSF,0,0,RADI+0.001,PPR
*SET,A,B
*SET,C,D
*SET,E,F
*END                                    *  END ESMARCH/CUFF LOOP
*DO,CONS,1,DIV-1,1
*SET,DIST,STAR+OVER                     *  SET INITIAL CONDITIONS FOR
*SET,DIST,-DIST                         *  CUFF P.D.
*SET,DIST,DIST+0.15
*SET,DIV,DIST/0.0025
*BEGIN,CONS                             *  BEGIN CUFF LOOP
*SET,B,A+LINC
*SET,H,H+LINC
*SET,D,COS(OMEG*H)
*SET,D,CC*D
*SET,D,D+DD
*SET,PPRE,C+D
*SET,PPR,PPRE/2.0
*SET,PPR,PPR*POCC
NSEL,Y,A-.001,B+.001
NRSEL,X,RADI+0.0005,RADI+0.002
PSF,0,0,RADI+0.001,PPR
*SET,A,B
*SET,C,D
*END                                    *  END CUFF LOOP
*DO,CONS,1,DIV-1,1
NALL
EALL
C***
C***
C***   END OF PROGRAM
C***
C***
```

```
C*************************************************************************
C***
C***   THIS PROGRAM PRODUCES THE OUTPUT FROM
C***   NON HOMOGENEOUS ESMARCH/CUFF LIMB COMPRESSION MODEL
C***
C***
STRESS,EX,25,37                         *  DEFINE STRAINS
STRESS,EY,25,38
STRESS,EZ,25,39
STRESS,EXY,25,40
SET,1,1
*SET,EMAX,MESH*60
ESEL,ELEM,1,EMAX,MESH*2                 *  PRINT STRAINS FOR RADIAL NERVE
PRSTRS
ESEL,ELEM,3,EMAX,MESH*2                 *  PRINT DATA FOR MUSCULO NERVE
PRSTRS
ESEL,ELEM,MESH,EMAX,MESH*2              *  PRINT DATA FOR MEDIAN AND ULNAR NERVES
PRSTRS
EALL
NALL
NSEL,NODE,1,481,16                      *  PRINT STRESSES FOR RADIAL NERVE
PRNSTR
NSEL,NODE,4,484,16                      *  PRINT STRESSES FOR MUSCULO NERVE
PRNSTR
NSEL,NODE,7,487,16                      *  PRINT STRESSES FOR MEDIAN AND ULNAR NERVES
PRNSTR
EALL
NALL


C*********************************************************
C***
C***   ROOT FILE TO SET THE PARAMETERS OF THE
C***   HOMOGENEOUS LIMB COMPRESSION MODEL
C***
/PREP7
/TITLE ARM SECTION - ****
*SET,PRES,2                             *  PRESSURE PROFILE
*SET,RADI,.05                           *  LIMB RADIUS
*SET,CUFF,.10                           *  CUFF WIDTH
*SET,OFFS,0.00                          *  OFFSET OF PRESSURE PROFILE
*SET,PEAK,1                             *  NUMBER OF PEAKS
*SET,BONN,1                             *  BONE/MUSCLE INTERFACE SETTING
*SET,SKIN,1                             *  SKIN/CUFF INTERFACE SETTING
*SET,ENDS,0                             *  AXIAL ENDS SETTING
*SET,MESH,7                             *  RADIAL MESH
*SET,ORTH,1                             *  MATERIAL TYPE (ISO OR ORTHO)
*SET,XMOD,15000                         *  MODULUS OF ELASTICITY (RADIAL AND HOOP)
*SET,YMOD,7500                          *  MODULUS OF ELASTICITY (AXIAL)
*SET,XYU,0.45                           *  POISSON RATIO (XY)
*SET,XZU,0.49                           *  POISSON RATIO (XZ AND YZ)
/INPUT,MODEL                            *  CALL THE PROGRAM TO BUILD THE MODEL
AFWRIT                                  *  COMPILE THE PROGRAM
FINISH
/EXE                                    *  EXECUTE THE PROGRAM
/INPUT,27
FINISH
/POST1
/INPUT,OUTPUT                           *  PERFORM ANALISYS ON OUTPUT
FINISH
C***
C***
```

```
C*************************************************************
C***
C***   THIS PROGRAM CONSTRUCTS THE HOMOGENEOUS
C***   LIMB COMPRESSION MODEL
C***
ET,1,25                                 *  CHOOSE ELEMENT TYPE
*IF,ORTH,EQ,0,HERE,8
EX,1,XMOD                               *  ORTHOTROPIC PROPERTIES
EY,1,YMOD
EZ,1,XMOD
NUXY,1,XYU
NUYZ,1,XYU
NUXZ,1,XZU
*GO,HERE,7
EX,1,XMOD                               *  ISOTROPIC PROPERTIES
EY,1,XMOD
EZ,1,XMOD
NUXY,1,XYU
NUYZ,1,XYU
NUXZ,1,XYU
C***
C***
C***   SET UP NODES AND ELEMENTS
C***
C***
EDELE,ALL                               *  ERASE AND COMPRESS ALL
NDELE,ALL                               *  NODES AND ELEMENTS
ECOMPR
NCOMPR
*SET,BONE,RADI*0.30                     *  SET PARAMETERS FOR
*SET,RINC,RADI-BONE                     *  CONSTRUCTION
*SET,RINC,RINC/MESH
*SET,AINC,0.0025
*SET,MES,MESH+1
*SET,X,BONE                             *  SET INITIAL CONDITIONS
*SET,NOD,1
*BEGIN,CONS                             *  LOOP TO PLACE NODES
N,NOD,X,0                               *  ON MODEL
NGEN,61,MES,NOD,NOD,1,,AINC
*SET,NOD,NOD+1
*SET,X,X+RINC
*END
*DO,CONS,1,MESH,1
E,1,2,MES+2,MES+1                       *  PLACE ELEMENTS ON MODEL
EGEN,MESH,1,1,1,1
EGEN,60,MES,1,MESH,1
WSORT,Y                                 *  SORT THE ELEMENTS IN THE
C***                                    *  AXIAL DIRECTION
C***
C***   SET THE BOUNDARY CONDITIONS
C***
C***
*SET,STAR,-CUFF/2
*SET,STAR,STAR+0.15
*IF,SKIN,EQ,0,HERE,10                   *  SET B.C. FOR CUFF/SKIN INTERFACE
NSEL,X,RADI-0.0001,RADI+0.0001          *  SKIN=0 : FREE TO SLIDE AXIALLY
DDELE,ALL                               *  SKIN=1 : RESTRAINED
NRSEL,Y,STAR-0.001,0.151
D,ALL,UY,0
NALL
EALL
*GO,HERE,5
NSEL,X,RADI-0.0001,RADI+0.0001
DDELE,ALL
NALL
EALL
*IF,BONN,EQ,0,HERE,7                    *  SET B.C. FOR BONE/MUSCLE INTERFACE
NSEL,X,BONE,BONE                        *  BONN=0 : FREE TO SLIDE AXIALLY
D,ALL,UX,0                              *  BONN=1 : RESTRAINED
D,ALL,UY,0
NALL
EALL
*GO,HERE,6
```

```
NSEL,X,BONE,BONE
DDELE,ALL
D,ALL,UX,0
NALL
EALL
*IF,ENDS,EQ,0,HERE,5                    *  SET B.C. FOR END OF MODEL
NSEL,Y,0,0                              *  ENDS=0 : FREE TO EXPAND AXIALLY
D,ALL,UY,0                              *  ENDS=1 : RESTRAINED
NALL
EALL
NSEL,Y,0.15,0.15                        *  SET B.C. AT SYMMETRY AXIS
D,ALL,UY,0
NALL
EALL
C***
C***
C***   SET THE PRESSURE DISTRIBUTION
C***
C***
*SET,CIRC,RADI*6.283185308              *  CALCULATE OCCLUSION PRESSURE
*SET,POCC,CIRC*16                       *  USING CUFF WIDTH AND LIMB RADIUS
*SET,POCC,POCC/CUFF
*SET,POCC,POCC*133.0
*SET,POCC,POCC+10000
*IF,PRES,EQ,2,HERE,8                    *  SET THE PRESSURE DISTRIBUTION
*IF,PRES,EQ,3,HERE,37                   *  PRES=1 : RECTANGULAR P.D.
PDELE,ALL                               *  PRES=2 : SINUSOIDAL P.D.
NSEL,Y,STAR-0.001,0.151                 *  PRES=3 : EXPONENTIAL P.D.
NRSEL,X,RADI-0.0001,RADI+0.0001
ENODE
PSF,0,0,RADI,POCC                       *  SET RECTANGULAR P.D.
*GO,HERE,73
*SET,A,STAR                             *  SET INITIAL CONDITIONS FOR
*SET,OMEG,CUFF**-1                      *  SINUSOIDAL P.D.
*SET,OMEG,OMEG*PEAK
*SET,OMEG,OMEG*6.2832
*SET,LINC,0.0025
*SET,H,0
*SET,C,OFFS
*SET,CC,OFFS-1.0
*SET,CC,CC/2.0
*SET,DD,OFFS+1.0
*SET,DD,DD/2.0
*SET,DIV,CUFF/0.005
PDELE,ALL
*BEGIN,CONS                             *  BEGIN SINUSOIDAL LOOP
*SET,B,A+LINC
*SET,H,H+LINC
*SET,D,COS(OMEG*H)
*SET,D,CC*D
*SET,D,D+DD
*SET,PPRE,C+D
*SET,PPRE,PPRE/2.0
*SET,PPRE,PPRE*POCC
NSEL,Y,A-.001,B+.001
NRSEL,X,RADI-0.0001,RADI+0.0001
PSF,0,0,RADI,PPRE
*SET,A,B
*SET,C,D
*END                                    *  END SINUSOIDAL LOOP
*DO,CONS,1,DIV-1,1
*GO,HERE,43
*SET,A,STAR                             *  SET INITIAL CONDITIONS FOR
*SET,MID,CUFF/2                         *  EXPONENTIAL P.D.
*SET,FACT,CUFF**-2
*SET,FACT,FACT*4
*SET,LINC,0.0025
*SET,H,0
*SET,C,0
*SET,DIV,CUFF/0.005
*IF,CUFF,LT,0.15,HERE,2
*SET,DIV,DIV-2
PDELE,ALL
```

```
*BEGIN,CONS                                  *  BEGIN EXPONENTIAL LOOP
*SET,B,A+LINC
*SET,H,H+LINC
*SET,D,MID-H
*SET,D,D**2
*SET,D,D*FACT
*SET,D,D**-1
*SET,D,D-1
*SET,D,-D
*SET,D,EXP(D)
*SET,D,D-1
*SET,D,-D
*SET,PPRE,C+D
*SET,PPRE,PPRE/2.0
*SET,PPRE,PPRE*POCC
NSEL,Y,A-.001,B+.001
NRSEL,X,RADI-0.0001,RADI+0.0001
PSF,0,0,RADI,PPRE
*SET,A,B
*SET,C,D
*END                                         *  END EXPONENTIAL LOOP
*DO,CONS,1,DIV-2,1
NALL
EALL
*IF,CUFF,LT,0.15,HERE,2
*SET,LINC,LINC*3
*SET,MIN,-LINC                               *  SET MIDDLE VALUES TO PMAX
*SET,MIN,MIN+.149                            *  FOR EXP. P.D.
NSEL,Y,MIN,0.151
NRSEL,X,RADI-0.0001,RADI+0.0001
PSF,0,0,RADI,POCC
NALL
EALL
C***
C***
C***    END OF PROGRAM
C***
C***
```

```
C*************************************************************************
C***
C***   THIS PROGRAM PRODUCES THE OUTPUT FROM THE
C***   HOMOGENEOUS LIMB COMPRESSION MODEL
C***
C***
STRESS,EX,25,37                         *  DEFINE STRAINS
STRESS,EY,25,38
STRESS,EZ,25,39
STRESS,EXY,25,40
SET,1,1
*SET,EMAX,MESH*60
ESEL,ELEM,1,EMAX,MESH*2                 *  PRINT STRAINS FOR RADIAL NERVE
PRSTRS
ESEL,ELEM,3,EMAX,MESH*2                 *  PRINT STRAINS FOR MUSCULO NERVE
PRSTRS
ESEL,ELEM,MESH,EMAX,MESH*2              *  PRINT STRAINS FOR MEDIAN AND ULNAR NERVES
PRSTRS
EALL
NALL
NSEL,NODE,1,481,16                      *  PRINT STRESSES FOR RADIAL NERVE
PRNSTR
NSEL,NODE,4,484,16                      *  PRINT STRESSES FOR MUSCULO NERVE
PRNSTR
NSEL,NODE,7,487,16                      *  PRINT STRESSES FOR MEDIAN AND ULNAR NERVES
PRNSTR
EALL
NALL
```

```
C*************************************************************
C***
C***   ROOT FILE TO SET THE PARAMETERS OF THE
C***   NON HOMOGENEOUS LIMB COMPRESSION MODEL
C***
/PREP7
/TITLE ARM SECTION - *****
*SET,PRES,2                            *  PRESSURE PROFILE
*SET,RADI,.05                          *  LIMB RADIUS
*SET,CUFF,.10                          *  CUFF WIDTH
*SET,OFFS,0.00                         *  OFFSET OF PRESSRE PROFILE
*SET,PEAK,1                            *  NUMBER OF PEAKS
*SET,FAT,10                            *  FAT CONTENT
*SET,BONN,1                            *  BONE/MUSCLE INTERFACE SETTING
*SET,SKIN,1                            *  SKIN/CUFF INTERFACE SETTING
*SET,ENDS,0                            *  AXIAL ENDS SETTING
*SET,MESH,7                            *  RADIAL MESH
/INPUT,MODEL                           *  CALL THE PROGRAM TO BUILD THE MODEL
AFWRIT                                 *  COMPILE THE PROGRAM
FINISH
/EXE                                   *  EXECUTE THE PROGRAM
/INPUT,27
FINISH
/POST1
/INPUT,OUTPUT                          *  PERFORM ANALISYS ON OUTPUT
FINISH
C***
C***
```

```
C*************************************************************
C***
C***   THIS PROGRAM CONSTRUCS THE NON HOMOGENEOUS
C***   LIMB COMPRESSION MODEL
C***
ET,1,25                                 *  CHOOSE THE ELEMENT TYPE FOR MUSCLE
EX,1,15000                              *  SET MATERIAL PROPERTIES
EY,1,7500
EZ,1,15000
NUXY,1,.45
NUYZ,1,.45
NUXZ,1,.49
ET,2,81                                 *  CHOOSE THE ELEMENT TYPE FOR FAT
EX,2,250000                             *  SET MATERIAL PROPERTIES
DENS,2,1000
C***
C***
C***   SET UP NODES AND ELEMENTS
C***
C***
EDELE,ALL                               *  ERASE AND COMPRESS ALL
NDELE,ALL                               *  NODES AND ELEMENTS
ECOMPR
NCOMPR
*SET,FAT,FAT/100
*SET,FAT,-FAT
*SET,FAT,FAT+1                          *  CALCULATE FAT THICKNESS
*SET,FAT,FAT**0.5                       *  FROM FAT %
*SET,FAT,-FAT
*SET,FAT,FAT+1
*SET,FAT,FAT*RADI
*SET,BONE,RADI*0.30                     *  SET PARAMETERS FOR
*SET,RINC,RADI-BONE                     *  CONSTRUCTION
*SET,RINC,RINC-FAT
*SET,RINC,RINC/MESH
*SET,AINC,0.0025
*SET,MES,MESH+3
*SET,X,BONE                             *  SET INITIAL CONDITIONS
*SET,NOD,1
*BEGIN,CONS                             *  LOOP TO PLACE NODES
N,NOD,X,0                               *  ON MODEL
NGEN,61,MES,NOD,NOD,1,,AINC
*SET,NOD,NOD+1
*SET,X,X+RINC
*END
*DO,CONS,1,MESH,1
*SET,X,X-RINC
N,NOD,X+FAT
NGEN,61,MES,NOD,NOD,1,,AINC
*SET,X,X+FAT
N,NOD+1,X+0.001                         *  DEFINE THE MUSCLE ELEMENTS
NGEN,61,MES,NOD+1,NOD+1,1,,AINC
MAT,1
TYPE,1
E,1,2,MES+2,MES+1
EGEN,MESH,1,1,1,1
EGEN,60,MES,1,MESH,1
MAT,2                                   *  DEFINE FATTY TISSUE ELEMENTS
TYPE,2
*SET,BB,MES+MESH
E,MESH+1,MESH+2,BB+2,BB+1
*SET,ELLI,MESH*60
*SET,ELLI,ELLI+1
EGEN,60,MES,ELLI,ELLI
MAT,1                                   *  DEFINE THE SKIN ELEMENTS
TYPE,1
*SET,ELL,MESH*60
*SET,ELL,ELL+61
*SET,CC,MES*2
E,MES-1,MES,CC,CC-1
EGEN,60,MES,ELL,ELL,1
WSORT,Y                                 *  SORT THE ELEMENTS IN THE
C***                                    *  AXIAL DIRECTION
```

```
*SET,D,COS(OMEG*H)
*SET,D,CC*D
*SET,D,D+DD
*SET,PPRE,C+D
*SET,PPRE,PPRE/2.0
*SET,PPRE,PPRE*POCC
NSEL,Y,A-.001,B+.001
NRSEL,X,RADI+0.0005,RADI+0.002
PSF,0,0,RADI+0.001,PPRE
*SET,A,B
*SET,C,D
*END                                    *  END SINUSOIDAL LOOP
*DO,CONS,1,DIV-1,1
*GO,HERE,43
*SET,A,STAR                             *  SET INITIAL CONDITIONS FOR
*SET,MID,CUFF/2                         *  EXPONENTIAL P.D.
*SET,FACT,CUFF**-2
*SET,FACT,FACT*4
*SET,LINC,0.0025
*SET,H,0
*SET,C,0
*SET,DIV,CUFF/0.005
*IF,CUFF,LT,0.15,HERE,2
*SET,DIV,DIV-2
PDELE,ALL
*BEGIN,CONS                             *  BEGIN EXPONENTIAL LOOP
*SET,B,A+LINC
*SET,H,H+LINC
*SET,D,MID-H
*SET,D,D**2
*SET,D,D*FACT
*SET,D,D**-1
*SET,D,D-1
*SET,D,-D
*SET,D,EXP(D)
*SET,D,D-1
*SET,D,-D
*SET,PPRE,C+D
*SET,PPRE,PPRE/2.0
*SET,PPRE,PPRE*POCC
NSEL,Y,A-.001,B+.001
NRSEL,X,RADI+0.0005,RADI+0.002
PSF,0,0,RADI+0.001,PPRE
*SET,A,B
*SET,C,D
*END                                    *  END EXPONENTIAL LOOP
*DO,CONS,1,DIV-2,1
NALL
EALL
*IF,CUFF,LT,0.15,HERE,2
*SET,LINC,LINC*3
*SET,MIN,-LINC                          *  SET MIDDLE VALUES TO PMAX
*SET,MIN,MIN+.149                       *  FOR EXP. P.D.
NSEL,Y,MIN,0.151
NRSEL,X,RADI+0.0005,RADI+0.002
PSF,0,0,RADI+0.001,POCC
NALL
EALL
C***
C***
C***   END OF PROGRAM
C***
C***
```

```
C***
C***   SET THE BOUNDARY CONDITIONS
C***
C***
*SET,STAR,-CUFF/2
*SET,STAR,STAR+0.15
*IF,SKIN,EQ,0,HERE,10                  *  SET B.C. FOR CUFF/SKIN INTERFACE
NSEL,X,RADI+0.0005,RADI+0.002          *  SKIN=0 : FREE TO SLIDE AXIALLY
DDELE,ALL                              *  SKIN=1 : RESTRAINED
NRSEL,Y,STAR-0.001,0.151
D,ALL,UY,0
NALL
EALL
*GO,HERE,5
NSEL,X,RADI+0.0005,RADI+0.002
DDELE,ALL
NALL
EALL
*IF,BONN,EQ,0,HERE,7                   *  SET B.C. FOR BONE/MUSCLE INTERFACE
NSEL,X,BONE,BONE                       *  BONN=0 : FREE TO SLIDE AXIALLY
D,ALL,UX,0                             *  BONN=1 : RESTRAINED
D,ALL,UY,0
NALL
EALL
*GO,HERE,6
NSEL,X,BONE,BONE
DDELE,ALL
D,ALL,UX,0
NALL
EALL
*IF,ENDS,EQ,0,HERE,5                   *  SET B.C. FOR END OF MODEL
NSEL,Y,0,0                             *  ENDS=0 : FREE TO EXPAND AXIALLY
D,ALL,UY,0                             *  ENDS=1 : RESTRAINED
NALL
EALL
NSEL,Y,0.15,0.15                       *  SET B.C. AT SYMMETRY AXIS
D,ALL,UY,0
NALL
EALL
C***
C***
C***   SET THE PRESSURE DISTRIBUTION
C***
C***
*SET,CIRC,RADI*6.283185308             *  CALCULATE OCCLUSION PRESSURE
*SET,POCC,CIRC*16                      *  USING CUFF WIDTH AND LIMB RADIUS
*SET,POCC,POCC/CUFF
*SET,POCC,POCC*133.0
*SET,POCC,POCC+10000.0
*IF,PRES,EQ,2,HERE,8                   *  SET THE PRESSURE DISTRIBUTION
*IF,PRES,EQ,3,HERE,37                  *  PRES=1 : RECTANGULAR P.D.
PDELE,ALL                              *  PRES=2 : SINUSOIDAL P.D.
NSEL,Y,STAR-0.001,0.151                *  PRES=3 : EXPONENTIAL P.D.
NRSEL,X,RADI+0.0005,RADI+0.002
ENODE
PSF,0,0,RADI+0.001,POCC                *  SET RECTANGULAR P.D.
*GO,HERE,73
*SET,A,STAR                            *  SET INITIAL CONDITIONS FOR
*SET,OMEG,CUFF**-1                     *  SINUSOIDAL P.D.
*SET,OMEG,OMEG*PEAK
*SET,OMEG,OMEG*6.2832
*SET,LINC,0.0025
*SET,H,0
*SET,C,OFFS
*SET,CC,OFFS-1.0
*SET,CC,CC/2.0
*SET,DD,OFFS+1.0
*SET,DD,DD/2.0
*SET,DIV,CUFF/0.005
PDELE,ALL
*BEGIN,CONS                            *  BEGIN SINUSOIDAL LOOP
*SET,B,A+LINC
*SET,H,H+LINC
```

```
C*************************************************************************
C***
C***   THIS PROGRAM PRODUCES THE OUTPUT FROM THE
C***   NON HOMOGENEOUS LIMB COMPRESSION MODEL
C***
C***
STRESS,EX,25,37                         *  DEFINE STRAINS
STRESS,EY,25,38
STRESS,EZ,25,39
STRESS,EXY,25,40
SET,1,1
*SET,EMAX,MESH*60
ESEL,ELEM,1,EMAX,MESH*2                 *  PRINT STRAINS FOR RADIAL NERVE
PRSTRS
ESEL,ELEM,3,EMAX,MESH*2                 *  PRINT STRAINS FOR MUSCULO NERVES
PRSTRS
ESEL,ELEM,MESH,EMAX,MESH*2              *  PRINT STRAINS FOR MEDIAN AND ULNAR NERVES
PRSTRS
EALL
NALL
NSEL,NODE,1,601,20                      *  PRINT STRESSES FOR RADIAL NERVE
PRNSTR
NSEL,NODE,4,604,20                      *  PRINT STRESSES FOR MUSCULO NERVE
PRNSTR
NSEL,NODE,7,607,20                      *  PRINT STRESSES FOR MEDIAN AND ULNAR NERVES
PRNSTR
EALL
NALL


C*************************************************************
C***
C***   ROOT FILE TO SET THE PARAMETERS OF THE
C***   FULL ARTERY SECTION MODEL
C***
/PREP7
/TITLE ARTERY SECTION - *****
*SET,PRES,3                             *  SET THE PRESSURE DISTRIBUTION
*SET,PMAX,10000                         *  SET MAXIMUM PRESSURE LEVEL
*SET,RAD1,.00265                        *  OUTER RADII OF THE ARTERY
*SET,THIC,0.0005                        *  THICKNESS OF THE ARTERY WALL
*SET,CUFF,.10                           *  CUFF WIDTH
*SET,OFFS,0.00                          *  OFFSET OF PRESSURE PROFILE
*SET,PEAK,1                             *  NUMBER OF PEAKS
*SET,ENDS,0                             *  AXIAL END SETTING
/INPUT,MODEL                            *  CALL THE PROGRAM TO BUILD THE MODEL
AFWRIT                                  *  COMPILE THE PROGRAM
FINISH
/EXE
/INPUT,27                               *  EXECUTE THE PROGRAM
FINISH

C***
C***
```

```
C*************************************************************
C***
C***   THIS PROGRAM CONSTRUCTS THE FINITE
C***   ELEMENT MODEL OF A FULL ARTERY
C***
ET,1,45                                 *  CHOOSE ELEMENT TYPE
EX,1,200000                             *  SET MATERIAL PROPERTIES
EY,1,550000
EZ,1,200000
NUXY,1,.45
NUYZ,1,.45
NUXZ,1,.49
ITER,3,-1
C***
C***
C***   SET UP NODES AND ELEMENTS
C***
C***
EDELE,ALL                               *  ERASE AND COMPRESS ALL
NDELE,ALL                               *  NODES AND ELEMENTS
ECOMPR
NCOMPR
CSYS,1
*SET,RINC,THIC/2                        *  SET PARAMETERS FOR
*SET,AINC,15                            *  CONSTRUCTION
*SET,LINC,0.0025
*SET,X,RADI-THIC                        *  SET INITIAL CONDITIONS
N,1,X,0
NGEN,3,1,1,1,1,RINC                     *  PLACE NODES ON MODEL
NGEN,25,3,1,3,1,,AINC
NGEN,61,75,1,75,1,,,LINC
E,1,2,5,4,22,23,26,25                   *  PLACE ELEMENTS ON MODEL
EGEN,2,1,1,1,1
EGEN,24,3,1,2,1
EGEN,60,75,1,48,1
WSORT,Z                                 *  SORT THE ELEMENTS IN THE
C***                                    *  AXIAL DIRECTION
C***
C***   SET THE BOUNDARY CONDITIONS
C***
C***
CSYS,0                                  *  SET B.C AT THE AXIS OF
NSEL,X,0,0                              *  SYMMETRY
D,ALL,UX,0
NSEL,Y,0,0
D,ALL,UY,0
NSEL,Z,0,0
D,ALL,UZ,0
NALL
EALL
NSEL,Z,0.15,0.15                        *  SET B.C AT THE AXIAL
*IF,ENDS,EQ,0,HERE,11                  *  END OF THE MODEL
*IF,ENDS,EQ,1,HERE,9
*IF,ENDS,EQ,2,HERE,5
D,ALL,UX,0
D,ALL,UY,0
D,ALL,UZ,0
*GO,HERE,5
D,ALL,UX,0
D,ALL,UY,0
*GO,HERE,2
D,ALL,UZ,0

NALL
EALL
C***
C***
C***   SET THE PRESSURE DISTRIBUTION
C***
C***
CSYS,1
*SET,STAR,-CUFF/2
*SET,STAR+0.15
```

```
*IF,PRES,EQ,2,HERE,8                    *  SET THE PRESSURE DISTRIBUTION
*IF,PRES,EQ,3,HERE,37                   *  PRES=1 : RECTANGULAR P.D.
PDELE,ALL                               *  PRES=2 : SINUSOIDAL P.D.
NSEL,Z,STAR-0.001,0.151                 *  PRES=3 : EXPONENTIAL P.D.
NRSEL,X,RADI+0.0005,RADI+0.002
ENODE
PSF,0,0,RADI,PMAX                       *  SET RECTANGULAR P.D.
*GO,HERE,73
*SET,A,STAR                             *  SET INITIAL CONDITIONS FOR
*SET,OMEG,CUFF**-1                      *  SINUSOIDAL P.D.
*SET,OMEG,OMEG*PEAK
*SET,OMEG,OMEG*6.2832
*SET,LINC,0.0025
*SET,H,0
*SET,C,OFFS
*SET,CC,OFFS-1.0
*SET,CC,CC/2.0
*SET,DD,OFFS+1.0
*SET,DD,DD/2.0
*SET,DIV,CUFF/0.005
PDELE,ALL
*BEGIN,CONS                             *  BEGIN SINUSOIDAL LOOP
*SET,B,A+LINC
*SET,H,H+LINC
*SET,D,COS(OMEG*H)
*SET,D,CC*D
*SET,D,D+DD
*SET,PPRE,C+D
*SET,PPRE,PPRE/2.0
*SET,PPRE,PPRE*PMAX
NSEL,Z,A-.001,B+.001
NRSEL,X,RADI,RADI
PSF,0,0,RADI,PPRE
*SET,A,B
*SET,C,D
*END                                    *  END SINUSOIDAL LOOP
*DO,CONS,1,DIV-1,1
*GO,HERE,43
*SET,A,STAR                             *  SET INITIAL CONDITIONS FOR
*SET,MID,CUFF/2                         *  EXPONENTIAL P.D.
*SET,FACT,CUFF**-2
*SET,FACT,FACT*4
*SET,LINC,0.0025
*SET,H,0
*SET,C,0
*SET,DIV,CUFF/0.005
*IF,CUFF,LT,0.15,HERE,2
*SET,DIV,DIV-2
PDELE,ALL
*BEGIN,CONS                             *  BEGIN EXPONENTIAL LOOP
*SET,B,A+LINC
*SET,H,H+LINC
*SET,D,MID-H
*SET,D,D**2
*SET,D,D*FACT
*SET,D,D**-1
*SET,D,D-1
*SET,D,-D
*SET,D,EXP(D)
*SET,D,D-1
*SET,D,-D
*SET,PPRE,C+D
*SET,PPRE,PPRE/2.0
*SET,PPRE,PPRE*PMAX
NSEL,Z,A-.001,B+.001
NRSEL,X,RADI,RADI
PSF,0,0,RADI,PPRE
*SET,A,B
*SET,C,D
*END                                    *  END EXPONENTIAL LOOP
*DO,CONS,1,DIV-2,1
NALL
EALL
```

```
*IF,CUFF,LT,0.15,HERE,2
*SET,LINC,LINC*3
*SET,MIN,-LINC                          *  SET MIDDLE VALUES TO PMAX
*SET,MIN,MIN+.149                       *  FOR EXP. P.D.
NSEL,Z,MIN,0.151
NRSEL,X,RADI,RADI
PSF,0,0,RADI,PMAX
NALL
EALL
CSYS,0
C***
C***
C***   END OF PROGRAM
C***
C***


C*************************************************************
C***
C***   ROOT FILE TO SET THE PARAMETERS OF THE
C***   QUARTER ARTERY SECTION MODEL
C***
/PREP7
/TITLE ARTERY SECTION - *****
*SET,PRES,3                             *  SET PRESSURE DISTRIBUTION
*SET,PMAX,10000                         *  SET MAXIMUM PRESSURE LEVEL
*SET,RADI,.00265                        *  OUTER RADII OF THE ARTERY
*SET,THIC,0.0005                        *  THICKNESS OF THE ARTERY WALL
*SET,CUFF,.10                           *  CUFF WIDTH
*SET,OFFS,0.00                          *  OFFSET OF PRESSURE PROFILE
*SET,PEAK,1                             *  NUMBER OF PEAKS
*SET,ENDS,0                             *  AXIAL END SETTING
/INPUT,MODEL                            *  CALL THE PROGRAM TO BUILD THE MODEL
AFWRIT                                  *  COMPILE THE PROGRAM
FINISH
/EXE
/INPUT,27                               *  EXECUTE THE PROGRAM
FINISH
C***
C***
```

```
C*************************************************************
C***
C***   THIS PROGRAM CONSTRUCTS THE FINITE
C***   ELEMENT MODEL OF A QUARTER ARTERY
C***
ET,1,45                                 *  CHOOSE THE ELEMENT TYPE
EX,1,15000                              *  SET MATERIAL PROPERTIES
EY,1,7500
EZ,1,15000
NUXY,1,.45
NUYZ,1,.45
NUXZ,1,.49
ITER,3,-1
C***
C***
C***   SET UP NODES AND ELEMENTS
C***
C***
EDELE,ALL                               *  ERASE AND COMPRESS ALL
NDELE,ALL                               *  NODES AND ELEMENTS
ECOMPR
NCOMPR
CSYS,1
*SET,RINC,THIC/2                        *  SET PARAMETERS FOR
*SET,AINC,15                            *  CONSTRUCTION
*SET,LINC,0.0025
*SET,X,RADI-THIC                        *  SET INITIAL CONDITIONS
N,1,X,0
NGEN,3,1,1,1,1,1,RINC                   *  PLACE NODES ON MODEL
NGEN,7,3,1,3,1,,AINC
NGEN,61,21,1,21,1,,,LINC
E,1,2,5,4,22,23,26,25                   *  PLACE ELEMENTS ON MODEL
EGEN,2,1,1,1,1
EGEN,6,3,1,2,1
EGEN,60,21,1,12,1
WSORT,Z                                 *  SORT THE ELEMENTS IN THE
C***                                    *  AXIAL DIRECTION
C***
C***   SET THE BOUNDARY CONDITIONS
C***
C***
CSYS,0                                  *  SET B.C AT THE AXIS OF
NSEL,X,0,0                              *  SYMMETRY
D,ALL,UX,0
NSEL,Y,0,0
D,ALL,UY,0
NSEL,Z,0,0
D,ALL,UZ,0
NALL
EALL
NSEL,Z,0.15,0.15
*IF,ENDS,EQ,0,HERE,11                  *  SET B.C AT THE AXIAL
*IF,ENDS,EQ,1,HERE,9                   *  END OF THE MODEL
*IF,ENDS,EQ,2,HERE,5
D,ALL,UX,0
D,ALL,UY,0
D,ALL,UZ,0
*GO,HERE,5
D,ALL,UX,0
D,ALL,UY,0
*GO,HERE,2
D,ALL,UZ,0

NALL
EALL
C***
C***
C***   SET THE PRESSURE DISTRIBUTION
C***
C***
CSYS,1
*SET,STAR,-CUFF/2
*SET,STAR+0.15
```

```
*IF,PRES,EQ,2,HERE,8                    *  SET THE PRESSURE DISTRIBUTION
*IF,PRES,EQ,3,HERE,37                   *  PRES=1 : RECTANGULAR P.D.
PDELE,ALL                               *  PRES=2 : SINUSOIDAL P.D.
NSEL,Z,STAR-0.001,0.151                 *  PRES=3 : EXPONENTIAL P.D.
NRSEL,X,RADI+0.0005,RADI+0.002
ENODE
PSF,0,0,RADI,PMAX                       *  SET RECTANGULAR P.D.
*GO,HERE,73
*SET,A,STAR                             *  SET INITIAL CONDITIONS FOR
*SET,OMEG,CUFF**-1                      *  SINUSOIDAL P.D.
*SET,OMEG,OMEG*PEAK
*SET,OMEG,OMEG*6.2832
*SET,LINC,0.0025
*SET,H,0
*SET,C,OFFS
*SET,CC,OFFS-1.0
*SET,CC,CC/2.0
*SET,DD,OFFS+1.0
*SET,DD,DD/2.0
*SET,DIV,CUFF/0.005
PDELE,ALL
*BEGIN,CONS                             *  BEGIN SINUSOIDAL LOOP
*SET,B,A+LINC
*SET,H,H+LINC
*SET,D,COS(OMEG*H)
*SET,D,CC*D
*SET,D,D+DD
*SET,PPRE,C+D
*SET,PPRE,PPRE/2.0
*SET,PPRE,PPRE*PMAX
NSEL,Z,A-.001,B+.001
NRSEL,X,RADI,RADI
PSF,0,0,RADI,PPRE
*SET,A,B
*SET,C,D
*END                                    *  END SINUSOIDAL LOOP
*DO,CONS,1,DIV-1,1
*GO,HERE,43
*SET,A,STAR                             *  SET INITIAL CONDITIONS FOR
*SET,MID,CUFF/2                         *  EXPONENTIAL P.D.
*SET,FACT,CUFF**-2
*SET,FACT,FACT*4
*SET,LINC,0.0025
*SET,H,0
*SET,C,0
*SET,DIV,CUFF/0.005
*IF,CUFF,LT,0.15,HERE,2
*SET,DIV,DIV-2
PDELE,ALL
*BEGIN,CONS                             *  BEGIN EXPONENTIAL LOOP
*SET,B,A+LINC
*SET,H,H+LINC
*SET,D,MID-H
*SET,D,D**2
*SET,D,D*FACT
*SET,D,D**-1
*SET,D,D-1
*SET,D,-D
*SET,D,EXP(D)
*SET,D,D-1
*SET,D,-D
*SET,PPRE,C+D
*SET,PPRE,PPRE/2.0
*SET,PPRE,PPRE*PMAX
NSEL,Z,A-.001,B+.001
NRSEL,X,RADI,RADI
PSF,0,0,RADI,PPRE
*SET,A,B
*SET,C,D
*END                                    *  END EXPONENTIAL LOOP
*DO,CONS,1,DIV-2,1
NALL
EALL
```

```
*IF,CUFF,LT,0.15,HERE,2
*SET,LINC,LINC*3
*SET,MIN,-LINC                          *  SET MIDDLE VALUES TO PMAX
*SET,MIN,MIN+.149                       *  FOR EXP. P.D.
NSEL,Z,MIN,0.151
NRSEL,X,RADI,RADI
PSF,0,0,RADI,PMAX
NALL
EALL
CSYS,0
C***
C***
C***    END OF PROGRAM
C***
C***
```

Appendix D

THICK-WALLED CYLINDER THEORY

The radial and circumferential stress profiles in a thick-walled cylinder are developed in accordance with the imposed boundary conditions and material properties associated with the limb compression phenomenon. Figure D.1 shows the thick-walled cylinder model under limb compression constraints.

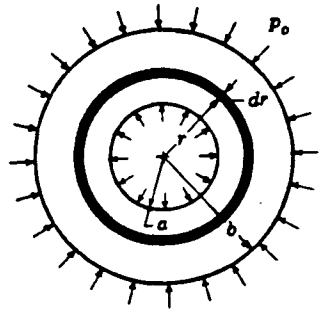

Figure D.1: **Thick-walled cylinder under limb compression constraints [50]**

The material properties were set as described in Chapter 3:

$$\left.\begin{aligned} E_r = E_\theta &= 15000\,Pa \\ E_z &= 7500\,Pa \\ \nu_{rz} = \nu_{\theta z} &= 0.45 \\ \nu_{r\theta} &= 0.49 \end{aligned}\right\} \qquad \text{(D.1)}$$

The boundary and loading conditions were set as follows:

$$\left.\begin{aligned} \sigma_r &= -P_0 \quad \text{at} \quad r = b \\ \varepsilon_\theta &= 0 \quad\;\; \text{at} \quad r = a \end{aligned}\right\} \tag{D.2}$$

Figure D.2 shows the free body diagram of a half-annulus of thickness dr.

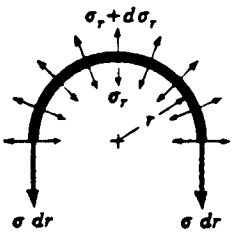

Figure D.2: **Free body diagram of a selected annulus [50]**

The resulting equilibrium equation follows:

$$2\sigma_\theta dr + 2\sigma_r r - 2(\sigma_r + d\sigma_r)(r + dr) = 0 \tag{D.3}$$

By simplifying and neglecting higher order terms, Equation D.4 is obtained.

$$\sigma_\theta - \sigma_r - r\frac{d\sigma_r}{dr} = 0 \tag{D.4}$$

By imposing a constant longitudinal strain along the full section of the cylinder the following relationship is established:

$$\varepsilon_z = -\frac{\nu_{\theta z}\sigma_\theta}{E_\theta} - \frac{\nu_{rz}\sigma_r}{E_r} \tag{D.5}$$

Since the material properties impose that $E_\theta = E_r = E$, and that $\nu_{\theta z} = \nu_{rz} = \nu$, it follows that:

$$-\frac{E\varepsilon_z}{\nu} = \sigma_\theta + \sigma_r = 2C_1 \quad C_1 = \text{a constant} \tag{D.6}$$

By combining Equations D.4 and D.6 the following relationship is found:

$$r\frac{d\sigma_r}{dr} + 2\sigma_r = 2C_1 \tag{D.7}$$

Multiplying each side by r:

$$r^2\frac{d\sigma_r}{dr} + 2r\sigma_r = 2rC_1 \tag{D.8}$$

And noting that:

$$\frac{d(r^2\sigma_r)}{dr} = r^2 d\sigma_r dr + 2r\sigma_r \tag{D.9}$$

By combining Equations D.8 and D.9, Equation D.10 results.

$$d(r^2\sigma_r) = 2rC_1 dr \tag{D.10}$$

Performing the integration results in these simplified relationships:

$$r^2\sigma_r = r^2C_1 + C_2 \qquad C_2 : \text{integration constant} \tag{D.11}$$

$$\sigma_\theta = 2C_1 - \sigma_r \qquad \text{from Equation D.6} \tag{D.12}$$

By substitution and simplification Equations D.13 and D.14 are generated.

$$\sigma_r = C_1 + \frac{C_2}{r^2} \tag{D.13}$$

$$\sigma_\theta = C_1 - \frac{C_2}{r^2} \tag{D.14}$$

The two constants are evaluated by applying the boundary conditions described above in Equation D.2. The boundary condition at $r = a$ can be expressed as follows:

$$\varepsilon_\theta = 0 = \frac{\sigma_\theta}{E_\theta} - \nu_{r\theta}\frac{\sigma_r}{E_r} \quad \text{or} \quad \sigma_r = \frac{\sigma_\theta}{\nu_{r\theta}}\left(\frac{E_r}{E_\theta}\right) \tag{D.15}$$

Note that $E_r/E_\theta = 1.0$ and therefore the boundary conditions can be written as follows:

$$\left.\begin{aligned} \sigma_r &= \tfrac{\sigma_\theta}{\nu_{r\theta}} \quad \text{at } r = a \\ \sigma_r &= -P_0 \quad \text{at } r = b \end{aligned}\right\} \tag{D.16}$$

Substituting into Equations D.13 and D.14 for $r = a$:

$$\left.\begin{array}{lll} \sigma_r = & \frac{\sigma_\theta}{\nu_{r\theta}} & = C_1 + \frac{C_2}{a^2} \\ \sigma_\theta = & \nu_{r\theta}\left(C_1 + \frac{C_2}{a^2}\right) & = C_1 - \frac{C_2}{a^2} \end{array}\right\} \tag{D.17}$$

An expression for C_1 is established by isolating it in Equation D.17.

$$C_1 = C_2\left(\frac{(1+\nu_{r\theta})}{a^2(1-\nu_{r\theta})}\right) \tag{D.18}$$

Substituting into Equations D.13 and D.14 for $r = b$, and replacing C_1 by its equivalent, Equation D.19 is generated.

$$-P_0 = C_2\left(\frac{(1+\nu_{r\theta})}{a^2(1-\nu_{r\theta})} + \frac{1}{b^2}\right) \tag{D.19}$$

By isolating C_2 in the previous equation:

$$C_2 = \frac{P_0}{\left(\frac{(1+\nu_{r\theta})}{a^2(1-\nu_{r\theta})} + \frac{1}{b^2}\right)} \tag{D.20}$$

Substituting Equations D.18 and D.20 back into Equations D.13 and D.14, the expressions relating radial and circumferential stress profiles along the radial axis are defined.

$$\sigma_r = \frac{-P_0 b^2}{b^2(1+\nu_{r\theta}) + a^2(1-\nu_{r\theta})}\left((1+\nu_{r\theta}) + \frac{a^2}{r^2}(1-\nu_{r\theta})\right) \tag{D.21}$$

$$\sigma_\theta = \frac{-P_0 b^2}{b^2(1+\nu_{r\theta}) + a^2(1-\nu_{r\theta})}\left((1+\nu_{r\theta}) - \frac{a^2}{r^2}(1-\nu_{r\theta})\right) \tag{D.22}$$

Note that in both expressions the only variable associated with the material properties of the cylinder is $\nu_{r\theta}$. However, this is only true in the case of symmetrically defined material properties.

Appendix E

LIMB COMPRESSION MODEL SIMULATIONS

For each of the simulations performed using the limb compression models (single-layer and multi-layer), a code name was given in order to uniquely define the associated parameter combination. Table E.1 defines all possible settings for each of the five positions in the code name.

Table E.1: **Code name nomenclature**

1^{st} position	2^{nd} position	3^{rd} position	4^{th} and 5^{th} positions
H : Single-layer N : Multi-layer	I : Isotropic O : Orthotropic	N : No Esmarch E : Esmarch	W : Cuff Width R : Limb Radius P : Pressure Profile BC : Boundaries O : Offset N : Number of Peaks F : Fat Content U : Esmarch Overlap V : Esmarch Width E : Esmarch Pressure

Example : HONWRXY ⟶ H : Single-layer
O : Orthotropic
N : No Esmarch
W : Cuff Width ⇒ X
R : Limb Radius ⇒ Y

All simulations performed on the limb compression models are described in the tables of this Appendix. Tables E.2 through E.9 show all simulations performed under simple tourniquet configurations, whereas Tables E.10 to E.12 show the simulations performed under Esmarch/tourniquet configurations. It should be noted that only two variables at a time are investigated while the others are held constant at their respective default value (listed below). In order to reduce the number of tables, the first three letters of the code names appear in the titles.

Parameter default values :

Pressure Profile	: Sinusoidal
Boundaries	: RRF
Offset	: 0.0
Peaks	: 1
Cuff Width	: 10 cm
Limb Radius	: 50 mm
Fat Content	: 10 %

Table E.2: **Cuff width vs limb radius (HON & NON)**

Limb Radius (mm)	Cuff Width (cm)							
	2.5	5.0	7.5	10.0	12.5	15.0	17.5	20.0
30	WR13	WR23	WR33	WR43	WR53	WR63	WR73	WR83
40	WR14	WR24	WR34	WR44	WR54	WR64	WR74	WR84
50	WR15	WR25	WR35	WR45	WR55	WR65	WR75	WR85
60	WR16	WR26	WR36	WR46	WR56	WR66	WR76	WR86
70	WR17	WR27	WR37	WR47	WR57	WR67	WR77	WR87

Table E.3: **Cuff width vs pressure profile (HON & NON)**

Profile	Cuff Width (cm)							
	2.5	5.0	7.5	10.0	12.5	15.0	17.5	20.0
Sin	WP1S	WP2S	WP3S	WP4S	WP5S	WP6S	WP7S	WP8S
Exp	WP1E	WP2E	WP3E	WP4E	WP5E	WP6E	WP7E	WP8E
Rec	WP1R	WP2R	WP3R	WP4R	WP5R	WP6R	WP7R	WP8R

Table E.4: **Limb radius vs pressure profile (HON & NON)**

Profile	Limb Radius (mm)				
	30	40	50	60	70
Sin	LP3S	LP4S	LP5S	LP6S	LP7S
Exp	LP3E	LP4E	LP5E	LP6E	LP7E
Rec	LP3R	LP4R	LP5R	LP6R	LP7R

Table E.5: **Offset vs peaks (HON & NON)**

Peaks	Offset					
	0.0	0.2	0.4	0.6	0.8	1.0
1	ON01	ON21	ON41	ON61	ON81	ONT1
2	ON02	ON22	ON42	ON62	ON82	ONT2
3	ON03	ON23	ON43	ON63	ON83	ONT3
4	ON04	ON24	ON44	ON64	ON84	ONT4

Table E.6: **Cuff width vs fat content (NON)**

Fat Content (%)	Cuff Width (cm)							
	2.5	5.0	7.5	10.0	12.5	15.0	17.5	20.0
5.0	WF11	WF21	WF31	WF41	WF51	WF61	WF71	WF81
10.0	WF12	WF22	WF32	WF42	WF52	WF62	WF72	WF82
15.0	WF13	WF23	WF33	WF43	WF53	WF63	WF73	WF83
20.0	WF14	WF24	WF34	WF44	WF54	WF64	WF74	WF84

Table E.7: **Fat content vs limb radius (NON)**

Limb Radius (mm)	Fat Content (%)			
	5.0	10.0	15.0	20.0
30	FR13	FR23	FR33	FR43
40	FR14	FR24	FR34	FR44
50	FR15	FR25	FR35	FR45
60	FR16	FR26	FR36	FR46
70	FR17	FR27	FR37	FR47

Table E.8: **Fat content vs pressure profile (NON)**

Profile (mm)	Fat Content (%)			
	5.0	10.0	15.0	20.0
Sin	FR1S	FR2S	FR3S	FR4S
Exp	FR1E	FR2E	FR3E	FR4E
Rec	FR1R	FR2R	FR3R	FR4R

Table E.9: **Boundary conditions (HON & NON)**

Bone/Muscle	Skin/Cuff	Axial Ends	Code
F	F	F	BCFFF
F	F	R	BCFFR
F	R	F	BCFRF
F	R	R	BCFRR
R	F	F	BCRFF
R	F	R	BCRFR
R	R	F	BCRRF
R	R	R	BCRRR

Table E.10: **Esmarch overlap vs Esmarch width (HOE & NOE)**

Width (mm)	Overlap				
	0.0	0.25	0.5	0.75	1.0
20	UV02	UV12	UV22	UV32	UV42
30	UV03	UV13	UV23	UV33	UV43
40	UV04	UV14	UV24	UV34	UV44
50	UV05	UV15	UV25	UV35	UV45

Table E.11: **Esmarch overlap vs Esmarch pressure (HOE & NOE)**

Pressure (%)	Overlap				
	0.0	0.25	0.5	0.75	1.0
10	UE01	UE11	UE21	UE31	UE41
20	UE02	UE12	UE22	UE32	UE42
30	UE03	UE13	UE23	UE33	UE43
40	UE04	UE14	UE24	UE34	UE44
50	UE05	UE15	UE25	UE35	UE45

Table E.12: **Esmarch width vs Esmarch pressure (HOE & NOE)**

Pressure (%)	Width (mm)			
	20	30	40	50
10	VE21	VE31	VE41	VE51
20	VE22	VE32	VE42	VE52
30	VE23	VE33	VE43	VE53
40	VE24	VE34	VE44	VE54
50	VE25	VE35	VE45	VE55